

THE UNIVERSITY *of* EDINBURGH

This thesis has been submitted in fulfilment of the requirements for a postgraduate degree (e. g. PhD, MPhil, DClinPsychol) at the University of Edinburgh. Please note the following terms and conditions of use:

- This work is protected by copyright and other intellectual property rights, which are retained by the thesis author, unless otherwise stated.
- A copy can be downloaded for personal non-commercial research or study, without prior permission or charge.
- This thesis cannot be reproduced or quoted extensively from without first obtaining permission in writing from the author.
- The content must not be changed in any way or sold commercially in any format or medium without the formal permission of the author.
- When referring to this work, full bibliographic details including the author, title, awarding institution and date of the thesis must be given.

Seismic and Hydroacoustic Monitoring of Bedload Transport in an Alluvial River

Bronwyn Matthews



Thesis submitted for the degree of Doctor of Philosophy

The University of Edinburgh

2025

Abstract

Monitoring the mobilisation and transport of bedload in rivers is key to understanding landscape evolution and sediment transfer, as well as providing valuable information for problems in the fields of ecology, river and landuse management, and civil engineering. When rivers transport bedload their erosive capacity increases which not only affects infrastructure such as rivers and dams, but it also influences channel change by eroding or aggrading bars and banks altering the channel capacity and subsequently flood risk. Bedload transport has traditionally been measured through the use of geomorphic measurements, such as manual sediment sampling, geomorphic mapping, and empirical equations. However, advances in measurement methods and technologies such as drone surveys, numerical modelling, and acoustic monitoring have been at the forefront of bedload transport studies over the last couple of decades. These methods extend the spatial and temporal resolution of monitoring efforts, allowing better understanding of the characteristics of sediment mobilisation and the effects of bedload transport over longer timescales. In particular, seismic monitoring has emerged as a valuable tool for monitoring river processes such as propagating flood waves and the movement of bedload. This provides an opportunity to indirectly monitor river processes over greater spatial and temporal scales to previous methods. A significant challenge remains in independently characterising the seismic signature of bedload transport from other sources such as turbulence. Additionally, there remains some uncertainty in the interpretation of seismic bedload transport signals in complex alluvial channels. This thesis examines seismic signals recorded adjacent to an alluvial mountain river in Scotland (the River Feshie) and presents a unique dataset combining three-component seismic data with complementary hydroacoustic measurements, to analyse bedload transport during high river flows.

In the first part of this thesis, I examine the characteristics of the recorded river-induced seismic signals during high river discharge events. Using data from eight seismic sensors located along the study reach along with local stream gauge data, I compare the site and event variabilities and find that there is greater variability in the signals recorded at different sites than there are over different hydrological events. Additionally, I observe that the sensor locations have a significant effect on the signals recorded with those on flatter ground and/or closer to the river, located in open areas, recording clearer and stronger seismic signals with more distinct bedload transport signals. This can inform on siting of seismic sensors in future seismic studies.

Through the analysis of seismic signals recorded over high flow events combined with independent interpretation of the occurrence of bedload mobilisation through hydroacoustic measurements, I then assess the consistency of bedload transport thresholds in response to changing flow conditions. Results indicate that bedload

entrainment thresholds vary from event to event and may show a link with event duration and magnitude, as well as being influenced by the occurrence of successive events due to armouring effects. This analysis also revealed that the relationship between bedload-induced seismic power and water level varied between events with events exceeding $\sim$ 1.40 m water level exhibiting distinct variations in this relationship between the rising and falling limb of the hydrograph with increased seismic power prolonged on the falling limb. Previous studies have used these hysteretic relationships as an indicator of bedload transport; however, my work reveals that bedload transport can occur without these relationships present in the data.

In the third part of this thesis, I explore the directional-component dominance of the seismic signals recorded adjacent to the river to interpret whether river-induced seismic signals, and specifically bedload signals, exhibit stronger signals in a single direction. Analysis of the three orthogonal components of the recorded seismic signals revealed that river-induced signals are strongest in the two horizontal directions, consistent with Love-wave propagation. This suggests that existing fluvial seismic models and studies may be incorrectly using the Rayleigh wave interpretation under the assumption that the dominant component of bedload-induced seismic signals is in the vertical direction. Additionally, the signals from the movement of bedload particles generally induce a stronger stream-parallel signal as a result of downstream particle motion.

This work adds to the growing body of research using indirect bedload transport monitoring methods, such as seismic and hydroacoustic measurements, to understand complex fluvial dynamics in alluvial rivers. By advancing the use of seismic monitoring, it improves understanding of sediment movement and its effects on river dynamics. Using a unique dataset from the River Feshie in Scotland, this research reveals: (1) the importance of sensor placement for clear seismic signals produced by bedload transport; (2) variability in bedload entrainment thresholds, which are influenced by event duration and magnitude, as well as the occurrence of successive events; and (3) a strong horizontal directional component to the seismic signals generated by bedload transport, challenging assumptions about vertical dominance. These findings demonstrate the value of combining independent datasets for long-term monitoring of bedload transport, offering insights into the spatial and temporal evolution of sediment mobilisation. This provides crucial information for effective river and land-use management, particularly as climate change alters the frequency and intensity of high-flow events.

Lay Summary

Monitoring how rivers move and carry sediment is essential for understanding how landscapes change and how sediment is transferred. This information is also useful for solving problems in ecology, river and land management, and civil engineering. When rivers move sediment, they become more erosive, which can impact infrastructure like dams and riverbanks, change the river channel, and affect flood risks. Traditionally, sediment movement has been measured using manual sampling, mapping, and equations. However, new methods such as drone surveys, computer models, and acoustic monitoring have greatly improved our ability to study these processes. Seismic monitoring of rivers, which involves measuring ground vibrations caused by water and sediment interactions with the river bed, has become a valuable tool for studying river processes over larger areas and longer times.

A major challenge is distinguishing the seismic signals of sediment movement from other sources like water turbulence, as well as interpreting these signals in complex river environments. This study examines seismic signals from the River Feshie in Scotland, combining seismic data with hydroacoustic (underwater sound) measurements to analyse sediment movement during high river flows.

First, I studied the seismic signals recorded during high river flow events. Using data from eight seismic sensors along with water level data, I found that the signals varied more between different sensor locations than between different events. Sensors placed on flat ground, closer to the river, and in open areas recorded clearer and stronger signals of sediment movement.

Next, I analysed the water level thresholds that control sediment movement. The results showed that these thresholds change from event to event and may be influenced by the duration and magnitude of the events, as well as by the presence of previous events. I also found that the relationship between seismic power and water level changes during high flow events, with increased seismic power lasting longer as the water level decreases.

Finally, I explored whether the direction of movement of the seismic signals could reveal more about sediment movement processes. The analysis showed that the signals produced by the river are strongest in the horizontal directions, suggesting that current seismic models might be incorrect in assuming that vertical signals are dominant for sediment movement. Additionally, I found that the signals for sediment movement were strongest in the direction parallel to the river.

This research contributes to the growing field of using seismic and hydroacoustic measurements to understand river dynamics. It highlights the importance of combining different types of data for long-term monitoring, providing valuable insights for effective river and land management in the face of climate change and its impact on high-flow events. Additionally, the research demonstrates that seismic monitoring is a promising tool for improving our understanding of how rivers move

sediment. It reveals key insights, such as: (1) how sensor placement affects the clarity of seismic signals from sediment movement; (2) how the conditions of each event can change the threshold at which sediment is moved; and (3) that seismic signals from sediment transport often show a stronger horizontal directional component, though this can vary depending on the specific conditions of the event and site. These findings can help improve sediment monitoring techniques, providing better data for managing rivers and infrastructure, particularly as climate change alters the frequency and intensity of high-flow events.

"The more that you read, the more things you will know. The more that you learn, the more places you'll go"

Dr Seuss

Acknowledgements

I can't believe I've finally made it to this stage. The past four years have been tough but incredibly rewarding, and I'm so grateful to everyone who has helped and supported me along the way. I apologise if I miss anyone in these acknowledgments.

First and foremost, it's been a privilege to be supervised by Mark Naylor and Hugh Sinclair. I've learned so much from their combined expertise, and their support and encouragement have kept me on track. Mark, thank you for sharing your geophysical knowledge, and Hugh, thank you for your insights into geomorphology. I also appreciate the laughs during fieldwork and your willingness to join me at Feshie, even in the pouring rain or snow. Special thanks to Matt Gervais, who has been amazing with technical and field support. Your willingness to jump in the Hilux for six-hour round trips to download data or change batteries made so much of this work possible. I think I speak for everyone on the project when I say we're incredibly grateful for your help. Thanks to Calum Cuthill for your early help with instrument deployment and seismic signal processing. Karen Mair and Karen Lythgoe, your guidance with the hydroacoustic and seismic data has been invaluable. Anna Smith, thanks for your fieldwork help and your Master's work on hydroacoustic signals at the Feshie.

Thanks also to my secondary supervisors, Richard Williams from Glasgow University and Michael Dietze from GFZ Potsdam, for your support in the geomorphological and seismic aspects. Richard, I appreciate your help with my first co-authored paper and allowing me to get involved in the drone surveys at the Feshie. Also, thanks to Andrew Black of the University of Dundee. Since my Master's dissertation, you helped me kickstart my professional career and have been a big help in this Ph.D. Thank you for connecting us with the contacts needed to undertake fieldwork in the Feshie, facilitating our fieldwork there, and providing access to your stream gauge and meteorological data.

Thank you to Glen Feshie estate and Wildlands Ltd. for allowing access to such a beautiful place for my fieldwork. Your rewilding efforts are inspiring, and I'm excited to follow your journey.

Additionally, a big thanks to the Engineering and Physical Sciences Research Council for funding this Ph.D.

I'm also grateful to the entire PGR team, especially Sophie Ramette, for supporting me throughout this Ph.D. and helping me navigate sick leave options when I injured my back. To Anya, Saraswati, Prakash, Polly, Nick, Louis, and Morag, thanks for the office chats and banter, even though I wasn't around much in the last year. Lou and Laura, thank you for your help during field trips.

On a personal note, I'm deeply grateful to my family and close friends for their encouragement and support, and for always believing in me. Mum, thank you for joining me on numerous weekends of bagging munros and cycling, offering a much-

needed distraction from Ph.D. work. And, to my fiancé, Connor, thank you for your unwavering support during this Ph.D., for being a shoulder to cry on during (many) stressful times, and for always reminding me of what I'm capable of.

Contents

Abstract ii

Lay Summary iv

Acknowledgements vii

Contents x

List of Figures xv

List of Tables xxvii

1 Introduction 1
- 1.1 Study site . . . 2
  - 1.1.1 Catchment characteristics . . . 2
  - 1.1.2 Catchment hydrological record . . . 4
  - 1.1.3 Catchment land-use . . . 4
- 1.2 Research aims and objectives . . . 6
- 1.3 Thesis outline . . . 7

2 Scientific Context 8
- 2.1 Background . . . 8
- 2.2 Importance of bedload transport monitoring . . . 10
- 2.3 Traditional bedload transport measurement techniques . . . 11
- 2.4 Numerical modelling of bedload transport . . . 12
- 2.5 Indirect bedload transport measurements . . . 12
- 2.6 Seismic monitoring of bedload transport . . . 13
  - 2.6.1 Fundamentals of environmental seismology . . . 14
  - 2.6.2 Use of geophones for river studies . . . 15
  - 2.6.3 Fluvial seismology models . . . 17
  - 2.6.4 Key bedload transport seismic studies . . . 18
    - 2.6.4.1 Comparisons of key fluvial seismology studies . . . 27
- 2.7 Hydroacoustic monitoring of bedload transport . . . 27

3 General Approach and Methods 30
- 3.1 Measurement methods . . . 30
  - 3.1.1 Seismic measurements . . . 32
  - 3.1.2 Seismic model . . . 34
  - 3.1.3 Hydroacoustic measurements . . . 35
  - 3.1.4 Water level measurements . . . 37

3.1.5 Timelapse cameras . . . 38
3.1.5.1 Cameras deployed on river banks . . . 38
3.1.5.2 Camera deployed in the channel . . . 40
3.1.6 Grain size measurements . . . 41
3.1.7 Channel geometry measurements . . . 44
3.1.8 Discharge measurements . . . 46
3.1.9 Active seismic surveys . . . 47
3.2 Site Characterisation . . . 49
3.2.1 Channel slope . . . 49
3.2.2 Hydrological regime . . . 49
3.2.3 Grain size distribution . . . 51
3.2.4 Entrainment thresholds and bedload flux . . . 53
3.2.5 Seismic properties of the site . . . 56
3.3 Experimental design . . . 59
3.3.1 Chosen stretch of the river . . . 59
3.3.2 Specific sites of deployed instruments . . . 60
3.4 Data Processing . . . 64
3.4.1 Seismic data processing . . . 64
3.4.2 Stream gauge data processing . . . 65
3.4.3 Hydroacoustic data processing . . . 66

4 Site and event variations in river-induced seismic characteristics 67
4.1 Introduction . . . 67
4.2 Methods . . . 69
4.2.1 Bedload transport model inputs . . . 69
4.2.2 Stream gauge data . . . 71
4.2.3 Seismic data . . . 71
4.2.4 Hydroacoustic data . . . 72
4.3 Results . . . 73
4.3.1 Bedload transport and turbulence model outputs . . . 73
4.3.2 River-induced seismic signals . . . 74
4.3.3 Site comparison . . . 76
4.3.3.1 Site Comparison Summary . . . 87
4.3.4 Event comparison . . . 88
4.3.4.1 Event Comparison Summary . . . 94
4.3.5 Seismic and hydroacoustic signal frequency content . . . 94
4.3.5.1 Comparison summary of seismic and hydroacoustic frequency content . . . 98
4.4 Discussion and Conclusion . . . 99
4.4.1 Distinction between bedload and turbulence induced signals . 99
4.4.2 Site and event comparisons . . . 101
4.4.3 Remaining challenges in seismic monitoring of bedload transport 103

5 Inferring bedload transport thresholds through seismic and hydroacoustic recordings 105
5.1 Introduction . . . 105
5.2 Methods . . . 110
5.2.1 Data collection . . . 110
5.2.1.1 Stream gauge data . . . 110

5.2.1.2 Seismic and hydroacoustic data . . . 111
5.2.2 Data processing and analysis . . . 113
5.3 Results . . . 114
5.3.1 Seismic signal characteristics . . . 115
5.3.2 Bedload transport characteristics . . . 118
5.3.2.1 Entrainment thresholds of coarse bedload . . . 118
5.3.2.2 Seismic power versus water level hysteresis relationships . . . 120
5.3.2.3 Bedload transport hysteresis observed using offset stream gauge data . . . 123
5.4 Discussion . . . 123
5.4.1 Seismic characteristics . . . 123
5.4.2 Bedload entrainment threshold variability . . . 125
5.4.3 Hysteresis patterns observed using collocated measurements . 126
5.4.4 Hysteresis patterns observed using offset seismic and stream gauge measurements . . . 127
5.5 Conclusions . . . 129

6 Comparison of the directional components of the river-induced seismic signals 130
6.1 Introduction . . . 130
6.1.1 Seismic wave types . . . 130
6.1.2 River-induced seismic signals . . . 131
6.1.3 HVSR method to understand site effects . . . 133
6.1.4 Chapter overview . . . 134
6.2 Methods . . . 134
6.2.1 Data . . . 134
6.2.2 Calculating HVSR of river-induced seismic signals . . . 135
6.3 Results . . . 137
6.3.1 HVSR observations from seismic signals at the River Feshie using the averaged horizontal components . . . 137
6.3.1.1 September-October 2022 event . . . 138
6.3.1.2 October 2023 event . . . 147
6.3.2 Comparing the HVSR values using the stream-parallel and stream-perpendicular components . . . 156
6.3.2.1 September-October 2022 event . . . 156
6.3.2.2 October 2023 event . . . 162
6.3.3 Frequency analysis of calculated HVSR . . . 168
6.3.4 Results Summary . . . 169
6.4 Discussion . . . 171
6.4.1 Are there stronger horizontal or vertical signals in river-induced seismic signals? . . . 171
6.4.2 Do river processes induce stream-parallel or stream-perpendicular seismic signals? . . . 174
6.4.3 HVSR method implications on seismic bedload transport studies 174
6.5 Conclusion . . . 175

7 Discussion **176**
7.1 Interpreting river-induced seismic signals 177
7.2 Importance of hydroacoustic measurements 178
7.3 Directional components of river-induced seismic signals 179
7.4 PhD challenges 180
7.5 Future work 181
7.6 Wider implications 183

8 Conclusions **186**

Bibliography **189**

Appendices **209**

A R 'eseis' Package Code **209**

B Active Seismic Survey **211**

C Grain Size Measurements **213**

D Bedload Flux Calculations **222**

E Additional Seismic Signals **225**

F ESPL manuscript of Chapter 5: Matthews et al. (2024) **227**

List of Figures

1.1 (a) Location of the River Feshie catchment in Scotland.(b) River Feshie catchment and confluence with River Spey. 2
1.2 River Feshie catchment characteristics (Soulsby et al., 2006). 3
1.3 SEPA gauged daily flow data dating back to the start of records in late 1992. Accessed from NRFA (2024). NRFA data is only available up until the end of the previous water year (October-September). . . 4
1.4 Clustering of SEPA 15 minute resolution water level data over the 5% flow exceedance value from NRFA (2024). Data presented includes values over that threshold for the last ten years as that was what was available through (SEPA, 2024). 5
1.5 The number of instantaneous peak flows in each month over 10 years of data from SEPA (2024) that exceeded the current NRFA (2024) POT (peak over threshold) value of 68.5 m^3s^{-1}. 5

2.1 Boundary layer characteristics showing the more uniform velocity gradient in thick boundary layers (*Boundary Layer — Definition & Characteristics* 2024) 9
2.2 Sediment trap deployment from a study by Bunte et al. (2007) to acquire information on bedload transport during events. 12
2.3 Examples of impact plate geophone set up (Wyss et al., 2014) and acoustic pipe hydrophone set up (Dell'Agnese et al., 2014) 13
2.4 Propagation of surface waves and body waves through the Earth. . . 15
2.5 Signal differences between seismic sensors located (b) adjacent to the source and (c) at distance from the source from a glacial lake outburst flood in a study by Cook and Dietze (2022) 17
2.6 Relationship between seismic power and water level measured over a full year at three different seismic stations along the river channel (shown in the left figure) from the study by Burtin et al. (2008) . . . 20
2.7 (left) Hysteresis patterns observed in the study by Roth et al. (2014) and (right) the relationship between their developed metric and sediment transport rates. 21
2.8 Variations in measured parameters with changing water levels in the study by Barrière et al. (2015) showing the varying hysteretic patterns observed. 22
2.9 Relationship between seismic noise and water level over a full typhoon period from Chao et al. (2015) 24

2.10 Top figure shows: (left) seismic power variations in frequency and time, (middle) hydrograph, and (right) infrasound data during a high discharge event from the study by Schmandt et al. (2013). Bottom figure shows the variation in seismic power versus discharge in three different frequency bands and the hydrograph of the event the data was collected over. 25
2.11 Seismic signature of wind and rain signals from Rindraharisaona et al. (2022) 26

3.1 Location of the River Feshie study reach in relation to (a) Scotland and (b) the River Feshie catchment showing locations of stream gauges, along with (c) the monitoring instrument locations. 31
3.2 (a) Hydrograph of water levels at SEPA Feshie Bridge stream gauge (at SG3) over the full monitoring period of this PhD. Stars show the five key events analysed in this thesis. (b) Timeline of sensor deployments over the monitoring period, showing the geophones in blue, hydrophones in pink, stream gauge sensors in green, timelapse cameras deployed on the banks in purple, and the underwater camera in yellow. The dashed borders for the cameras are included to indicate intermittent recording throughout these periods. 32
3.3 Geophone site deployment showing (a) the geophone connected to the data logger in the box and (b) the data logger, battery and GPS inside the box. 33
3.4 Technical set-up of the geophones deployed in this study site. Image from the DATA-CUBE^3 User Manual `https://digos.eu/wp-content/uploads/2020/07/DATA-CUBE-User-Manual-2020-05.pdf` 34
3.5 Hydrophone set-up showing each electrical component. Image provided by Matt Gervais from the project team. 36
3.6 Hydrophone deployment in the study reach showing hollowed out granite block and custom 3D printed instrument mount inside. 36
3.7 The (a) LiDAR sensor and (b) its deployment setup, and the (c) ultrasound sensor and (d) its installation diagram. From `https://ichydro.github.io/Riverlabs/index.html` 37
3.8 (a) Local stream gauge sensor deployment on remains of an old wooden bridge in the centre of the study reach. (b) Custom mount to house both the Lidar and ultrasound sensors. 38
3.9 Field photographs of the two time-lapse cameras deployed at site W_05 that are facing (a) downstream and (b) upstream of the site. . 39
3.10 Photos from the River Feshie fieldsite looking upstream and downstream from W_05 during high flow and low flows. Images are taken from February and March 2021 as these had the clearest conditions and are representative of general high and low flows at the site. During the low flow event the SEPA stream gauge at Feshie Bridge measured a water level of 0.76 m and the high flow event photographed here peaked at 2.15 m. 40
3.11 Screenshots of video recordings taken (a,b) prior to September-October 2022 event and (c,d) following the September-October 2022 event. . . 41
3.12 Axes of a pebble (Harrelson et al., 1994) 42

3.13 Locations of the grain size measurements shown by the crosses. The pink cross indicates where multiple grain size measurements were taken adjacent to site W_07. 43

3.14 (a) A photographic grain size analysis transect example and (b) a chest-height photograph example with a scale. 43

3.15 Photographs from the sieving grain size analysis. (a) The location of the sieved sample on the gravel bar adjacent to site W_07. (b) The excavated hole in which sediment was measured from. 44

3.16 Schematics of the steps taken to measure the slope of the channel by measuring (a) the horizontal distances and (b) the vertical elevation change. 45

3.17 Schematic of the procedure taken to measure the channel profile. . . . 46

3.18 Diagram showing a typical seismic refraction survey to measure the layers of the subsurface (SHINE, 2022). Seismic refraction survey undertaken for this thesis is shown in Appendix B. 48

3.19 Comparison between the water level measurements measured using the Lidar and ultrasound sensors for a period when both instruments were recording. 50

3.20 Rating curve of water depth versus flow discharge (Q_w) at the River Feshie study site, using Manning's equation and measured channel geometry parameters. 50

3.21 Empirical Cumulative Distribution Function (ECDF) of grain sizes measured adjacent to five geophone sites, showing the variation in the median grain size D_{50}. 51

3.22 Log normal distribution of grain sizes measured adjacent to five geophone sites. 52

3.23 Entrainment thresholds of the average D_{50}, and D_{84} from the River Feshie study reach, showing accepted range of critical shear stress (grey band) and the widely used median value of 0.045 (red dashed line). 54

3.24 Bedload flux calculation outputs from commonly used sediment transport equations, using data from the largest event analysed in this thesis. 55

3.25 Seismic wiggle trace showing arrival times of the seismic refraction survey at geophones along the transect. The red dashed line indicates the picked arrivals of the direct waves and the green dashed line shows the picked arrivals of the refracted waves. The blue dashed line indicates the possible third layer that is more visible on some traces than others (see Figure 3.27). 56

3.26 (a) Distance versus time plot of the picked first refracted wave arrivals at the geophones along the transect from five shots, showing the two layers identified. Stars indicate the shot locations. (b) A detailed velocity-depth profile showing the paths of the seismic waves. (c) Simple 2D schematic of the two subsurface layers identified in the seismic refraction data. 57

3.27 (a) Distance versus time plot of the picked first refracted wave arrivals at the geophones along the transect from five shots, showing the three possible layers identified. Stars indicate the shot locations. (b) A detailed velocity-depth profile showing the paths of the seismic waves. (c) Simple 2D schematic of the three subsurface layers identified in the seismic refraction data. 57

3.28 (a) Example of a seismic waveform of the first arrival of a refracted wave measured by a single geophone, showing an envelope fitted to the data (dashed line) to identify the maximum amplitude. (b) Maximum amplitude of the seismic trace envelopes at each geophone along the transect plotted against geophone distance from the source. 58

3.29 Map of study site and instrument locations. 60

3.30 Field photographs of the River Feshie study site taken near site W_05 looking (a) upstream and (b) downstream showing the locations of sites within view of the photographs. 63

4.1 Hydrographs of the local stream gauge data at SG2 for the five selected high flow events. 72

4.2 'eseis' package bedload and turbulence models with varying parameters. (a) The effects of varying water depth along with the corresponding bedload flux, (b) the effects of varying the median grain size, and (c) the effects of varying the distance between the sensor and the river. The colours of the lines correspond to whether it is the bedload spectrum (warm colours) or the turbulence spectrum (cool colours). 74

4.3 Hydrograph from local stream gauge sensor SG2 of the November 2022 event along with a plot of seismic power as a function of frequency and time (spectrogram) of the stream-parallel seismic data recorded at site W_05. The magenta lines indicate the start and end of high power signal in the 15-40 Hz band, and the black lines indicate the rough start and end of the high power in the 40-85 Hz band. . . . 76

4.4 Maps showing active geophones during each of the five selected high flow events. 77

4.5 Spectrograms of seismic data from all sites in the study reach for the March 2022 event. One site is shown per row with the control site in the top row, followed by the sites on the west bank, and then by the sites on the east bank. Sites that did not record are shown as blank plots. Each column contains the Vertical, stream-parallel and stream-perpendicular directional components of the signals, respectively. . . . 79

4.6 Spectrograms of seismic data from all sites in the study reach for the September-October 2022 event. One site is shown per row with the control site in the top row, followed by the sites on the west bank, and then by the sites on the east bank. Sites that did not record are shown as blank plots. Each column contains the Vertical, stream-parallel and stream-perpendicular directional components of the signals, respectively. 81

4.7 Spectrograms of seismic data from all sites in the study reach for the November 2022 event. One site is shown per row with the control site in the top row, followed by the sites on the west bank, and then by the sites on the east bank. Sites that did not record are shown as blank plots. Each column contains the Vertical, stream-parallel and stream-perpendicular directional components of the signals, respectively. . . . 83

4.8 Spectrograms of seismic data from all sites in the study reach for the September 2023 event. One site is shown per row with the control site in the top row, followed by the sites on the west bank, and then by the sites on the east bank. Sites that did not record are shown as blank plots. Each column contains the Vertical, stream-parallel and stream-perpendicular directional components of the signals, respectively. . . . 85

4.9 Spectrograms of seismic data from all sites in the study reach for the October 2023 event. One site is shown per row with the control site in the top row, followed by the sites on the west bank, and then by the sites on the east bank. Sites that did not record are shown as blank plots. Each column contains the Vertical, stream-parallel and stream-perpendicular directional components of the signals, respectively. . . . 87

4.10 Spectrograms of seismic data from site E_06 during all five selected events. One event is shown per column with each row containing a different directional component. Sites that did not record are shown as blank plots. 89

4.11 Spectrograms of seismic data from site W_03 during all five selected events. One event is shown per column with each row containing a different directional component. Sites that did not record are shown as blank plots. 90

4.12 Spectrograms of seismic data from site W_04 during all five selected events. One event is shown per column with each row containing a different directional component. Sites that did not record are shown as blank plots. 90

4.13 Spectrograms of seismic data from site W_05 during all five selected events. One event is shown per column with each row containing a different directional component. Sites that did not record are shown as blank plots. 91

4.14 Spectrograms of seismic data from site W_07 during all five selected events. One event is shown per column with each row containing a different directional component. Sites that did not record are shown as blank plots. 92

4.15 Spectrograms of seismic data from site E_03 during all five selected events. One event is shown per column with each row containing a different directional component. Sites that did not record are shown as blank plots. 93

4.16 Spectrograms of seismic data from site E_04 during all five selected events. One event is shown per column with each row containing a different directional component. Sites that did not record are shown as blank plots. 93

4.17 Spectrograms of seismic data from site E_08 during all five selected events. One event is shown per column with each row containing a different directional component. Sites that did not record are shown as blank plots. 94

4.18 Hydrographs of the five high flow events showing the points at which the PSD values are calculated. The colours of the dots for each event correspond to the colours of the PSD lines in Figure 4.19. 95

4.19 Seismic and hydroacoustic Power Spectral Density (PSD) plots during the five selected high flow events showing the frequency content of the signals during periods when bedload is and is no being transported. The line colours for each event correspond to the dot colours in Figure 4.18. The hydroacoustic data for the March 2022 event in (b) is labelled with the gain value the data logger recorded at. 96

4.20 Same figure used for Figure 4.3 with labels highlighting the interpreted sources of the different seismic contributions to the signal. The bedload and turbulence frequencies are shown to overlap between 40 Hz and 60 Hz, as discussed in the text. The pale peach arrows highlight the period of observed bedload transport from the hydroacoustic audio files. 101

5.1 Maps of the River Feshie fieldsite at the (a) catchment scale showing the three stream gauge sites, (b) reach scale showing the sites of instruments used in this study, and (c) national scale. Photos of the field deployments can be found in Chapter 3. 109

5.2 Stage measurements from SEPA stream gauge at SG3 from 27th October 2015 to 31st December 2022. Red stars mark the three largest events in 2022 that are analysed in this study. Red line marks the water level of the largest event in 2022, with peaks that have previously exceeded this value also marked in red. 110

5.3 Data for two distinct high flow events in March and September-October 2022, one in each column. Included in this plot are; (a, b) the time-series of the water level at SG2, (c, d) the spectrograms of the geophone data (in 1 minute windows) at the control site to highlight environmental noise such as wind and rain, and (e, f) the spectrograms of the geophones at the river site which is dominated by signals of turbulence and sediment transport. 115

5.4 Seismic power variations in frequency and time during the high flow event in October 2023 at sites E_03, E_04, W_07. 117

5.5 Plots summarising the time series of the water level (blue line) and seismic power averaged over the frequency range 50-60 Hz (points coloured by time) for the three largest flow events in 2022. Each column displays a different event showing; (a, b) the aPSD and water level timeseries' for the control site highlighting the environmental noise around the water level peaks, (c, d, e) the aPSD timeseries for the river site layered on top of the independent classification of bedload transport activity using the hydroacoustic data (white shading shows gaps in the data or when the hydrophone was exposed, blue shows periods where the hydrophone records only turbulence, peach shows when bedload transport starts (phase 1) and beige shows when there is an audible shift to lower frequencies on the hydrophone interpreted to be mobilisation of larger grains during bedload transport (phase 2)), (f, g, h) the PSD versus stage relationship with the hydrophone bedload transport classifications shown as bars for the rising and falling limbs of the hydrological peaks. Red stars in d) show the timings of the hydrophone recordings included in Audio 1-3 in the published manuscript, labelled A1, A2 and A3. 118

5.6 aPSD variations against time and water level for the October 2023 event at the three selected sites, E_03, E_04, and W_07. The peach shading indicates the periods of bedload transport as categorised in the hydroacoustic data. The first row shows the aPSD over time (coloured dots) overlain on the hydrograph (blue line). The black numbers indicate the three peaks of the event. The second row shows the aPSD against stage for the full duration of the event, and the following three rows show the aPSD versus stage for each of the three consecutive peaks, labelled in the top right corner of each panel. . . . 119

5.7 (a) Superposition of the PSD versus water level relationships for three distinct high flow events to enable a clearer comparison of the similarities and differences between each event. (b) Bedload activity transitions from independent interpretation of hydroacoustic data that occurred on the rising limbs of flood peaks for all three events; note that for the March and September events bedload started being transported at a water level of ∼1.00-1.10 m whilst transport during the November 2022 event initiated at a water level of ∼0.80 m. (c) Bedload activity transitions from independent interpretation of hydroacoustic data that occurred on the falling limbs flood peaks for all three events; note that for the March 2022 event bedload stopped being transported at a water level of ∼1.00 m whilst the arrest of bedload transport occurred at ∼0.85 m for the September and November 2022 events. 121

5.8 Waveform of the north-south component at site W_07 during the September-October 2022 event demonstrating the saturation in the PSD at high water levels is not because of clipping of the waveform amplitudes. 122

5.9 Hysteresis patterns produced when using offset and co-located water level and seismic measurements for all three 2022 events. (a, d, g) When using upstream water level measurements relative to the seismic measurements an anticlockwise hysteresis is apparent. (b, e, h) A generally more linear relationship is observed when using co-located measurements, however the larger September-October 2022 event shows a more complicated behaviour with a degree of hysteresis at intermediate water levels and a linear relationship at high water levels. (c, f, i) Using downstream water level measurements relative to seismic measurements results in clear clockwise hysteresis for all three events. 124

5.10 SG2 water level versus PSD summed over 20-30 Hz for the N-S component at site W_07 for all three 2022 events. This reveals a similar behaviour to the higher frequency band in Figure 5.5. 127

5.11 Examples of sources of hysteresis in the relationship between water level and seismic power. When the stream gauge and geophone are offset (a), hysteresis will be introduced as an artefact of the temporal offset even when the form of the seismic power and water level curves are the same. If water level is measured upstream of the seismic data an anticlockwise hysteresis pattern will occur (b, f). If water level and seismic measurements are co-located, no hysteresis will be observed (c, g). If water level is measured downstream of the seismic measurements then a clockwise hysteresis pattern will occur (d, h). Changes in the shape of the seismic power curve with respect to the water level curve as a result of increased source-to-sensor distance for the seismic data can also result in a hysteretic relationship (e, i). . . . 128

6.1 Ground displacement associated with (a) Love and (b) Rayleigh waves (Shearer, 2009; Burtin et al., 2016). 131

6.2 Map showing which geophone sites were recording during the events analysed in this chapter. 136

6.3 (a) Hydrograph from local stream gauge (SG2), with three plots showing the spectrograms of the seismic signal recorded at site E_04 during the September-October 2022 event in (b) the vertical component, (c) the stream-parallel component, and (d) the stream-perpendicular component. (e) The resulting HVSR values in frequency and time using the 'averaged' horizontal component and the vertical component. (f) The 'averaged' HVSR in the 15 - 35 Hz and the 40 - 60 Hz frequency ranges. The pale pink and beige blocks in (a) and (f) correspond to the hydroacoustically observed periods of bedload transport as described in Chapter 5, with the dashed lines of corresponding colour in (e) indicating the onset and arrest of these transport phases. The inset map on the right shows the location of this site in relation to the other geophone sites in the study reach. 140

6.4 (a) Hydrograph from local stream gauge (SG2), with three plots showing the spectrograms of the seismic signal recorded at site W_04 during the September-October 2022 event in (b) the vertical component, (c) the stream-parallel component, and (d) the stream-perpendicular component. (e) The resulting HVSR values in frequency and time using the 'averaged' horizontal component and the vertical component. (f) The 'averaged' HVSR in the 15 - 35 Hz and 60 - 80 Hz frequency ranges. The pale pink and beige blocks in (a) and (f) correspond to the hydroacoustically observed periods of bedload transport as described in Chapter 5, with the dashed lines of corresponding colour in (e) indicating the onset and arrest of these transport phases. The inset map on the right shows the location of this site in relation to the other geophone sites in the study reach. 142

6.5 (a) Hydrograph from local stream gauge (SG2), with three plots showing the spectrograms of the seismic signal recorded at site W_05 during the September-October 2022 event in (b) the vertical component, (c) the stream-parallel component, and (d) the stream-perpendicular component. (e) The resulting HVSR values in frequency and time using the 'averaged' horizontal component and the vertical component. (f) The 'averaged' HVSR in the 20 - 30 Hz and 50 - 60 Hz frequency ranges. The pale pink and beige blocks in (a) and (f) correspond to the hydroacoustically observed periods of bedload transport as described in Chapter 5, with the dashed lines of corresponding colour in (e) indicating the onset and arrest of these transport phases. The inset map on the right shows the location of this site in relation to the other geophone sites in the study reach. 144

6.6 (a) Hydrograph from local stream gauge (SG2), with three plots showing the spectrograms of the seismic signal recorded at site W_07 during the September-October 2022 event in (b) the vertical component, (c) the stream-parallel component, and (d) the stream-perpendicular component. (e) The resulting HVSR values in frequency and time using the 'averaged' horizontal component and the vertical component. (f) The 'averaged' HVSR in the 15 - 30 Hz and 40 - 80 Hz frequency ranges. The pale pink and beige blocks in (a) and (f) correspond to the hydroacoustically observed periods of bedload transport as described in Chapter 5, with the dashed lines of corresponding colour in (e) indicating the onset and arrest of these transport phases. The inset map on the right shows the location of this site in relation to the other geophone sites in the study reach. 146

6.7 (a) hydrograph from local stream gauge (SG2), with three plots showing the spectrograms of the seismic signal recorded at site E_03 during the October 2023 event in (b) the vertical component, (c) the stream-parallel component, and (d) the stream-perpendicular component. (e) The resulting HVSR values in frequency and time using the 'averaged' horizontal component and the vertical component. (f) The 'averaged' HVSR in the 10 - 15 Hz and 50 - 60 Hz frequency ranges. The pale pink blocks in (a) and (f) correspond to the hydroacoustically observed periods of bedload transport as described in Chapter 5, with the dashed lines of corresponding colour in (e) indicating the onset and arrest of bedload transport. The inset map on the right shows the location of this site in relation to the other geophone sites in the study reach. 149

6.8 (a) hydrograph from local stream gauge (SG2), with three plots showing the spectrograms of the seismic signal recorded at site E_04 during the October 2023 event in (b) the vertical component, (c) the stream-parallel component, and (d) the stream-perpendicular component. (e) The resulting HVSR values in frequency and time using the 'averaged' horizontal component and the vertical component. (f) The 'averaged' HVSR in the 15 - 35 Hz and 60 - 80 Hz frequency ranges. The pale pink blocks in (a) and (f) correspond to the hydroacoustically observed periods of bedload transport as described in Chapter 5, with the dashed lines of corresponding colour in (e) indicating the onset and arrest of bedload transport. The inset map on the right shows the location of this site in relation to the other geophone sites in the study reach. 151

6.9 (a) hydrograph from local stream gauge (SG2), with three plots showing the spectrograms of the seismic signal recorded at site W_04 during the October 2023 event in (b) the vertical component, (c) the stream-parallel component, and (d) the stream-perpendicular component. (e) The resulting HVSR values in frequency and time using the 'averaged' horizontal component and the vertical component. (f) The 'averaged' HVSR in the 15 - 35 Hz and 60 - 80 Hz frequency ranges. The pale pink blocks in (a) and (f) correspond to the hydroacoustically observed periods of bedload transport as described in Chapter 5, with the dashed lines of corresponding colour in (e) indicating the onset and arrest of bedload transport. The inset map on the right shows the location of this site in relation to the other geophone sites in the study reach. 153

6.10 (a) hydrograph from local stream gauge (SG2), with three plots showing the spectrograms of the seismic signal recorded at site W_07 during the October 2023 event in (b) the vertical component, (c) the stream-parallel component, and (d) the stream-perpendicular component. This site only recorded until 09:00 on the 9th October. (e) The resulting HVSR values in frequency and time using the 'averaged' horizontal component and the vertical component. (f) The 'averaged' HVSR in the 20 - 35 Hz and 50 - 70 Hz frequency ranges. The pale pink blocks in (a) and (f) correspond to the hydroacoustically observed periods of bedload transport as described in Chapter 5, with the dashed lines of corresponding colour in (e) indicating the onset and arrest of bedload transport. The inset map on the right shows the location of this site in relation to the other geophone sites in the study reach. 155

6.11 Data from geophone site E_04 during the September-October 2022 event. (a) Hydrograph from local stream gauge (SG2). The resulting HVSR values in time and frequency using (b) the 'averaged' horizontal component, (c) the stream-parallel component, and (d) the stream-perpendicular component. (e) The HVSR values averages across the 15 - 35 Hz and 40 - 60 Hz frequency ranges in the three calculated HVSRs - labelled 'Av.' for the 'averaged' component, '$\parallel$' for the stream-parallel component, and '$\perp$' for the stream-perpendicular component. The two frequency ranges have been colour filled with the colour of the greatest HVSR to show which component is strongest. The pale pink and beige blocks in (a) and (e) correspond to the hydroacoustically observed periods of bedload transport as described in Chapter 5, with the dashed lines of corresponding colour in (b)-(d) indicating the onset and arrest of bedload transport. The inset map on the right shows the location of this site in relation to the other geophone sites in the study reach. 157

6.12 Data from geophone site W_04 during the September-October 2022 event. (a) Hydrograph from local stream gauge (SG2). The resulting HVSR values in time and frequency using (b) the 'averaged' horizontal component, (c) just the stream-parallel component, and (d) just the stream-perpendicular component. (e) The 'averaged' HVSR in the 15 - 35 Hz and 60 - 80 Hz frequency ranges in the three calculated HVSRs - labelled 'Av.' for the 'averaged' component, '$\parallel$' for the stream-parallel component, and '$\perp$' for the stream-perpendicular component. The two frequency ranges have been colour filled with the colour of the strongest HVSR to show which component is dominant. The pale pink and beige blocks in (a) and (e) correspond to the hydroacoustically observed periods of bedload transport as described in Chapter 5, with the dashed lines of corresponding colour in (b)-(d) indicating the onset and arrest of bedload transport. The inset map on the right shows the location of this site in relation to the other geophone sites in the study reach. 159

6.13 Data from geophone site W_07 during the September-October 2022 event. (a) Hydrograph from local stream gauge (SG2). The resulting HVSR values in time and frequency using (b) the 'averaged' horizontal component, (c) just the stream-parallel component, and (d) just the stream-perpendicular component. (e) The 'averaged' HVSR in the 15 - 30 Hz and 40 - 80 Hz frequency ranges in the three calculated HVSRs - labelled 'Av.' for the 'averaged' component, '$\parallel$' for the stream-parallel component, and '$\perp$' for the stream-perpendicular component. The two frequency ranges have been colour filled with the colour of the strongest HVSR to show which component is dominant. The pale pink and beige blocks in (a) and (e) correspond to the hydroacoustically observed periods of bedload transport as described in Chapter 5, with the dashed lines of corresponding colour in (b)-(d) indicating the onset and arrest of bedload transport. The inset map on the right shows the location of this site in relation to the other geophone sites in the study reach. 161

6.14 Data from geophone site E_04 during the October 2023 event. (a) Hydrograph from local stream gauge (SG2). The resulting HVSR values in time and frequency using (b) the 'averaged' horizontal component, (c) just the stream-parallel component, and (d) just the stream-perpendicular component. (e) The 'averaged' HVSR in the 20 - 30 Hz and 40 - 60 Hz frequency ranges in the three calculated HVSRs - labelled 'Av.' for the 'averaged' component, '$\parallel$' for the stream-parallel component, and '$\perp$' for the stream-perpendicular component. The two frequency ranges have been colour filled with the colour of the strongest HVSR to show which component is dominant. The pale pink and beige blocks in (a) and (e) correspond to the hydroacoustically observed periods of bedload transport as described in Chapter 5, with the dashed lines of corresponding colour in (b)-(d) indicating the onset and arrest of bedload transport. The inset map on the right shows the location of this site in relation to the other geophone sites in the study reach. 163

6.15 Data from geophone site W_04 during the October 2023 event. (a) Hydrograph from local stream gauge (SG2). The resulting HVSR values in time and frequency using (b) the 'averaged' horizontal component, (c) just the stream-parallel component, and (d) just the stream-perpendicular component. (e) The 'averaged' HVSR in the 15 - 35 Hz and 45 - 60 Hz frequency ranges in the three calculated HVSRs - labelled 'Av.' for the 'averaged' component, '$\parallel$' for the stream-parallel component, and '$\perp$' for the stream-perpendicular component. The two frequency ranges have been colour filled with the colour of the strongest HVSR to show which component is dominant. The pale pink and beige blocks in (a) and (e) correspond to the hydroacoustically observed periods of bedload transport as described in Chapter 5, with the dashed lines of corresponding colour in (b)-(d) indicating the onset and arrest of bedload transport. The inset map on the right shows the location of this site in relation to the other geophone sites in the study reach. 165

6.16 Data from geophone site W_07 during the October 2023 event. (a) Hydrograph from local stream gauge (SG2). The resulting HVSR values in time and frequency using (b) the 'averaged' horizontal component, (c) just the stream-parallel component, and (d) just the stream-perpendicular component. (e) The 'averaged' HVSR in the 20 - 35 Hz and 50 - 70 Hz frequency ranges in the three calculated HVSRs - labelled 'Av.' for the 'averaged' component, '$\parallel$' for the stream-parallel component, and '$\perp$' for the stream-perpendicular component. The two frequency ranges have been colour filled with the colour of the strongest HVSR to show which component is dominant. The pale pink and beige blocks in (a) and (e) correspond to the hydroacoustically observed periods of bedload transport as described in Chapter 5, with the dashed lines of corresponding colour in (b)-(d) indicating the onset and arrest of bedload transport. The inset map on the right shows the location of this site in relation to the other geophone sites in the study reach. 167
6.17 Frequency content of the HVSR signals at site W_07 during the September-October 2022 event for periods when there was (a) no bedload motion and (b) bedload transport inferred from the hydroacoustic data. 168
6.18 Frequency content of the HVSR signals at site W_07 during the October 2023 event for periods when there was (a) no bedload motion and (b) bedload transport inferred from the hydroacoustic data. . . . 169

B.1 Seismic refraction survey setup at the River Feshie site, showing the geophone transect lines, the node locations, and the shot locations. . 212

E.1 Seismic signal at site W_07 of a vehicle driving through the ford away from the sensor. 226
E.2 Seismic signal at site W_07 of the magnitude 3.3 earthquake that struck the west of Scotland in November 2021. 226

List of Tables

3.1 Specifications of 3-D PE-6/B 4.5Hz Geophones. 33
3.2 Local stream gauge sensor specifications 38
3.3 Underwater camera specifications 40
3.4 Slope measurements of the study reach using the laser range finder. . 49
3.5 Grain size distributions measured adjacent to 5 sites. All values are in [mm] 52
3.6 Grain size classes from sieved data 53
3.7 Grain size distributions from Wolman count method, photographic analysis, and sieved data 53

4.1 Parameters used in the R 'eseis' package turbulence and bedload models 70

C.1 Grain sizes measured using Wolman count method adjacent to five geophone sites. Units [cm]. 213
C.2 Grain sizes measured using photographic analysis on gravel bar adjacent to site W_07. 215
C.3 Continuation of photographic grain sizes. 217
C.4 Continuation of photographic grain sizes. 219
C.5 Mass of grain size classes from sieve measurements. 221

D.1 Parameters used in bedload flux calculations 222

Chapter 1

Introduction

Coarse gravels and cobbles that move along a riverbed by bouncing, rolling and sliding are termed bedload. The mobilisation and transport of bedload in rivers is an important mechanism for the transfer of sediment from production to deposition areas (Reid et al., 1985; Hoey and Sutherland, 1991; Lisle, 1995; Burtin et al., 2010; Roth et al., 2017). Understanding the timings and flux of bedload transport is important for not only predicting channel evolution and understanding sediment transfer, but it also provides valuable information for problems in the fields of ecology, river and landuse management, and civil engineering (Turowski et al., 2011; Roth et al., 2017). Channel evolution can affect the likelihood and distribution of flood events and thus understanding the effect of bedload transport on channel geometry is of high importance.

The mobilisation of coarse sediments can have a significant impact on communities that live on or utilise alluvial plains. The deposition of bedload in alluvial plains can cause long-term damage and disruptions to agricultural land and practices, and the erosive power of bedload in flood events can cause significant damage to infrastructure, such as buildings, dams and embankments (Bakker et al., 2020). With changes in climate potentially leading to more frequent and more severe flood events, bedload transport has the potential to cause more widespread and devastating damage to the landscape. Thus, it is of interest to develop a good understanding of the processes that govern bedload transport and how that translates into channel evolution and ultimately flood risk.

Bedload transport has traditionally been determined through manual sampling techniques, applying numerical models to data (Cao and Carling, 2002; Tsai et al., 2012; Gimbert et al., 2014), or the use of in-stream geophones and hydrophones (Rickenmann et al., 2014; Geay et al., 2020). However, manual techniques can be time-consuming, unsafe and fail to capture the temporal variability of bedload transport; numerical models can fail to accurately represent the stochasticity and inherent natural variability of bedload transport (Kasprak et al., 2019); and in-stream sensors can contaminate the data by altering the flow field around the equipment and are subject to equipment damage or loss in large events (Roth et al., 2016). An emerging interest in the use of indirect seismic sensors to monitor ground vibrations caused by bedload transport has offered an opportunity to acquire data over geomorphologically relevant timescales while minimising labour-intensiveness, cost and danger (Govi et al., 1993; Burtin et al., 2008; Schmandt et al., 2013). Despite these advances there still lies some uncertainty in identifying the onset and behaviour

of bedload transport from seismic measurements, due to difficulties in differentiating the signal of bedload transport from other sources of seismic noise, including turbulence.

The overall aim of this thesis is to explore the seismic signals recorded near an alluvial mountain river to assess the seismic characteristics of river-induced seismic noise, and combine it with other datasets, such as hydroacoustic data, to identify the signal characteristics of bedload transport. We use the River Feshie in Scotland as our case study due to its active nature and regular transport events. It provides a challenging yet rewarding setting to develop a bedload seismic monitoring system to analyse the signals produced by river processes. The Feshie has been the object of extensive research since the mid 1970s, with focus on bar development (Ferguson and Werritty, 1983), sediment transport (Ferguson et al., 1992), geomorphic change (Brasington et al., 2000; Brasington et al., 2003), and hydrology (Soulsby et al., 2006). Substantial research has been undertaken in the braided stretch immediately upstream of the study site for this thesis mainly looking at morphological changes from catchment to grain scale (Hodge et al., 2009; Wheaton et al., 2013).

1.1 Study site

1.1.1 Catchment characteristics

The River Feshie is situated in the western Cairngorm mountains in the Scottish Highlands (Figure 1.1). The roughly 40 km long River Feshie drains a catchment area of approximately 240 km^2, flowing generally northwards into the larger River Spey (Ferguson and Werritty, 1983; Werritty and McEwen, 2007). The drainage basin in underlain mainly by resistant Moinian schist (which dominates the coarse bedload) at elevations of 700 - 1000 m, with a maximum catchment altitude of about 1265 m due to a granite batholith to the north-east (Werritty and McEwen, 1993; Kasprak et al., 2019) and a minimum altitude of approximately 220 m (Figure 1.2).

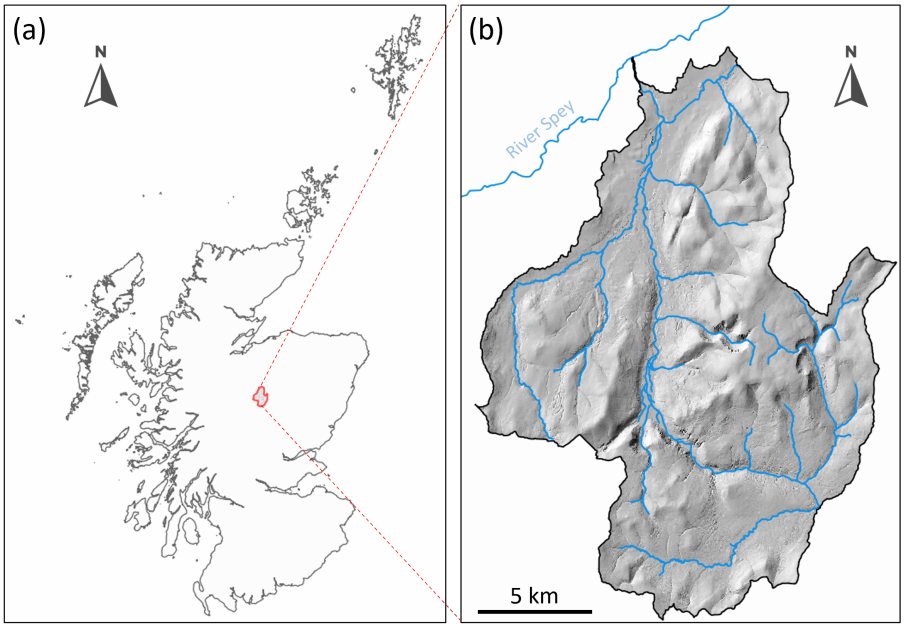


Figure 1.1: (a) Location of the River Feshie catchment in Scotland.(b) River Feshie catchment and confluence with River Spey.

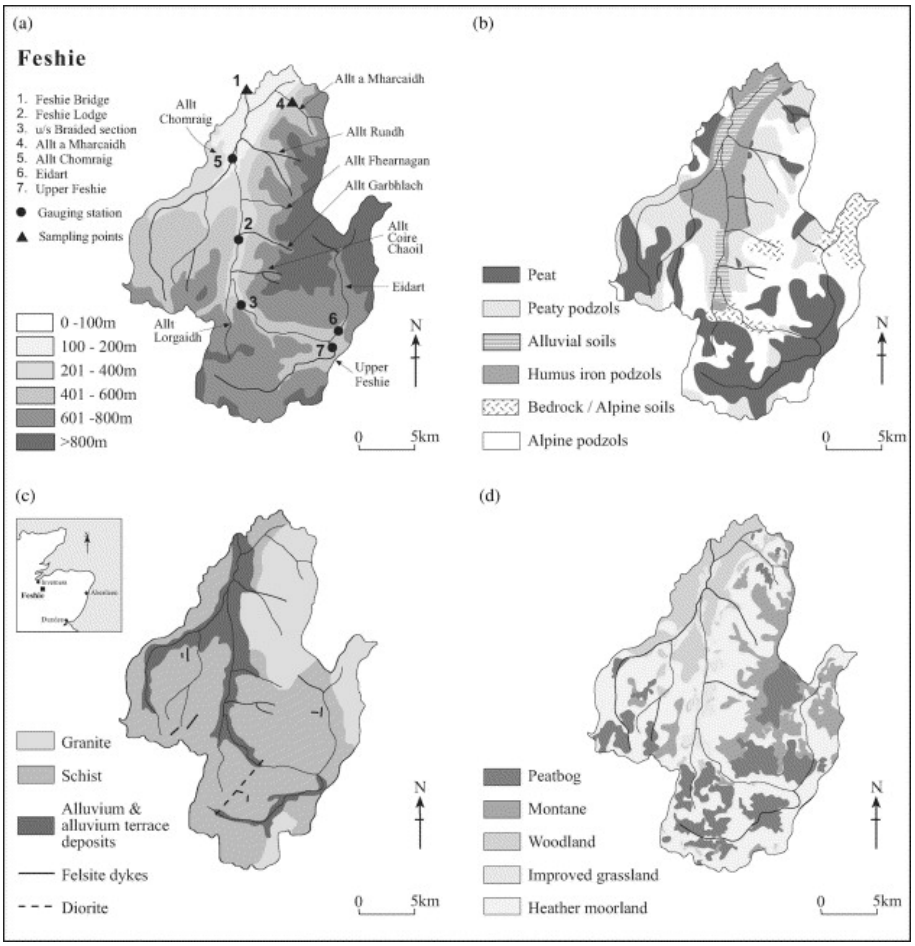


Figure 1.2: River Feshie catchment characteristics (Soulsby et al., 2006).

The headwaters flow eastwards over steep impermeable slopes then turn and flow north through a glacial trough that bisects the basin. The wider, lower valley is composed of glacial till and outwash gravels and has greater floodplain connectivity and substrate mobility (Young and Davies, 1991; Werritty and McEwen, 1993; Gilvear et al., 2000). Here the Feshie is characteristically braided except where constrained by post-glacial terraces or bedrock (Werritty and Ferguson, 1980; Ferguson and Werritty, 1983). Braiding has occurred in Glen Feshie due to a combination of substantial coarse sediment availability coupled with steep channel gradients, high runoff, and a consequential high stream power and flashy flow regime (high peak discharge to mean discharge ratio) (Ferguson and Werritty, 1983). The steep valley slopes, low bedrock permeability and saturation of peat in the most elevated parts of the catchment mean the infiltration of water is limited, favouring overland flow (Gilvear et al., 2000).

According to Werritty and Ferguson (1980), historical maps and aerial photographs illustrate frequent changes in the River Feshie's channel patterns, affecting braiding configurations, sinuosity levels, and the extent of exposed gravel (Ferguson and Werritty, 1983; Werritty and McEwen, 2007). Nowadays, in three reaches the river has the ability to migrate laterally and is actively reworking glacial outwash gravels provided by upstream sediment supply from neighbouring hillslopes (Ferguson and Werritty, 1983). These occur at its confluence with the River Spey, at the Allt Chomhraig confluence, and in the stretch adjacent to Glenfeshie Lodge. The latter of these, a 3 km stretch, is the most active and dynamic braided section

(Wheaton et al., 2013). Glen Feshie represents a rich assemblage of fluvio-glacial derived landforms, such as terraces and alluvial fans, which are abundant in the mid-lower parts of the catchment with up to 10 m thick outwash material. The lower course of the river at Feshie Bridge is confined locally by bedrock, upstream of the formation of a braided delta system and low angle alluvial fan as the Feshie enters the River Spey (Werritty and Brazier, 1991).

1.1.2 Catchment hydrological record

The Scottish Environmental Protection Agency (SEPA) provides a reliable and continuous record of 15 minute resolution discharge and water level data at Feshie Bridge dating back to late 1992 (Figure 1.3). This gauge is located in a fairly confined stretch following a bedrock constrained section and approximately 1.5 km upstream of the large alluvial fan at the confluence with the River Spey, and 10 km downstream of the primary field site. This gauge has recorded peak flows exceeding 100 m^3s^{-1} and maximum instantaneous peak flows of up to 260 m^3s^{-1} (on 30th December 2015) since records began.

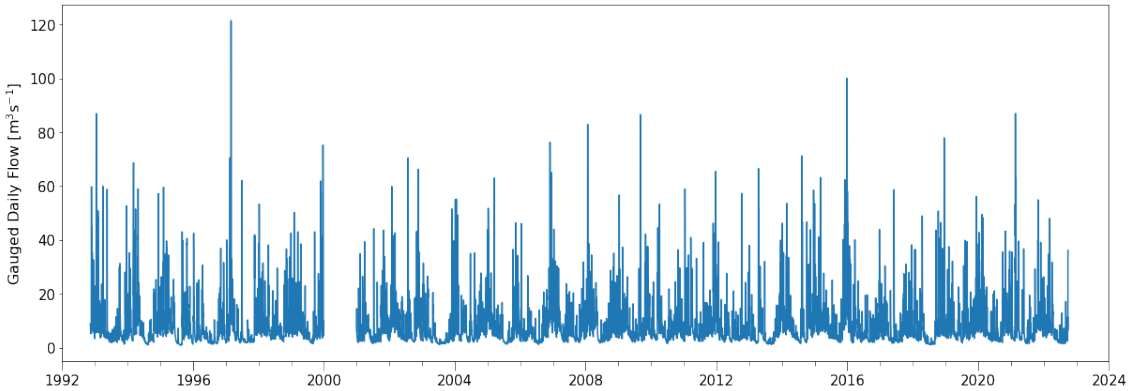


Figure 1.3: SEPA gauged daily flow data dating back to the start of records in late 1992. Accessed from NRFA (2024). NRFA data is only available up until the end of the previous water year (October-September).

Due to the steep channel hillslopes and impermeable headwaters, the river is characterised by a distinct flashy flow regime (Figure 1.3). The river's discharge is highly influenced by high rainfall and snowmelt. Although the river is subject to high flows throughout the year, there is a clear clustering of high flows during early spring, late autumn and winter (Figure 1.4). Over the past 30 years of the SEPA station recording period, the majority ($>$ 83%) of peak flow events have occurred between September and March, with the occasional convective summer storm resulting in peak flows in June, July and August (Figure 1.5). No peak flows have occurred in April or May.

1.1.3 Catchment land-use

In the nineteenth and twentieth centuries, Glen Feshie had been used for extensive livestock and red deer grazing. Combined with increases in timber felling this resulted in drastic declines of native woodlands (Gullett et al., 2023). Increased numbers of deer were maintained in the estate than would be natural to aid the boom in stag shooting. Large herds of deer dramatically contribute to the decline in woodland, as they browse young saplings before they have had a chance to establish

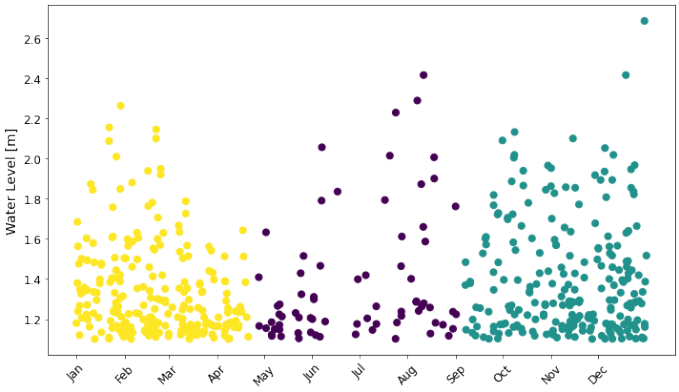


Figure 1.4: Clustering of SEPA 15 minute resolution water level data over the 5% flow exceedance value from NRFA (2024). Data presented includes values over that threshold for the last ten years as that was what was available through (SEPA, 2024).

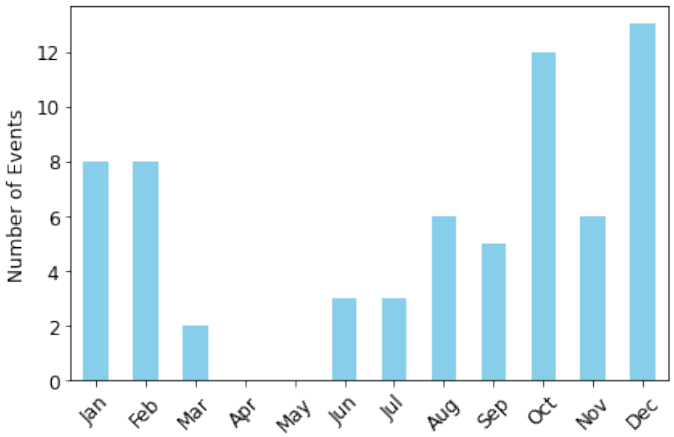


Figure 1.5: The number of instantaneous peak flows in each month over 10 years of data from SEPA (2024) that exceeded the current NRFA (2024) POT (peak over threshold) value of 68.5 m^3s^{-1}.

themselves meaning there was minimal tree regeneration to replace old trees that were either naturally dying or were felled (Gullett et al., 2023). This reduction in tree cover is likely to have had impacts on the broader landscape and ecosystem, damaging habitats and natural ecosystems, influencing factors such as slope stability, soil erosion affecting hydrological processes, water quality and aquatic habitats.

This situation persisted until Glen Feshie estate was acquired by Scottish conservation organisation Wildlands Ltd in 2006. Since then the area has been the object of an extensive rewilding effort, mainly through controlling red deer populations and minimising grazing of young saplings. However, the controversy surrounding deer culling slowed the implementation of this strategy (Turnbull, 2016). Once the rewilding effort got underway it saw the culling of red deer increase since the early 2000s with the number of red deer reducing from more than 35 per km^2 to around 2-5 per km^2 in 2021 (Gullett et al., 2023). This marked reduction in deer numbers in Glen Feshie has meant that young native saplings could grow without the threat of being eaten or damaged. It has been noted through routine monitoring of deer populations and vegetation growth, that controlling the deer numbers had a significantly positive impact on the regeneration of natural woodlands, with a decrease in damage and increase in seedling emergence, and on diversifying the natural ecology of the catchment (Gullett et al., 2023).

1.2 Research aims and objectives

The aim of this project is thus to monitor bedload transport in the highly dynamic setting of the Feshie, by applying a combination of measurement techniques, such as seismic sensors, hydrophones, topographic analysis, grain size measurements, and time-lapse photos. Due to the nature of the river and the anthropogenically quiet location, the Feshie provides a good location to deploy seismic sensors on the channel banks. However, modelling of alluvial rivers remains uncertain (Cao and Carling, 2002). Braided systems, like the Feshie, are highly dynamic and models tend to oversimplify the nature of the rivers (Cao and Carling, 2002). By applying a variety of techniques and correlating the resulting data, it is hoped that the characteristics of bedload transport induced seismic signals can be analysed to contribute to the existing science understanding sediment transfer and better informing flood risk models for a range of river systems.

The aim of this research is to record and analyse seismic data from the River Feshie to identify and characterise the seismic signals associated with bedload transport. By combining seismic measurements with other complementary techniques, such as hydroacoustics, topographic analysis, and grain size measurements, the research seeks to deepen the understanding of the seismic properties of bedload transport signals and their variability across different river conditions. This integrated approach will enable the identification of distinct seismic signatures of bedload movement, providing valuable insights into the dynamics of sediment transport in river environments.

To achieve this aim, the research is guided by the following key objectives:

Objective 1. To capture seismic recordings of bedload transport and analyse the variability in signals across different sites and events: This objective aims to assess the influence of site characteristics and event conditions on the seismic signals produced by bedload transport, improving sensor placement strategies for future studies.

Objective 2: To compare seismic and hydroacoustic recordings of high-flow events to identify signals and patterns of bedload transport: This will help establish how seismic and hydroacoustic data can complement each other in tracking sediment movement, leading to a more comprehensive understanding of river dynamics.

Objective 3: To evaluate which directional component of the river-induced seismic signals contains the strongest bedload transport signals: By analysing the strength of seismic signals in horizontal and vertical directions, this objective will provide insights into how the directionality of the seismic signals reflects bedload movement and contribute to improving current seismic bedload transport models.

Together, these objectives aim to refine the methodology for using seismic sensors in sediment transport studies, providing valuable data for more accurate river

management and flood risk predictions, especially in light of climate change and increasing extreme weather events. By combining seismic and hydroacoustic techniques, this research presents a more robust and innovative approach to monitoring bedload transport, with significant implications for environmental management, engineering, and ecology.

1.3 Thesis outline

The main data chapters of this thesis (chapters 4-6) provide the key research outputs. Chapter 5 has been through review with the Earth Surface Processes and Landforms (ESPL) journal and is currently in preparation for publication. For each chapter, I have clearly outlined my contributions at the start. The thesis structure is as follows:

- **Chapter 2** outlines the key literature relating to the subject area of this thesis, focusing on the importance of monitoring bedload transport in rivers, the methodologies that have been adopted, and the developments within the field of environmental seismology.
- **Chapter 3** provides an overview of the approach adopted in this thesis and the methods used. The methods used are quite general to the overall thesis and thus this section provides a detailed explanation of data collection and analysis methods, but more specific methods and data analysis are included within each data chapter. This chapter also discusses the site characteristics as identified through a number of these measurement methods.
- **Chapter 4** analyses the river-induced seismic signals, and explores the variability in recorded signals between sites and between hydrological events. This chapter provides the fundamental analysis and interpretations for the following two data chapters.
- **Chapter 5** explores monitoring bedload transport using a combination of hydroacoustic and seismic data and what the effect of consecutive events can have on the transport of bedload through thresholds of entrainment and hysteresis patterns. The material presented here has been adapted from the accepted manuscript in Earth Surface Processes and Landforms (ESPL) to avoid repetition, embed the work within the main body of the thesis effectively, and provide additional data and results that were not available at the time of writing the manuscript. The version of the manuscript that is in preparation for publication is presented in Appendix F.
- **Chapter 6** analyses the strength of river-induced seismic signals recorded in three orthogonal directional components and discusses which component contains the strongest bedload and turbulence signals.
- **Chapter 7** collates all of the research undertaken in this thesis and discusses the findings in relation to the wider research context, suggesting potential avenues for future research.
- **Chapter 8** provides concluding remarks and summarises the main findings of the thesis.

Chapter 2

Scientific Context

2.1 Background

Rivers are one of the most important agents of erosion and deposition on Earth. They respond to tectonic and climatic signals and evidence this by changes in the landscape. They are also the primary process for sediment to be exported from source to sink (continent to oceans). Fluvial sediment transport is the study of the interaction between channelised, unidirectional flows and natural sediment (Cheng, 2004). The flow regimes of a setting are the primary control on sediment transport. As a broad description, there are two fundamental ways fluids flow: as laminar and turbulent flow. Between these two end members there is a wide gradation in the flow regime, generally termed transitional flows as a whole. Laminar flow occurs when water molecules move in straight, parallel lines and are characteristic of shallow, slow moving water or highly viscous fluids, such as ice. Turbulent flows, on the other hand, are characterised by a more complex pattern of motion of water molecules where molecules can move in all directions (Lajeunesse et al., 2010). Turbulent flows are most common in nature and are important for transporting sediment as it promotes particle entrainment.

Sediment is transported by four key transport modes: dissolved or solute load, washload, suspended load, and bed load (Babiński, 2005; Meunier et al., 2006). Dissolved load includes dissolved material within the flow, whereas washload is the fine particle fraction that once entrained in the flow typically does not interact with the bed (Babiński, 2005; Dingle and Venditti, 2023). Suspended load is the finer fraction and is transported in suspension and intermittently comes to rest on the bed, while bed load is the coarser fraction which moves in contact with the river bed by rolling, sliding and saltating (Babiński, 2005; Meunier et al., 2006). The transport mode depends on the size of sediment particles, the river's transport capacity and flow velocity, and the boundary shear stress, which is the stress component acting along the channel bed (Chaudhry, 2008). Once a grain is lifted into the flow it can either stay in the flow and be carried as suspended load or it will be transported by rolling or bouncing along the bed as bedload. The mobilisation of sediments is influenced by various forces acting on particles within a flow. One key force is the bed shear stress, which is the force exerted by the fluid flow on the sediment bed surface (Shields, 1936). Bed shear stress governs both the rolling of particles along the bed and the lifting force that can suspend particles in the water column. This stress plays a critical role in sediment transport dynamics, as it directly influences

the mobilisation of particles. It is influenced by flow conditions (such as flow speed within the boundary layer), gravity, friction with the bed, sediment characteristics, and channel slope, making it a fundamental parameter in predicting sediment transport rates (Rhoads, 2020). Bed shear stress (τ) increases with increasing fluid density, slope, and water depth that affects pressure on grains:

$$\tau = \rho_w g h S \tag{2.1}$$

where ρ_w is the water density, g is the acceleration due to gravity, h is the average water depth, and S is the water surface slope.

In a thick boundary layer, the flow velocity at the top of grains is not much different from that at the bottom of grains, resulting in lower bed shear stress and making sediment less likely to move (Figure 2.1). In a thin boundary layer, the bed shear stress is higher, and grains are more likely to move down flow. However, in gravel bed rivers, the boundary layer is typically turbulent due to bed roughness. This turbulence creates variations in flow velocity near the bed, significantly increasing the potential for sediment transport.

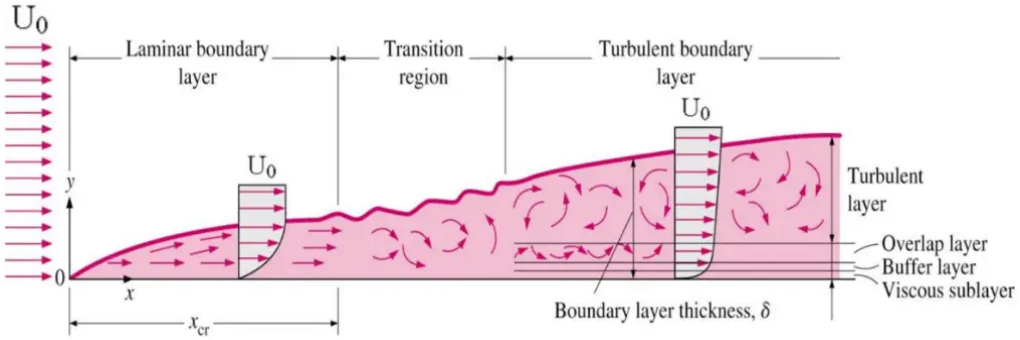


Figure 2.1: Boundary layer characteristics showing the more uniform velocity gradient in thick boundary layers (*Boundary Layer — Definition & Characteristics* 2024)

The threshold of particle entrainment in a flow occurs when the shear forces overcome the resistive forces (inertia, friction). The shear stress at this threshold is called the critical shear stress τ_{cr}. Resistive forces include the grain's weight and are influenced by its position relative to neighbouring grains in the bed, such as its protrusion and pivot angle. Protrusion refers to how much a grain extends above the surrounding grains, with more protrusion increasing the grain's exposure to flow and reducing its resistance to movement. The pivot angle is the angle at which a grain can rotate around a contact point with other grains, affecting its stability and resistance to movement. Greater resistive forces, such as increased grain weight or a more embedded position, increase the critical shear stress and make it more difficult for particles to move.

Bedload controls characteristics of channel bed such as roughness, bedforms, sediment erosion and deposition, and aquatic habitat suitability. Therefore bedload transport forecasts are important for monitoring fluvial morphology (Schumm, 1977), restoring river habitats (Buffington et al., 2004), and managing natural risks for humans (Badoux et al., 2014). Bedload can represent a significant fraction (up to 60%) of total sediments transported within rivers, especially for headwaters (Meunier et al., 2006; Liu et al., 2008). However, Babiński (2005) says that it is generally accepted that bedload contributes a much smaller fraction that suspended load. The

precise proportions will depend on factors such as the flow power of the river, the availability of sediments, the hydrological regime, anthropogenic activities, and the geological structure and composition of the catchment (Babiński, 2005). Bedload transport calculations for gravel-bed rivers are often based on reach-averaged shear stress values, however, the complex flow field structures in these transport systems result in wide distributions of shear stresses within one reach (Monsalve et al., 2020). Shields (1936) proposed that sediment mobility could be seen as a threshold process in which particles start moving when the dimensionless shear stress induced by the water flow (i.e. Shields stress $\tau*$) exceeds a critical value (critical Shields stress $\tau*_{cr}$):

$$\tau^* = \frac{\tau}{(\rho_s - \rho_w)gD} > \tau*_{cr} \tag{2.2}$$

where ρ_s is the sediment density and D is the grain size. If the stress of flowing water is less than the critical shear stress, particles within the river will remain motionless (du Boys, 1879; Shields, 1936; Burtin et al., 2008). Only when stress exerted by the flow exceeds the critical shear stress, movement of particles will occur.

Shields (1936) proposed a unique critical Shields parameter, however, over the years the Shield's theory has been revisited and developed with different particle mobility values found (Meyer-Peter and Müller, 1948; Parker et al., 2003). The critical Shields stress value can be influenced by many factors including methodological bias but is independent of grain size. It has been found that calculation of an accurate critical Shields stress in the case of mountain rivers is challenging due to large bed roughness relative to flow depth (Lamb et al., 2008; Prancevic and Lamb, 2015). As a result of the shallow waters, particle shape and exposure are also important factors (Ashida and Bayazit, 1973). The presence of poorly sorted material and the positioning of grains with respect to neighbouring grains also influences entrainment as a result of hiding and protrusion effects between particles of different size (Wilcock, 2001). In previous studies, typical values of critical shear stress (Shield stress) for gravel bed rivers range from 0.03 to 0.06 for coarse gravel, as noted by Buffington and Montgomery (1997), with a widely used assumption of 0.045 for many studies. For finer gravel or sand-sized particles, critical shear stress values can range from 0.02 to 0.05. These values depend on sediment size, flow conditions, and bed roughness.

2.2 Importance of bedload transport monitoring

The mobilisation and transport of bedload in rivers is an important mechanism for the transfer of sediment from production to deposition areas (Burtin et al., 2010; Turowski et al., 2011; Roth et al., 2016; Roth et al., 2017). Understanding the timings and flux of bedload transport is important for not only predicting channel evolution, understanding bedform dynamics in river channels (Best, 1988; Bertoldi et al., 2009), and understanding global sediment budgets delivered by rivers to oceans (Syvitski and Milliman, 2007), but it also provides valuable information for problems in the fields of ecology, river and landuse management, and civil engineering (Turowski et al., 2011; Roth et al., 2017). Quantification of bedload transport

is a key element to understand, manage and restore the physical and ecological functioning of fluvial systems (Le Guern et al., 2020).

Channel evolution can affect the likelihood and distribution of flood events and thus understanding the effect of bedload transport on channel geometry is of high importance. The mobilisation of coarse sediments can have a significant impact on communities that live on or utilise alluvial plains (Badoux et al., 2014). The deposition of bedload in alluvial plains can cause long-term damage and disruptions to agricultural land and practices, and the erosive power of bedload in flood events can cause significant damage to infrastructure, such as buildings, dams and embankments (Bakker et al., 2020). With changes in climate potentially leading to more frequent and more severe flood events, bedload transport has the potential to cause more widespread and devastating damage to the landscape. Thus, it is of interest to develop a good understanding of the processes that govern bedload transport and how that translates into channel evolution and ultimately flood risk. Predicting bedload transport is therefore important for managing these risks, however, due to the spatial and temporal variations in sediment transport processes and the added complexity of the effects of changing climate and land use, sediment transport is very difficult to forecast.

2.3 Traditional bedload transport measurement techniques

Measurements of bedload transport rates have been traditionally conducted using direct measurements and manual sampling to measure the amount of material transported over a given time (Bunte et al., 2004; Downs et al., 2016). However, these traditional methods are labour-intensive, can be costly, and at high-flows can often be dangerous (Thorne, 2014; Downs et al., 2016; Gaeuman, 2016; Geay et al., 2020). Such measurement methods are therefore often collected during mild hydrologic events and at shorter timescales than are of geomorphological relevance. Therefore measurements are often missing during periods of high flows when most sediments are mobilised (Burtin et al., 2010; Chao et al., 2015; Downs et al., 2016; Gaeuman, 2016). Since bedload transport is a stochastic process and transport rates are highly variable in both space and time, it is difficult to assess and traditional methods have struggled to capture this variability (Jerolmack and Paola, 2010; Gaeuman, 2016; Roth et al., 2017). Automatic bedload samplers, commonly known as sediment traps, have been developed and widely used for continuous surveys, however, there are many challenges and limitations associated with these methods (Figure 2.2). These samplers are placed directly on the riverbed in areas of active sediment transport, either resting on the surface with a nozzle directing sediment into a bag or buried flush with the bed to trap sediment in a container, depending on the design and study requirements. They provide direct measurements of sediment transport, including particle sizes and transport rates. However, installation requires access to the channel bed, which can be logistically challenging, and their sampling duration is limited by the sampler's capacity to hold bedload material (Cook and Dietze, 2022).

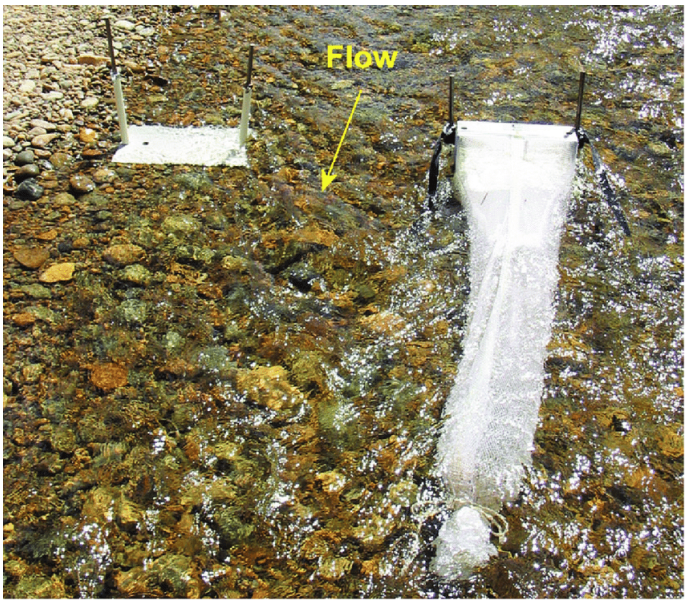


Figure 2.2: Sediment trap deployment from a study by Bunte et al. (2007) to acquire information on bedload transport during events.

2.4 Numerical modelling of bedload transport

As an alternative to traditional methods, engineers tend to rely on numerical models or empirical formulae to understand bedload transport (Geay et al., 2020). These model formulae have ranged from simple models looking at unidirectional flow of particles of uniform size to gradually more complex equations, incorporating numerous parameters to model bedload of mixed grain size using three-dimensional flow momentum equations (Dey, 2014; Rheinheimer and Yarnell, 2017). Simplification of these empirical equations relative to complexities of natural bedload transport processes in rivers, and the challenge of estimating grain size distribution, shear stress, and bed morphology among other factors, results in considerable uncertainties in the sediment transport predictions (Dey, 2014; Downs et al., 2016; Rheinheimer and Yarnell, 2017; Geay et al., 2020). Empirical relationships that have been calculated at low river flows or from data obtained through laboratory experiments can fail to capture the true behaviour of natural rivers at high flows, and data measured over short timescales fail to represent transport-rates over longer term (Roth et al., 2016). This is a particularly important challenge in mountain rivers where high suspended load can modify the transport of bedload (Quick et al., 2023), as these relationships struggle to account for the interaction between different particle transport modes.

2.5 Indirect bedload transport measurements

In recent years methods of measuring bedload transport have advanced to the use of active and passive sensors. Active sensors emit their own signals and record the response, and include methods such as Acoustic Doppler Current Profilers (ADCP) to determine apparent flow and bedload velocity (Rennie and Villard, 2004; Kostaschuk et al., 2005) and smart tracer particles which enable the tracking of particles in a river system (Singh et al., 2023). In contrast, passive sensors record signals that are generated naturally. These include the use of hydrophones suspended in the water

column to record particle impact generated noise (Geay et al., 2020), geophones embedded under impact plates to record sound vibrations of impacting particles (Rickenmann et al., 2014), and Japanese pipe hydrophones which record acoustic waves generated by particles impacting the sensor (Stark et al., 2024) (Figure 2.3). These measurement techniques provide information over longer timescales than traditional methods and are able to capture high-flow events. However, since many of them are situated in-stream there is a risk of damage or loss of equipment and the altered stream flow and transport patterns around the sensors can cause contamination of the data (Roth et al., 2016; Bakker et al., 2020). Although useful for exploring temporal patterns of bedload, single geophone impact plates or hydrophone sensors fail to fully capture the considerable lateral shift in sediment paths with discharge (Soar and Downs, 2017). Thus it is important to not rely entirely on the data from a single sensor and is useful to set up a cross-sectional array of sensors in the river channel or compare the data from the single sensor with data from other measurement techniques (Soar and Downs, 2017). Larger flow velocities are also often associated with greater particle velocities which has the potential to cause greater saltation/step lengths for saltating particles. Misset et al. (2020) suggest that the larger saltation lengths could explain the weaker signal seen at the Séveraisse catchment in the French Alps with increasing flow velocities, as the particles often don't come into contact with the geophone impact plate. Impact plates are also less sensitive to smaller grain sizes and thus the smallest grains are often not fully represented in resulting seismic spectra (Barrière et al., 2015).

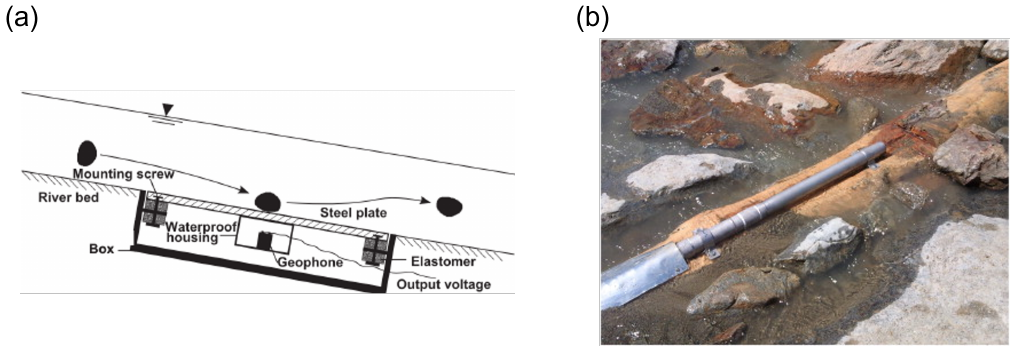


Figure 2.3: Examples of impact plate geophone set up (Wyss et al., 2014) and acoustic pipe hydrophone set up (Dell'Agnese et al., 2014)

2.6 Seismic monitoring of bedload transport

Increased support for low-cost, non-invasive and continuous indirect measurement techniques has led to an emerging method using seismometers to detect bedload-induced seismic vibrations (Govi et al., 1993; Hsu et al., 2011; Schmandt et al., 2013; Roth et al., 2014; Barrière et al., 2015; Roth et al., 2016). Modern seismic sensors such as geophones and broadband seismometers are sensitive enough to detect processes that emit only minimal impact energy to the ground, such as raindrops and wind turbulence (Dietze et al., 2020). Geophones are analogue instruments that convert ground vibrations into a voltage. A spring-mounted wire coil moves past a magnet as a result of the vibrations and creates an electric signal.

The use of seismic data and techniques in environmental seismology has emerged

as a method to study a large variety of processes, mainly related to hydrology and meteorology (Diaz et al., 2023). In the study of earthquake seismology, signals from surface processes were normally considered as unwanted noise. However, from the late 1900s studies linked seismic signals to geomorphic activities (Govi et al., 1993), landslides (Brodsky et al., 2003), glacial processes (Ekström et al., 2003), and debris flows (Coviello et al., 2018). Seismological techniques can also be used in astronomy and astrophysics (e.g. tracking electromagnetic storms) and biological and ecological studies for animal communications and behaviours (e.g. elephant migration and salmon nest building (Dietze et al., 2020)).

Seismics can be used within geomorphology to study the occurrence and timing of geomorphic events, the dynamics of geomorphic processes, and fluvial bedload transport (Cook and Dietze, 2022). Seismic data was first used in a fluvial study by Govi et al. (1993) to measure the coarse sediment delivery mechanism during flood events, in which they found a correlation between seismic signals and bedload transport mechanisms. Particle impacts on the river bed transfer momentum which in turn generates elastic (seismic) waves which propagate through the bed (Hsu et al., 2011; Tsai et al., 2012; Roth et al., 2017). Seismic sensors deployed outside the channel can distinguish the frequency and intensity of waves generated by bedload transport. Other surface processes such as landslides and water turbulence, as well as anthropogenic noise, can also induce elastic waves and thus can complicate the discrimination of the bedload transport signal, however they have previously been determined by the frequency and characteristics of the seismic energy (Burtin et al., 2008; Burtin et al., 2014; Gimbert et al., 2014). The use of seismic sensors for monitoring purposes allows increased spatial and temporal resolution to previously used direct measurement techniques (Burtin et al., 2010), and thus can be used to determine the timing and characteristics of bedload transport over timescales of geomorphic relevance. These indirect and non-invasive techniques also have advantage over in-stream sensors since they don't cause local change in the flow field near the sensor (Rickenmann et al., 2012).

2.6.1 Fundamentals of environmental seismology

The displacement of mass at the Earth's surface generates elastic seismic waves that propagate from the source through the surrounding medium until they are detected by a seismic receiver. Seismic signals are usually recorded as voltage fluctuations and converted to counts and then ground velocity by using the sensitivity of the sensor and data logger. Principally there are two classes of seismic waves: those that propagate in three directions from the source (body waves), and those that propagate along the free surface of the Earth (surface waves) (Figure 2.4)(Stein and Wysession, 1991). In most environmental problems, seismic signals are dominated by surface waves. However, usually all wave types occur. Following its emission from the source, seismic energy is radiated and dissipated by waves (Cook and Dietze, 2022). During seismic energy dissipation, the amplitude of source signal declines due to two major effects: geometric spreading and anelastic attenuation (Stein and Wysession, 1991). Geometric spreading refers to the amplitude decline of a wave as it radially spreads from the source. The amplitude decline varies for body waves (1 over distance squared) and for surface waves (1 over distance) (Stein and Wysession, 1991). Anelastic attenuation is where the elastic energy

associated with the wave is gradually absorbed by the medium it travels through. The ratio of initial energy to dispersed energy is known as the ground quality factor Q which describes the dampening effect. The dissipation of the seismic signals is dependent on the frequency content (Lekić et al., 2009). Low frequency seismic signals are less sensitive to attenuation effects than high frequency seismic signals. Therefore events that generate low frequency seismic signals can be recorded at high distances from the source, while those that generate high frequency signals will be dissipated much quicker and the signal can be lost at far distances from the source. This is cause for consideration in the experimental design of a seismic monitoring system. The ground through which seismic waves travel modifies the signal further through scattering at rock fractures, amplification locally due to topographic and rock structural effects, and altered by anisotropic or stratified ground conditions (Sánchez-Sesma and Campillo, 1993). These effects along with geometric spreading and anelastic attenuation are referred to as the Green's function or ground impulse response.

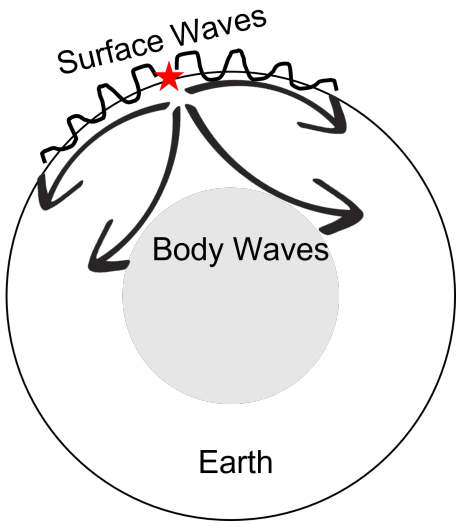


Figure 2.4: Propagation of surface waves and body waves through the Earth.

2.6.2 Use of geophones for river studies

Following the initial findings of Govi et al. (1993) that fluvial processes generate high-frequency (> 1 Hz) ground vibrations and could therefore be used to monitor rivers, several studies from the early 21st century confirmed these findings. It was suggested that river-induced ground vibrations were caused by two important sources: water flow and sediment impacting with the river bed (bedload) (Burtin et al., 2008; Hsu et al., 2011; Roth et al., 2014). This bedload-induced portion of the seismic signals were inferred by the presence of hysteresis in the relationship between flow stage or water discharge and seismic power, in which different levels of ground vibration were observed for similar flow conditions on the rising and falling limbs of flood events (Barrière et al., 2015). The behaviours of these hysteretic patterns have been attributed to different degree and processes of bedload transport during the monitoring period (Burtin et al., 2008; Hsu et al., 2011; Schmandt et al., 2013; Chao et al., 2015). Some studies have used additional measurements as evidence of bedload transport in the generated ground vibrations to compare with the seismic

power measurements through the use of sediment samples (Burtin et al., 2011), and geophone impact plate measurements (Roth et al., 2016). However, as mentioned these methods also come with considerable limitations and uncertainties. Progress in the understanding of river-induced ground vibrations was aided by the observation that hysteresis between water discharge or flow stage and seismic power was less significant at low frequencies (<10 Hz) than at high frequencies (>10-15 Hz) (Schmandt et al., 2013; Gimbert et al., 2014), leading authors to suggest that water flow and bedload transport generate ground vibrations at different frequencies.

The potential of using seismic sensors for bedload transport monitoring has been highlighted in a variety of settings: the Himalayas (Burtin et al., 2008; Burtin et al., 2010), alpine-style catchments (Burtin et al., 2014), Grand Canyon rivers (Schmandt et al., 2013), mountain sections of rivers in Taiwan (Hsu et al., 2011; Roth et al., 2014; Chao et al., 2015), controlled experiments (Schmandt et al., 2017), and engineered channels in Israel and Switzerland (Turowski et al., 2009; Rickenmann et al., 2014). These studies have typically been conducted in high altitude, steep mountain catchments with significant bedload availability and thus a large bedload signal. Lower river catchments generally have more anthropogenic noise due to their increased accessibility owing to more pronounced human activities, thus they are more challenging to apply seismic monitoring methods to. Bedload signals are generally weak and largely depend on the grain size of mobile particles, the channel slope and water discharge (Tsai et al., 2012; Barrière et al., 2015). Smaller rivers and flatter catchments are therefore generally more challenging to monitor. Burtin et al. (2011), however, did show that it was possible to detect the motion of bedload in moderate discharge mountain torrents with flows of 1-5 m^3/s. Despite studies reporting signals of bedload transport, Gimbert et al. (2014) showed through a physical model that many seismic energy recordings are largely influenced by turbulent flow induced noise, such as in the studies by Burtin et al. (2008) and Schmandt et al. (2013).

Understanding the source generating the seismic signal is imperative to being able to filter out the signal component that is required. Schmandt et al. (2013) found that there were in fact three distinct fluvial sources for seismic noise observed from a controlled flood experiment in the Grand Canyon: bedload transport at 15-45 Hz, fluid traction on the rough river bed at 0.73 Hz, and interactions between fluid and air such as breaking waves at 6-7 Hz. Although typically the two dominant sources found were water flow and bedload transport. Burtin et al. (2011) found a link between signals at 3-9 Hz being linked to river level, with an assumed linear relationship between seismic noise and water level. However, this relationship is limited by the river remaining within bankfull depths. It is therefore important to consider the sources of seismic signals when designing seismic monitoring systems, such as the distance between the seismic station and the path of the flow which influences the frequency as well as the power of the signals (Cook et al., 2018). In fluvial seismology, the combination of moving sources and frequency-dependent attenuation of seismic energy with distance makes it challenging to decipher these signals and are crucial factors to consider in the design of a system. Sensors placed near the river channel will primarily record activity in the local part of the flow path, with the measured signals being strongly influenced by the movement of flow relative to the sensor. Sensors deployed further from the source can provide an overview of the entire event, especially if the distance from the moving source (such as a flood

wave or bedload pulse) to the sensor does not change much over the duration of the event (Cook et al., 2018). This behaviour is highlighted in Figure 2.5, which shows an impulsive response to a passing flow front at a station adjacent to the river, but a more gradual emergent response from a station located at distance from the river as a result of recording signals over a larger area. Figure 2.5b shows two high energy seismic pulses from the initial flow front and then the trailing pulse of bedload.

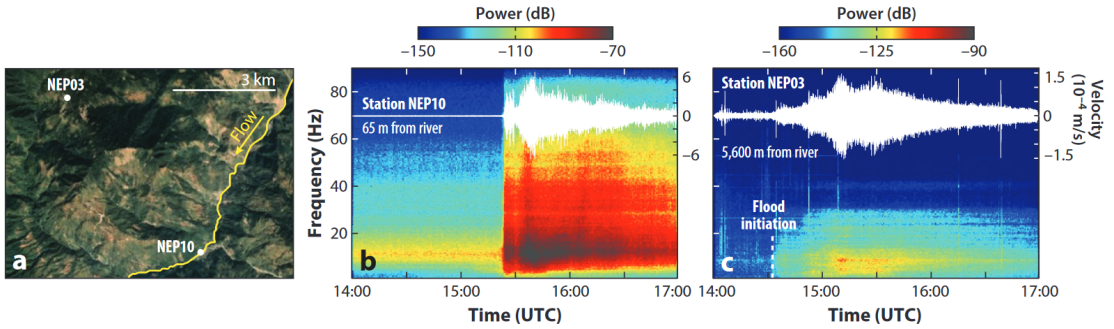


Figure 2.5: Signal differences between seismic sensors located (b) adjacent to the source and (c) at distance from the source from a glacial lake outburst flood in a study by Cook and Dietze (2022)

Although the majority of findings presented have been mainly obtained through the use of single seismic sensors, bedload transport has also been monitored using multiple sensors installed in vicinity of rivers. Schmandt et al. (2017) used an array of 76 sensors around a 700 m stretch of river to analyse the spatial distribution of seismic amplitudes, and Burtin et al. (2010) and Chao et al. (2015) used arrays of sensors to analyse the phase delays between the sensors. These methods allowed the identification of river sections that were subject to high bedload fluxes and the downstream propagation of an event observed as the event front or distinct bedload pulses arrive at different stations.

Seismic monitoring offers extremely high temporal resolution, enabling precise timing of events (Cook and Dietze, 2022). It can be used for retrospective analysis or near-real time monitoring with event picking systems in place which can provide foundation of early warning systems for geomorphic hazard mitigation. This picking is best for events with impulsive characteristics, however those with gradual onsets are harder to detect.

2.6.3 Fluvial seismology models

Significant advances in the field of fluvial seismology were made through the development of models for understanding the seismic signal generated by bedload transport (Tsai et al., 2012; Gimbert et al., 2019) and turbulent flow Gimbert et al. (2014).

Tsai et al. (2012) developed a model which predicts the seismic spectrum generated by the impact of bedload particles moving along the channel bed. It requires knowledge of stream and sediment characteristics to constrain source terms, such as channel geometry, grain size distributions, and ground properties affecting wave propagation. They found that grain size plays an important part in the strength of bedload-induced ground vibrations with the seismic power as a result of bedload transport scaling roughly as the bedload flux multiplied by cube of the 94^{th} percentile of the considered grain size. According to their model, we can assume that seismic power scales linearly with bedload flux and with the diameter of the coarsest

fraction of the sediment mixture to the third power. However, this model assumes that the particles are roughly spherical and of the same size, meaning the effects of particle hiding are not included.

Gimbert et al. (2014) developed a physical model for the seismic power of force fluctuations exerted on the river bed by turbulent motions in the water column. They found that, along with channel slope and bed roughness, the seismic power is strongly influenced by water flow stage. A key output from the model is that it predicts that turbulent flow generates lower frequency seismic signals than bedload transport, emphasising the importance of locating seismic sensors depending on the sources intended to monitor. Sensor location is critical, as different frequencies are subject to varying levels of attenuation in the subsurface, affecting the quality and range of seismic signals that can be effectively recorded. Gimbert et al. (2014) focus on the vertical directional component of seismic signals but acknowledge that turbulent flow noises generate a combination of Rayleigh and Love waves in the frequency range of 1-100 Hz. Rayleigh waves are surface seismic waves that have a retrograde elliptical polarisation, while Love waves are horizontally polarised surface waves that generate shearing motion along the Earth's surface. Additionally, the model suggests that the seismic power of turbulent flow can be related to flow velocity through a power law, and as such the power would therefore change linearly with the log of flow velocity. They suggest that the strength of hysteresis patterns observed in water discharge or flow stage and seismic power depends on the contribution of bedload transport to the overall noise that is dominated by turbulent flow-induced processes.

While these models advance the understanding on the role of turbulence in bedload transport and the characteristics of the seismic signals associated with these processes, they face challenges related to the complexity of the natural turbulence and bedload processes that occur within river systems as they rely of simplified assumptions of natural systems. They may also be limited at different spatial and temporal scales or in environments with high fluxes, i.e. more concentrated flows, or with highly variable conditions.

2.6.4 Key bedload transport seismic studies

As discussed, a number of studies since the early 2000s have undertaken fluvial seismology studies based on the initial findings of Govi et al. (1993). These studies have been undertaken in a range of fluvial settings at a range of spatial and temporal scales. Here I review a selection of these key papers to highlight the methodology and results previously obtained. These papers cover a range of geographical locations with varying channel morphologies, as well as a range of timescales. This is by no means an exhaustive review of all seismic bedload transport studies, and other key studies have been, and will be, referenced throughout this thesis and included in the bibliography.

Burtin et al. (2008):

In a study by Burtin et al. (2008), continuous seismic data from the Hi-CLIMB (Himalayan Tibetan Continental Lithosphere during Mountain Building experiment) network along the Trisuli River in the Himalayas (Figure 2.6) highlights significant spatial and temporal fluctuations in high-frequency seismic energy. A

diurnal as well as seasonal variation in seismic energy was observed which correlated with both regional meteorological and hydrological data. They found that although stream turbulence was partly the cause of the river-induced seismic signals, it did not account for the full signal and did not explain the clockwise hysteresis of seismic noise amplitude versus water level. This is where the amplitude of seismic noise recorded at the beginning of the monsoon is larger than that recorded at the end of the monsoon for equivalent water levels. They deduced that bedload transport better explained the signal patterns observed as if turbulence was the only source of seismic noise a linear relationship between amplitude of seismic noise and water level would be expected. It was observed that there was a north-south variability in the high-frequency seismic signal that coincided with a spatial variability of bedload type and hydrodynamics along the channel, with steep vertically incised river channels in the north with coarse bedload with large boulders and gentler gradient wider channels in the south with finer bedload of smaller pebbles. One interpreted cause of the hysteresis was that bedload that was available at the beginning of the monsoon had been removed at the end of the monsoon causing a decrease in seismic noise since only the largest boulders remain which can't be transported. However, a more likely explanation is that the river bed undergoes restructuring, making sediment more difficult to mobilise. In addition to this, they observed a constant amplitude of seismic noise above water levels of about 3.25 m despite a constant increase in the water levels. This was attributed to a threshold behaviour under the concept of critical shear stress needed to transport material from Shields (1936) and du Boys (1879). It is suggested that if the all available river bedload is in motion, an increase in water level should have no influence on seismic noise. Weak signals and correlations with meteorological and hydraulic conditions were observed in sites that had a low discharge and sheltering from precipitation at high altitudes, and due to too small bed load that is not easily detected. Burtin et al. (2008) pointed out the potential of using such methods for continuous bedload transport monitoring and to understand the spatial patterns.

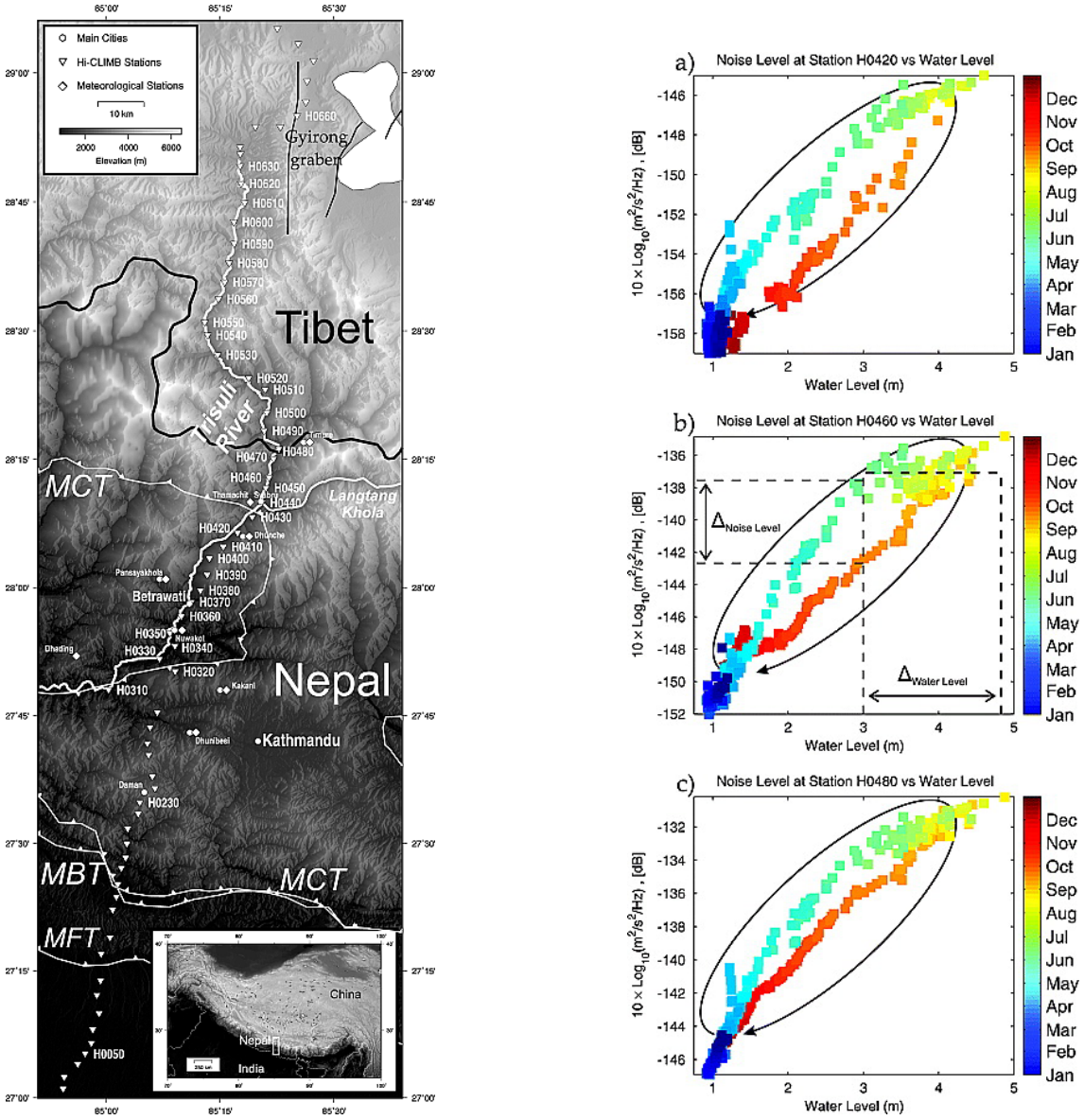


Figure 2.6: Relationship between seismic power and water level measured over a full year at three different seismic stations along the river channel (shown in the left figure) from the study by Burtin et al. (2008)

Roth et al. (2014):

Roth et al. (2014) explored the relationship between seismic signals recorded near rivers and river bedload transport. They used high-frequency broadband seismic data recorded at multiple sites along the Chijiawan River in northern Taiwan. By comparing floods of similar magnitudes with and without bedload transport, the researchers observe changes in the amplitude of seismic shaking at various river stages. A quantitative metric was developed which acts as a measure of the "normalised magnitude of seismic hysteresis during individual floods" and aids in discerning the relationship between seismic signals and bedload transport rates. The study found a qualitative correlation between this metric and sediment transport rates, indicating that the metric can reflect relative transport rates over time and between different locations along the river (Figure 2.7). Specifically, they found a dominance of bedload transport on the rising limbs of both storms, which they speculate to be from the time-dependent evolution of the bed due to processes such as grain packing, armoring, or temporal lag between stage and bedform growth. They also observed a

peak in hysteresis further downstream for the second event which is consistent with a migrating sediment pulse. Therefore, their results suggest that hysteresis in the relationship between seismic signals and river stage could serve as a tool for tracking sediment transport.

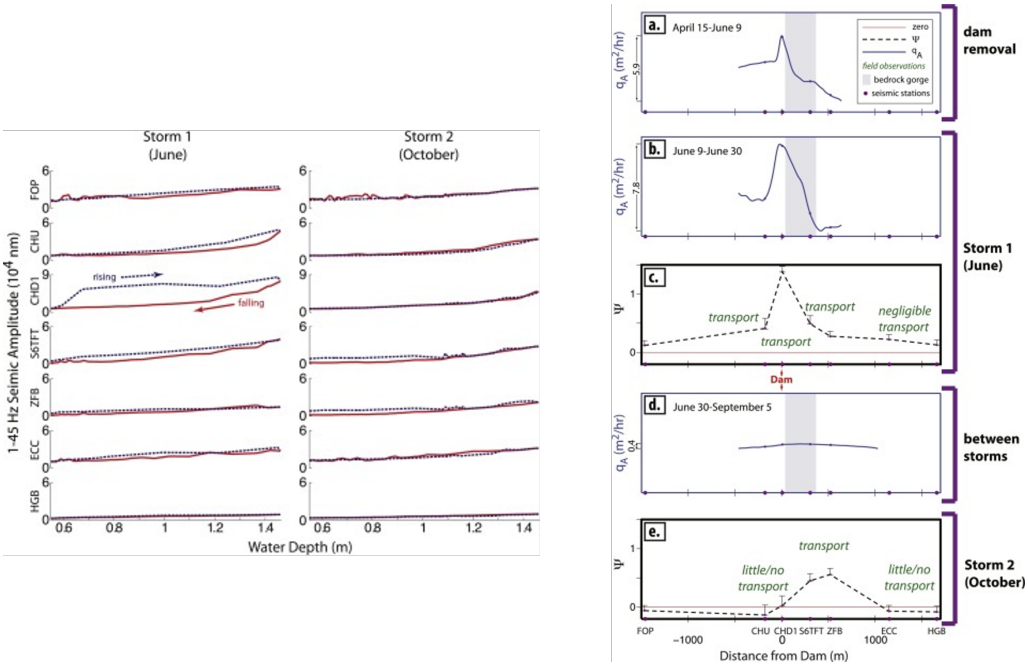


Figure 2.7: (left) Hysteresis patterns observed in the study by Roth et al. (2014) and (right) the relationship between their developed metric and sediment transport rates.

Barrière et al. (2015):

This study was one of the first to apply seismic monitoring of bedload transport to a low gradient gravel bed stream (maximum discharge of $< 2.3\ m^3/s$), following years of prior studies focused on steep mountain rivers. Their study combined seismic observations, hydroacoustic measurements, and hydromorphodynamic modeling. They used impact-plate hydroacoustic sensors to record the number and intensity of particle impacts on the river bed and deployed one seismic sensor on the river bank about 2m from riverbed and 30 m upstream from stream gauge. Two more sensors were deployed at larger distances: one next to a farm 100 m from the river station to capture noise from a nearby settlement, and the other about 1 km away in a quiet environment. A hydrophone was located 20 m downstream of the river station, with a sediment trap buried downstream of it.

When analysing the seismic power variations with frequency and time, they selected the tenth percentile of the original signal since the bedload transport signals were expected to be of low energy. They found that only the site closest to the river showed clear variations in seismic power over the course of the flood event and that seismic power closely correlated with changes in water level at that site at frequencies between 10-70 Hz. They also found that seismic and hydroacoustic measurements were less sensitive to the smallest grain fraction (1 mm).

Additionally they found that using the horizontal components of the seismic signals resulted in a 10 dB shift to higher magnitude and a 10 Hz shift to lower frequency content than when using the vertical component. As a result, based on the findings of Gimbert et al. (2014), Barrière et al. (2015) consider that horizon-

tal components are more sensitive to water flow processes than bedload transport. However, due to overlapping frequency bands, it is difficult to distinguish the seismic signatures of different fluvial processes.

They found that clockwise hysteresis was present for simulated bedload transport rate, hydroacoustic measurements and the seismic power (Figure 2.8). However, since flow velocity also exhibited a hysteretic behaviour, it suggests that hysteresis is not necessarily direct evidence of bedload effect. However, the rather limited flow velocity versus water level hysteresis does not explain the significant hysteresis in seismic power versus water level, suggesting flow velocity is not sole influence. They found that a seismic sensor located on the riverbank is sensitive enough to detect the start and end of gravel motion in even small streams with low discharge. However, they did not observe a frequency dependency of the signal with bedload at higher frequencies, which they suggest might be more common in coarser sediment and higher transport rates.

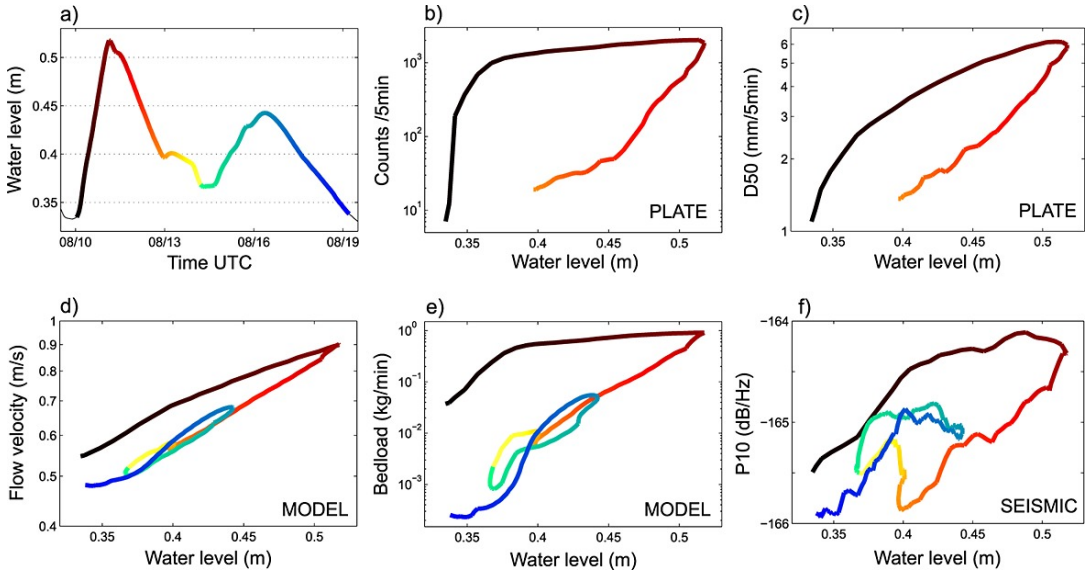


Figure 2.8: Variations in measured parameters with changing water levels in the study by Barrière et al. (2015) showing the varying hysteretic patterns observed.

Chao et al. (2015):

Based on the work of Burtin et al. (2008), this study investigates the correlation between bedload transport and river-induced seismic noise levels over a typhoon period, rather than a single flood event. Seismic data is collected from a short-period seismic array which was deployed along the gravel-bed Chishan River in southern Taiwan. A hydrological station is located several kilometres downstream of the stations, however due to rapidly changing cross sections there is a lack of continuous and reliable measurements of water discharge, therefore hourly water discharge data was calculated from a rating curve, using power-law relationship between water level and water discharge. The data reveals large-amplitude short-period seismic signals during the typhoon passage present in the frequency range of 5 - 15 Hz. They also observe that the high-frequency seismic noise is less dominant at a station located 1700 m from the river than a station 600 m from the river, demonstrating that river-induced noise from small-magnitude typhoon events have a limited propagation distance. They also found a strong clockwise hysteresis in the high frequency seismic noise relative to the hydrological parameters (Figure 2.9) which is not explained by the turbulence-induced seismic noise since it is expected to have a linear relationship (Burtin et al., 2008). In this study the hydrological measurements are roughly 25 km offset from the seismic measurements, and so to check that the hysteresis patterns are not caused by this spatial offset they compare the computed temporal lag between the seismic and hydrological data, using field-measured flow velocities, to the temporal difference between the peak in seismic power and the peak in water level. Since the computed lag is much less than the seismic power versus water level lag, this indicates that the majority of the hysteresis is not due to the spatial offset between the seismic and river gauge stations. They further estimate a number of hillslope failures identified from the seismic data are likely to have fed sediment directly into the river. More hillslope failures occurred on the rising limb than the falling limb, which they predicted to cause clockwise hysteresis which matches that observed. This indicates that transport capacity was higher on the rising limb, coinciding with higher sediment supply from hillslope failures. Therefore, they attribute the hysteresis observed to a change in sediment supply. However, they do not have detailed grain size data or riverbed evolution observations and therefore cannot exclude the possibility that the observed hysteresis is due to other factors, such as the time-dependent evolution of riverbed. They further assess the temporal changes of sediment flux ratio by using the seismic inversion model of Tsai et al. (2012). They found that the transition from bedload to suspended load depends on the sediment grain size and the transport stage and is very complex between the typhoon passage and off-typhoon periods.

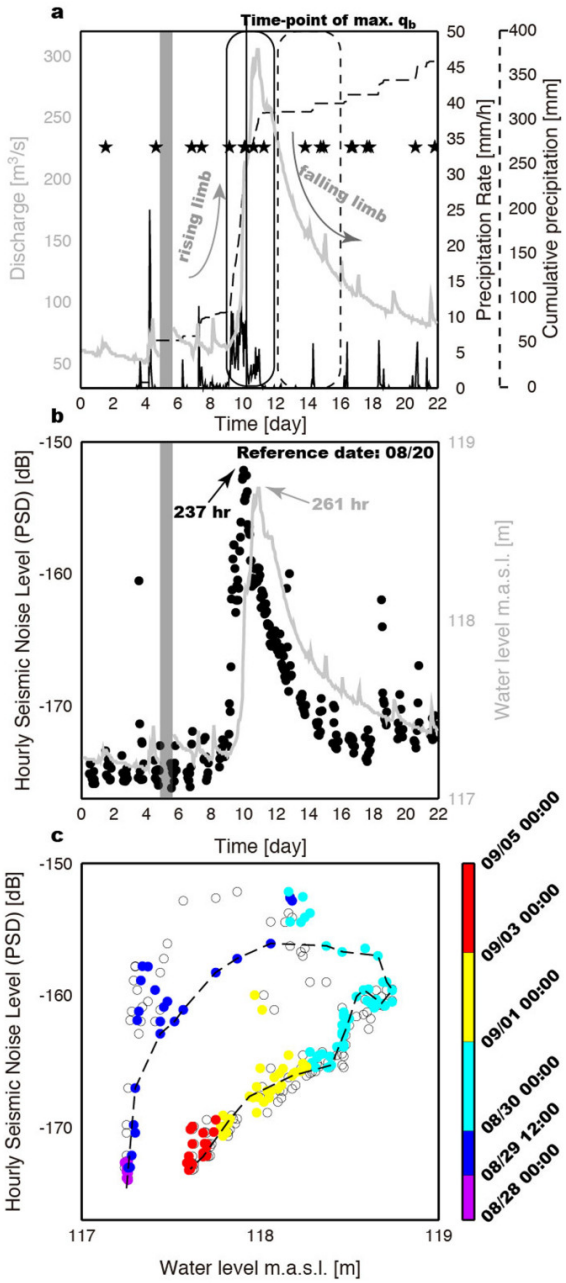


Figure 2.9: Relationship between seismic noise and water level over a full typhoon period from Chao et al. (2015)

Schmandt et al. (2013):

Schmandt et al. (2013) carried out seismic and infrasound measurements during a controlled flood experiment at the Colorado River in the Grand Canyon. They identified the presence of three distinct signals in their data: one from bedload transport, and two from fluid transport processes. The bedload mobility excited frequencies of 15-45 Hz, while fluid tractions with the rough riverbed resulted in a maximum seismic power increase at 0.73 Hz and the fluid-air interactions generated a 6-7 Hz signal (Figure 2.10). Additionally, they observed a similar hysteretic relationship between discharge and seismic power to previous studies, with the bedload-induced signal identified by clockwise hysteresis with a series of increases in bedload transport rate in the rising limb (Figure 2.10). Unlike previous studies, they also compare the signals recorded in the vertical and horizontal directional components, revealing that

the power of the bedload transport signal is nearly equal in both components. They suggest that Love and Rayleigh waves should be considered to seismologically monitor bedload flux, with factors such as bed roughness or rolling and sliding of grains being important mechanisms in the generation of enhanced horizontally-polarised waves.

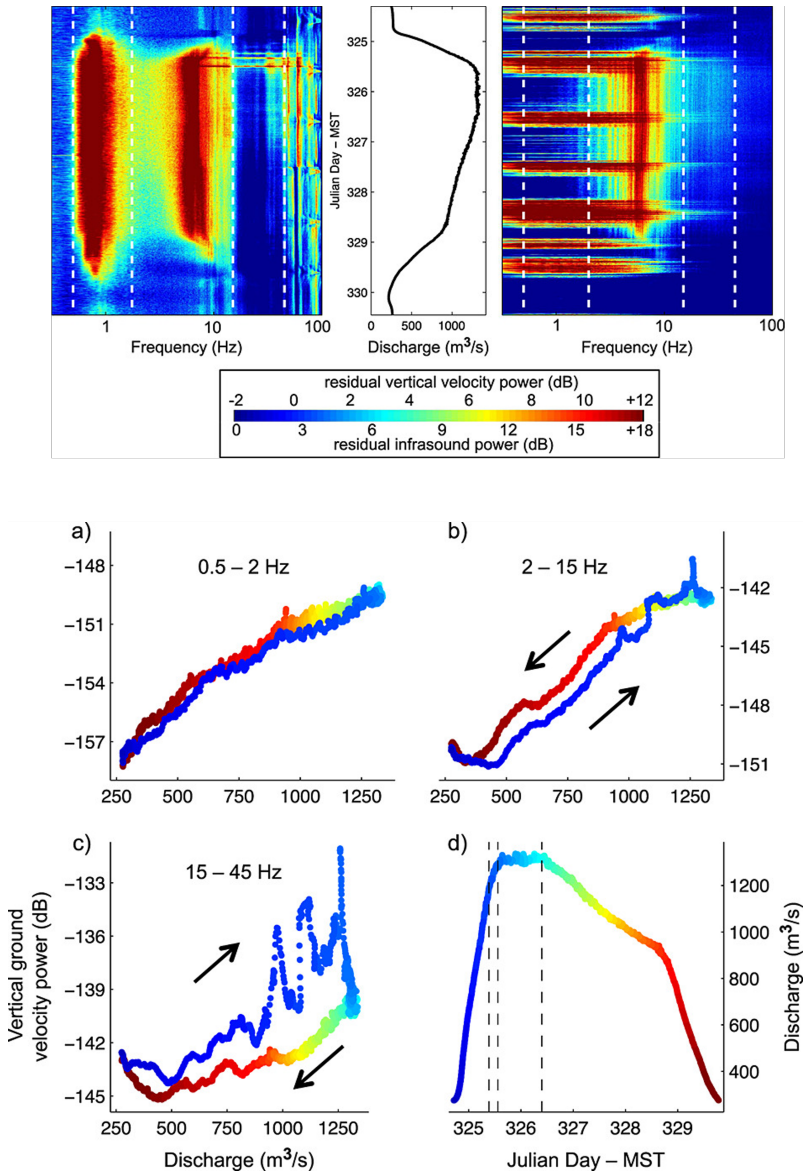


Figure 2.10: Top figure shows: (left) seismic power variations in frequency and time, (middle) hydrograph, and (right) infrasound data during a high discharge event from the study by Schmandt et al. (2013). Bottom figure shows the variation in seismic power versus discharge in three different frequency bands and the hydrograph of the event the data was collected over.

Rindraharisaona et al. (2022):

In addition to the studies looking at the fluvial seismic signals, some studies such as that by Rindraharisaona et al. (2022) have analysed the seismic signature of rain and wind. This is an important mechanism to understand and identify in any environmental seismology studies. Particularly in the case of the monitoring of flood events in rivers, as commonly an increase in water discharge is preceded by prolonged rainfall. These signals could therefore create challenges in differentiating the river-induced signals. Rindraharisaona et al. (2022) found that rain- and wind-induced seismic signals were most prominent at frequencies > 60 Hz and exhibited a broad range (Figure 2.11). This frequency range coincides with some of the observed frequency ranges of river-induced seismic signals discussed earlier. They additionally found that the soil type and the burial depth of the geophones influenced the seismic signature of rain observed, with increasing burial depth and soils with bigger grain sizes causing the most attenuation of rain signals. This is an important observation to consider in the deployment of geophones for fluvial seismology studies, in order to minimise the influence of rain drop impacts with the ground on the seismic signature recorded.

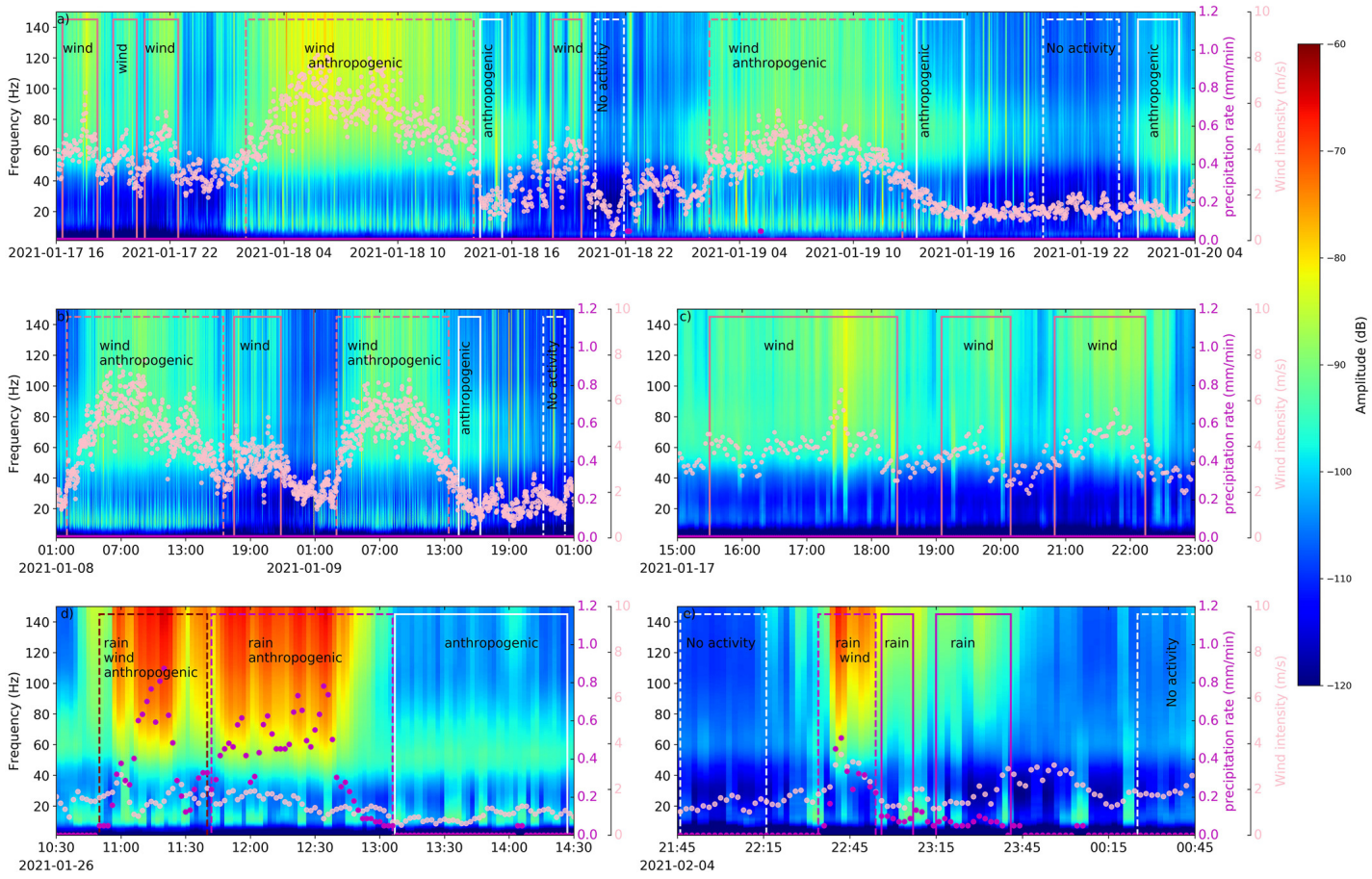


Figure 2.11: Seismic signature of wind and rain signals from Rindraharisaona et al. (2022)

2.6.4.1 Comparisons of key fluvial seismology studies

The reviewed studies highlight the versatility of seismic monitoring for investigating bedload transport processes across diverse river settings. All studies discussed identified hysteresis between seismic signals from rivers and hydrological parameters, with variations attributed to factors such as sediment supply, riverbed restructuring, and sediment pulses. The research covered both steep mountain rivers (Burtin et al., 2008; Roth et al., 2014) and low-gradient streams (Barrière et al., 2015), with timescales ranging from single flood events to seasonal changes such as monsoons and typhoons (Chao et al., 2015). Methods ranged from combining seismic measurements with hydroacoustic sensors to infrasound (Schmandt et al., 2013), and the studies explored different seismic components and frequency sensitivities. While most studies focused on vertical seismic signals, horizontal components showed distinct responses in some studies and were identified to be more sensitive to water flow processes (Barrière et al., 2015), although their role in bedload transport is still unclear. The studies reported bedload transport signals mainly in the 10–70 Hz range (Barrière et al., 2015) and 15–45 Hz range (Schmandt et al., 2013), with some noting frequencies as low as 5–15 Hz during typhoon events (Chao et al., 2015). Despite differences in methods, all the studies highlight the usefulness of seismic techniques for monitoring sediment transport and river dynamics in various river and environmental settings.

However, despite significant advancements in using seismic sensors to monitor bedload transport, several key research questions remain. These include how to more effectively distinguish seismic signals associated with bedload transport from those linked to other fluvial processes, such as turbulence, and how the spatial arrangement of seismic sensors influences the interpretation of river-induced seismic noise across diverse channel morphologies. The long-term impact of extreme events on sediment transport and seismic signals is also not yet well understood. Although the horizontal seismic component has been identified as important for reflecting water flow and bedload transport processes, its role has not been fully explored, warranting further investigation. There's also a need to better combine seismic methods with hydroacoustic and hydrodynamic models, as well as improve instrumentation and data processing to get more accurate and reliable seismic readings.

2.7 Hydroacoustic monitoring of bedload transport

Over the past 20 to 30 years, researchers have explored the idea that sound produced by collisions between mobile bed material could serve as a proxy for estimating bedload transport (Thorne, 2014). This has commonly been explored through the use of hydrophones. A hydrophone is a sensor which records the sound waves travelling through water. Hydroacoustic monitoring provides another non-invasive long term measurement method that can be used to monitor fluvial processes. They are often used in scenarios in which the direct measurement of river processes is either too dangerous or is unpredictable. Hydrophones can be used to measure the sound from bedload transport within rivers, as well as the sound from water turbulence. However, the use of hydrophones to monitor bedload transport is currently mainly limited to gravel-bed rivers (Le Guern et al., 2020).

Hydrophones are commonly deployed within pipes to record bedload impacts with the instrument or suspended in the water column to record sound waves as they propagate through the water. Additionally they can also be attached to the bottom of ADCP style boats deployed on the water surface (Le Guern et al., 2020). Hydrophones deployed on boats provide the potential to quantify bedload transport in large river with high spatial variability of sediment transport and map bedload transport at large scales.

Hydrophones can be used to measure bedload transport by recording interparticle impacts and impacts between particles and the bed (Thorne, 2014). The signal amplitude recorded from hydrophones strongly depends on the particle impact velocity and the number of impacting particles (Thorne, 2014). In addition to this, according to Thorne (2014), there appears to be an inverse relationship between the size of the impacting particles and the central frequency of the seismic spectra, meaning that larger particles generally result in lower frequencies.

Acoustic power measured using hydrophones can be correlated with bedload sampler measurements, as shown by Geay et al. (2020), to analyse the bedload transport signal. It also enables the analysis of the influence of grain size on hydroacoustic measurements. Geay et al. (2020) found that the relationship between the hydroacoustic frequencies recorded and the grain sizes measured was weak, but that the signal was more strongly linked to the riverbed slope and therefore the propagation effects.

Similarly to geophones, hydrophones are also limited by the size of the transported grains, as impacts from smaller particles are more difficult to distinguish from the background signal, restricting their use to studying larger grain sizes (Geay et al., 2017). Additionally, because hydrophones are deployed within the channel, they are susceptible to damage during high flows.

Summary

This chapter explored the foundational scientific background pertinent to this thesis, providing an extensive review of existing literature on methods used to monitor bedload transport in rivers. It sets the stage for the following chapter (Chapter 3), which will detail the methodologies used throughout this thesis to address the research objectives introduced in Chapter 1. Additionally, Chapter 3 will offer insights into the characteristics of the study sites, drawn from various on-site measurements conducted.

Chapter 3

General Approach and Methods

The initial aim of this PhD was to use seismic sensors to record and monitor bedload transport in the River Feshie during high flow events, and use this data to infer about the fluvial processes at play. We had initially deployed geophones and a stream gauge sensor in order to capture this information. However, early on in my PhD it was clear that natural alluvial river-induced seismic data is quite complex and therefore bringing in other measurement methods would compliment the analysis and make it stronger. This chapter gives a more detailed insight into the methods used in Chapters 3, 4, and 5, as well as a brief discussion of data collection methods that either did not work as intended or were not included in the final version of the results chapters of this thesis. It also discusses the site characteristics identified through some of these measurements, the chosen experimental design and set-up, as well as the steps for processing the seismic, water level and hydroacoustic data.

Fieldwork was undertaken throughout the duration of my PhD to deploy new sensors, download data, and maintain equipment. Unfortunately, I started my PhD during the height of the Covid-19 pandemic and therefore initial fieldwork was restricted. Luckily, unlike several of my fellow Covid-19 PhD colleagues, I was able to perform my first field visit in December 2020. This trip involved the initial deployment of a selection of geophones along with a stream gauge sensor. Subsequent routine field visits were performed throughout the course of my PhD, every roughly 1 to 4 months, to maintain equipment that was already deployed and install new instruments as the project progressed. Some field visits included additional geomorphic and seismic measurements that were performed with the help of other colleagues within the University of Edinburgh and from the University of Glasgow.

3.1 Measurement methods

As mentioned previously, the key continuous measurement methods used to monitor bedload transport in this thesis included seismic, hydroacoustic and water level data. Along with these, timelapse imagery was gathered to record visual evidence of morphological change of the river channel in the stretch of interest. The locations of the continuous measurement instruments are shown in Figure 3.1. The instruments are described throughout this section and the chosen sitings of the geophones are described in more detail in section 3.3. The first instruments were deployed in December 2020 with additional instruments deployed throughout the monitoring period (Figure 3.2b). For this thesis, data from five high flow events in 2022-2023

are analysed as there were a number of geophones recording along with at least one of each of the other measurement methods (Figure 3.2). These events occurred on the 11th-14th March 2022, 30th September - 1st October 2022, 2nd-3rd November 2022, 24th-25th September 2023, and 7th-9th October 2023. In addition to these continuous recordings, grain size and channel geometry measurements were performed to gain a better understanding of the sediment characteristics and dynamics of the channel. These methods are described in more detail in the following subsections.

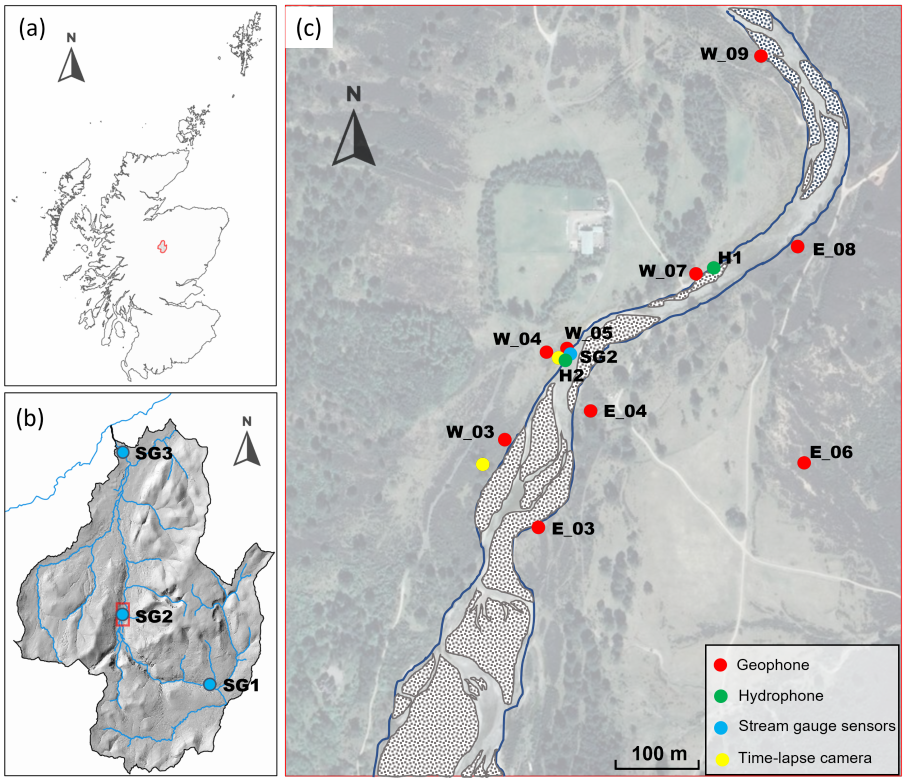


Figure 3.1: Location of the River Feshie study reach in relation to (a) Scotland and (b) the River Feshie catchment showing locations of stream gauges, along with (c) the monitoring instrument locations.

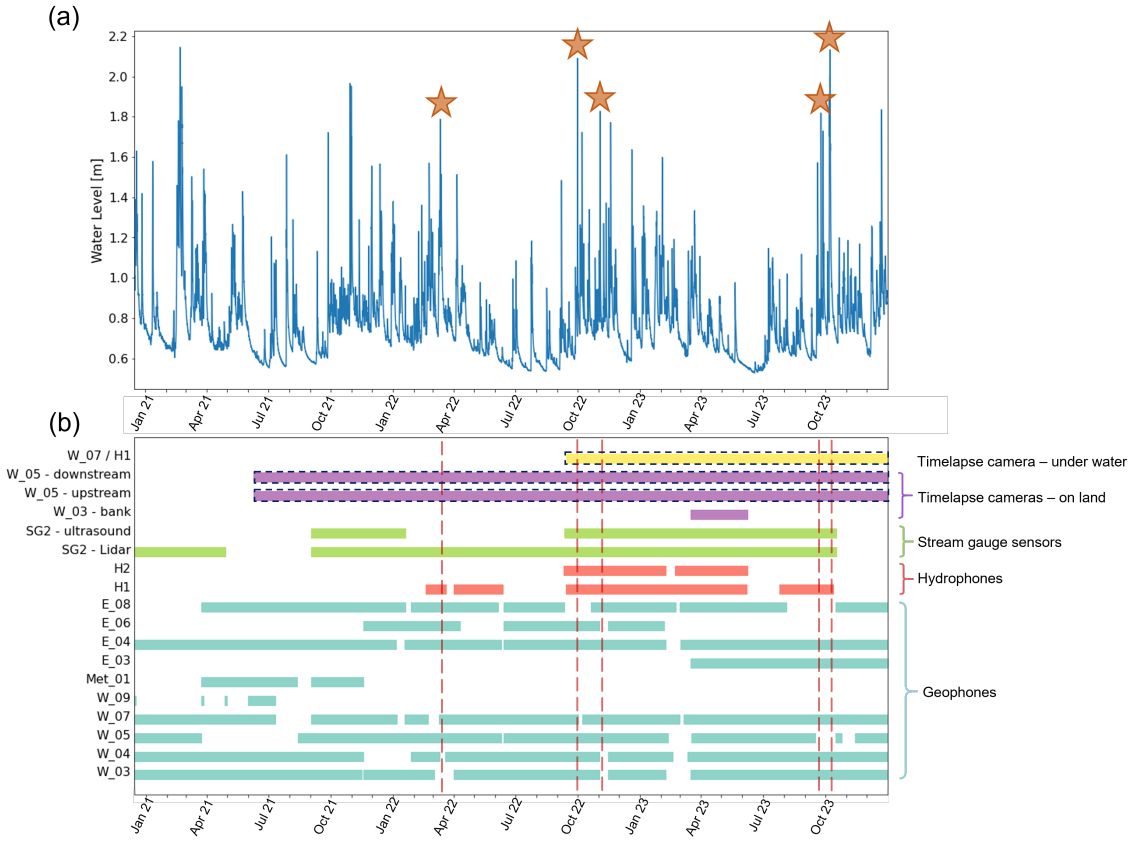


Figure 3.2: (a) Hydrograph of water levels at SEPA Feshie Bridge stream gauge (at SG3) over the full monitoring period of this PhD. Stars show the five key events analysed in this thesis. (b) Timeline of sensor deployments over the monitoring period, showing the geophones in blue, hydrophones in pink, stream gauge sensors in green, timelapse cameras deployed on the banks in purple, and the underwater camera in yellow. The dashed borders for the cameras are included to indicate intermittent recording throughout these periods.

3.1.1 Seismic measurements

To record the environmental seismic signals we had a set up at each geophone site consisting of geophones connected to GPS units (for real time timestamps), data loggers (recording and storing the data), and batteries (for providing power to the data loggers). These instruments were housed together in a plastic storage box which was painted brown to camouflage it (Figure 3.3). The boxes were generally tucked into bushes or wedged next to trees to keep the boxes hidden, but to also protect them from flood waters.

As mentioned earlier there are various different styles of seismic sensors that can be used. For our study we used 3-D PE-6/B 4.5 Hz geophones (specifications provided in Table 3.1), which are 3-component geophones with a reinforced plastic land case and three steel spikes (Figure 3.4). Internally it houses three sensors: one SM-6/U-B 4.5 Hz vertical geophone, and two SM-6/H-B 4.5 Hz horizontal geophones mounted perpendicular to each other. These sensors record the vertical motion and the North-South and East-West horizontal motions. The North-South component direction was marked on the plastic casing of the geophone with an arrow, and for this study was oriented in the downstream river direction (with the North arrow pointing downstream) to capture the stream-parallel signals. Consequently the East-West component was oriented at right angles to the river channel therefore capturing the stream-perpendicular signals.

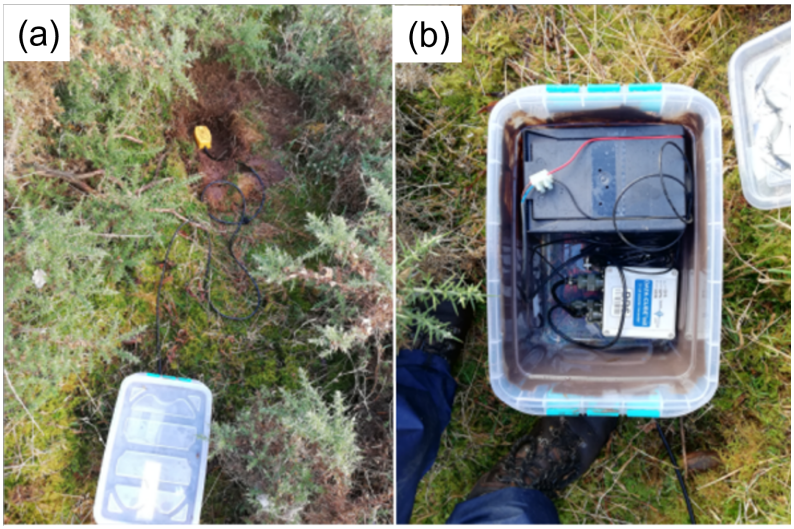


Figure 3.3: Geophone site deployment showing (a) the geophone connected to the data logger in the box and (b) the data logger, battery and GPS inside the box.

The geophones were connected to Digos DataCube loggers (DATA-CUBE^3 Type 2) sampling at 200 samples per second, which can resolve frequencies up to 100 Hz, with a gain of 16. These data loggers had an external cycled GPS which allowed the device to operate for long time measurements with continuous time correction. The exact GPS model varied as we had to order new units for new geophone sites or to replace broken units at existing sites, but all GPS units had an operating frequency of 1575.42 MHz and voltage of 3V-5V. Using an external GPS allowed flexibility with the instrument housing and location. This gives the option to externally locate the GPS outwith the plastic box in better satellite view while keeping the box hidden out of sight. The Digos DATA-CUBE^3 has an internal capacity of up to 32 GB and a full day of data recorded as part of this PhD on one three-component geophone at 200 samples per second totals approximately 220 MB. This results in the data logger being able to store up to approximately four and a half months of data. The DataCubes were also connected to 9V 155-165Ah Air Alkaline batteries that provided enough power to continue recording for around 5-6 months at optimal efficiency. In reality, cold weather, flooded batteries, dud batteries etc. meant that the recording times varied significantly from just a few days up to around 5 months. Despite these challenges, they offer greater reliability compared to solar power (which is affected by low light conditions) and wind power (prone to turbines icing up during winter).

Table 3.1: Specifications of 3-D PE-6/B 4.5Hz Geophones.

Sensitivity	28.8 Vs/m
Response	4.5 Hz to >150 Hz
Damping	0.56
Weight	1kg
Operating Temperatures	-40 to + 100 °C
2 Zeros	z1, z2 = 0
2 Poles	p1 = -19.78 20.20i p2 = -19.78 -20.20i



Figure 3.4: Technical set-up of the geophones deployed in this study site. Image from the DATA-CUBE^3 User Manual `https://digos.eu/wp-content/uploads/2020/07/DATA-CUBE-User-Manual-2020-05.pdf`

3.1.2 Seismic model

In addition to recording the seismic signals from the study site and analysing the characteristics of the data, I also used a pre-developed seismic model to predict the expected signal content from bedload and water turbulence induced ground vibrations. Dietze (2018b) developed a free and open source package for the programming language R called 'eseis'. This package provides a toolbox for environmental seismology for the processing, analysis, and visualisation of environmental seismic data. The package aims to streamline the workflow for researchers in environmental seismology by providing tools to handle seismic data from the initial processing to advanced analysis and visualisation. The package contains a selection of 51 different functions, two example data sets, and a reference manual to help in the processing and analysis of seismic data. The package can be installed through CRAN or from GitHub repositories as described in Dietze (2018b). Data can be analysed through written code in R or using the graphical user interface developed for exploring data and functions with the 'eseis' package.

Included in this package are two model functions to calculate the seismic spectrum due to impacting bedload particles with the river bed and the hydraulic turbulence of the channel flow. The bedload transport model (`model_bedload`) uses the model predictions of Tsai et al. (2012), as discussed in Chapter 2, and the turbulence model (`model_turbulence`) uses the predictions of Gimbert et al. (2014). The model assumes that the seismic spectrum recorded adjacent to a river is dominated by signal from the activity in the channel from a combination of turbulent flow and sediment particles impacting with the river bed during bedload transport. Other sources of seismic noise, such as wind and rain or anthropogenic activity, are assumed to be less significant. It is under these conditions that the seismic models of Tsai et al. (2012) and Gimbert et al. (2014) could be combined.

Specifically, the seismic spectrum as a result of particles impacting with the bed is based on the Hertzian theory (Brogan, 1962). The energies of the impacts are calculated for a mobile sediment layer which is composed of particles whose sizes are calculated from a raised cosine distribution function (Tsai et al., 2012). The sediment layer is also characterised by its velocity, height and settling velocity. The

model then calculates the seismic power for each frequency increment of the output spectrum, accounting for seismic ground properties that determine frequency-dependent amplitude changes. The seismic spectrum as a result of turbulent flow interacting with the bed (Gimbert et al., 2014) is determined using the drag, lift, and cross-stream force fluctuations. These force fluctuations are converted to ground velocity and then to a seismic power spectrum representative of the vertical directional component.

I use the R 'eseis' package functions of `model_turbulence` and `model_bedload` by Dietze (2018b) in Chapter 4 to model the numerically expected seismic spectrums from turbulence and bedload transport using the R code in Appendix A. I use a combination of field measured data and default parameters as described in the work in Chapter 4.

3.1.3 Hydroacoustic measurements

To independently characterise bedload motion recorded within the study site, we deployed custom built hydrophone recorders (Figure 3.5) within the river at sites H1 and H2 (Figure 3.1), to record the hydro-acoustic signals. Matt Gervais took the lead in designing and building these instruments for the project. The hydrophones used (Jez Riley French D-series, `https://jezrileyfrench.co.uk/hydrophones.php`) have very little documentation providing information on the characteristics of the devices. The recorders consisted of:

- Hifiberry DAC + ADC Pro - a digital-to-analogue and analogue-to-digital converter that was used to record signal from the hydrophones, sampling at 44.1 kHz
- PiJuice Zero - a power controller and real-time clock to keep track of time and schedule recordings, and manage the system power.
- Power - power was supplied by 12V deep cycle batteries. We intially deployed 90 Ah batteries but swapped to 45 Ah batteries as they were lighter and more convenient to carry into the field. The recorder also had an internal 5000 mA battery which allowed the system to continue running for a short time when the lead acid batteries were disconnected during service runs. The 45 Ah batteries provided approximately 6-7 weeks of runtime with the default system configurations.
- Raspberry Pi Zero - a computer processor to control the system.
- Voltage converter - a generic 10-30 V to 5 V step down converter was used to convert the 12 V battery voltage to 5 V as needed by the Raspberry Pi.

In previous hydro-acoustic studies hydrophones have been deployed in metal pipes or attached to metal plates embedded in the river bed (Barrière et al., 2015), attached to the bottom of boats or river surveying equipment such as river boards (Geay et al., 2020), or attached to man-made infrastructure, such as bridges or metal frames (Belleudy et al., 2010), however, this was logistically not an option in our study site. Instead, the hydrophones were deployed inside approximately 20 cm diameter bores within approximately 30x30x30 cm granite blocks using custom

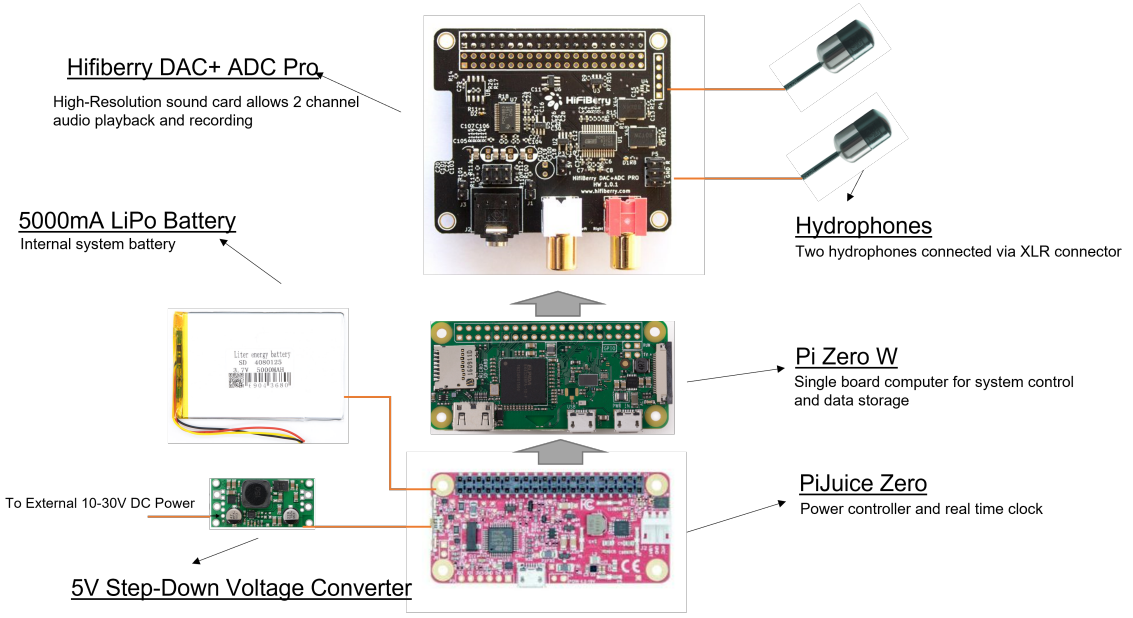


Figure 3.5: Hydrophone set-up showing each electrical component. Image provided by Matt Gervais from the project team.

3D printed mounts (Figure 3.6). The bores were oriented perpendicular to the river flow. The hydrophone block at H1 was located approximately 5 m downstream of the geophone at site W_07 and 40cm from the river bank (Figure 5.1). The block was sat on the gravel bar adjacent to the bank which was exposed until water levels at SG2 reached approximately 0.75 m. The hydrophone at H2 was located beneath an old bridge adjacent to geophone site W_05, which was underwater until water levels dropped below around 0.20 m. Cables between the hydrophones and dry equipment were protected by plastic piping and buried beneath large cobbles to protect against moving material.

Due to the size of the data files, only 30 second sound samples were recorded every 15 minutes. Data were generally recorded at two different gains of 30 dB and 40 dB to manage potential issues of data quality. In addition to measuring collisions between particles and the bed, like geophones, acoustic hydrophones have the potential to record collisions of particles in suspension depending on the size of transported sediment. The hydroacoustic data was used as a complementary data set to the seismic data to confirm the occurrence and timing of bedload motion. For the research in this thesis, data from H1 was used as it was working over the duration of the PhD monitoring period.

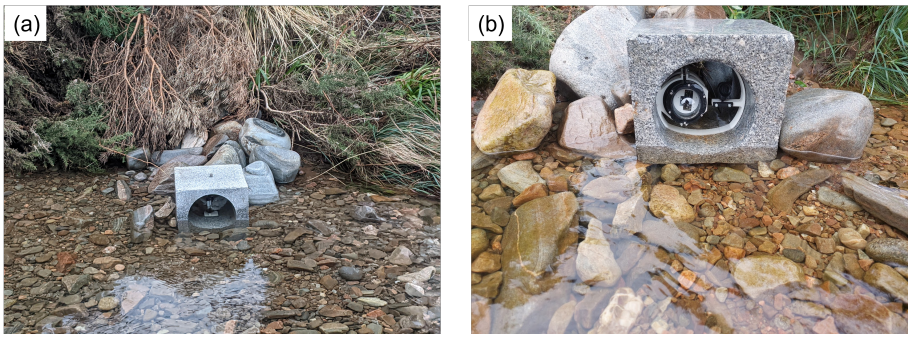


Figure 3.6: Hydrophone deployment in the study reach showing hollowed out granite block and custom 3D printed instrument mount inside.

3.1.4 Water level measurements

A research group at Imperial College London (Riverlabs) led by Professor Wouter Buytaert have developed low-cost water level sensors that can be developed with a range of technologies depending on the application, including ultrasound, LiDAR, RADAR and pressure transducers. For our study we utilised LiDAR and ultrasound sensors to provide information on water level (Figures 3.7 and 3.8b). Both sensors work by emitting either a laser pulse or an ultrasound beam and measuring the time it takes for the pulse to return to the sensor once reflected off the water surface. The specifications of the two sensors are shown in Table 3.2 but the key installation difference of the sensors is that the ultrasound sensors are most accurate when deployed perpendicular to the water surface as errors may be induced by the diverging beam of ultrasound signal, whereas the LiDAR based sensor has the advantage of being able to measure at angles up to 40° with minimal loss of accuracy due to the very low divergence of the LiDAR beam. Both sensors are powered by a rechargeable 3.7V 18650 lithium battery with a capacity of around 2000 mAh. The LiDAR sensors takes one measurement every 5 minutes, where the ultrasound sensor takes 10 repeat measurements every 5 minutes in which the median can be taken to smooth out noise in the measurements.

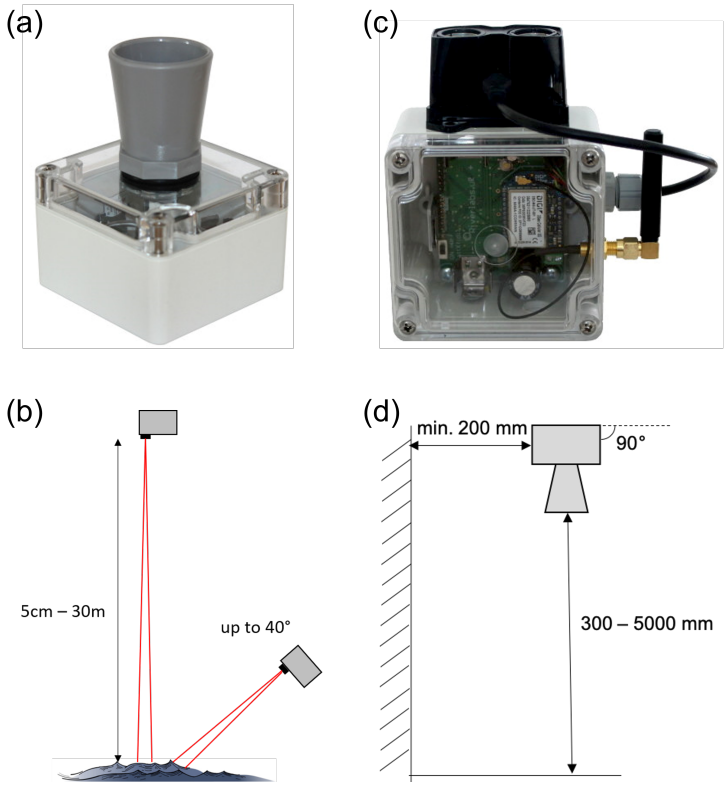


Figure 3.7: The (a) LiDAR sensor and (b) its deployment setup, and the (c) ultrasound sensor and (d) its installation diagram. From `https://ichydro.github.io/Riverlabs/index.html`

The remains of an old wooden footbridge central to the study reach was used to deploy the water level sensors, as shown in Figure 3.8. The sensors were attached to the bridge using a pole and a custom-made 3D printed mount, which enabled the sensors to be oriented the correct way to avoid data loss by scattering.

We also had access to water level and discharge data collected at stream gauges SG1 and SG3, located approximately 10km upstream and downstream of our site

(Figure 3.1). These data are managed by Dr Andrew Black (University of Dundee) and SEPA, respectively. We use the SEPA data as the historic record since our local sensor has only been operational since the end of 2020. The data from SG1 is intermittent and is therefore not used in much of the analysis in this thesis.

Table 3.2: Local stream gauge sensor specifications

	Wari (ultrasound sensor)	**WMOnode (Lidar sensor)**
Sensor	Maxbotix MB7389 Ultrasound	Garmin Lidarlite v3HP sensor
Range	0.3 - 5 m	0.05 - 35 m
Resolution	1 mm	1 cm
CPU	Atmel Atmega328	Atmel Atmega328
Bootloader	Arduino Pro Mini	Arduino Pro Mini

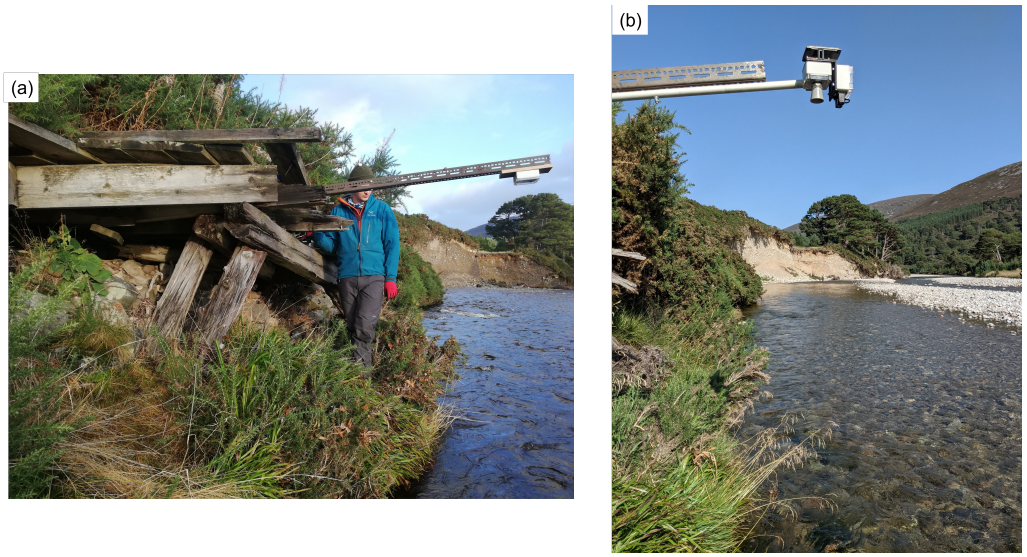


Figure 3.8: (a) Local stream gauge sensor deployment on remains of an old wooden bridge in the centre of the study reach. (b) Custom mount to house both the Lidar and ultrasound sensors.

3.1.5 Timelapse cameras

3.1.5.1 Cameras deployed on river banks

Timelapse cameras designed to capture wildlife were deployed in the site to acquire visual evidence of morphological changes to the immediate channel. Two brands/models of camera were deployed: Browning Recon Force Elite HP5 and Wingscapes TimelapseCam Pro (Figure 3.9). These cameras could be set to record any number of images at a specified frequency. The Wingscapes images could be recorded with four resolution settings from low (2115x1188p) to enhanced (6080x3420p). Neither camera was able to record at night. Cameras were fitted with 32GB SD cards for recording data, and AA batteries to provide power. According to the manuals, the Wingscapes TimelapseCam batteries could last up to about 6 months and Browning camera batteries could last up to 20 months, depending on the environment and usage factors. For efficiency, we just downloaded data and changed batteries whenever we were doing a service run for other instruments which occurred around every 1-4 months.

During the monitoring period three cameras were deployed: two at site W_05 and one upstream of W_03, as shown in Figure 3.1. These cameras were set to capture an image once every 15 minutes, however, the cameras regularly failed to capture images or had issues with the time scheduling. This was likely due to inadequate knowledge of how to properly configure the camera settings, as well as the requirement to reset the settings after each download, a process not all field members were familiar with. Additionally, water entering the camera housing interrupted recordings, and cold temperatures caused batteries to deplete quickly. The setup could have been improved by ensuring that all field members were properly trained in camera configuration and by changing batteries more frequently in cold weather. However, this was challenging due to the distance to the site and the frequency of service runs. Each image contained a timestamp which allowed easy comparison to other datasets, but due to scheduling issues it was often difficult to accurately determine the time of the images. Unfortunately, none of the cameras recorded images during the events analysed in this thesis, however, Figure 3.10 shows the state of the river at high and low flows typical of that observed during the selected events.

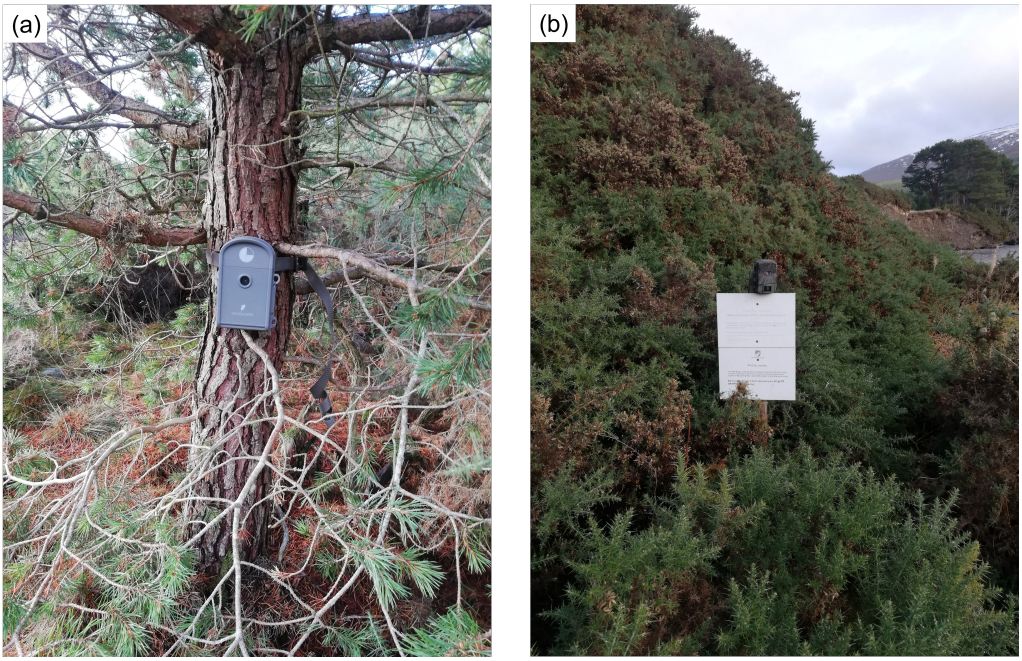


Figure 3.9: Field photographs of the two time-lapse cameras deployed at site W_05 that are facing (a) downstream and (b) upstream of the site.

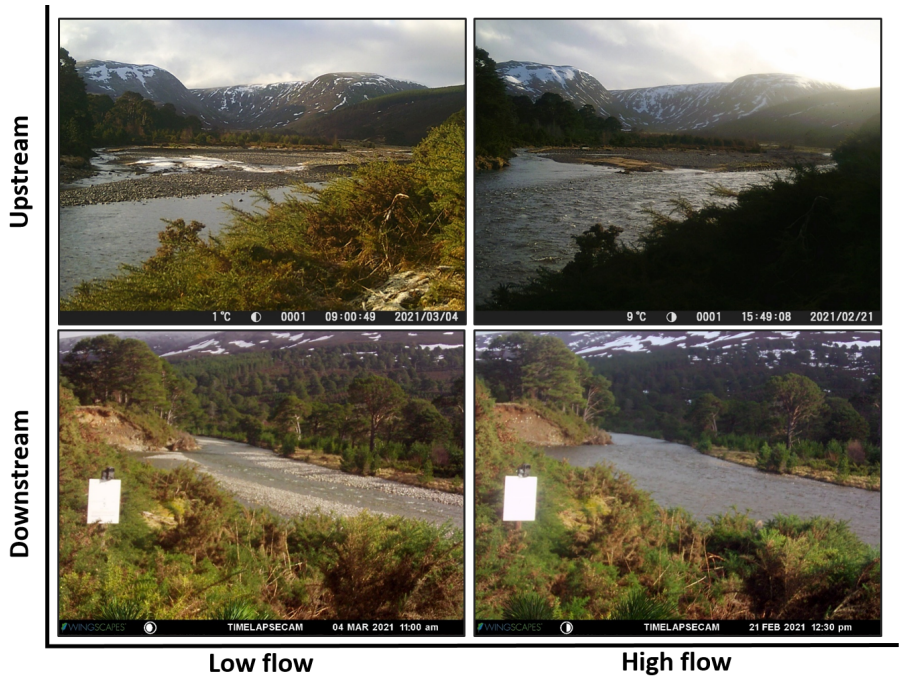


Figure 3.10: Photos from the River Feshie fieldsite looking upstream and downstream from W_05 during high flow and low flows. Images are taken from February and March 2021 as these had the clearest conditions and are representative of general high and low flows at the site. During the low flow event the SEPA stream gauge at Feshie Bridge measured a water level of 0.76 m and the high flow event photographed here peaked at 2.15 m.

3.1.5.2 Camera deployed in the channel

In addition to the timelapse cameras deployed on the river banks to capture channel morphological changes, we deployed a camera mounted on a custom 3D printed mount by Matt Gervais within the same granite block as the H1 hydrophone adjacent to site W_07 (Figure 3.6). This camera was housed in a watertight enclosure with a clear domed endcap, to capture video snippets of the channel perpendicular to the river flow. The scheduling and recordings components of the system were housed in a watertight enclosure on the bank, and were set to record a 30s snippet every 30 minutes. The specifications of the camera can be found in Table 3.3.

Table 3.3: Underwater camera specifications

Camera module	5 MP Fisheye OV5647 Raspberry Pi camera
Aperture (F)	2.35
Focal length	adjustable
Field of view (diagonal angle)	160°
Field of view (horizontal angle)	120°
Resolution	1080p max.

This camera was originally deployed in the hopes that we could capture the movement of bedload particles and develop a method for extracting the grain sizes of the particles experiencing motion. However, the technical camera setup had a few issues that were not fully resolved and we therefore failed to capture recordings of active pebble movements. It did, however, record a few video snippets that showed the rearrangement following high flow events. Figure 3.11 includes four photos captured by this camera; two prior to a high flow event in late September-early October 2022, and two following the event. From these we can clearly see that

the grain sizes on the river bed prior to and following the event are significantly different, with much larger grains deposited on the bed and bar following the event. These larger grains have also infilled the small channel that ran between the camera and the gravel bar at low flows, extending the bar towards the bank. Unfortunately, there are no video snippets available before and after the other four events selected for analysis in this thesis.

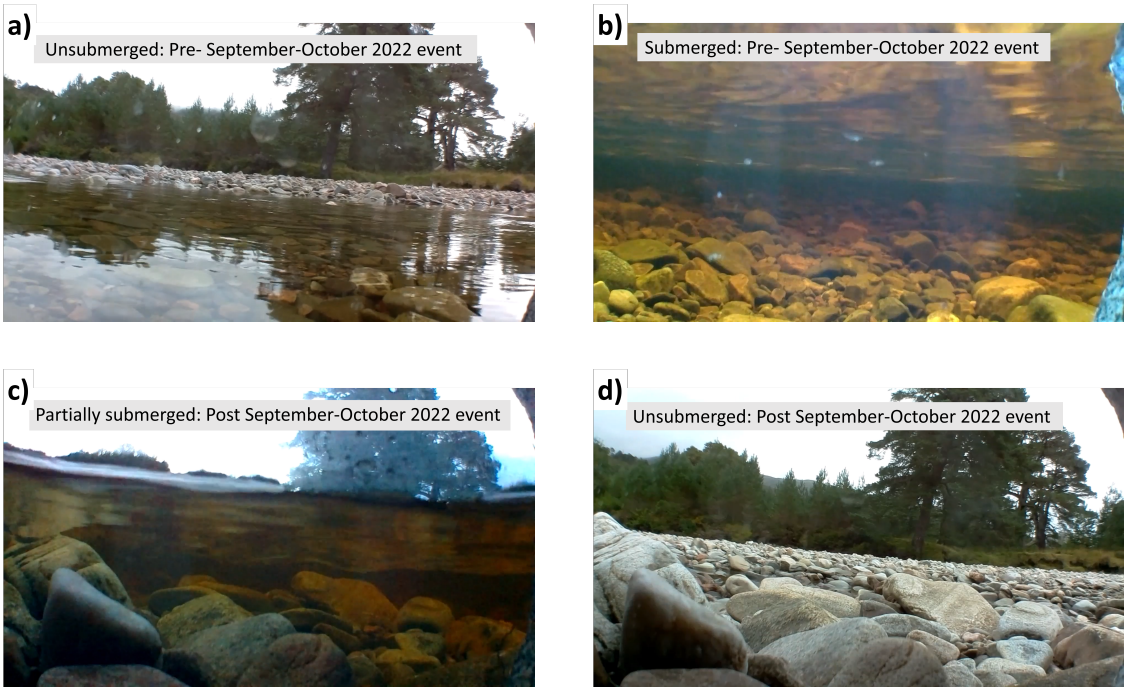


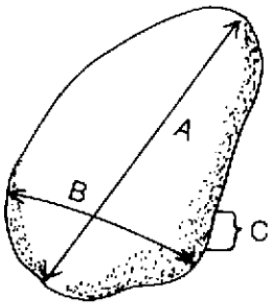
Figure 3.11: Screenshots of video recordings taken (a,b) prior to September-October 2022 event and (c,d) following the September-October 2022 event.

3.1.6 Grain size measurements

The composition of stream beds and banks are important stream characteristics and influence channel form, hydraulics, erosion rates, and sediment supply (Harrelson et al., 1994). The composition of the stream bed (substrate) can be documented through quantitative descriptions of material. Measurements of the grain sizes in the study reach were undertaken through a variety of methods and repeated several times throughout the duration of my Ph.D.

The main and most frequent method used was the Wolman pebble count (Wolman, 1954) in which an observer walks a selected transect of the stream/channel and randomly selects substrate. Substrate are described as having three axes of measurement/size: (A) - long axis, (B) - intermediate axis, (C) - short axis (Figure 3.12). For all Wolman pebble counts, the 'b-axis' was measured, as it is the axis most likely to be used by the pebble for downstream travel, aligning with the direction of flow and allowing for easier, more stable transport. There are multiple methods for undertaking a pebble count method including a step-toe method, laying out a linear transect or a grid and measuring the pebble at regular intervals along the transect, or randomly selecting particles in a small area of the channel. For measurements on gravel bars, I used a 2 m x 2 m grid method in which a pebble was measured every 0.2 m spacing to achieve 100 measurements per grid. At each 0.2 m spacing I

selected the pebble that was directly under the distance marker and measured the b-axis. Measurements taken in the wetted channel were done as a random sample across the section. With my eyes averted, I reached in and selected one pebble at a time, measuring the b-axis, and repeating this process 100 times to complete the sample. I performed this method of 100 random pebble measurements several times at the bar near the ford site (W_07), as it was an important location in our reach, and once at four other localities adjacent to geophone sites, as shown in Figure 3.13. One of those localities (W_05) used the random sampling in the wetted channel as there was no gravel bar adjacent to the site and the water level was shallow enough to safely undertake measurements. The other sites all had measurements taken on gravel bars which I ensured where taken on portions of the gravel bars that appeared to be mobilised regularly and were representative of the grain sizes present.



A = LONGEST AXIS (LENGTH)

B = INTERMEDIATE AXIS (WIDTH)

C = SHORTEST AXIS (THICKNESS)

Figure 3.12: Axes of a pebble (Harrelson et al., 1994)

In addition to the Wolman pebble count method, I also undertook some photographic grain size analysis on the gravel bar adjacent to W_07 (Figure 3.14). This required me to take photos looking perpendicularly down to a gravel bar with a known scale in the image, such as a small ruler or a lip balm tube (Figure 3.14b). On gravel bars, pebbles tend to lie with their short axis perpendicular to the surface and therefore the intermediate and long axes are exposed. Consequently, in the photographs the longest visible axis will be the long axis of the pebble and the shorter visible axis will be the intermediate axis of the pebble which is what is measured. Linear transects were laid out along gravel bars and photographs were taken at regular 1.0 m intervals. All photos were taken at chest height perpendicular to the gravel bar surface. Photographs were then loaded into the image analysis software ERDAS IMAGINE. I overlaid the images with a grid layer that included 100 line intersections and used the measuring tool to measure the intermediate axis of the pebble found at each grid intersection. In best practice, there should be no more than one intersection that lands on any one pebble. This is not always possible to avoid, especially in channels with large boulder-scale clast sizes. Fortunately, the mobile particles at the study site on the River Feshie are of smaller scale gravel-cobble size and therefore this was not a regular occurrence. Where it did occur and a pebble covered more than one intersection, it was measured the respective number

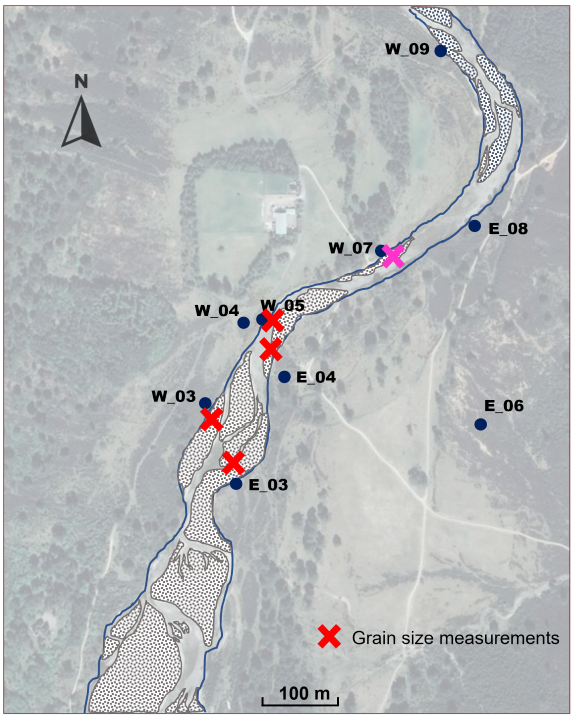


Figure 3.13: Locations of the grain size measurements shown by the crosses. The pink cross indicates where multiple grain size measurements were taken adjacent to site W_07.

of times. As stated by Attal et al. (2015), this can lead to uncertainties in estimating the median grain size (D_{50}) and 84th percentile grain size (D_{84}) values with more substantial effects on the D_{84} estimates. The scale item was also measured in this software which is then used to convert to real scale pebble measurements. The conversion is achieved by dividing the length measured in the photo by the image measured scale and then multiplying by the true size of the scale. For example, if the scale is 85 mm but is measured as 100 units in the photograph we need to apply a conversion so that it will convert to 85 mm ($x/100 \times 85$ mm). This can then be applied to all pebble measurements in the dataset replacing x with the image measured grain size.

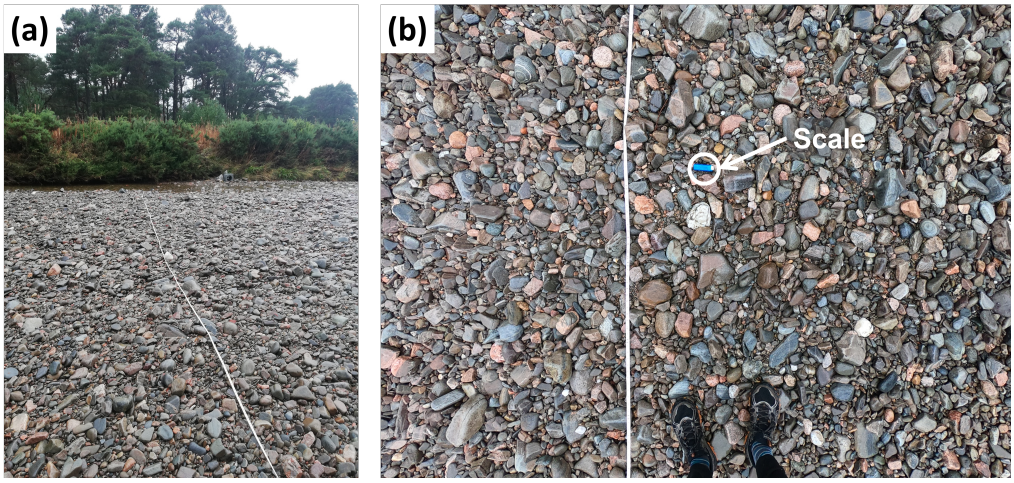


Figure 3.14: (a) A photographic grain size analysis transect example and (b) a chest-height photograph example with a scale.

The final grain size measurement method used in this study is a sieve analysis,

which was undertaken in collaboration with another University of Edinburgh Ph.D. student, Anya Towers, and her supervisor Dr Mikael Attal. In this method we assessed the surface and near-subsurface particle size distribution of the gravel bar adjacent to W_07 by digging a roughly 0.5 m^3 hole (Figure 3.15) and filtering material through a series of sieves with progressively smaller mesh sizes and weighing the contents of each class. This was a much more physically demanding and time consuming measurement method than the surface measurements, but it allowed some information on the subsurface grain size distributions which are important to know during very large events when more than the top surface of the bar gets mobilised. The sieves used allowed us to separate sediment into the following grain size classes: $<$ 10 mm, 10-20 mm, 20-40 mm, 40-80 mm, 80+ mm. The relative proportions of each class were calculated by finding the percentage mass each class contributes to the total sample mass.



Figure 3.15: Photographs from the sieving grain size analysis. (a) The location of the sieved sample on the gravel bar adjacent to site W_07. (b) The excavated hole in which sediment was measured from.

3.1.7 Channel geometry measurements

In order to measure the geometry of the channel which is used for bedload flux calculations and discharge conversions I used a LTI TruPulse 360 laser range finder. A range finder is a device commonly used to measure the gradient of a surface and optical principles to work out the angle of inclination between the device and the surface being measured. It uses a laser beam that is directed towards the surface and reflects back to the rangefinder. The time taken for the beam to travel to the surface and back is used by the device to calculate the distance. The rangefinder also measures the vertical distance using a built-in inclinometer. The slope can then be found by combing the two distance measurements. We also had use of a laser range finder which fired two shots at remote locations and would calculate the horizontal distance, vertical distance and slope between the two points.

To acquire measurements of channel width the observer simply fired the two-shot laser rangefinder at a point on the water's edge of both banks. The horizontal distance returned was then the width of the channel at that point.

To acquire the slope of the channel a laser range finder was also used. Generally the observer would either stand on the river bank and measure the vertical and horizontal distance to a certain point on the same bank, or they would stand in the thalweg (the deepest point in the channel) and measure horizontal and vertical distances to a specified point on a surveyors stave. However, in this study reach visibility when standing on one bank and looking up or downstream is poor due

to tall vegetation and the thalweg is too deep at points to safely walk. Therefore, the observer (normally myself) stood at the water's edge on one bank while another person stood on the opposite bank with a survey staff (Figure 3.16). The observer measured the horizontal distance (H_1, H_2 and H_3 in Figure 3.16a) and vertical distance (corresponding V_1, V_2 and V_3, not shown in the figure) to a specific marked point on the staff and noted down the values. The person with the staff would then walk downstream or upstream a short distance and the measurements were repeated. This was repeated at three points along the reach, stretching the largest distance that the staff could be easily located with the rangefinder. Measurements were chosen to be undertaken where the reach was fairly straight which allowed the assumption that three points were along a linear path. With the first measurement directly opposite the observer (Figure 3.16a), we could then use Pythagoras' Theorem to work out the horizontal and vertical distances between the staff localities. The horizontal distance was simply found using Equation 3.1 and the vertical offset of two consecutive staff measurements was found through a simple subtraction (Equation 3.2). Consequently, the gradient between two staff localities could be found by simply dividing the vertical offset by the horizontal distance as in Equation 3.3 and shown in Figure 3.16b.

$$H_{12} = \sqrt{{H_2}^2 - {H_1}^2} \tag{3.1}$$

$$V_{12} = V_2 - V_1 \tag{3.2}$$

$$S_{12} = \frac{V_{12}}{H_{12}} \tag{3.3}$$

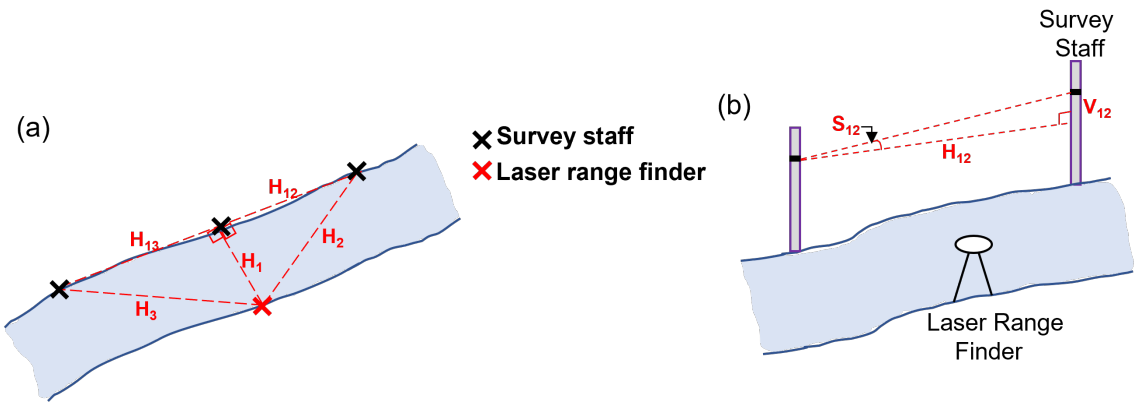


Figure 3.16: Schematics of the steps taken to measure the slope of the channel by measuring (a) the horizontal distances and (b) the vertical elevation change.

We also measured channel cross-sections at two points: adjacent to W_07 and W_05. For these measurements a taut tape measure was set up from bank to bank across the channel. The observer stood on one bank and one person held the staff with the marked measurement point. They started on the far bank and walked towards the observer, stopping at regular intervals along the measuring take to allow the observer to record the vertical and horizontal distances. These distances were then corrected for the height of the observer to provide channel cross-section profiles, as shown in Figure 3.17.

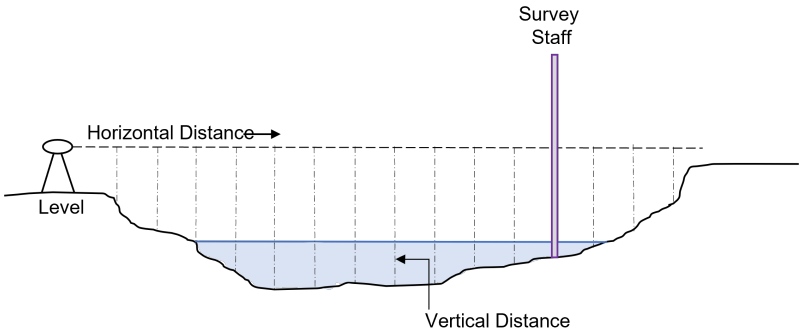


Figure 3.17: Schematic of the procedure taken to measure the channel profile.

3.1.8 Discharge measurements

We initially attempted to use ADCP measurements to gather discharge data. ADCPs measure water velocity by transmitting acoustic signals into the water column and recording the reflected signals off particles in the water. They can then build up a velocity profile, measuring the velocities in multiple layers of the water column. It is a commonly used method to use ADCPs from a moving boat or board for measuring streamflow and converting to discharge. This is typically done by running the ADCP across a river transect and repeating for calibration and result validation. We set up a couple transects across the area of channel in the vicinity of W_07 using ropes to pull the board across. However, due to the large amounts of sediment in the channel there were sections where the water was too shallow for the ADCP to gather any measurements. Therefore, we chose not to use these measurements. We did, however, repeat this down at a footbridge over a confined bedrock section of the river about 5 km downstream of our site. This site was much easier to take measurements from due to the deep channel and the steep river banks. Unfortunately, between our study reach and this footbridge there is one substantial tributary that enters the River Feshie (Allt Garbhlach) and contributes significantly to the discharge recorded at this footbridge. Without also running ADCP surveys across this channel it would have been a large estimation on the proportion of the discharge that would flow through our Feshie site. Therefore, I chose not to use the discharge measurements acquired through the ADCP surveys as I did not consider it to be an accurate enough estimation.

Instead, I chose to apply the widely used Manning's equation (Equation 3.4) to calculate discharge using channel geometry measurements. Manning's equation allows us to calculate the uniform depth-averaged flow velocity, V, using the hydraulic radius R by dividing the area by the wetted perimeter ($R = \frac{A}{P}$) at certain flow depths found through channel geometry measurements, the slope (S) of the channel which was measured using the laser range finder and a roughness coefficient called manning's coefficient, n. Manning's n values are often selected from tables that have been produced from previous studies that have determined the best values to represent different flow settings, or it can be back calculated using field measurements and observations. Here we use a combination of the two. Using a procedure developed by Cowan (1956) (Equation 3.5) we calculated what a representative range of manning's coefficients would be for our study site at the Feshie. In using either the pre-determined n-values from literature or by calculating our own there can be significant variations in the values selected as they are based on observations and

are relatively arbitrary. n values can be assigned for conditions that exist during a specific flow event, for average conditions over a range in stage, or for anticipated conditions for a future event. This method is applicable for one-dimensional, open-channel flow. Many factors affect the selection of n value for a channel but the most important factors are the type and size of materials that the bed and banks are composed of, and the shape of the channel.

$$V = \frac{1}{n} R^{\frac{2}{3}} S^{\frac{1}{2}} \tag{3.4}$$

where,

$$n = (n_b + n_1 + n_2 + n_3 + n_4)m \tag{3.5}$$

where,

n_b = base value for a straight, uniform, smooth channel in natural materials
n_1 = correction factor for the effect of surface irregularities
n_2 = a value for variations in shape and size of the channel cross-section
n_3 = a value for obstructions
n_4 = a value for vegetation and flow conditions, and
m = a correction factor for meandering of the channel.

The discharge, Q_w, can then be found by multiplying the area of the wetted channel by the flow velocity at each water level measurement.

$$Q_w = AV \tag{3.6}$$

This provides a good approximation of discharge at varying water levels at our site.

3.1.9 Active seismic surveys

In September 2022, our project team, along with University of Edinburgh PhD student Lou Parkes, conducted an active seismic refraction survey at our study site. These surveys help reveal subsurface velocity and layer interface structures by analysing the first arrival times of P-waves at the Earth's surface. Our goal was to test if these surveys could provide useful information about the site's properties and the propagation of seismic waves. This data could shed light on the nature and characteristics of river-induced seismic signals recorded at the geophone sites.

Ideally, we would have performed an active seismic survey at each geophone site to gather specific site characteristics. However, due to accessibility and logistical challenges, this was not possible. Additionally, time constraints led us to choose the most accessible site with the largest flat area, W_07.

The survey involved placing wired seismic sensors at regular intervals along a line to record the signal as it traveled. We used a sledgehammer striking a solid metal baseplate as the signal source, varying its location from one end of the line to the other and at several points along the line to capture the seismic propagation in both directions. By analysing the time differences between seismic waves recorded at successive geophones, we determined the site's velocity profile.

We conducted one survey line along the floodplain, roughly parallel to the river channel, and another across the channel. These setups are illustrated in Figure B.1 in

Appendix B. If we had more time, we would have liked to repeat the measurements at additional sites to analyse the signals in greater detail and better understand the site specific propagation and attenuation properties. Appendix B includes the survey setup figure and additional descriptions of the methods.

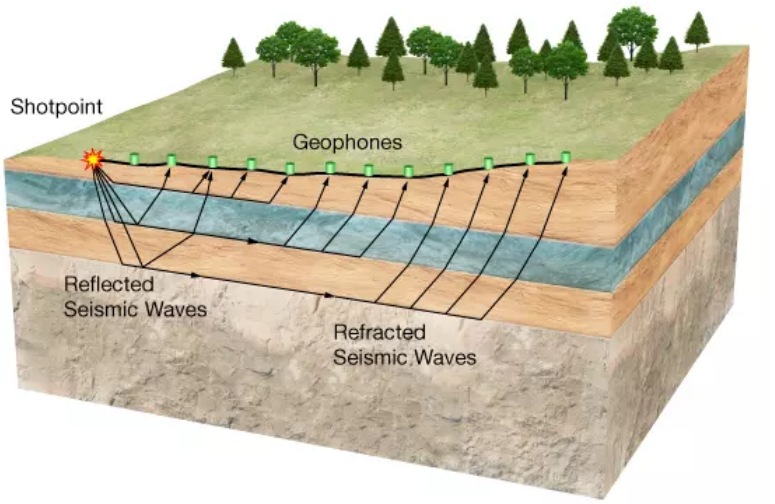


Figure 3.18: Diagram showing a typical seismic refraction survey to measure the layers of the subsurface (SHINE, 2022). Seismic refraction survey undertaken for this thesis is shown in Appendix B.

3.2 Site Characterisation

Using the aforementioned methods, I have gathered detailed information on the site's channel geometry, hydrological regime, grain size distributions, bedload motion thresholds, bedload fluxes, and seismic properties. This data is crucial for understanding the scale of the system and developing an effective monitoring system.

3.2.1 Channel slope

Channel geometry measurements were obtained using the methods detailed in section 3.1.7. The study reach exhibited an average slope of 0.0068 radians (Table 3.4), which is considered moderately steep. Channel slope can affect the sediment transfer into the river, the velocity of the water flow, and thus the stream power. The measurements of slope at our site were challenging to take accurately using the laser range finder as it relied on consistent picking of the channel edge by the observer and a steady hand. As can be seen in Table 3.4 the values acquired vary considerably with a standard deviation of 0.0025, but an average has been used to give a representative of the slope in the study reach.

Table 3.4: Slope measurements of the study reach using the laser range finder.

vertical	horizontal	slope
0.37	76.64	0.004
0.84	105	0.008
0.76	78.98	0.0096
0.3	64.45	0.0057
	Average slope	0.006825
	Standard Deviation	0.0025

3.2.2 Hydrological regime

The hydrological regime of the River Feshie from the SEPA data at Feshie Bridge has already been described in Chapter 1. Similar hydrological characteristics can be observed using the locally measured water depth data, with noticeably more high flow events occurring in early spring, late autumn, and winter. The measurements taken with the LiDAR and ultrasound sensors are in good agreement with each other throughout the monitoring period (Figure 3.19). However, due to a more complete record of data through the monitoring period of my PhD (Figure 3.2), I chose to use the LiDAR sensor data for the analysis in this thesis.

Using Manning's equation I calculated the discharge values expected for a range of water levels in the study reach. A manning's coefficient of 0.0045 was selected based on the method of Cowan (1956). Through the calculations I was able to estimate a discharge profile with water depth (rating curve) for the two channel geometry locations, adjacent to sites W_05 and W_07. The resulting rating curves are shown in Figure 3.20. Due to uncertainties in the channel geometry measurements and assumptions and estimations in the Manning's equation, the rating curves are not very accurate and predict that the discharge will continually grow with increasing depth. However, this is not the case when the river overtops its banks. We

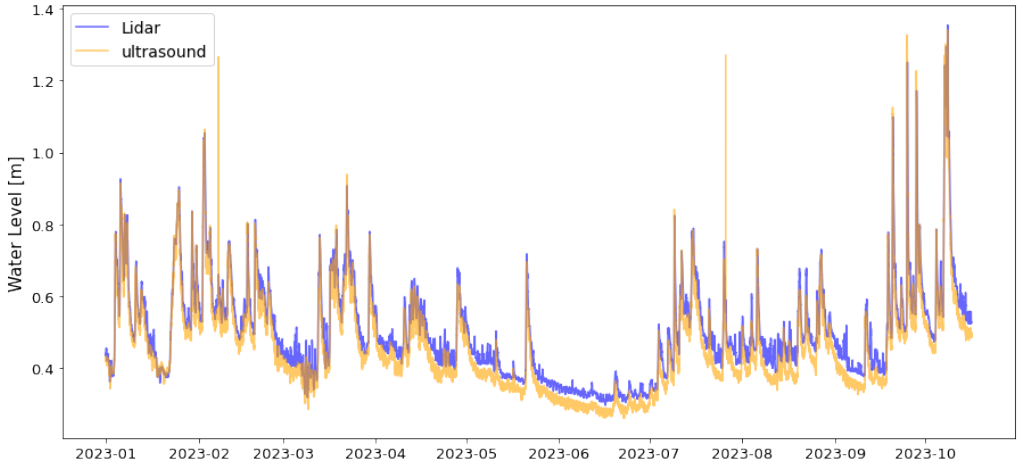


Figure 3.19: Comparison between the water level measurements measured using the Lidar and ultrasound sensors for a period when both instruments were recording.

decided it was best to use just water stage as previous fluvial seismology studies had also successfully analysed their signals against water stage.

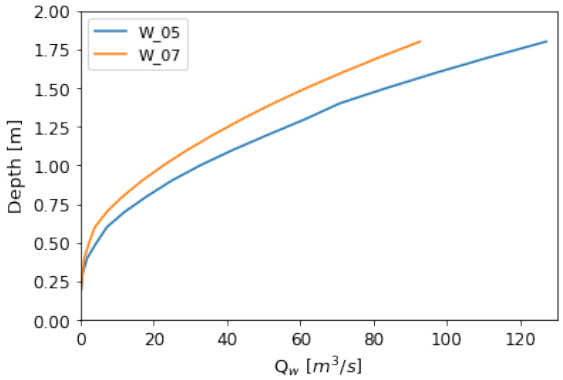


Figure 3.20: Rating curve of water depth versus flow discharge (Q_w) at the River Feshie study site, using Manning's equation and measured channel geometry parameters.

3.2.3 Grain size distribution

Using the methods described in section 3.1.6, the grain size distributions (GSD) at the study site were measured. All measurements are included in Appendix C. Figure 3.21 and Table 3.5 show the measurements taken using the Wolman count method (Wolman, 1954) adjacent to five of the geophone sites. These were done to provide an understanding of the spatial variability of the grain sizes to inform the story of the bedload transport. Figure 3.21 shows the graphical cumulative distribution of the grain size measurements taken adjacent to the five geophone sites, and Table 3.5 shows the numerical distribution through grain size fractions. It is clear that although there is some variation, particularly at site E_03, there is a relatively consistent grain size distribution through the study stretch. The measurements adjacent to E_03 were taken along a small side channel that at the time of monitoring was only active during very high flows. This may account for the smaller GSD seen at this site. Also, the measurements at W_05 were taken within the channel, which may account for the slightly larger GSD seen here. Grain sizes are commonly expressed as percentiles of the grain size distribution (GSD), representing different fractions of the material: the finer grains (D_{16}), the median grain size (D_{50}), and the coarser grains (D_{84}). The D_{16} corresponds to the 16^{th} percentile, highlighting the finer fraction of the distribution. The D_{50}, as the median, is a central measure widely used to represent the "average" grain size. The D_{84} reflects the 84^{th} percentile, offering insight into the coarser fraction and the largest grains in the distribution.

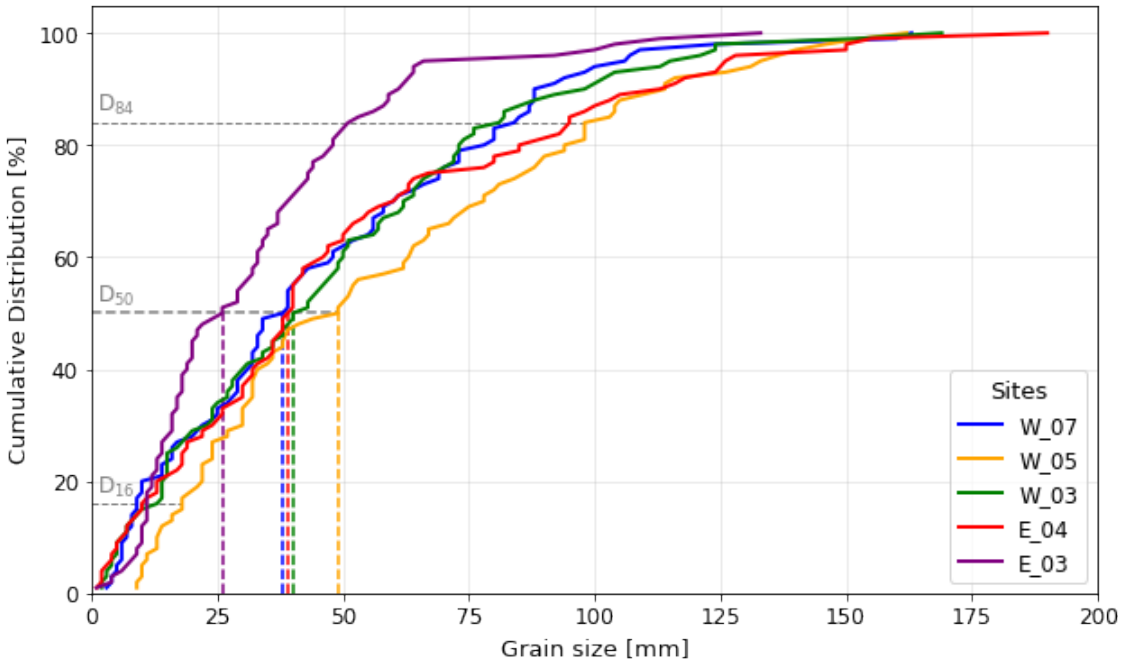


Figure 3.21: Empirical Cumulative Distribution Function (ECDF) of grain sizes measured adjacent to five geophone sites, showing the variation in the median grain size D_{50}.

Figure 3.22 shows the individual grain size distributions at each Wolman count measurement site. The similar GSDs for sites W_03, W_07 and E_04 are emphasised here, whereas the GSD for site W_05 shows a greater concentration in grain sizes of 50-110 mm and therefore a longer tail in the normal distribution. And that for site E_03 shows a much shorter tail as a result of a greater concentration of smaller

Table 3.5: Grain size distributions measured adjacent to 5 sites. All values are in [mm]

Site	Min	D_{16}	D_{50}	D_{84}	Max
W_03	2	13	40	81	169
W_05 (in-channel)	9	18	49	98	162
W_07	3	9	38	84	163
E_04	1	10	39	95	190
E_03	1	11	26	51	133
Average	3.2	12.2	38.4	81.8	163.4

grain size between 10 mm and 60 mm.

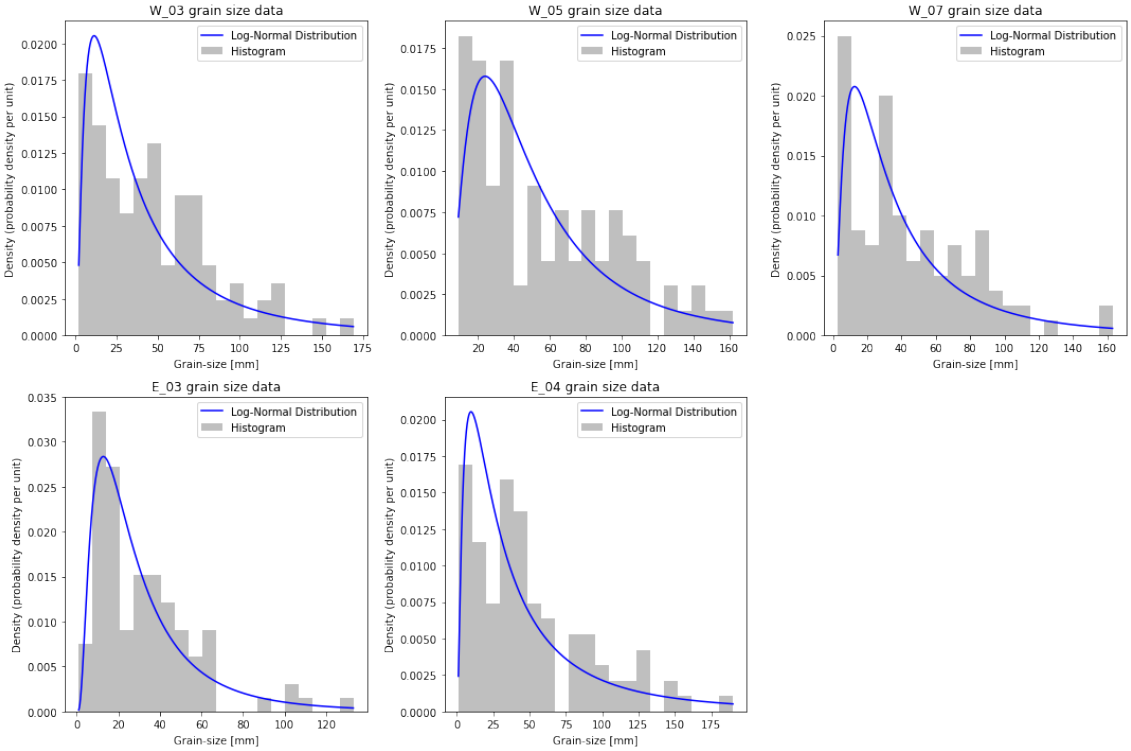


Figure 3.22: Log normal distribution of grain sizes measured adjacent to five geophone sites.

Through the sieved data we were able to acquire weights of the grains that were separated into the sieve size classes (Table 3.6). A relative portion of each class was then found by diving the class weight by the total combined weight of all classes. Plotting the grain size class against the cumulative class proportions enabled the identification of the relationship between grain size and proportion of sample. This enabled estimates of the D_{16}, D_{50}, and D_{84} values to be found (Table 3.7. Sieved grain size fractions are very uncertain as it is using a weight in a set size fraction and working out the proportion from there rather than from actual size measurements. The smallest sieve size fraction is anything less than 1cm. A sample bag collected from site could be dried out and further sieved into smaller grain size classes, however, since the sand content at the Feshie is minimal we opted to keep the five classes listed in Table 3.6 below, assuming a sand content of zero.

Table 3.7 provides a summary of the grain size distributions found using the three methods of grain size analysis: Wolman count, photographic, and sieving. The values found using the Wolman count method and photographic analysis through ERDAS IMAGINE software are very similar for all grain size fractions. The values

Table 3.6: Grain size classes from sieved data

Size Class	**< 1cm**	**1-2 cm**	**2-4 cm**	**4-8 cm**	**8+ cm**
Weight [kg]	29.54	18.76	24.12	22.04	46.25
Sieved Proportion [%]	21	13	17	16	33

estimated from the sieve analysis are within somewhat close agreement with the other methods, especially for the D_{50} value. However, as mentioned these values are more uncertain due to the lack of actual size measurements. Throughout the rest of the thesis I choose to refer to the grain sizes measured through the Wolman count method as they are consistent with the other methods, but provide a better spatial story and were easy to repeat during field visits.

Table 3.7: Grain size distributions from Wolman count method, photographic analysis, and sieved data

Grain size fraction	**min.**	**D_{16}**	**D_{50}**	**D_{84}**	**max.**
Wolman count [mm]	3.2	10.6	38.4	81.8	163.4
Photographic [mm]	4.2	13.6	34.8	71.8	168.0
Sieving [mm]	-	8.8	39	113	-

3.2.4 Entrainment thresholds and bedload flux

Using equations 2.1 and 2.2, it is possible to infer entrainment thresholds of specific grain sizes. I combined these equations to calculate the dimensionless shear stress (Shields parameter) for the D_{50} and D_{84} values acquired through the Wolman count, photographic and sieving grain size analysis at a variety of water depths typical of the study reach (Figure 3.23). In order for particles to be mobilised the Shields parameter must exceed the threshold for particle entrainment ($\tau*_{cr}$), which has been widely accepted to fall within an average of 0.03 and 0.06 from studies since the mid-20th century (Petit et al., 2015). The most frequently used value is 0.045, the median of the range proposed in literature findings. However, these values are estimations, and the actual critical Shields stress can vary significantly depending on factors such as sediment size, bed structure, flow conditions, and other site-specific variables. Figure 3.23 shows these calculated dimensionless shear stress values with the widely accepted critical shear stress values marked by the shaded grey box with 0.045 shown by the red dashed line. These values are provided to give an approximate indication of particle movement. The D50 is expected to be transported at shear stresses between 0.8 - 1.1 m, while the D84 is mobilised between 1.2 - 1.9 m. These ranges should be viewed as general estimations, as actual transport thresholds can vary depending on specific conditions and sediment characteristics.

Using the measured channel geometry and grain sizes the typically expected bedload fluxes can also be computed to give an idea of the scale of the system. I applied a selection of widely used bedload flux calculations from various studies since 1948, which account for different channel characteristics and critical shear stress values (see Appendix D for details on these calculations). A comprehensive discussion of bedload flux calculations can be found in van Rijn (1984).

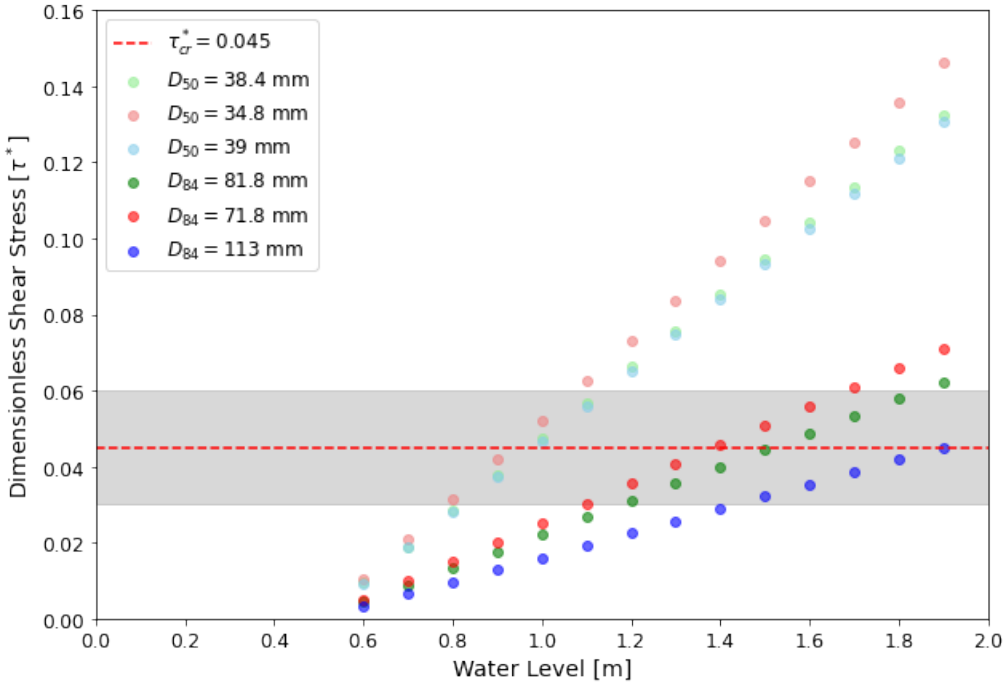


Figure 3.23: Entrainment thresholds of the average D_{50}, and D_{84} from the River Feshie study reach, showing accepted range of critical shear stress (grey band) and the widely used median value of 0.045 (red dashed line).

Many equations estimate bedload flux based on the excess Shields stress above the critical value, with Meyer-Peter and Müller (1948) being one of the earliest and most widely used formulations. I include calculations using the critical shear stress values from Meyer-Peter and Müller (1948) and van Rijn (1984, Equation 22). Additionally, I incorporate bedload flux calculations based on dimensionless transport rates from Nielsen (1992), Ashida and Michue (1972), and Wilson (1996)—as cited in White et al. (1973), Quick et al. (2023), and Apsley (n.d.)—each of which employs different approaches to estimate bedload transport rates (Appendix D). These methods typically use a selected grain size diameter, such as D_{50} or D_{84}, to predict the flux of a representative grain size of the channel.

Further, I include calculations using the dimensionless transport rates of Einstein (1950) and the volumetric transport rate equation of Wilcock and Crowe (2003, Equation 2), both of which treat each grain size fraction individually before summing the results. Einstein (1950) pioneered this approach, while Wilcock and Crowe (2003) simplified the computation by focusing on a two-fraction grain size of sand and gravel.

The choice of method depends on the characteristics of the sediments and the level of detail required. The critical shear stress value from Meyer-Peter and Müller (1948) is most suitable for coarse, uniform sediments with simple bedforms. The dimensionless transport rate of Einstein (1950) accounts for both bedload and suspended load but requires more complex and data-intensive calculations. In contrast, the equation from Wilcock and Crowe (2003, Equation 2) provides improved accuracy for natural riverbeds with diverse sediment sizes by incorporating grain size distribution effects.

I performed these equations using the maximum water depth of the largest monitored event on the 30th September 2022 (1.69 m). As can be seen in Figure 3.24 the equations result in similar output values of bedload transport rate (or bedload flux)

within about 2-3 orders of magnitude. The Wilcock and Crowe (2003, Equation 2) equation results in the lowest values of 0.001 kg/s per metre width, with Wilson (1996) predicting the greatest values of around 0.027 kg/s per metre width. These variations arise because of differences in defining critical shear stress, variations in the sediment size distributions, as well as the complexity of the equations. The equation of Wilcock and Crowe (2003, Equation 2) likely results in lower flux values due to its detailed treatment of mixed-size sediments, including the hiding effect and variable reference shear stresses for different grain size fractions.

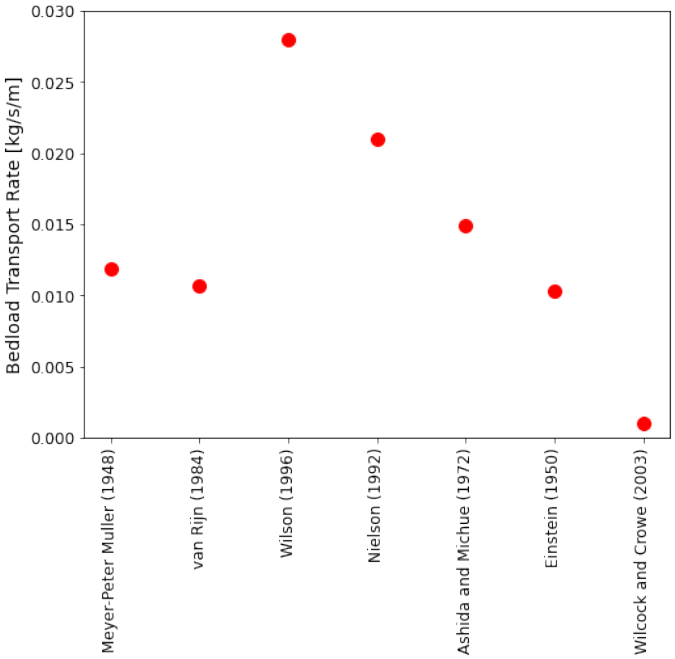


Figure 3.24: Bedload flux calculation outputs from commonly used sediment transport equations, using data from the largest event analysed in this thesis.

3.2.5 Seismic properties of the site

The active seismic refraction survey provides valuable insights into the seismic properties of the monitored site. Here, I present the velocity profile of the subsurface and the attenuation of seismic waves at the River Feshie study reach. As mentioned, accessibility limitations meant that we only performed this survey adjacent to the site W_07, however, this provides an understanding of the characteristics of the reach as a whole as it is assumed that the subsurface in this short stretch is relatively homogeneous.

Figure 3.25 illustrates an example of the seismic signals recorded by each wired geophone along the transect, which was set parallel to the river with a single shot located at the first geophone (Figure B.1). The seismic wave arrivals marked with a red dashed line represent direct waves traveling straight from the source to the receiver. These waves do not provide subsurface structural information. In contrast, the arrivals marked with a green or blue dashed line represent refracted waves, which have traveled through the subsurface and refracted off underlying structures. These refracted waves are crucial for analysing subsurface characteristics.

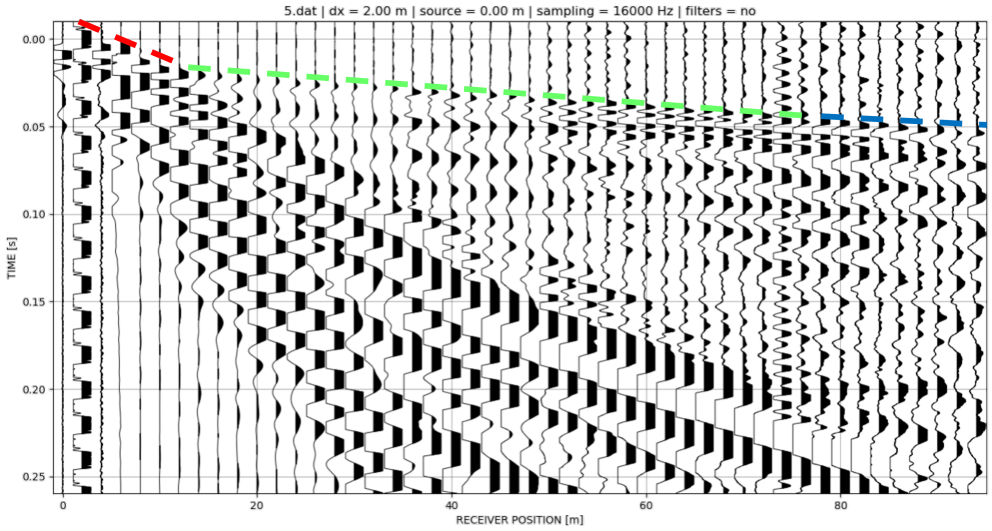


Figure 3.25: Seismic wiggle trace showing arrival times of the seismic refraction survey at geophones along the transect. The red dashed line indicates the picked arrivals of the direct waves and the green dashed line shows the picked arrivals of the refracted waves. The blue dashed line indicates the possible third layer that is more visible on some traces than others (see Figure 3.27).

To extract subsurface information, I identified the first arrivals of refracted waves at each geophone along the transect and plotted them against the distance between each geophone and the source. This process was repeated for four additional shots: two positioned 30 metres beyond each end of the line, one at the transect's other endpoint, and one at the center of the geophone array.

The velocity of seismic waves is represented by the slope of these plots. A straight-line slope with a constant gradient suggests a uniform subsurface material, whereas changes in slope indicate different subsurface layers, as depicted in Figure 3.18. Interpreting the number of subsurface layers proved challenging, leading to two potential models: a two-layer subsurface and a three-layer subsurface. Plotting the time-distance relationships resulted in Figures 3.26a and 3.27a, which show the first arrival picks from each seismic refraction survey. In both scenarios (Figures 3.26a and 3.27a), a noticeable break in slope occurs around 0.03-0.04 seconds across

all shot lines, indicated by the transition from red to green dots. This break in slope suggests a change in subsurface composition and a potential waveguide. Figure 3.26a presents a two-layer model with a single significant slope change, while Figure 3.27a suggests the presence of a third layer, indicated by a subtle slope variation at later timestamps (marked in blue). The data contains some ambiguity, making it challenging to precisely resolve the subsurface structure using this method; however, it still provides a useful indication.

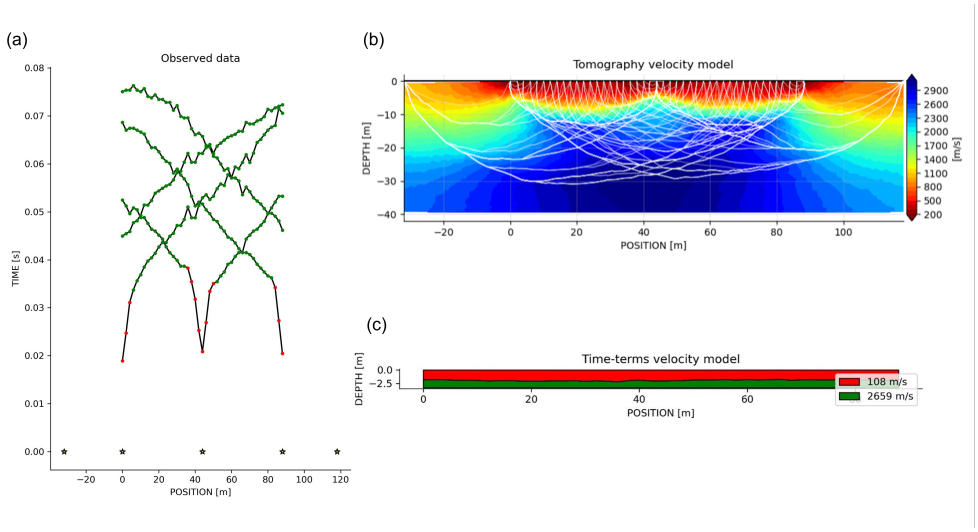


Figure 3.26: (a) Distance versus time plot of the picked first refracted wave arrivals at the geophones along the transect from five shots, showing the two layers identified. Stars indicate the shot locations. (b) A detailed velocity-depth profile showing the paths of the seismic waves. (c) Simple 2D schematic of the two subsurface layers identified in the seismic refraction data.

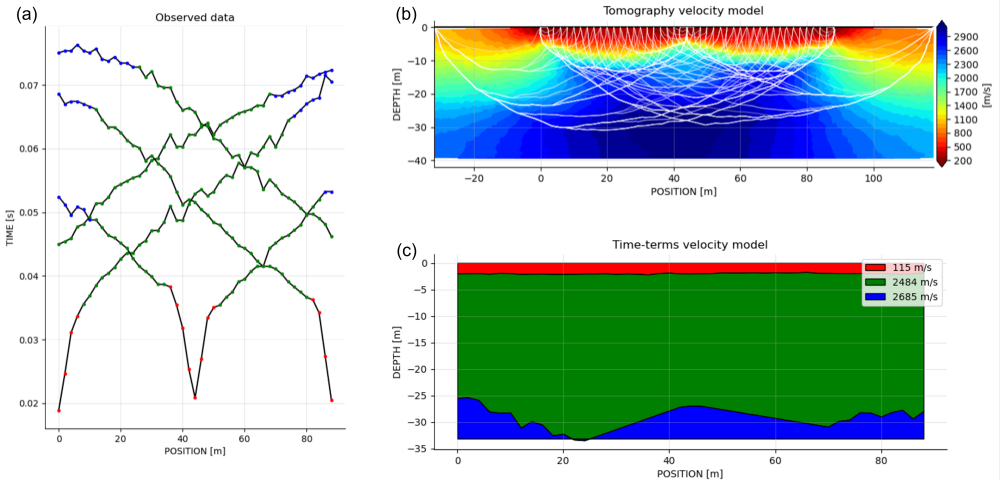


Figure 3.27: (a) Distance versus time plot of the picked first refracted wave arrivals at the geophones along the transect from five shots, showing the three possible layers identified. Stars indicate the shot locations. (b) A detailed velocity-depth profile showing the paths of the seismic waves. (c) Simple 2D schematic of the three subsurface layers identified in the seismic refraction data.

Using the travel times and distances from Figures 3.26a and 3.27a, I estimated the velocity-depth profile of the subsurface. In the two-layer model, the top layer exhibits a low velocity of approximately 108 m/s, while the second layer has a significantly higher velocity of 2659 m/s, as shown in Figure 3.26c. The three-layer model suggests a shallow layer with a velocity of 115 m/s, a second layer

with 2484 m/s, and a third layer with 2685 m/s (Figure 3.27c). In both scenarios, these velocities indicate that the top layer consists of low-velocity soft sediments, while the underlying layers contain high-velocity materials. The top layer's velocity is slightly lower than typical soil values (Barman, 2023), which may be a result of porous but dry soils, whereas the second layer aligns with clast-supported glacial till (McDowell et al., 2002). If a third layer exists, its slightly higher velocity suggests weathered bedrock. These interpreted subsurface layer compositions are consistent with the geological structure of the catchment area illustrated in Figure 1.2 (Chapter 1, section 1.1.1). Given the presence of observed bedrock outcrops around 5 km upstream and downstream of the site, the three-layer interpretation in Figure 3.27 is likely the most accurate, suggesting that seismic waves reach a weathered bedrock layer at their maximum propagation depth ($\sim$ 30 m). This interpretation is also consistent with site observations, where tall several-metre-high riverbanks were cut by the river, revealing a thin layer of soils and sands were vegetation roots were growing, underlain by a heavily clast-supported substrate with no bedrock visible beneath it.

Figures 3.26b and 3.27b provide a detailed velocity-depth profile, with white lines representing approximate seismic paths from shot locations to each geophone along the transect. This profile supports the findings from Figure 3.27c and indicates that seismic waves reach depths of approximately 30-35 meters. Based on the P-wave velocities, deeper waves likely travel through weathered bedrock, suggesting that bedrock lies at depths of around 30 meters or more at the site.

In addition to calculating the estimated velocity profile of the shallow subsurface, the seismic refraction survey also enabled the indication of the seismic power attenuation over distance. This was achieved by finding the maximum amplitude of the first P-wave arrival (Figure 3.28a) at each geophone and plotting against distance from the source (Figure 3.28b). This reveals that the seismic power decays exponentially with distance from the source, with distances of less than 40 metres showing considerably stronger signals. This can inform on the best placement of seismic sensors to capture the seismic noise from the river source.

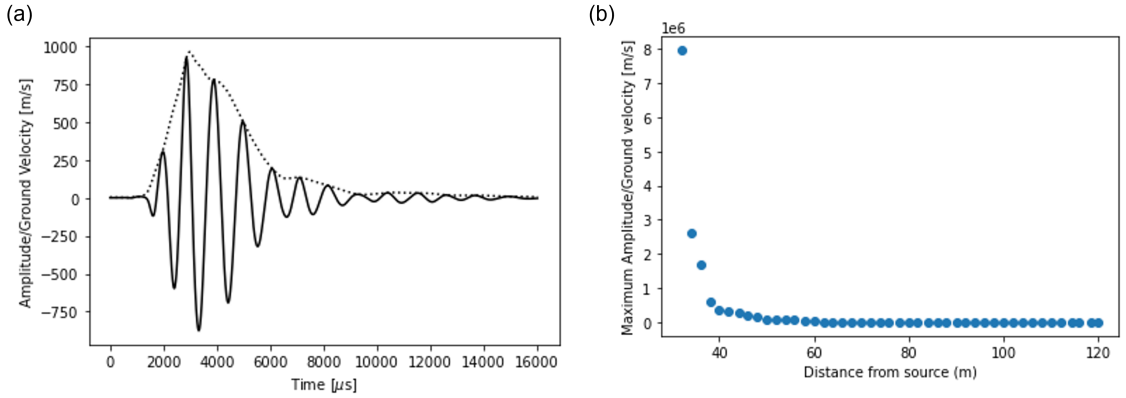


Figure 3.28: (a) Example of a seismic waveform of the first arrival of a refracted wave measured by a single geophone, showing an envelope fitted to the data (dashed line) to identify the maximum amplitude. (b) Maximum amplitude of the seismic trace envelopes at each geophone along the transect plotted against geophone distance from the source.

3.3 Experimental design

3.3.1 Chosen stretch of the river

The specific stretch of the River Feshie that was chosen as the field site for this work was selected because of its channel characteristics and sediment availability. It is located roughly midway along the full reach of the Feshie immediately downstream of the first heavily braided section of the river, as described in Chapter 1. The stretch chosen is a roughly 1km long section that is relatively confined (Figure 3.29). At the upstream end of the stretch there is a large partially stable gravel bar, as well as a frequently laterally shifting bar between sites W_05 and W_07 and a smaller more stable bar adjacent to site W_05. Midway through the section there are the remains of an old footbridge on both banks. This site is easily accessible by vehicle with permission from the estate managers which meant deployment and maintenance of equipment was logistically manageable.

In terms of placement of the various instruments, several factors had to be considered. The geophones that were intended to record the river-induced signals had to be located close enough to the river channel to capture those signals but not too close or on floodplains that they would be easily flooded. As shown in the attenuation profiles, the seismic signals rapidly attenuate with distance, with distances above 40 m showing considerably weaker signals. Additionally, since the public had access to the area for recreational activities the geophones and their setups had to be easily hidden out of view, for instance by tucking the boxes into bushes or among trees. The final factor that influenced the exact siting of the instruments was realised at the point of deployment when digging the shallow holes for the geophones. The substrate the ground was composed of determined where was logistically possible to site geophones, such as soil or till.

The hydrophones had to be deployed in sections of the channel that were easily accessible during low flows but that were definitely covered by water during high flows. The time-lapse cameras had to be well sited to get good views of the upstream and downstream reaches of the stretch. And finally, the stream gauge sensors had to be deployed on a sturdy structure that allowed them to hang over the river roughly perpendicular to the water surface.

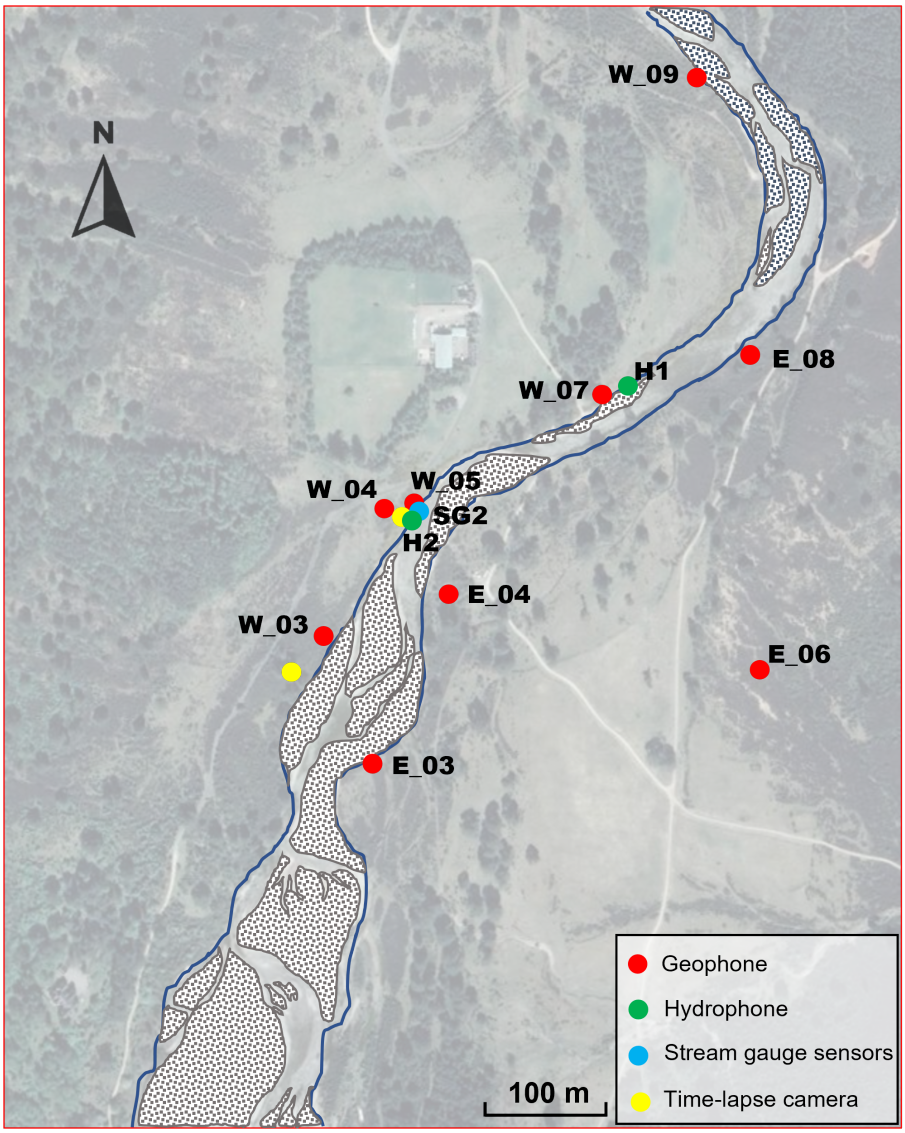


Figure 3.29: Map of study site and instrument locations.

3.3.2 Specific sites of deployed instruments

The selected sites for geophone instrument deployments were named based on the instrument location. Geophone sites were assigned a name starting with either a 'W' for locations on the west bank of the river or an 'E' for those on the east bank. The numbers following these letters increase in the downstream direction. Sites were named according to their geographical location as they were deployed, with gaps left in the numbering to accommodate potential future deployments between existing sites.

W_03

Site W_03 is located the furthest upstream in our stretch on the west bank (Figure 3.29). This site is adjacent to a large gravel bar which has formed following the constricted end of the large braided section. The geophone is located approximately 3 m from the river edge, but the main channel of the river moved over the course of the monitoring period. It is buried approximately 2 m above bankfull up a steep rocky bank among small young pine trees. It wasn't until 16th October 2023 that a time-lapse camera was deployed on a steep open bank ~20 m adjacent to the

geophone at site W_03, overlooking the large gravel bar in the uppermost part of our study reach (Figure 3.29). The geophone and camera were sited here to capture movement of bedload particles in the upper part of this study stretch and any morphological changes to the channel and bar.

W_04
W_04 is sited adjacent to the small estate road leading to Glenfeshie lodge up a bank approximately 5 m above W_05, and 8-10 m above and 20 m in from the river. It is sited on flat ground composed of soil, and hidden within gorse bushes. This site was initially selected to provide a comparison to the site beneath it to inform on elevation site effects and instrument placement.

W_05
W_05 is located directly above the river at the top of a steep roughly 2 m bank. The ground that the geophone is buried in is a flat ledge with soily composition. The recording instruments are tucked into the low lying gorse bushes. This site not only has the geophone set-up; there are also the two stream gauge sensors (at SG2 in Figure 3.1), two time-lapse cameras and a hydrophone that was not deployed until 9th October 2022 (H2 in Figure 3.29). This hydrophone was not used for the analysis included in this thesis as I wanted to use consistent data across all events, and this hydrophone unfortunately did not record the large events that occurred prior to October 2022. One time-lapse camera was attached to a small tree looking downstream from the site, and the other one was attached to a signpost looking upstream from the site (Figure 3.9). This allowed visual evidence of any changes to the channel morphology that occurred on the large gravel bar immediately upstream of the site or the smaller bar downstream of the site. Having a suite of co-located measurements allows direct comparison between datasets without having to undertake conversion methods that introduce uncertainties in data.

W_07
This site was first deployed back in February 2020 prior to me starting my PhD. My external co-supervisor, Micha Dietze, led an introductory session to site scoping and instrument deployment with Mark Naylor, Hugh Sinclair, and Karen Mair. Due to the interruptions and restrictions posed by the Coronavirus outbreak this site was not revisited until the first trip undertaken as part of my PhD in December 2020. The geophone was sited approximately 19 m from the channel thalweg and 4 m back from the river bank on the flat floodplain tucked in gorse bushes for protection from flood waters (Figure 3.29). On the 8th October 2021 a hydrophone was deployed in the hollowed-out concrete block approximately 15 m downstream of this geophone (H1 in Figure 3.29). The block was in the channel tucked against the river bank with the recording equipment and power supply housed in large black heavy duty equipment cases situated within gorse bushes on the river bank directly adjacent to the block. In mid-September 2022 the underwater camera was mounted within the same concrete block as the hydrophone and connected to recording and power equipment, again housed in the equipment boxes.

W_09
This site was deployed in December 2020 and was used mainly by Calum Cuthill to

test the potential of telemetering data from the Feshie. This geophone was located approximately 5 m from the river bank among young pine trees and gorse bushes (Figure 3.29). The area was very flat and feared prone to flooding at high water levels and therefore we made the decision to raise the recording equipment and power supplies by fastening them into a nearby tree. On the same tree Calum deployed an antenna used for telemetry purposes that was connected to the seismic setup. This site is not used for any analysis in this thesis as it did not record the events of interest.

E_03
Site E_03 was the latest addition to the set-up and was deployed on 17th March 2023. At the time of deployment this geophone was located approximately 35 m from the main channel, adjacent to ($<$ 5 m from) a large gravel bar that was only active during very high flows. From field visits undertaken by the project team after the main monitoring period for my PhD, it was noticed that the river has changed course at this locality and now has an active sub-channel that runs alongside the geophone location. The geophone is nestled into heather bushes and a young pine tree on a stable portion of the flat floodplain. This site was selected to potentially provide some information in the activation of the smaller channels around the large gravel bar or any channel avulsions, which unfortunately happened outwith the PhD monitoring period.

E_04
E_04 was deployed in the main field deployment visit in December 2020, opposite W_04 and W_05 (Figure 3.29). This geophone was sited among some dense young trees and gorse bushes on the flat floodplain on the east bank of the channel. This site was chosen to provide some comparison with the steep bank measurements from W_04 and W_05 on the opposite bank. Here, the top layer of the ground was soft peaty soil which made for easy deployment of the geophone.

E_08
This was the furthest downstream site in the study reach on the east bank and was located approximately 140 m downstream from W_07 on the opposite bank (Figure 3.29). This geophone was sited in a semi-open area with a few young pine trees in the immediate vicinity and some old much larger Scots Pine trees approximately 20 m away. The ground was relatively flat where the geophone was sited but up a steep roughly 1 m river bank.

Met_01
In March 2021, we chose to deploy a geophone adjacent to a meteorological station deployed and maintained by Andrew Black of the University of Dundee. With access to the local meteorological data, we had hoped this would provide a good control site to the river-adjacent geophones to tell us information about meteorological signals that could be compared to the meteorological data and more general environmental signals. This station was located up a steep hill above the estate buildings, nestled among some large old larch and pine trees as well as a lot of young pine trees (Figure 3.29). Due to the boom in growth of the young trees surrounding the meteorological station, it turned out it was not performing optimally and therefore we didn't have accurate meteorological data to compare with the seismic data.

E_06

Due to the challenge of accessing the geophone located at Met_01 and the poor meteorological data, we decided to re-site the control station and moved it to the east bank of the channel in November 2021. The ground on the east of the channel is much flatter than on the west and so we were able to site the geophone at a good distance approximately 300 m from the river to record general environmental noise (Figure 3.29). We chose to locate it as far from the channel as we could before the ground elevation started to rise rapidly up towards the Munro Mullach Clach a'Bhlair. At this distance the signals from the river were expected to have attenuated considerably, according to Figure 3.28, therefore providing a good control site.



Figure 3.30: Field photographs of the River Feshie study site taken near site W_05 looking (a) upstream and (b) downstream showing the locations of sites within view of the photographs.

3.4 Data Processing

3.4.1 Seismic data processing

The initial steps of data processing required me to convert the data files from their original Data-Cube file type to a file type that could be imported into common processing systems, such as Python, for further scientific analysis. I used the GIPPtools collection of software utilities produced by the GFZ in Potsdam, which has built-in programs to pre-process the recorded data from Data-Cube^3 recorders. These tools give the option to convert from Cube file format to ASCII text formats, miniSEED format and SEG-Y format. For this work I chose to convert to miniSEED format based on recommendations from my supervisory team and because I had experience handling miniSEED data previously. The next step involved removing the instrument response from the signal to ensure the recorded data truly reflects the ground motion. The instrument response essentially refers to the way a seismometer reacts to ground motion and includes features of the sensor such as the sensitivity, frequency range, and damping characteristics. Failure to remove the instrument response can lead to inaccurate data interpretation, such as disproportionate amplification of seismic signal at the instruments peak sensitivity. I used the Python package `ObsPy` and input information on the specific instrument specifications provided by Digos to remove the instrument response and apply a bandpass filter to the data in the frequency domain (between 4.5 Hz and 99 Hz to match the frequency range of the instrument) to remove frequencies most affected by the instrument noise. Finally the data was detrended to smooth out any mean trend in the signal. In the removal of the instrument response the signal is also converted to ground velocity (in SI units m/s).

From here, the data can be examined in the desired way. The simplest way to view the data is as a time series of ground velocity, also known as seismograms or waveforms. The most common tool to characterise a seismic signal is an analysis in the time-frequency domain. The continuous seismic signal is typically divided into short segments, a window function is applied to each segment, and a fast Fourier transform (FFT) is performed to obtain a series of spectra or power spectral density (PSD) estimates. These are compiled over time to create a spectrogram, which shows the distribution of seismic power across time and frequency. Frequencies outside of the 4.5-99 Hz range used in the removal of the instrument response should be ignored as the pre-processing steps cause a rapid decline in the power of the signal.

Preliminary analysis for this thesis involved inspecting the frequency content of the signal by calculating the Fourier transform to obtain the spectrum or PSD estimate. This was done using the `'specgram'` function from the Matplotlib library module `matplotlib.pyplot` in Python. Several methods exist in the literature to reduce the variance of the spectrum that results from the basic use of FFT. Among them is Welch's averaging method (Welch, 1967), where a time series is split into multiple overlapping segments, and the PSD is computed for each segment individually. Throughout this thesis, I used a window length of 1 minute with no overlap unless otherwise stated. This Python function also produces spectrograms, providing visual displays of the power and frequency content of a signal over time (Cook and Dietze, 2022). This method was used in my analysis to distinguish between different seismic sources manifesting in different frequency ranges. PSDs and spectrograms are shown in units of decibels (dB), a logarithmic unit (1 dB =

10 $\log_{10}$ $m^2/s^2/Hz$). Additional methods for analysing the seismic data were used throughout the thesis and are detailed in the relevant data chapters.

3.4.2 Stream gauge data processing

As already mentioned, for the analysis in my thesis I had access to stream gauge data from SEPA's Feshie Bridge site (SG3) approximately 10 km downstream of the study site, as well as data from a stream gauge sensor approximately 10 km upstream of the study site maintained by Andrew Black (SG1) (Figure 3.1b). Both sets of data are provided at 15 minute resolution and in both water level and discharge. I have chosen to use the water level data throughout my thesis as we only have water level measured at our site and so it provided easy comparison. The SEPA Feshie Bridge station provided near-real time data which I used to keep an eye on the rough conditions at the study site of this thesis.

As mentioned, the stream gauge data collected at the study site (at SG2) recorded the distance from the two sensors to the surface of the water once every 5 minutes for the LiDAR sensor and 10 measurements every 5 minutes for the ultrasound sensor. The first step of processing involved calculating the mean value from the 10 consecutive measurements by the ultrasound sensor, to provide just one value for each 5 minute timestamp. Then the measurements by both sensors had to be corrected for the sensor height above the river bed to provide an approximate measurement of water depth, assuming the river bed was fixed. Repeat measurements of the distance from the sensor to the river bed confirmed that the bed was stable at this location and the elevation of the bed remained constant during our study period. Depending on the specific analysis and dataset comparisons the stream gauge data were resampled in time accordingly. Where this has been done is clearly stated in the text of the thesis.

Comparing water levels across the three stream gauge sites, we observed that the timing of measurements at our site (SG2) closely aligned with those recorded upstream at SG1 and downstream at SG3. While comparing absolute water levels between sites is challenging due to differences in channel dimensions, the close correlation in the relative timing of peak events and their magnitudes suggests that water levels—and thus discharges—were responding similarly at all sites. A visible lag was also observed between data from SG1 and SG2, as well as between SG2 and SG3, reflecting the downstream distance and suggesting that the main events analysed were not localised along the river.

It was important to find a way to use data from any of the stream gauges to inform on water levels at the other gauge sites, in case there was an issue in recording data. Since the SEPA stream gauge at Feshie Bridge was also the only near-real time monitoring site for Feshie water levels, it was useful to know how the water levels there corresponded to water levels at our study site and at Andrew Black's stream gauge. This allowed us to keep an eye on changing water levels during wet periods to identify when large events occurred or to inform on when we should perform service runs of our equipment. In order to get this information, I selected the peak water level values at each gauging site (using just the LiDAR sensor for SG2) for all high flow events that were over 1m at our site. This water level was chosen as it was observed that at this level the channel bar was submerged at site W_07 which provided a good identification of high flow events. The empirical relationship

between each pair of stations as obtained by performing a linear regression on the data are as follows:

$$L = 0.6A + 0.42 \tag{3.7}$$

$$L = 0.71S - 0.003 \tag{3.8}$$

$$A = 1.08S - 0.53 \tag{3.9}$$

where, L is the water level at the LiDAR sensor at SG2, A is the water level at the sensor at SG1, and S is the water level at the sensor at SG3.

3.4.3 Hydroacoustic data processing

The hydroacoustic data was recorded by the setup described in section 3.1.3 as Waveform Audio File Format (WAV). This file type was easy to play with in any media player software as well as load in to audio editor software and coding scripts. Therefore, it did not require any general processing prior to analysis. The specific details on any data analysis steps are included in the relevant chapters, such as Chapters 4 and 5.

Summary

This chapter detailed the methodologies and data processing techniques employed in this thesis to achieve the research objectives outlined in Chapter 1. Additionally, it provided an overview of site characteristics such as the hydrological regime, seismic properties, channel grain sizes, expected transport thresholds, and sediment fluxes. Chapters 4 to 6 form the core data chapters of the thesis, focusing on the analysis of seismic and hydroacoustic signals recorded at the field site. Each of these chapters discusses the methods used, presents results, and provides comprehensive discussions. The thesis concludes with overall discussions and conclusions in subsequent sections.

Chapter 4

Site and event variations in river-induced seismic characteristics

In this first key data chapter of the thesis, seismic recordings from all geophones during the five selected events outlined in Chapter 1 are analysed to understand their signal characteristics. This comprehensive analysis serves as the foundation for the research presented in this thesis, as it allows for a detailed comparison of signals across different events and locations. By examining these recordings, the chapter investigates how factors such as event magnitude and duration, and site conditions influence the seismic signals captured.

The analysis begins by processing and examining the seismic data from each geophone, focusing on key metrics such as signal amplitude and frequency content. Through these comparisons, the chapter identifies patterns and variations in the signals that correspond to differences in event characteristics and site-specific conditions. This detailed examination helps in understanding the underlying mechanisms that drive seismic activity and their manifestations in recorded data.

Furthermore, this chapter delves into the frequency characteristics of both seismic and hydroacoustic recordings. By analysing the frequency spectra of the recorded signals, the chapter provides initial insights into how different frequencies are affected by various factors such as geological features, water depth, and distance from the seismic source. These insights are crucial for developing more accurate models and forecasts of seismic activity, as well as for improving the design and placement of geophones and hydrophones in future studies.

In summary, this chapter lays the groundwork for the entire thesis by thoroughly analysing the seismic and hydroacoustic data from multiple perspectives. It establishes a detailed understanding of the signal characteristics and their dependencies on various factors, setting the stage for subsequent chapters to build upon these findings and further explore the complex dynamics of seismic events.

4.1 Introduction

As described in more detail in Chapter 2, bedload transport dynamics can have a substantial effect on river morphology, infrastructure, aquatic ecology, and water quality and availability (Church, 2006; Turowski et al., 2011; Hauer et al., 2018).

Unfortunately, this process in inherently challenging to measure within a river due to the often stochastic and transient nature of the hydrograph signal and the associated danger in undertaking traditional in-stream measurements (Gomez and Church, 1989; Jerolmack and Paola, 2010). As a result advanced measurement and modelling methods have been developed in recent decades, to address these limitations and provide more precise measurements and observations of bedload transport dynamics. In the last two decades there has been a large increase in the use of indirect seismic sensors to monitor environmental and geomorphic processes (e.g. Burtin et al., 2008; Turowski et al., 2013; Roth et al., 2016; Dietze and Gimbert, 2019). These sensors can record ground vibrations caused by a variety of environmental processes, including bedload transport (Gaeuman and Jacobson, 2007; Rickenmann et al., 2014; Geay et al., 2020). Bedload particles interacting with the river bed induce small seismic waves in the ground which propagate to the seismic sensors (Dietze et al., 2020). These seismic sensors are located outwith the river channel and increase the spatial and temporal resolution of current bedload transport monitoring, enabling precise timing of events, and can be used for either retrospective analysis or near-real time monitoring (Burtin et al., 2010; Hsu et al., 2011).

Geophones record a range of environmental signals, including precipitation, wind, traffic, river turbulence, and bedload impacts on the river bed. Differentiation of the different sources of seismic noise has been achieved by analysing the signal characteristic such as the dominant frequencies and durations by performing analysis in the frequency domain (Burtin et al., 2008; Burtin et al., 2014; Gimbert et al., 2014). In fluvial seismology studies, the two dominant signals to differentiate are produced from turbulent motion in the rivers and bedload transport. Previous studies have suggested that bedload transport induces more broadband, higher frequency seismic waves than continuous signal from river turbulence (Schmandt et al., 2013; Gimbert et al., 2014; Vore et al., 2019). Typical frequencies of seismic bedload transport signals found in previous studies fall within the range of roughly 5 Hz to 80 Hz, depending on the recording instrument specifications and site characteristics (Burtin et al., 2008; Tsai et al., 2012; Gimbert et al., 2014; Roth et al., 2016; Coviello et al., 2018; Lagarde et al., 2021). However, due to overlapping frequency ranges of these signals, it remains difficult to distinguish bedload transport through seismic measurements alone. Previous studies have generally used the vertical directional component of seismic waves for bedload transport analysis. Given the general near-vertical direction of bedload impacts with the riverbed, it was assumed that the emitted seismic waves would be best represented by Rayleigh waves with vertical displacements (Tsai et al., 2012; Dietze et al., 2019). However, due to the downstream movement of pebbles and the rolling and sliding nature of bedload particles, there is likely to be a significant horizontal signal especially in the stream-parallel component (Schmandt et al., 2013; Roth et al., 2016). Numerical models and empirical equations have been continually developed to fill bedload measurement gaps and provide a framework for estimations and hypothesis testing (such as Tsai et al. (2012) and Gimbert et al. (2014)). These models are typically semi-empirical and use some field measured data to design and test the model runs. There are, however, some significant limitations with these models. Simplification of these models and equations relative to the complex natural behaviours of bedload transport in rivers, mean they fail to capture the true stochastic nature of natural river systems and result in considerable uncertainties in sediment transport estimations (Dey, 2014;

Downs et al., 2016). However, they are useful in providing initial analysis to inform on more in depth field seismic setups, measurements and analysis.

Care must be taken when designing a seismic monitoring system to ensure it is optimally designed to record the desired sources of seismic noise. The distance between the source and sensor, and the substrate in which the seismic sensors are deployed are key factors to consider when designing such a near-surface system for bedload transport monitoring. Seismic energy dissipates with distance and sees preferential attenuation of high frequencies (Cook et al., 2018), which is important when trying to measure bedload transport as they produce rapidly attenuating high frequency (10^1 - 10^2 Hz) signals. The substrate softness and thickness influences the speed of seismic waves and their amplification effects, with softer substrates such as soil reducing the wave speed but causing an amplification of power (PNSN, 2024). This is why earthquakes are more destructive in areas underlain by thick unconsolidated sediments.

This section of the thesis undertakes initial analysis of the seismic signals recorded in the study reach at the River Feshie. First, I use the R package 'eseis' developed by Dietze (2018b) along with channel geometry, grain size and water level measurements taken in the field to provide model the estimated seismic signature of bedload and turbulence at the study site. This provides information on the dominant frequencies both processes are expected to exhibit. I then analyse seismic data during five high flow events to understand the signals produced by different seismic sources, such as turbulence and bedload referring back to the outputs of the model. By looking at recordings from all 8 geophone stations over the five events, I compare the variabilities in recordings across each of the events and at each site. Using seismic data recorded in all three directional components, I am also able to do some initial analysis and interpretation of the dominant direction of seismic wave propagation by different sources. I introduce the hydroacoustic data here by analysing and comparing the frequency content of the seismic and hydroacoustic data during each of the five events. This section forms the foundations of the seismic data analysis of this thesis and sets up challenges faced in interpreting river-induced seismic signals which are further addressed in the two other data chapters that follow.

4.2 Methods

4.2.1 Bedload transport model inputs

Dietze (2018a) developed an R package called 'eseis' to provide a toolbox for environmental seismology for the processing, analysis, and visualisation of environmental seismic data. The package aims to streamline the workflow for researchers in environmental seismology by providing tools to handle seismic data from the initial processing to advanced analysis and visualisation. Included in this package are two functions to calculate the seismic spectrum for bedload transport and hydraulic turbulence. The bedload transport model (`model_bedload`) uses the model outputs of Tsai et al. (2012), as discussed in Chapter 2, and the turbulence model (`model_turbulence`) uses the outputs of Gimbert et al. (2014). I used the R 'eseis' package functions of `model_bedload` and `model_turbulence` by Dietze (2018b) to model the effects of changing key parameters on the frequency characteristics of the estimated bedload and turbulence induced seismic signals. Several parameters

in the models were either assumed from other studies or the defaults were used. However, some measured parameters from our study reach were used to provide the model more relevance to the seismic findings of this thesis. The parameters and values used are shown in Table 4.1. I used the median grain sizes from the study reach from Table 3.7, the average slope and channel width measured using the laser range finder Table 3.4, the flow depth as measured using the LiDAR and ultrasound stream gauge sensors, and a range of distances incorporating the rough distances from the sensors to the river from field measurements. Rough shear wave velocities were found through undertaking an active seismic refraction survey in the study reach. The survey was undertaken at only one site, due to logistical limitations, so I have made the assumption that the seismic site characteristics are constant throughout the reach since the reach is quite small and the substrate is unlikely to change substantially between geophone sites. However, the active seismic survey provided us with rough P-wave velocities of approximately 2484 m/s (Section 3.2.5), which is not too dissimilar from the values found by Tsai et al. (2012) (2206 m/s). Given this similarity, I have adopted the default parameter for Rayleigh wave phase velocity from Tsai et al. (2012), as shown in Table 4.1. The bedload flux values were acquired from the calculations in Appendix D. The flux values were selected for the transport of the median grain size from the calculations of Wilcock and Crowe (2003), as these accounted for mixed-size sediments which is best representative of the River Feshie. I chose to vary the water depth from 0.8 m to 1.6 m, as these were typical ranges of hydrographic peaks at the study site, and used the corresponding D_{50} bedload flux to model how changing water levels affect the seismic characteristics. The turbulence model does not have a 'bedload flux' parameter, so only the water depth was varied. Base values of water depth (1.6 m), bedload flux (0.0009 kg/s/m), D_{50} (38 mm), and distance from sensor to river (20 m) were used respectively when that parameter was not being adjusted. These values were chosen to represent the transport at high water levels at a distance typical of the river-adjacent geophones in the River Feshie study reach.

Table 4.1: Parameters used in the R 'eseis' package turbulence and bedload models

Parameter	Value	Unit	Source
Mean sediment grain diameter	0.026 - 0.049	m	Measured
Standard deviation of sediment grain diameter	0.42	m	Measured
Specific sediment density	2650	kg/m^3	Dietze (2018a)
Bedload flux	0.0001-0.0009	kg/m/s	Calculated
Fluid density	1000	kg/m^3	Dietze (2018a)
Water depth	0.8-1.6	m	Measured
Channel width	30	m	Measured
Channel slope	0.0068	-	Measured
Station-to-river distance	2-300	m	Measured
Reference frequency	1	Hz	Dietze (2018a)
Model frequency range	(1, 100)	Hz	Measured
Quality factor	20		Tsai et al. (2012)
Rayleigh wave phase velocity	1295	m/s	Tsai et al. (2012)
Green's function coefficients	(0.6, 0.8)		Dietze (2018a)

4.2.2 Stream gauge data

Using the processed stream gauge data from the local measurements taken within our study reach, as described in section 3.4.2, I chose a selection of the largest events that occurred during the entire monitoring period of the thesis (December 2020 to November 2023). I also narrowed down this selection by choosing the events for which the local stream gauge measurements at SG2 (Figure 3.1) were recorded. Five key events were selected for this analysis (as shown in Figure 4.1) and are listed below along with the short name that they will be referred to throughout this chapter and subsequent chapters that refer to these events:

- **11^{th} - 14^{th} March 2022 = March 2022 event**
  This event comprised of three peaks in water level reaching successively greater values. It was most likely the result of rainfall on snow combined with snowmelt, as derived from regional meteorological and climate data as well as incomplete precipitation data provided by Andrew Black. The event reached a peak discharge of 84 m^3s^{-1} at the Feshie Bridge SEPA gauge (SG3, Figure 3.1), and a maximum water level of 1.27 m at SG2.

- **30^{th} September - 1^{st} October 2022 = September-October 2022 event**
  This event in late September to early October 2023 consisted of one very large peak in water level with a maximum water level of 1.69 m at SG2 and a peak discharge of 131 m^3s^{-1}. The event was of a much shorter duration than the March 2022 event as was the result of intense rainfall in the catchment that coincided with the tailend of Hurricane Fiona that hit Canada in mid-late September 2022 that potentially influenced the weather.

- **2^{nd} - 3^{rd} November 2022 = November 2022 event**
  This event was another single peak event reaching a discharge of 90 m^3s^{-1} at SG3 and a maximum water level of 1.30 m at SG2. This was the result of high rainfall from an early winter storm.

- **24^{th} - 25^{th} September 2023 = September 2023 event**
  The September 2023 event actually comprised of 3 peaks in water level over 9 days, but to avoid losing detail in the spectrogram signals I just selected one peak. This event reached a peak water level of 1.35 m at SG2 and a maximum discharge of 88.40 m^3s^{-1} at SG3.

- **7^{th} - 9^{th} October 2023 = October 2023 event**
  The final event used in this study occurred as a result of high levels rainfall, reaching maximum discharge value of 138.35 m^3s^{-1} at SG3 and peak water level of 1.48 m at SG2. This event was also not available in the local stream gauge data so I have used the SEPA Feshie Bridge data.

4.2.3 Seismic data

The raw seismic signals that were recorded by the geophones during these events were converted into miniSEED format and processed as described in section 3.4.1. To analyse the characteristics of the seismic signals I calculated and plotted spectrograms. A spectrogram is a visual representation of signal strength over time at various frequencies. The plotted spectrogram has one time axis and one frequency axis,

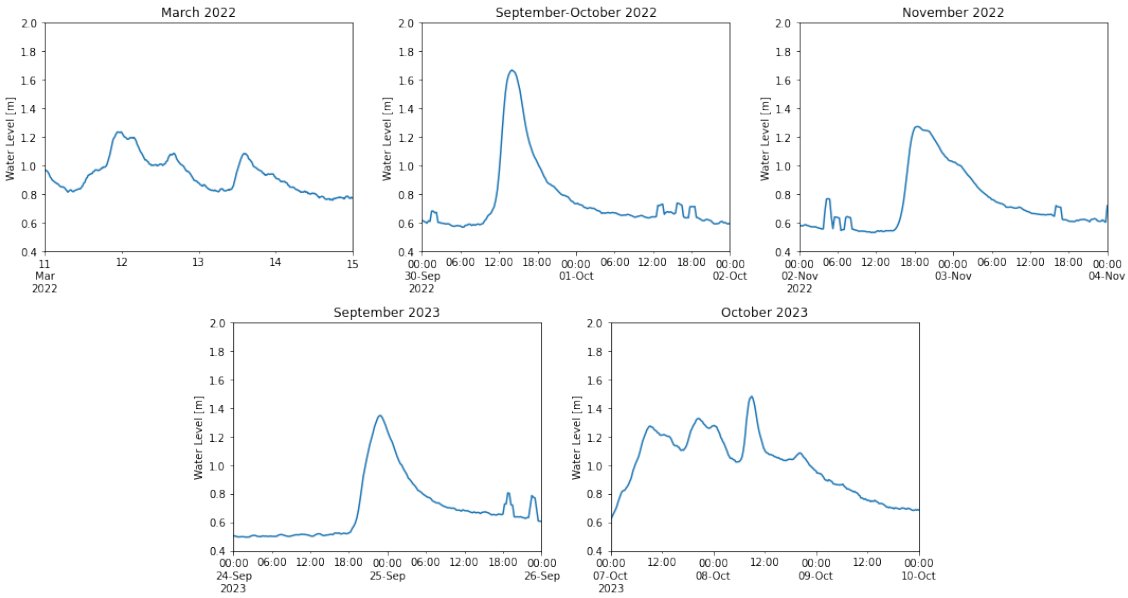


Figure 4.1: Hydrographs of the local stream gauge data at SG2 for the five selected high flow events.

and the magnitude (or seismic power) of each frequency at each time is represented on a colour scale. A spectrogram is calculated by splitting the signal into overlapping sections with a window function. Each window is then Fourier transformed to the frequency domain, to give the short-term frequency content which represents the value for an instant in time. For the analysis in this thesis I used Python package MatplotLib's built in `matplotlib.pyplot.specgram` function which computes and plots a spectrogram of the input data. The length segments can be specified as can the amount of overlap of each segment. For this work I computed the Power Spectral Density (PSD) with a 1-minute window and no overlap. Since the geophones are comprised of three components I performed these calculations on each component of the signals analysed. Since the N-S component was oriented parallel to the river and the E-W component was oriented perpendicular to the channel, I refer to them as stream-parallel and stream-perpendicular, respectively. To compare the site and event seismic characteristics, I then plotted the resulting spectrograms for all sites recording during the five selected events. I additionally analyse the variation in seismic power across the full frequency range during the events to identify any changes in the dominant frequencies. Unfortunately, not all geophones were recording during all events so not all sites and events can be directly compared.

4.2.4 Hydroacoustic data

The hydroacoustic data is recorded as WAV type audio files that can be read into coding and audio analysis software. For this chapter, I analyse the frequency content of the hydroacoustic data using the same method as used for the seismic data. The hydrophone at site H1 (Figure 3.29) was recording during all five events and was therefore used for this analysis. In plotting the frequency against hydroacoustic signal power I can directly compare to the frequency versus seismic power data to analyse the level of agreement between the two. By audibly listening to the sound files I also identify if bedload is being transported or not and use this to compare the variations in seismic and hydroacoustic signals during periods of transport.

There is a distinct audible signal from turbulence (gurgling) and particles being transported (tinkling, tapping and knocking). The recordings were categorised as 'Bedload Transport' if they were dominated by moving pebbles with more than 10 pebble hits over a 5 second window, however, if there was only the occasional pebble movement ($\simeq$10 per 5 seconds) and it was dominated by turbulence noises the files were classified as 'No Bedload Transport'.

4.3 Results

4.3.1 Bedload transport and turbulence model outputs

In the results of the R 'eseis' package model outputs (Figure 4.2), the estimated turbulence signal dominates from 1-50 Hz depending on the parameter specifications and the bedload signal generally dominates from around 30-40 Hz to 100 Hz. However, both spectra show a significant degree of overlapping across the full frequency range. Adjusting the parameters shifts the frequencies at which each process dominates and changes the resulting strength of the signals. Here we can see that an increase in water depth, and subsequently an increase in bedload flux, results in an increase in the seismic power with the intersection of the bedload and turbulence spectra shifting to lower frequencies (50 Hz to 35 Hz), meaning that at higher water levels it would be expected that the distinction between bedload and turbulence may be clearer with turbulence dominating up to around 35 - 40 Hz and bedload dominating above that (Figure 4.2a). In Figure 4.2b I have kept the base parameters and only varied the grain size of the D_{50} fraction from field observations. This has a larger effect on the bedload spectra than the turbulence spectra showing a progressive increase in the power, particularly at higher frequencies. The turbulence spectra remains fairly constant but with a very slight decrease in power as the D_{50} increases. As a result the intersection of the spectra decreases slightly from around 40 Hz to 25 Hz. The final panel (Figure 4.2c) indicates the effects of varying the distance between the sensor and the source, i.e. the river. It is clear that this parameter has a significant effect on the modelled spectra, with larger distances resulting in a significant drop in seismic power at higher frequencies. This causes the intersection of the spectra to decrease rapidly from approximately 40 Hz to 20 Hz. The majority of our sites are less than 30 m from the river and will therefore likely show little effect of distance on the signals recorded. However, the control site (E_06) is located at around 300 m from the river and would therefore be expected to exhibit a significantly reduced power and frequency of the river-induced signals.

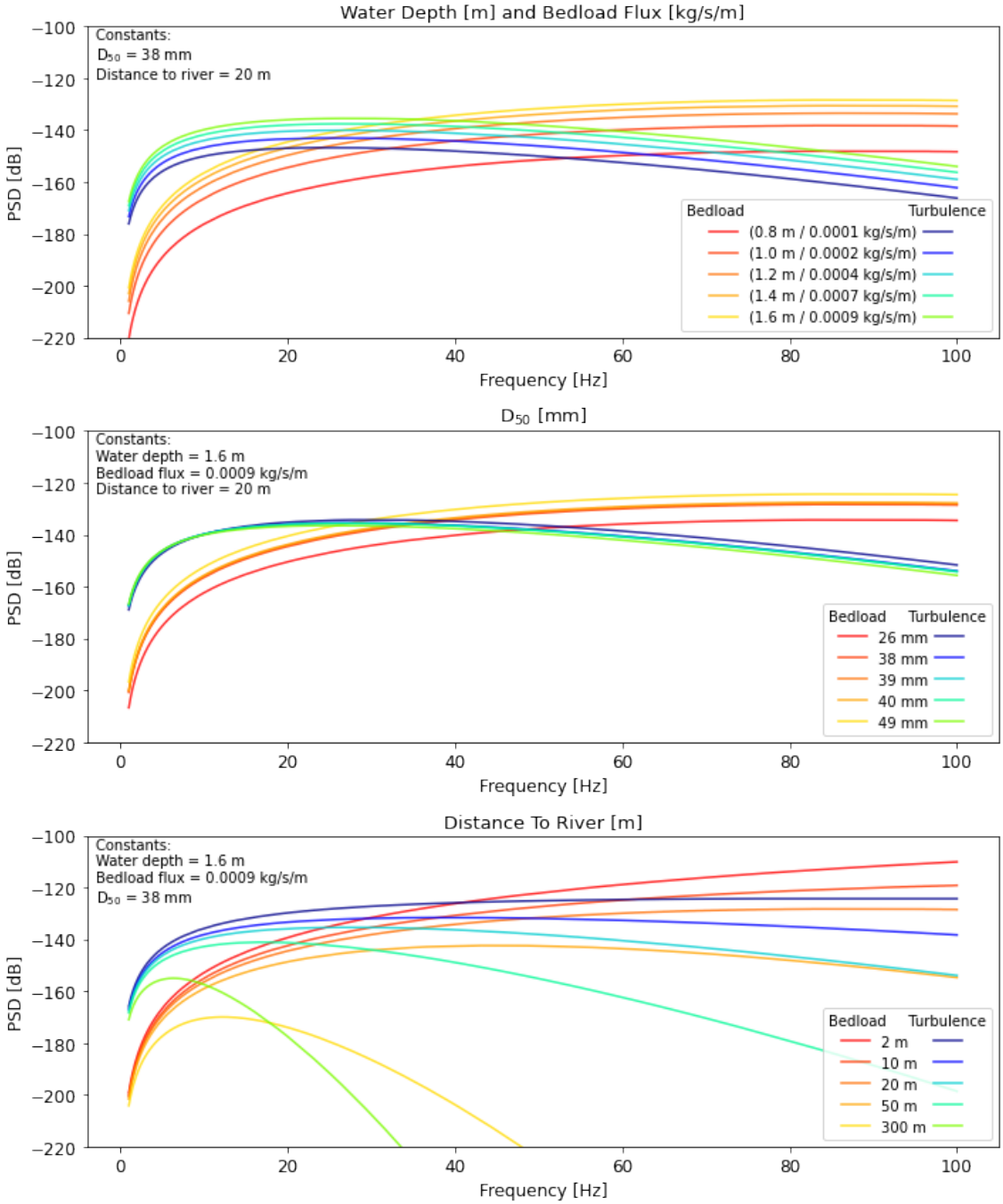


Figure 4.2: 'eseis' package bedload and turbulence models with varying parameters. (a) The effects of varying water depth along with the corresponding bedload flux, (b) the effects of varying the median grain size, and (c) the effects of varying the distance between the sensor and the river. The colours of the lines correspond to whether it is the bedload spectrum (warm colours) or the turbulence spectrum (cool colours).

4.3.2 River-induced seismic signals

Seismic data recorded from the geophone at site W_05 during the November 2022 event will be used here to assess how well seismic sensors can record river-induced ground vibrations to infer about river processes. This site was chosen as it was central to our study reach and adjacent to the water level measurements, and the event was chosen as it was a simple single peaked high flow. The spectrogram of the seismic data will be analysed to identify changes in seismic power and frequency content in relation to the changing water levels. Figure 4.3 shows the signal recorded

at geophone site W_05 during the November 2022 event. Here I have chosen to show just the stream-parallel component to introduce the characteristics of seismic signals observed. It is clear that the strong increase in seismic power coincides with the increase in water level during the event. Throughout the whole plotted period (two days) there is a distinct constant signal across 15-40 Hz at around -155 to -150 dB, which increases in power to greater than -130 dB during the higher water levels. The magenta lines in Figure 4.3 indicate the rough start and end of this high power signal in the lower frequency band. To give a rough indication of the timings of the start and end of this signal I visually identified when the constant signal of greater than roughly -145 dB started and when it ended. The onset is quite sharp and easy to identify, however, the end of the signal is very gradual over the falling limb of the hydrograph and is therefore harder to pick the exact time. The onset was observed to be at around 16:30 on the 2nd November with the end estimated at 04:30 on the 3rd, corresponding to water levels of 0.83 m and 0.82 m respectively. We can see that during this period of increased water levels there is additional high power seismic signals recorded at 40-85 Hz but strongest between 40 Hz and 60 Hz. The duration of this signal is shorter than that for the lower frequency band with the start at around 16:45 on the 2nd and the end at 02:30 on the 3rd, shown by the black dashed lines in Figure 4.3b. Again, these start and end points have been selected where the seismic power is greater than approximately -145 dB. These correspond to water levels of 0.93 m and 0.92 m, respectively. There is uncertainty in these timings and values due to the difficulty in visually identifying the changes in seismic power and also due to the 15 minute resolution of the water level recordings. In addition to the increased seismic power bands during the increased water levels, there are also some strong signals occurring sporadically throughout the plotted period that are more regular in the six hours prior to the increase in water levels. These signals span a broad frequency range (herein referred to as 'broadband') from about 5 Hz to 80 Hz.

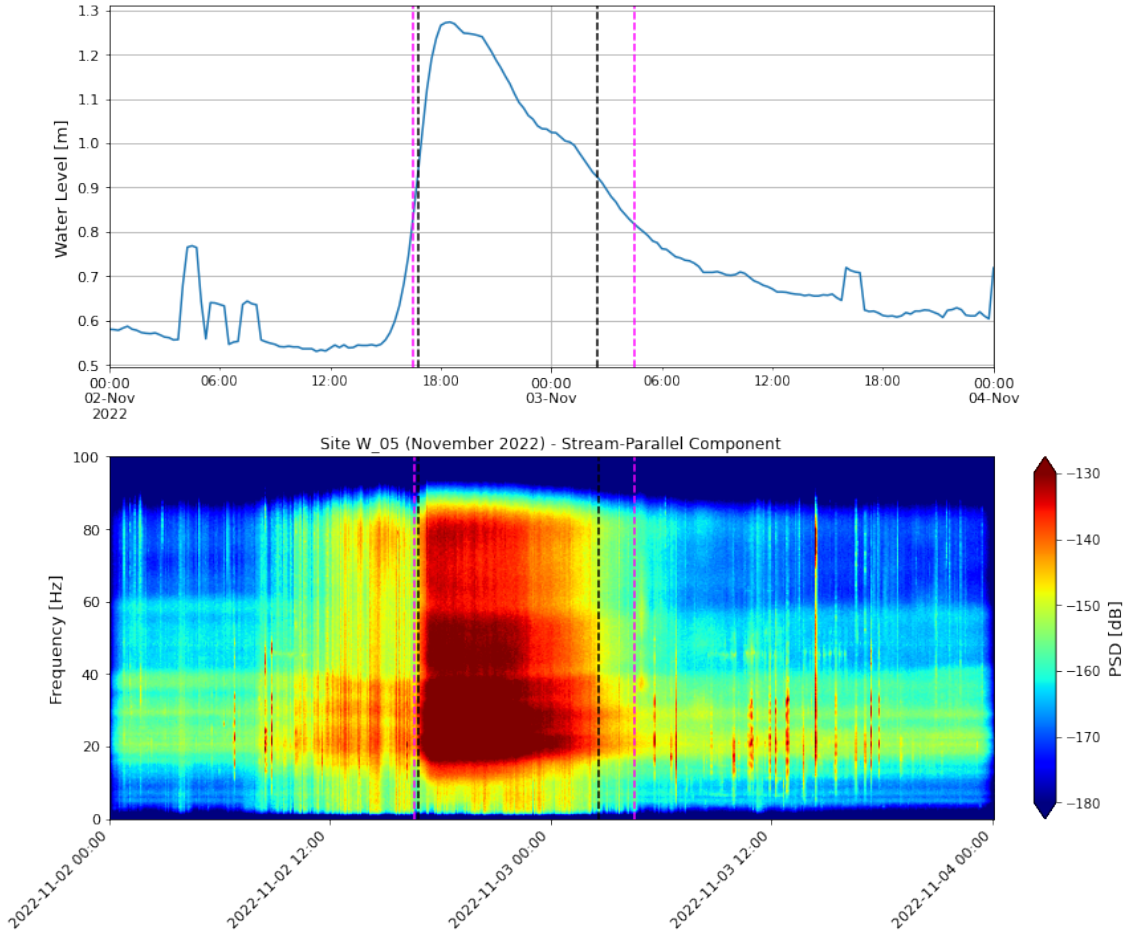


Figure 4.3: Hydrograph from local stream gauge sensor SG2 of the November 2022 event along with a plot of seismic power as a function of frequency and time (spectrogram) of the stream-parallel seismic data recorded at site W_05. The magenta lines indicate the start and end of high power signal in the 15-40 Hz band, and the black lines indicate the rough start and end of the high power in the 40-85 Hz band.

4.3.3 Site comparison

Here I am going to compare the seismic signals recorded in three components at each geophone site for each of the selected events. Figure 4.4 shows the sites that were recording during each event. I will discuss recorded signals on an event-by-event basis making reference to both the hydrograph (Figure 4.1) and the seismic signals for each. Each grid figure has one row for each geophone site with each column corresponding to the directional component of the instrument (vertical, stream-parallel, or stream-perpendicular). All subplots are labelled with the station name and the component. Blank subplots in the figure correspond to geophone sites that did not record during that event. This section is also used to provide a general description of the characteristics of each signal plotted which is used for the subsequent sections.

11^{th} - 14^{th} March 2022

During the high flow event in March 2022 (Figure 4.1a), five geophone sites were recording; four adjacent to the river and one control site approximately 300 m from the river (E_06) (Figure 4.5). Each of the three river sites show close correlation with the hydrograph, increasing in seismic power during the three peaks of the event. Whereas the control site shows higher broadband streaks of seismic power between the hydrograph peaks, with greater seismic power recorded in the horizon-

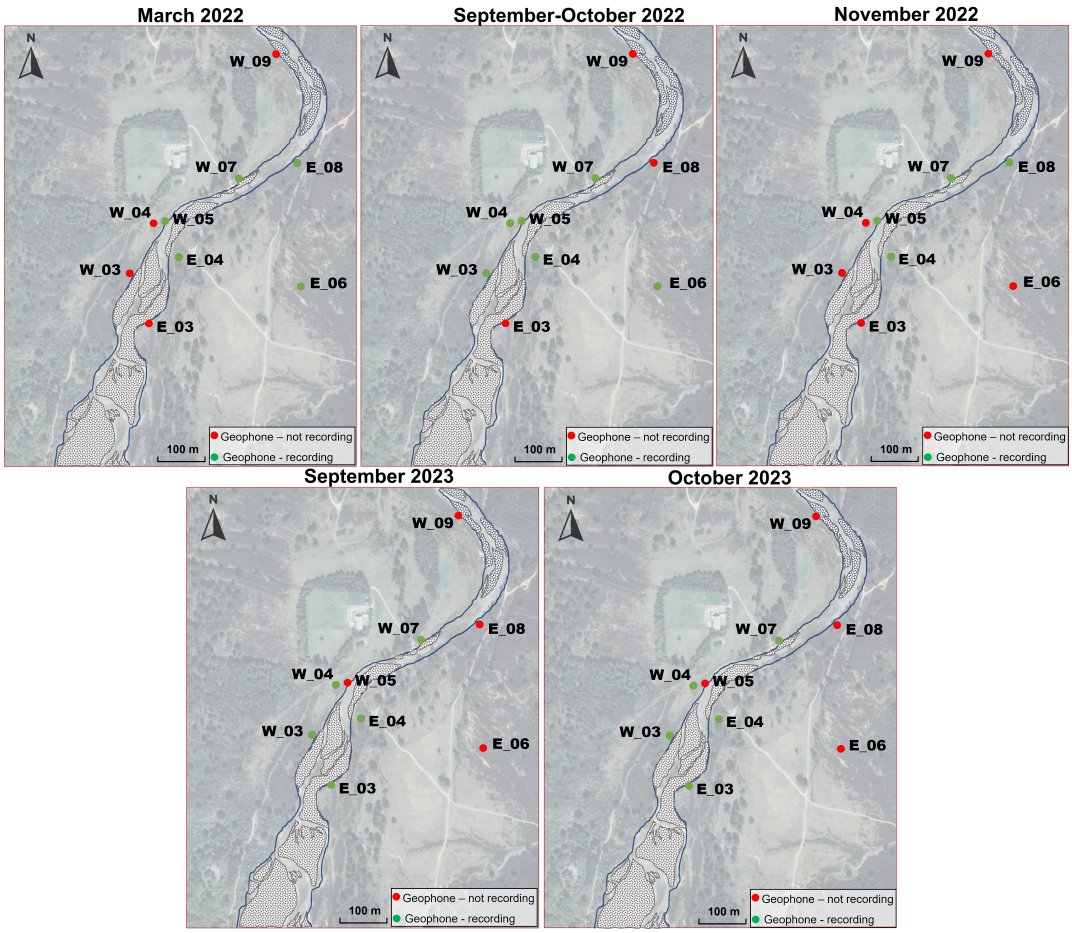


Figure 4.4: Maps showing active geophones during each of the five selected high flow events.

tal components than the vertical component, specifically the stream-perpendicular component. There is no clear continuous seismic signal over the duration of this period at E_06.

In contrast, W_05 shows a continuous high power seismic signal (-140 to -130 dB) at around 20 - 35 Hz over the full period plotted in the two horizontal components, but this is absent in the vertical component (Figure 4.5). All components show an increase in seismic power between roughly 20 Hz and 85 Hz at the same time as the peaks in the hydrograph reaching values of up to -111dB, with the continuous low frequency band in the horizontal components showing simultaneous increases in power. These seismic power increases occur at roughly 1.00 - 1.10 m water level. There is a sharp onset of the high-power high-frequency seismic signals and a slight tapering off the maximum frequencies to lower frequencies, particularly evident during the falling limb of the whole event following the third peak.

W_07 shows very similar characteristics to W_05, particularly in the horizontal components (Figure 4.5). Both the stream-parallel and stream-perpendicular components show the strong continuous 15-30 Hz signal and the increases in seismic power in frequencies up to 85 Hz corresponding with the peaks in water level. However, the vertical component shows a slightly weaker signal at W_07 compared to W_05, with the peak in power at lower frequencies around 20 - 50 Hz. The cyan and green colours show a weak continuous signal between 15 Hz and 50 Hz over the full period for the vertical component with an injection of an increase in seismic power

between 50 Hz and 85 Hz during the hydrograph peaks.

Site E_04, which is directly opposite W_05 on the flat east bank shows an interesting signal in all three components. There are still general increases in the seismic power at frequencies above 10 Hz corresponding with the hydrograph peaks in all three components, but these signal don't reach frequencies greater than about 70 Hz and are clearest in the horizontal components. There is also not a very clear continuous signal on any of the components. Additionally, there are some very high power broadband streaks (strongest above 50 Hz) that generally occur prior to the hydrograph peaks.

E_08 exhibits signals most similar to W_07 in that there are clear increases in the seismic power between about 10 Hz and 85 Hz corresponding to water levels above approximately 1.00 - 1.10 m. However, the continuous signal, although weak, appears to have frequencies between 10 Hz and 50 Hz with the high power 50-85 Hz signals occurring in tandem with the hydrograph peaks. This site also exhibits some similar signal characteristics to site E_04 with high power broadband streaks (strongest between 50 Hz and 85 Hz) occurring prior to and between the water level peaks. Again we can see a tapering of the high frequency signals during the falling limbs of the hydrograph peaks, clearest on the falling limb of the final peak.

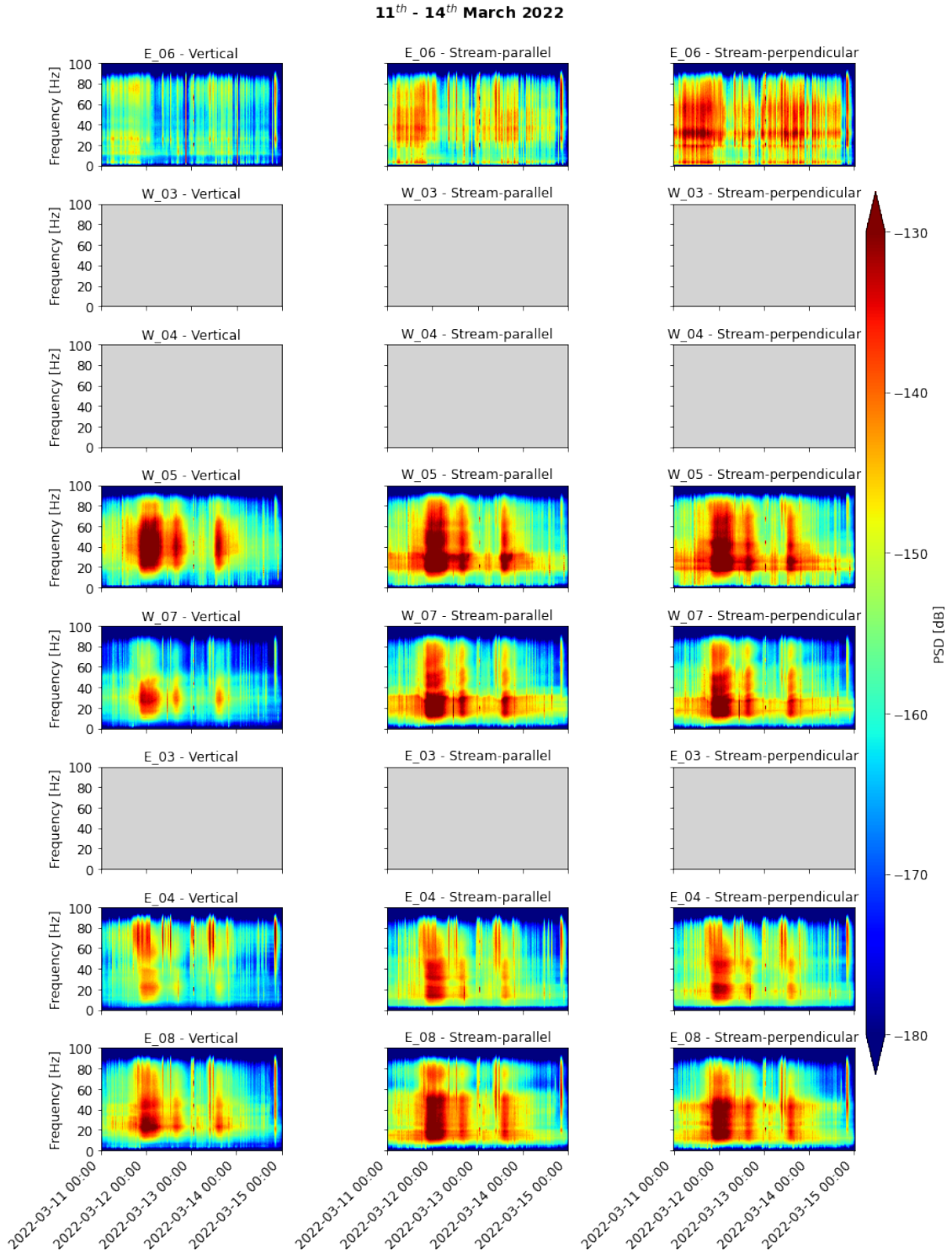


Figure 4.5: Spectrograms of seismic data from all sites in the study reach for the March 2022 event. One site is shown per row with the control site in the top row, followed by the sites on the west bank, and then by the sites on the east bank. Sites that did not record are shown as blank plots. Each column contains the Vertical, stream-parallel and stream-perpendicular directional components of the signals, respectively.

30th September - 1st October 2022

During the high flow event that occurred at the end of September and into October 2022 (Figure 4.1b) there were six geophone sites recording; five river-adjacent sites and the control site, E_06 (Figure 4.6). Much like during the March 2022 event, E_06 shows strong broadband seismic signals prior to the event that stop abruptly

as the water level begins to rise. There is the occasional high-power short-duration broadband signal during and following the hydrograph peak that are randomly occurring.

W_03 is the most upstream geophone on the steep, gravelly west bank of the channel. This site shows strong broadband peaks prior to the water level increase in all three components, and then a continuously strong signal spanning 10 - 80 Hz during the peak in the hydrograph (water levels above approximately 1.00 m). This high seismic power gently tapers off during the falling limb of the hydrograph until base water levels are reached again. There appears to be two strong continuous seismic bands at approximately 35 Hz and 60 Hz in all three components with a broader continuous signal spanning the full frequency range (5-85 Hz). All three components at this site exhibit very similar signals over the full duration of the event.

W_04, which is located on the top of a steep bank above site W_05, shows a clear increase in seismic power between about 10 Hz and 85 Hz during the hydrograph peak in all three components which tapers off over the falling limb. However, the two horizontal components show stronger seismic power between 60 Hz and 85 Hz than the vertical component at these times. All three components have some high power broadband signals prior to the rising limb of the hydrograph, as well as a continuous signal between 10 Hz and 40 Hz over the full period plotted which is slightly stronger on the horizontal components.

W_05 exhibits a signal very similar to that of W_04, with high seismic power during the hydrograph peak and broadband signals prior to the rising limb, although for this site these broadband signals are strongest at slightly lower frequencies (10 - 50 Hz). The signal recorded during the hydrograph peak has stronger high frequency (60-85 Hz) contribution than the signal at W_04 but also shows the tapered frequency reduction of high frequencies. There is a weak continuous signal in all three components from 20 - 60 Hz, with a stronger band at 20 - 40 Hz in both horizontal components.

W_07 is similar to W_05, however, the distinction between the continuous lower frequency band and the high frequency signals during the hydrographs are more clear, especially in the horizontal components. This continuous signal occurs at frequencies of 10 - 40 Hz in the horizontal components, with the higher frequency component between 40 Hz and 85 Hz. These higher frequency signals exhibit and interesting drop in dominant frequency at the peak of the hydrograph which is visible in all three components. The vertical component shows the strongest signal at a dominant frequency of around 20 Hz with very much lower power in the highest frequencies than the horizontal components. All components show high-power broadband signals prior to the rise in water level, similar to that of the other sites.

The only geophone on the east bank that recorded during this event, E_04 again shows a seismic power increase during the high water levels (> approximately 1.00 m) like the previous mentioned sites. The horizontal components show a weak continuous signal at 5-30 Hz in which the seismic power increases during the increased water levels. In addition to this, there is also a higher frequency (30 - 85 Hz) signal that is present during these high water levels. These characteristics are less obvious in the vertical component. All three components show the broadband high power signals prior to the event and periodically after the event.

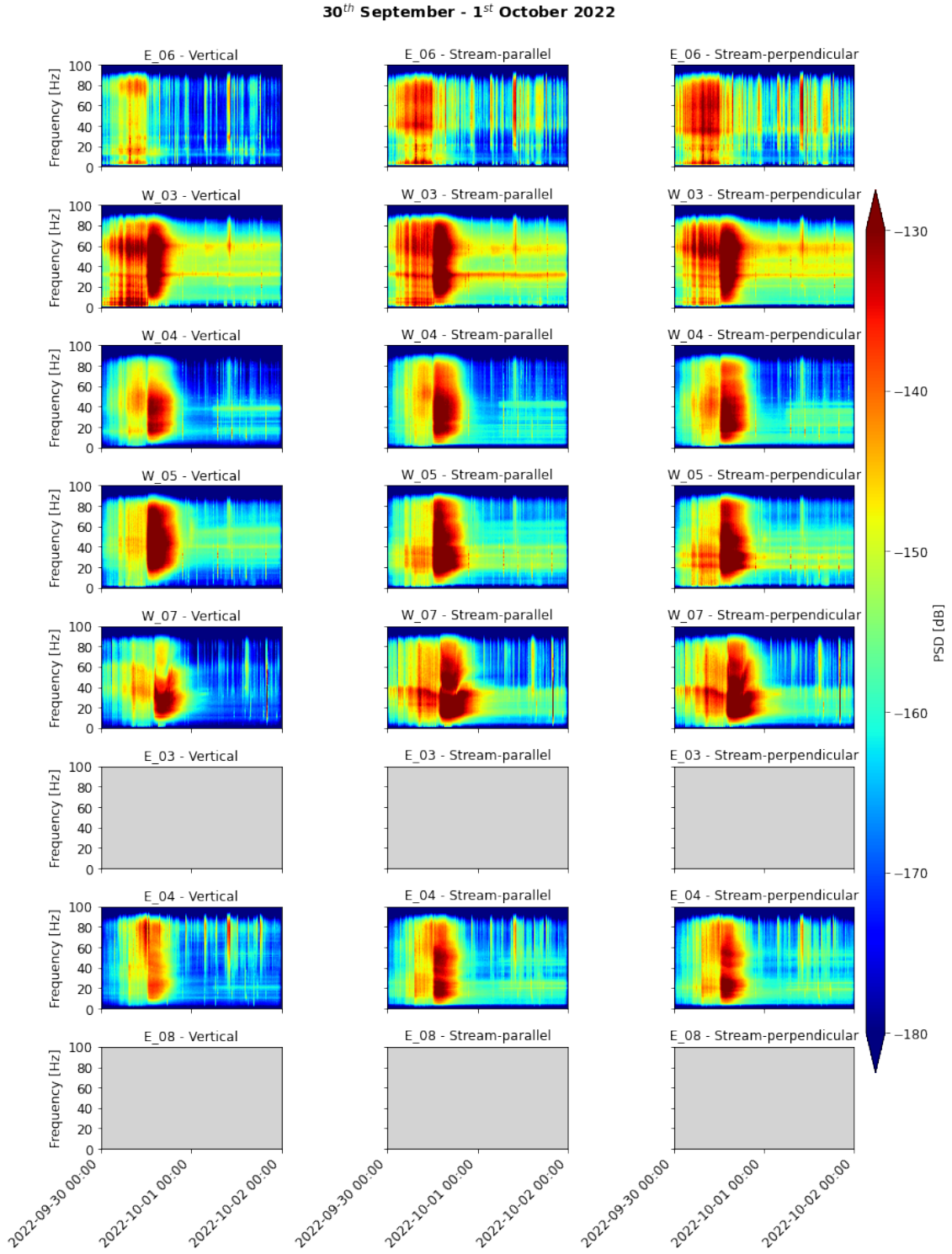


Figure 4.6: Spectrograms of seismic data from all sites in the study reach for the September-October 2022 event. One site is shown per row with the control site in the top row, followed by the sites on the west bank, and then by the sites on the east bank. Sites that did not record are shown as blank plots. Each column contains the Vertical, stream-parallel and stream-perpendicular directional components of the signals, respectively.

2nd - 3rd November 2022

There were only four geophones recording during the November 2022 event; two on the west bank and two on the east bank directly opposite those on the west (Figure 4.7). The control site E_06 failed to record this event.

W_05 shows a clear strong seismic signal during the single peak of this event in all

directional components. The onset of this signal is very sharp in all components and the dominant frequencies also show a gradual decrease in frequency during the falling limb of the event (Figure 4.1c). There are broadband high power signals occurring prior to the large signal in all three components. There is a continuous signal at 15 - 60 Hz present in all components but stronger in the horizontal components, particularly between 20 Hz and 40 Hz.

W_07 exhibits similar characteristics to W_05. The continuous signal is very evident in the horizontal components at 15 - 40 Hz but almost unnoticeable in the vertical component. There are again short duration broadband signals prior to the increase in water level in all three components. During the increased water levels there is a high-power high-frequency (40 - 85 Hz) signal along with an increase in power in the continuous lower frequency signal, which both taper out through the falling limb of the hydrograph. The high frequency component of this signal is not as strong in the vertical directional component as it is in the horizontal components.

Almost directly opposite W_05, at E_04 the signal is similar but shows some distinct differences. There is a clear continuous signal in the two horizontal components at 15 - 30 Hz which is not present in the vertical component data. All components show strong broadband short-duration signals prior to the rise in water level with dominant frequencies of 40 - 85 Hz. There are high-power signals (15 - 85 Hz) present during the peak of the event when water levels are above approximately 0.90 m in all three components with the vertical component showing the weaker signal. The dominant frequencies in the horizontal components are 15-60 Hz which can be subdivided into two bands (15-30 Hz and 30+ Hz). Frequencies above 60 Hz are present but are slightly weaker.

E_08 shows a very distinct onset of a strong seismic signal at 10 - 80 Hz as water levels begin to rise above about 0.90 m. In the horizontal components this signal can be subdivided into two bands; a continuous 10-35 Hz signal and a 35-80 Hz signal that is only present during the increased water levels. The vertical component, however, does not exhibit these two dominant frequency bands, with less seismic power in the higher frequencies. There is a clear tapering in seismic power and frequency of the signal on the falling limb of the hydrograph in all three components. Additionally, all components show broadband high seismic power prior to the increased water levels.

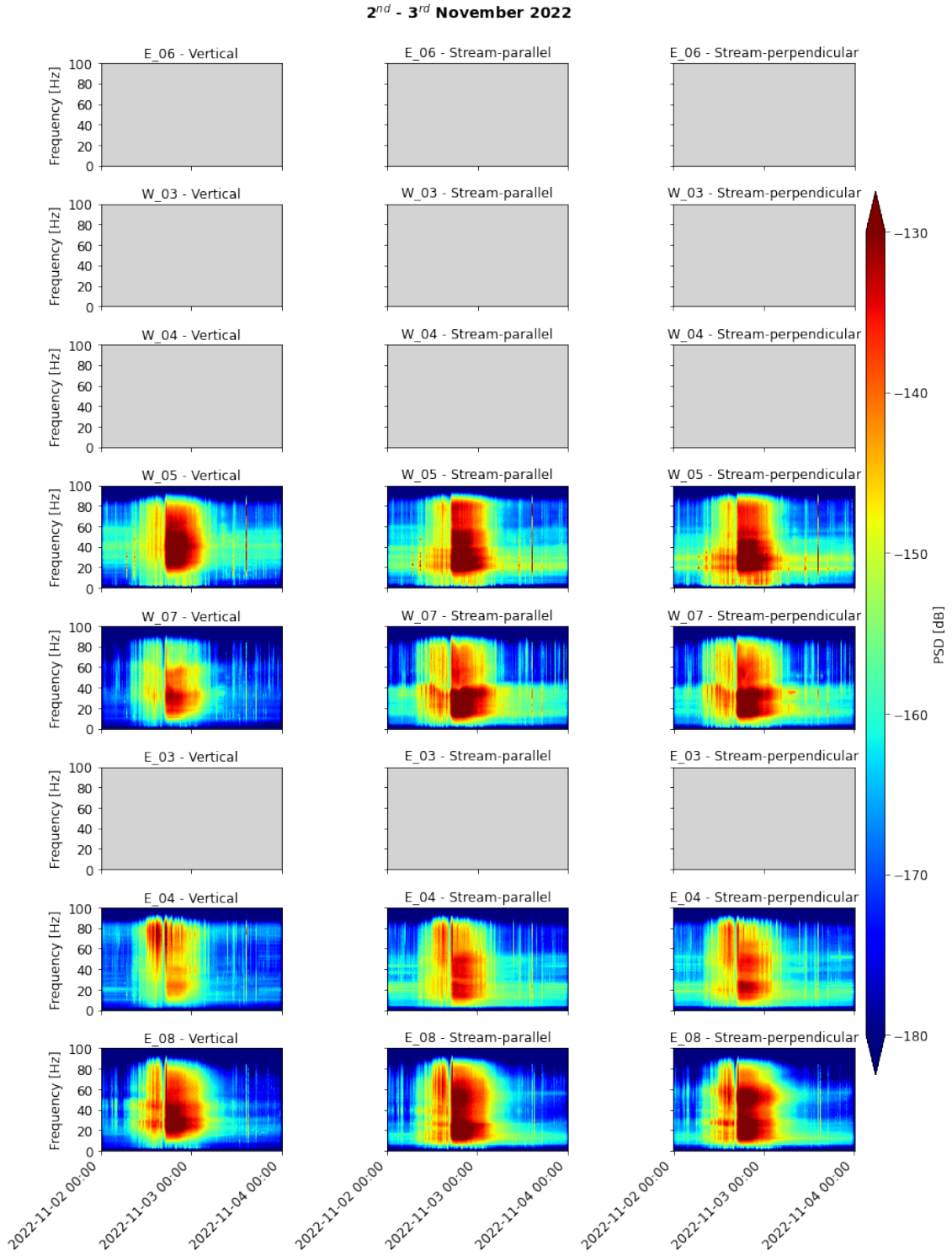


Figure 4.7: Spectrograms of seismic data from all sites in the study reach for the November 2022 event. One site is shown per row with the control site in the top row, followed by the sites on the west bank, and then by the sites on the east bank. Sites that did not record are shown as blank plots. Each column contains the Vertical, stream-parallel and stream-perpendicular directional components of the signals, respectively.

24th - 25th September 2023

During the event in September 2023 (Figure 4.1d), five river-adjacent geophones were recording; three on the west bank and two on the east bank (Figure 4.8). Unfortunately the control site, E_06, failed to record this event.

Site W_03 shows a clear strong seismic signal during the increased water levels

in all three components, with slightly higher seismic power in the horizontal components particularly at higher frequencies. Additionally, there are broadband peaks in seismic power prior to the rising limb of the hydrograph in all components, but also some following the event.

W_04 shows these broadband peaks in seismic power before and after this event clearer than W_03. Although these short duration peaks are present throughout the plotted period, they get stronger in the three hours prior to the increase in water level in all components. Due to the seismic noise surrounding the peak in the hydrograph it is hard to identify any continuous signals, however, it appears that there is a dominance in frequencies of around 20-40 Hz and 60-80 Hz.

W_07 again shows these abundant broadband peaks but to a lesser power than W_04, reducing the noise surrounding the signal recorded during the changing water levels. The horizontal components both show evidence of two distinct frequency bands (15-40 Hz and 40-80 Hz), with the lower frequency band presenting as a continuous signal over the full plotted duration. The higher frequency band is only present during the increased water levels and is most evident in the horizontal components. This band also exhibits a dip in the dominant frequencies at the peak of the hydrograph.

E_03 looks most similar to the signal recorded at W_03. Although all three components show an increase in seismic power at 5 - 70 Hz that coincides with the increased water levels, the horizontal components have a stronger signal particularly at higher frequencies (40-70 Hz). Here too, there are broadband peaks throughout the plotted period but are strongest immediately prior to the high power seismic signal as the water level rises.

E_04 shows an increase in seismic power at 10 - 60 Hz in all three directional components coinciding with the increase in water level during this event. All three components also show faint distinctions between two frequency bands (10 - 30 Hz and 30 - 60 Hz), the lower of which appears to be somewhat continuous in the horizontal components. Additionally, all components have the short-duration broadband signals throughout the plotted period, with increased seismic power in the three hours leading up to the increase in water level.

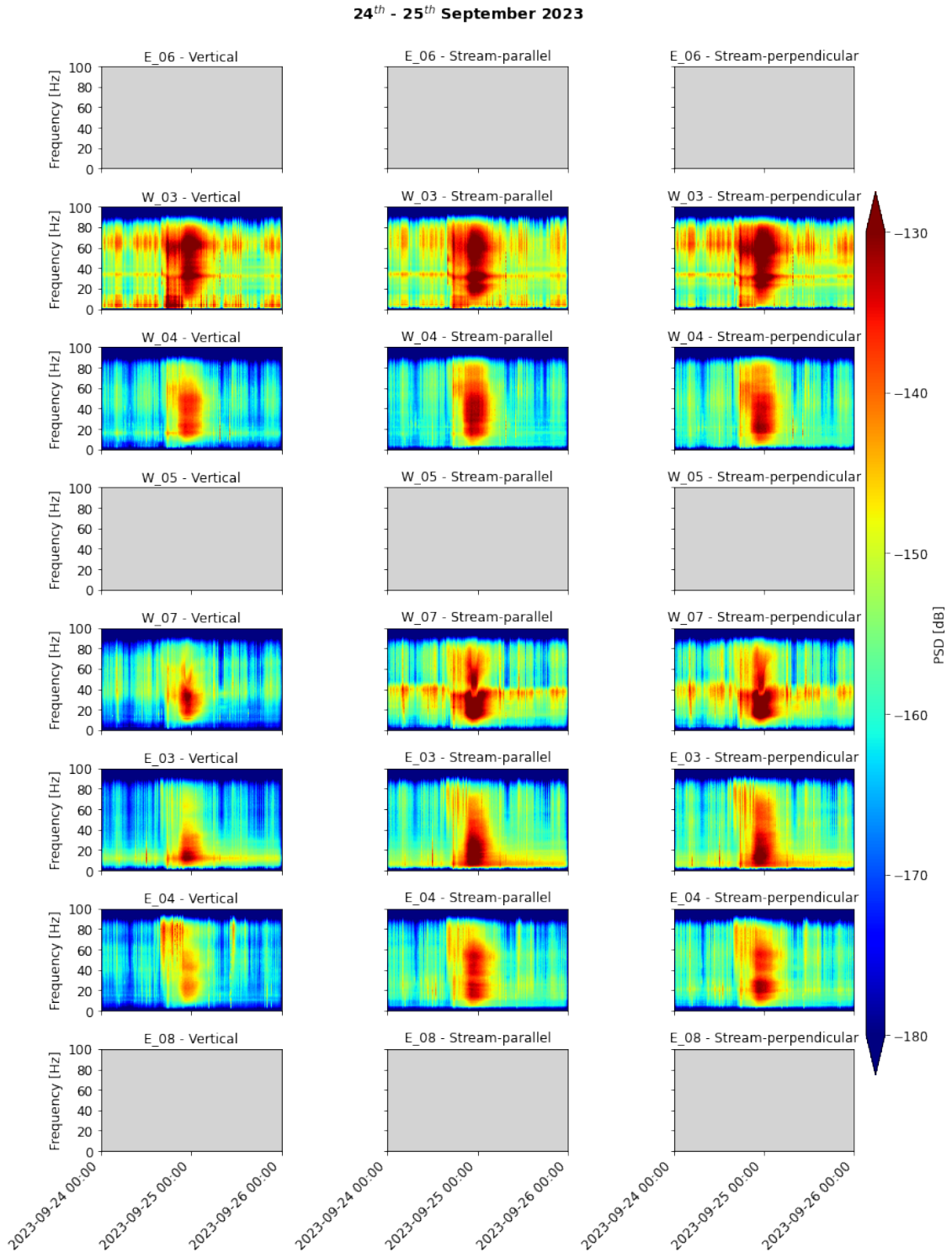


Figure 4.8: Spectrograms of seismic data from all sites in the study reach for the September 2023 event. One site is shown per row with the control site in the top row, followed by the sites on the west bank, and then by the sites on the east bank. Sites that did not record are shown as blank plots. Each column contains the Vertical, stream-parallel and stream-perpendicular directional components of the signals, respectively.

7th - 9th October 2023

During this event in October 2023 (Figure 4.1e), five geophones were recording; three sites on the west river bank and two sites on the east bank (Figure 4.9). Control site E_06 did not record this event.

This event consisted of three peaks in water level. W_03 recorded three periods

of increased seismic power coinciding with the peaks in water level. The dominant frequencies in the horizontal components at W_03 during the hydrograph peaks span from 10 - 80 Hz, whereas the vertical component exhibits dominant frequencies of 10 - 60 Hz. In all three components, the onset of the high seismic power is very sharp but the decrease in seismic power following the third peak of the event is very gradual with the dominant high frequencies slowly dropping to lower frequencies.

W_04 too shows increased seismic power during the three periods of increased water levels with a fairly abrupt onset of the signal and a more gradual termination. In all three components there appear to be two dominant frequency bands (15-40 Hz and 45-75 Hz) which are particularly evident during the high water level but are still present, although weaker, following the third peak. Prior to the initial increase in seismic power coinciding with the water level increase there are some short-duration signals at 30-80 Hz in all three components, which are faintly evident between each of the three peaks in seismic power especially prior to the third peak.

W_07 has two distinct dominant frequency bands at 15-35 Hz and 40-80 Hz which are particularly evident in the two horizontal components. The lower frequency band exhibits a continuous behaviour throughout the entire three day period plotted with distinct increases in seismic power coinciding with the three periods of water level increase in the hydrograph. The higher frequency band appears to turn on at times when the high water levels exceed around 1.1 m (Figure 4.1) and off at levels below this. This band also shows a dip in the dominant frequency during the second and third peaks of the event, but not during the first peak. The vertical component shows a much weaker 40-80 Hz frequency band, but still exhibits some of the characteristics observed in the horizontal components.

Although E_03 doesn't show two clear and distinct dominant frequency bands like W_07, it can be seen that a continuous signal is present at 5-20 Hz throughout the full three-day period and during the water level peaks the dominant frequency range extends up to around 75 Hz whilst also strengthening the signal in the 5-20 Hz range. The seismic power recorded in the horizontal directions is significantly stronger than in the vertical direction, particularly at higher frequencies (> 40 Hz). In all three components there is a clear sharp onset of high seismic power as the water level increases and a gradual termination of the signal over the falling limbs, particularly evident following the third peak. Prior to the three peaks there are also some short-duration spikes in seismic power at 50-80 Hz present in all directional components.

E_04 recorded much stronger short-duration 40-80 Hz seismic signals prior to the peaks in water level than E_03, which are particularly strong in the vertical component but present in all three components. It also recorded increases in seismic power during the increased water levels in two frequency bands (10-30 Hz and 35-60 Hz) most clearly seen in the stream-perpendicular component. Here, again there is a sharp onset of high seismic power as the water levels rise during the first peak in the hydrograph and a more gradual decrease is seismic power during the falling limb of the third and final peak of the event.

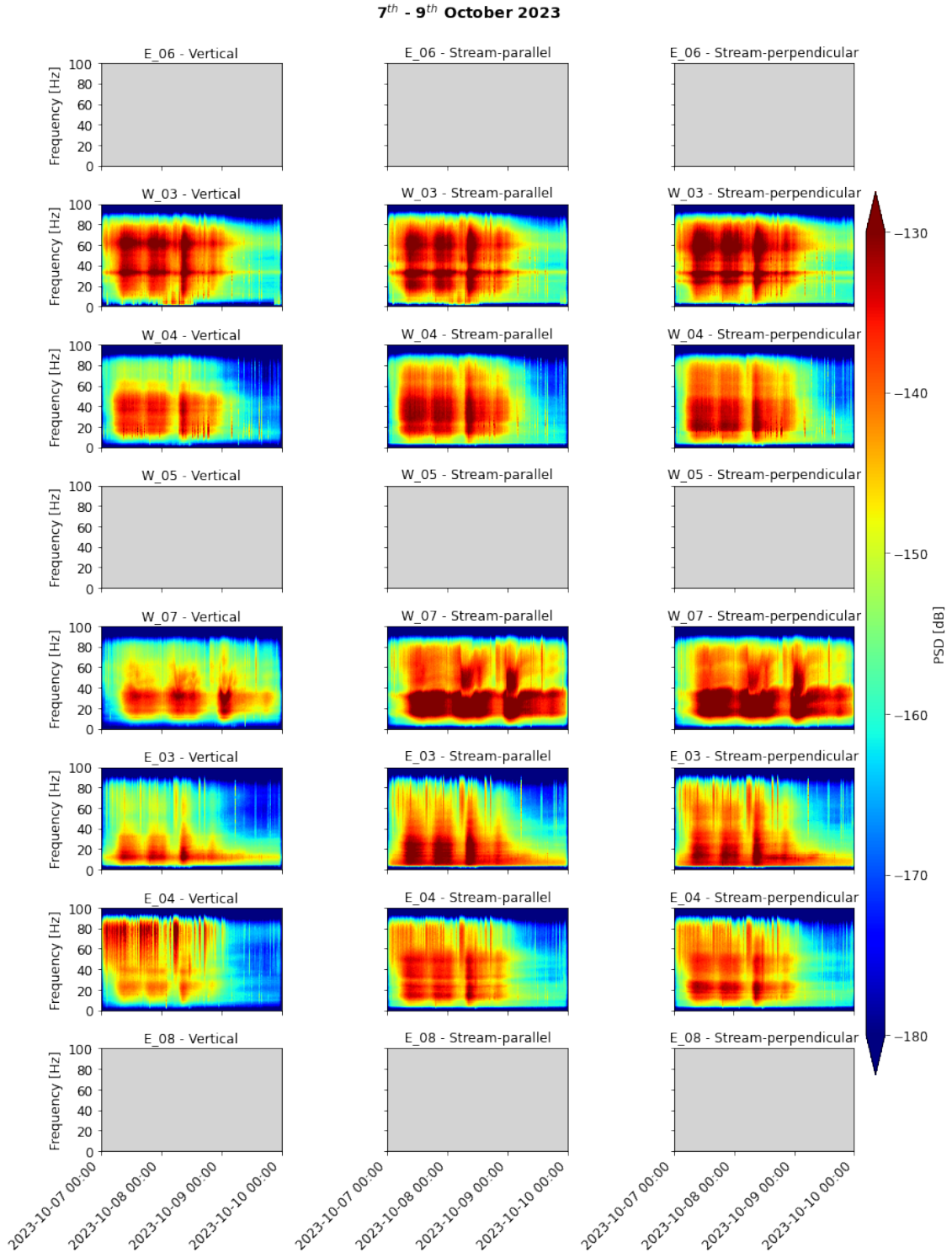


Figure 4.9: Spectrograms of seismic data from all sites in the study reach for the October 2023 event. One site is shown per row with the control site in the top row, followed by the sites on the west bank, and then by the sites on the east bank. Sites that did not record are shown as blank plots. Each column contains the Vertical, stream-parallel and stream-perpendicular directional components of the signals, respectively.

4.3.3.1 Site Comparison Summary

Across all events, most sites show a significant increase in seismic power corresponding to rising water levels (typically around 1.00 m or above), evident in all components (vertical, stream-parallel, and stream-perpendicular) of the geophone

signals. After the water level peaks, seismic power often tapers off, especially in higher frequencies, as the water levels decrease. Site characteristics, including proximity to the river and terrain, likely influence these signals. Sites close to the river, such as W_05 and W_07, exhibit continuous low-frequency seismic signals (10-40 Hz), with clear increases in power and the onset of higher frequency signals during water level peaks. W_05 shows a more consistent high-frequency signal (40-85 Hz), while W_07 covers a broader frequency range with more pronounced fluctuations in power.

In contrast, W_04, the highest site above the river and set back 20 m, shows a less pronounced increase in seismic power at higher frequencies. The signals here are concentrated within a narrower frequency range (15-40 Hz), likely due to the site's elevation and distance from the river.

The east bank sites show more varied characteristics. E_03, located approximately 35 m from the active channel, displays lower-magnitude, lower-frequency seismic signals, likely due to its distance from the river and lack of immediate hydrodynamic influence. E_04 and E_08, at similar distances from the river and on relatively flat ground among young trees and shrubs, show distinct frequency bands — broadband short-duration frequencies prior to the water level increase and two frequency bands (10-35 Hz and 35-80 Hz) during the peak water levels. E_06, located in open land furthest from the river at 300 m, presents sporadic high-power broadband signals but lacks the continuous signals seen at river-adjacent sites.

4.3.4 Event comparison

The following eight figures compare the seismic signal characteristics from recordings from each of the five chosen events listed above at each site on a site-by-site basis. Each grid figure has one column for each event, with each row corresponding to each of the three directional components (vertical, stream-parallel, stream-perpendicular). All subplots are labelled with the event name and the component. Blank subplots are included for events that were not recorded by the instrument at that site. Full descriptions of each signal at each site was included in the previous subsection and this subsection serves as a general comparison between different events.

Site E_06

E_06, the control site, only recorded for two events: March 2022 and September-October 2022 (Figure 4.10). Comparing with the hydrograph in Figure 4.1 it is clear that the strong broadband (5-85 Hz) seismic signals are recorded prior to the peaks in water level. In the March 2022 event these broadband signals are very dominant in the lead up to the first of the three hydrograph peaks. They diminish significantly over the roughly six hours of the first peak before becoming active again prior to the second peak. The single water level peak of the September-October 2022 event makes the occurrence of these broadband signals prior to the increase in water level very clear. In the seven hours lead up to the increased water levels the pulsed broadband signals span frequencies of 5-85 Hz. During and following the event, there is the occasional short-duration high power signal but these seem to follow no obvious pattern. For both events, the signal exhibits the same frequency and duration characteristics in all three components but is weakest in the vertical

direction and strongest in the stream-perpendicular direction.

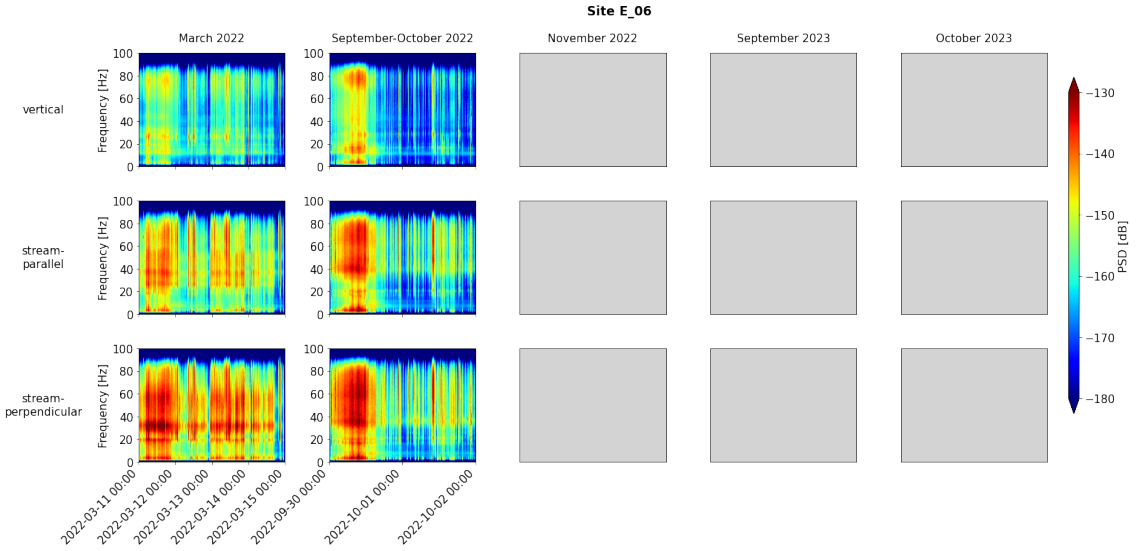


Figure 4.10: Spectrograms of seismic data from site E_06 during all five selected events. One event is shown per column with each row containing a different directional component. Sites that did not record are shown as blank plots.

Site W_03

The furthest upstream site on the west bank, W_03, recorded three of the five selected events (Figure 4.11). All events show similar characteristics, with only some slight variations in the signals recorded. Unlike some of the other sites, this site shows very similar recordings in all three components. All three events show similar broadband streaks prior to the increase in water levels as was seen at the control site, E_06. These again extend from 5 Hz to 85 Hz and are of short durations. All three of the events show the seismic power across this full frequency range increases in coincidence with the increase in water levels, specifically as water levels exceed 0.90 - 1.10 m. This strong seismic power signal gradually decreases in power and peak frequency over the course of the falling limb of the hydrographs before reaching base values. There are two continuous high-power narrow-frequency bands at around 35-40 Hz and 60-65 Hz running throughout the entire plotted periods of all three events that exhibit generally higher power (at $\sim$ -145 to -135 dB) than the other frequencies at each time segment. These signals are very similar in all three components, but the 35 Hz continuous higher power band appears stronger in the stream-parallel component and the 60 Hz continuous band appears stronger in the stream-perpendicular component.

Site W_04

W_04, which is located approximately 8-10 m above the river recorded signals during three of the selected events (Figure 4.12). Seismic signals of all three events show strong correlation with the hydrographs with a very abrupt onset of high power as water levels exceed 0.90 - 1.10 m and a gradual reduction in power and maximum frequencies over the falling limbs of the hydrograph events. Signals at this site span 10-85 Hz with the horizontal components exhibiting overall stronger signal than the vertical component, especially in the higher frequencies ($>$ 60 Hz). The signal is generally weaker in the September 2023 and October 2023 events than the

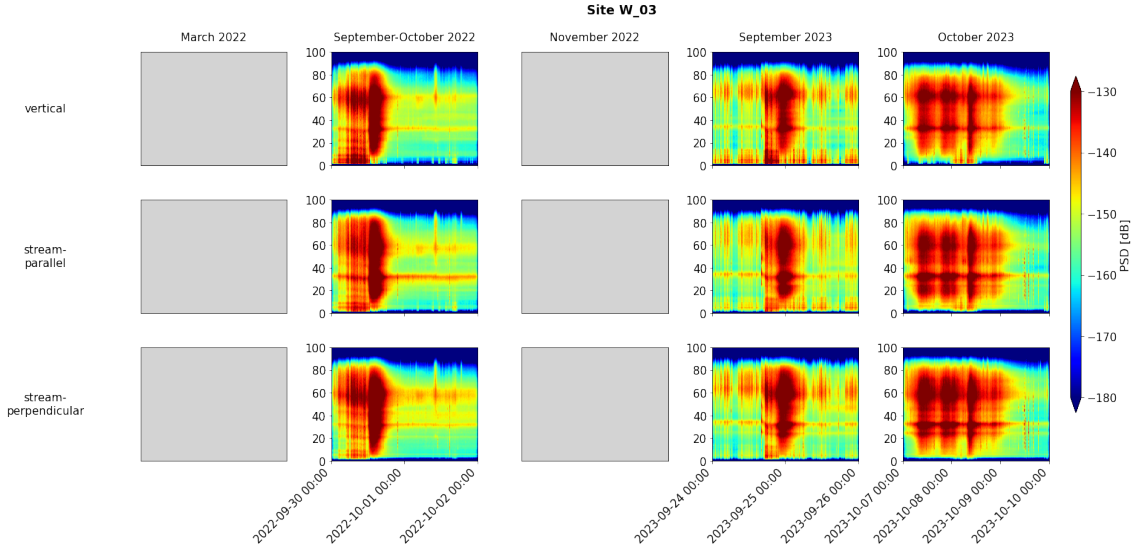


Figure 4.11: Spectrograms of seismic data from site W_03 during all five selected events. One event is shown per column with each row containing a different directional component. Sites that did not record are shown as blank plots.

September 2022 event, but this is most likely due to the water levels being lower in these two events. There are also some broadband short-duration bursts of high seismic power prior to the increases in water levels in all events, but less obvious in the October 2023 event.

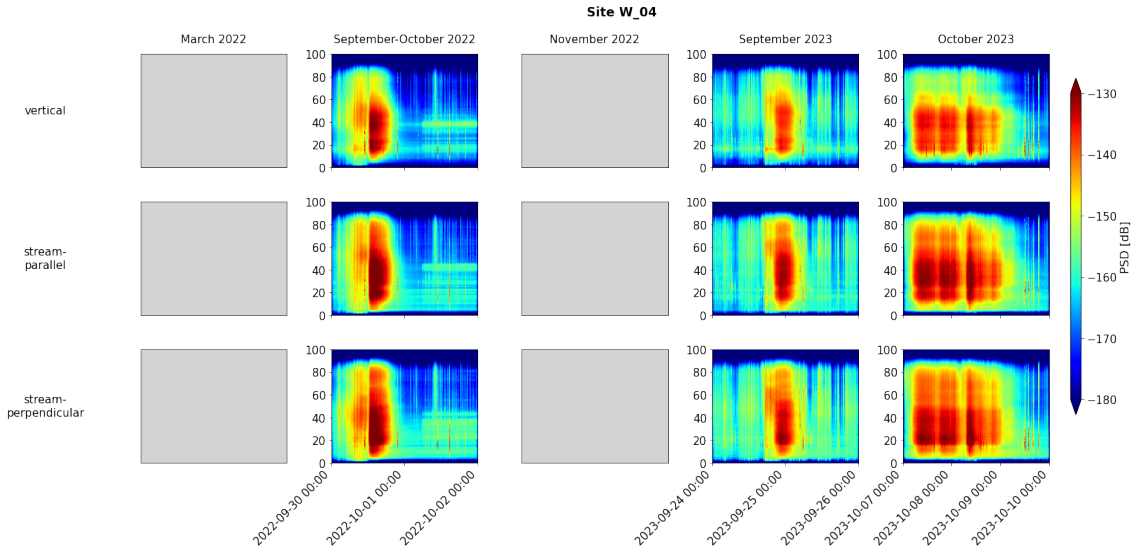


Figure 4.12: Spectrograms of seismic data from site W_04 during all five selected events. One event is shown per column with each row containing a different directional component. Sites that did not record are shown as blank plots.

Site W_05

This site recorded during the first three of the selected events and exhibits very similar characteristics for all three events (Figure 4.13). The largest variations in recordings at this site occur between the different components. All three events have increased seismic power across similar dominant frequency ranges (around 10-85 Hz) that coincides with the increases in water levels during each event, with the March 2022 event showing three key seismic signals for the three peaks in this event.

All events show an abrupt increase in seismic power as water levels increase above around 0.90 - 1.10 m and a more gradual decline in power over the falling limb of the hydrograph. There was a slight increased power from 20 Hz to 60 Hz in all three components through the duration of all three events, but the horizontal components recorded a constant higher power signal at around 20-40 Hz, which was not visible in the vertical component. All three events show short-duration increases in seismic power immediately prior to any increases in water level, but this is clearest in the larger September-October 2022 and November 2022 events.

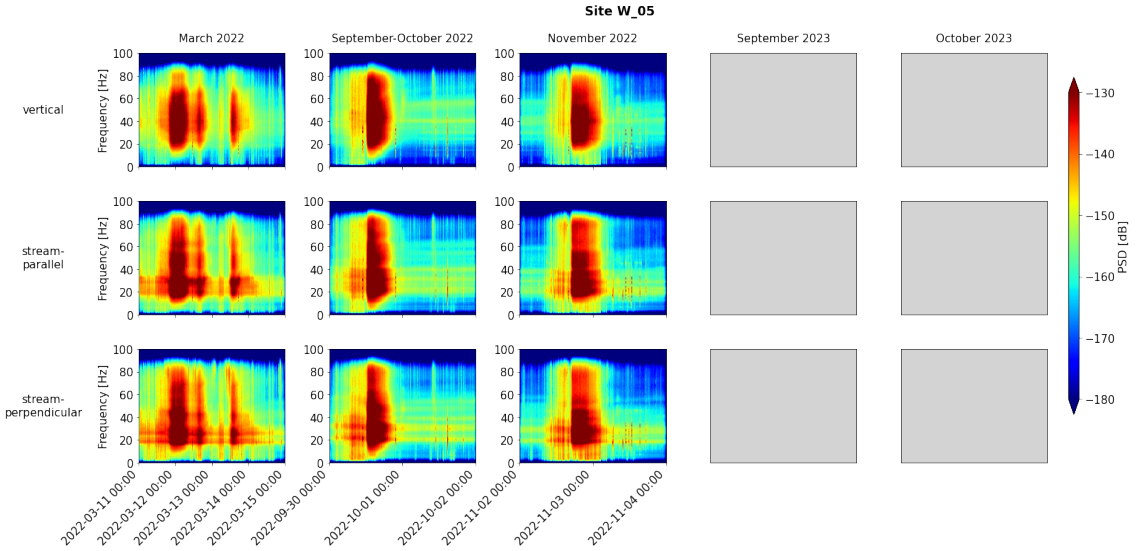


Figure 4.13: Spectrograms of seismic data from site W_05 during all five selected events. One event is shown per column with each row containing a different directional component. Sites that did not record are shown as blank plots.

Site W_07

This was one of two sites that recorded all five of the selected events (Figure 4.14. Very similar characteristics are exhibited across all events with the biggest variations occurring between the different seismic components. All five events show a good correlation between increased seismic power in the 10-85 Hz range and increased water levels above 0.90 - 1.10 m. Additionally, recordings at this site show two very distinct frequency bands in the signals at 10-40 Hz and 40-85 Hz. Examining the stream-parallel and stream-perpendicular components, the lower frequency band is consistently present across all five plotted events, even at low water levels, though with reduced power. The higher frequency band emerges during periods of high water levels and persists for approximately the duration of the high flow event. The vertical component exhibits a weaker signal compared to the horizontal components across all five events, with no apparent continuous signal at lower frequencies. All events show some increased power in broadband short-duration pulses prior to the increases in water level, but are most obvious in the September-October 2022, November 2022 and September 2023 events. Each event demonstrates a drop in the dominant frequency of the two bands, most notably in the higher frequency band during the peaks of the high flow events, as previously mentioned. However, this behavior is most evident during the events of September-October 2022, September 2023, and October 2023.

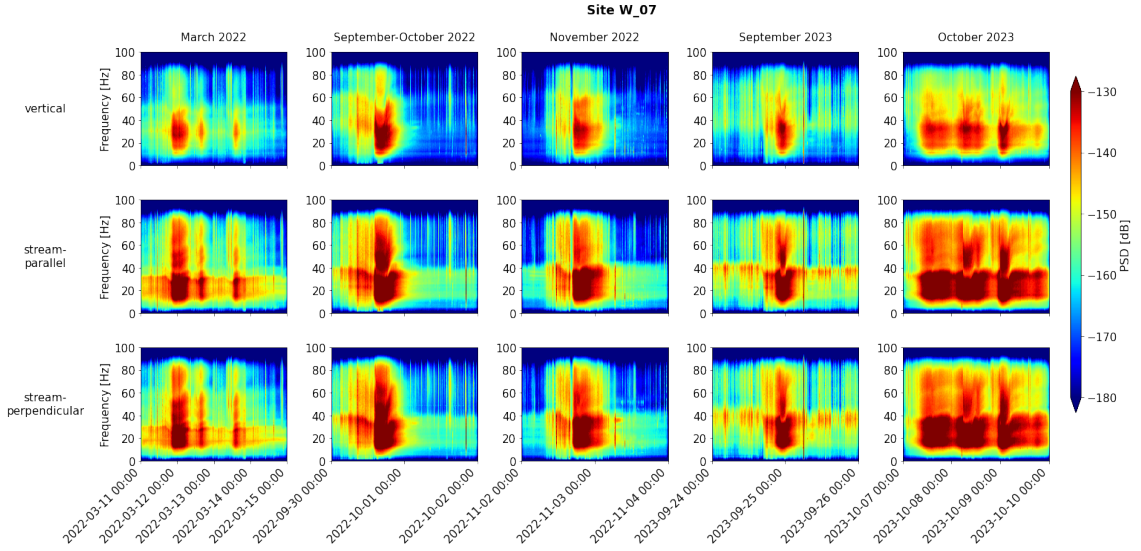


Figure 4.14: Spectrograms of seismic data from site W_07 during all five selected events. One event is shown per column with each row containing a different directional component. Sites that did not record are shown as blank plots.

Site E_03

This site recorded only the final two events because it was deployed in March 2023 (Figure 4.15). The behaviour of the seismic signals during the September 2023 and October 2023 events are very similar. The increased seismic power correlates with higher water levels across all three components. However, the signals are strongest in the horizontal components and extend to higher frequencies. Both events exhibit constant moderate power (∼-150 dB) low-frequency (5-10 Hz) signals throughout their entire durations, along with an abrupt onset of high-power seismic signals extending up to 70 Hz. Broadband streaks reaching up to 85 Hz appear prior to the increases in water level, particularly before each peak in the October 2023 event. Additionally, both events show a gradual decrease in seismic power and maximum frequency on the falling limb of the hydrographs until the dominant signal returns to the base signal band of 5-10 Hz.

Site E_04

This site successfully recorded all five events, producing similar recordings for each (Figure 4.16). Although the signal strength at this site is generally weaker compared to other sites, it still shows a good correlation with changes in water level for all events. Similar to W_07, the two horizontal components display a slightly stronger lower frequency (10-30 Hz) band that is visible throughout the entire duration of all events. The power in this band increases during the peaks in water level, at which time a second band from 30-80 Hz also increases in power. This higher frequency band appears only during the increased water levels. All events exhibit strong high-frequency, short-duration signals prior to the increases in water levels, which become less abundant after the initiation of high water levels.

Site E_08

The furthest downstream site on the east bank, E_08, recorded only the March 2022 and November 2022 events (Figure 4.17). This site exhibits the most variation in seismic signal characteristics between individual events. Both events show a

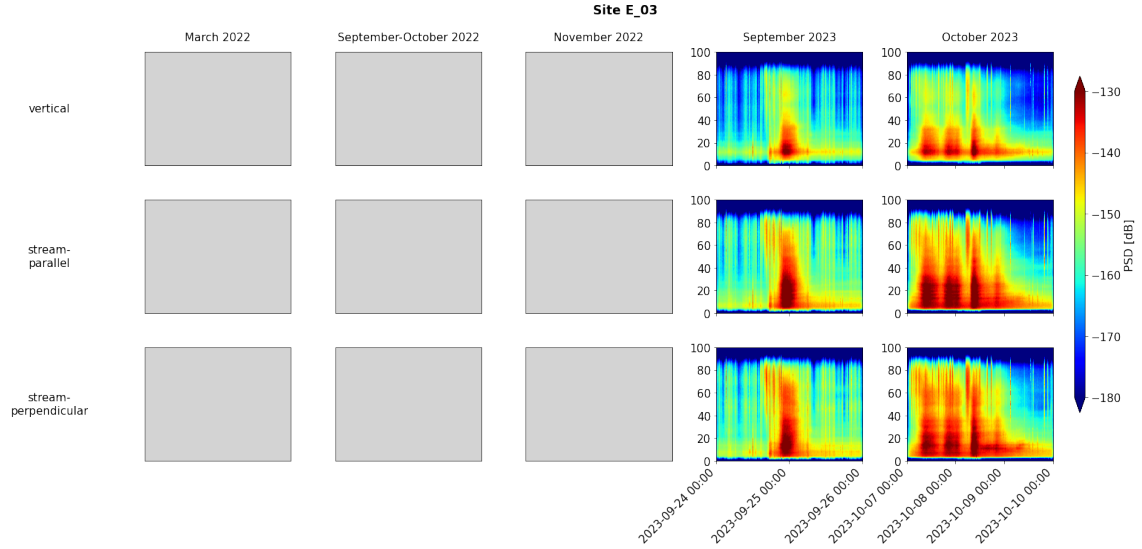


Figure 4.15: Spectrograms of seismic data from site E_03 during all five selected events. One event is shown per column with each row containing a different directional component. Sites that did not record are shown as blank plots.

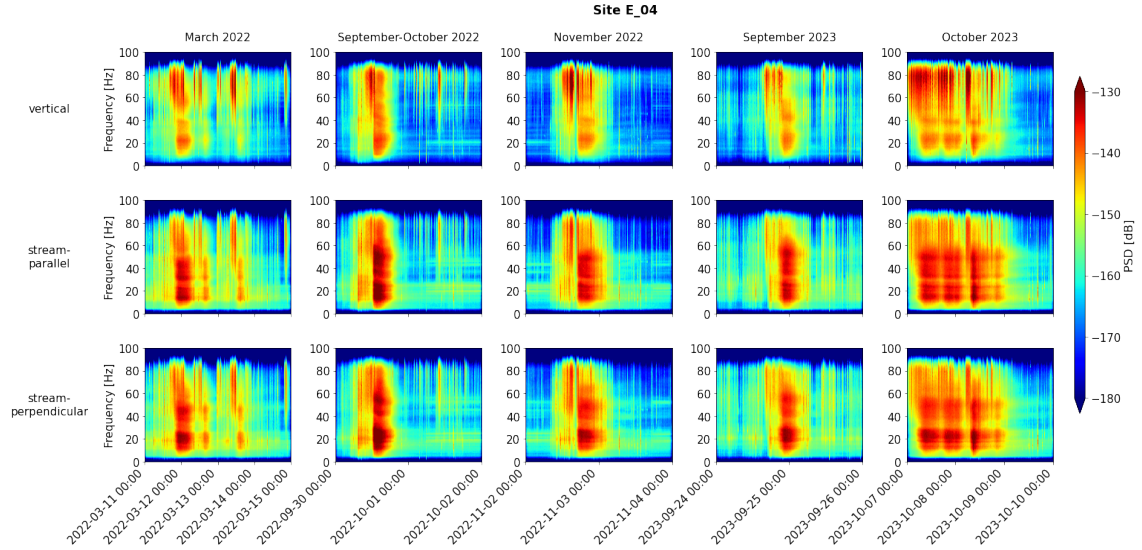


Figure 4.16: Spectrograms of seismic data from site E_04 during all five selected events. One event is shown per column with each row containing a different directional component. Sites that did not record are shown as blank plots.

good correlation between increased seismic power and rising water levels, but the exact frequency characteristics differ. The March 2022 event features a somewhat continuous signal at 10-50/60 Hz over the four-day period, with increased power in this band during hydrograph peaks. There is also some high-power signal at higher frequencies (60-80 Hz) during high water levels, but it is not present for the entire duration. In contrast, the November 2022 event shows a weak constant signal at 10-35 Hz across all three components, which increases in power during the period of increased water level. An additional high-power seismic energy band at around 40-80 Hz appears only during hydrograph peaks, most clearly in the two horizontal components. The November 2022 event also has a much sharper onset of the high-power signal as water levels rise compared to the March 2022 event, with a more gradual reduction in power during the falling limb of the hydrograph. Both events exhibit short-duration broadband signals prior to the water level increase.

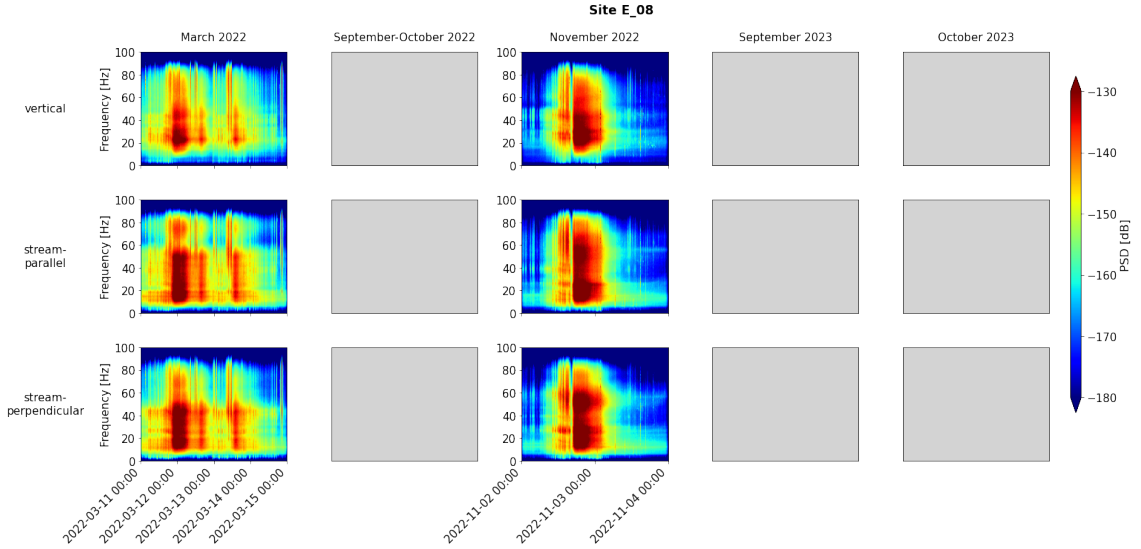


Figure 4.17: Spectrograms of seismic data from site E_08 during all five selected events. One event is shown per column with each row containing a different directional component. Sites that did not record are shown as blank plots.

4.3.4.1 Event Comparison Summary

Across all events and sites, seismic signals exhibited consistent patterns correlating with changes in water levels. Higher frequency signals (40-85 Hz) were prominent during water level peaks above approximately 0.8-1.1 m, and broadband short-duration peaks in seismic power were clearly observed for all events and across all sites prior to the rise in water levels. In the March 2022 and October 2023 events, broadband streaks were also seen prior to the successive peaks in water levels.

The September-October 2022 event, the largest in terms of water level, displayed the greatest increase in seismic power during the peak, with a very abrupt onset of high frequency seismic activity as water levels exceeded 0.8-1.1 m. In comparison, the other events, being of similar water level magnitude to each other, exhibited similar seismic power responses. The March 2022 event showed a more gradual onset of seismic power, with increases correlating with the steady rise in water levels prior to the first and largest peak. Conversely, the October 2023 event demonstrated incremental increases in seismic power with each successive peak, reflecting the largest peak occurring last.

These consistent patterns across all sites highlight the strong correlation between seismic power and hydrodynamic activity. High-frequency signals (40-85 Hz) appeared to onset only during peaks in water level above approximately 0.8-1.1 m, emphasising the close relationship between seismic signals and changing river dynamics.

4.3.5 Seismic and hydroacoustic signal frequency content

Using co-located seismic and hydroacoustic data from site W_07 during each of the five events analysed we can compare the frequency content of the signals at different water levels (Figures 4.18 and 4.19). Using the audio hydroacoustic files, periods of bedload transport and non-transport were classified. These classifications enable the analysis of both seismic and hydroacoustic signal variations during bedload movement and periods of just flow turbulence. Although the hydrophone at site H1

recorded all five events, it experienced issues causing significant instrument noise. This noise was mildly heard and observed in three events but was very pronounced in two events. Despite the strong noise in these two events, they could still be distinguished through audible analysis. However, plotting the frequency content of the hydroacoustic signals for these events revealed little information, as the instrument noise overshadowed the subtle audible observations. In Figure 4.19 the seismic and hydroacoustic data is included for all five events. I have calculated the seismic and hydroacoustic power spectrum density (PSD) for selected water levels on the rising and falling limbs, as well as the peaks of the events (Figure 4.18), based on the manual classification of hydroacoustic data indicating whether bedload is being transported or not. The chosen water levels for each event are consistent for both seismic and hydroacoustic data to facilitate easy comparison. These PSD figures also enable comparison with the expected outputs of the 'eseis' package models, as discussed in section 4.3.1.

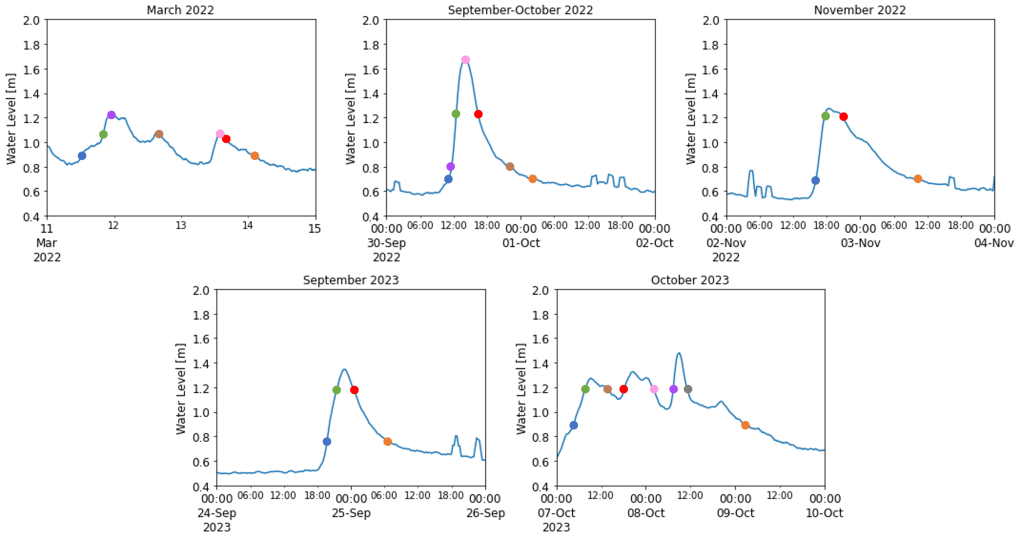


Figure 4.18: Hydrographs of the five high flow events showing the points at which the PSD values are calculated. The colours of the dots for each event correspond to the colours of the PSD lines in Figure 4.19.

The March 2022 event consists of three water level peaks (Figure 4.1). I have therefore chosen a water level on the rising and falling limb prior to and after the three peaks where bedload transport is not occurring, as well as a water level on both limbs where bedload is being transported. In addition to this I have included the PSD values for the maximum water level of all three peaks. The seismic signals during the March 2022 event (Figure 4.19a) reveal that the seismic power for periods where bedload transport is occurring (red, purple, brown and pink) is greater than that for periods when there is no bedload transport occurring (blue and orange lines). Additionally, although the periods with and without bedload transport all show a peak in seismic power at around 10-30 Hz, the signals during periods of bedload transport also show a smaller peak in power at around 40-60 Hz. The first (and largest) water level peak of the event shows a stronger seismic signal across the full frequency range. The hydroacoustic data in Figure 4.19b does not permit a useful comparison between the recordings. This is because, for unknown reasons, the hydrophone data logger recorded data at varying amplitude gain levels throughout the event. Consequently, the hydroacoustic data files at the selected water levels were recorded at different gain levels. This variation led to recordings at higher gains

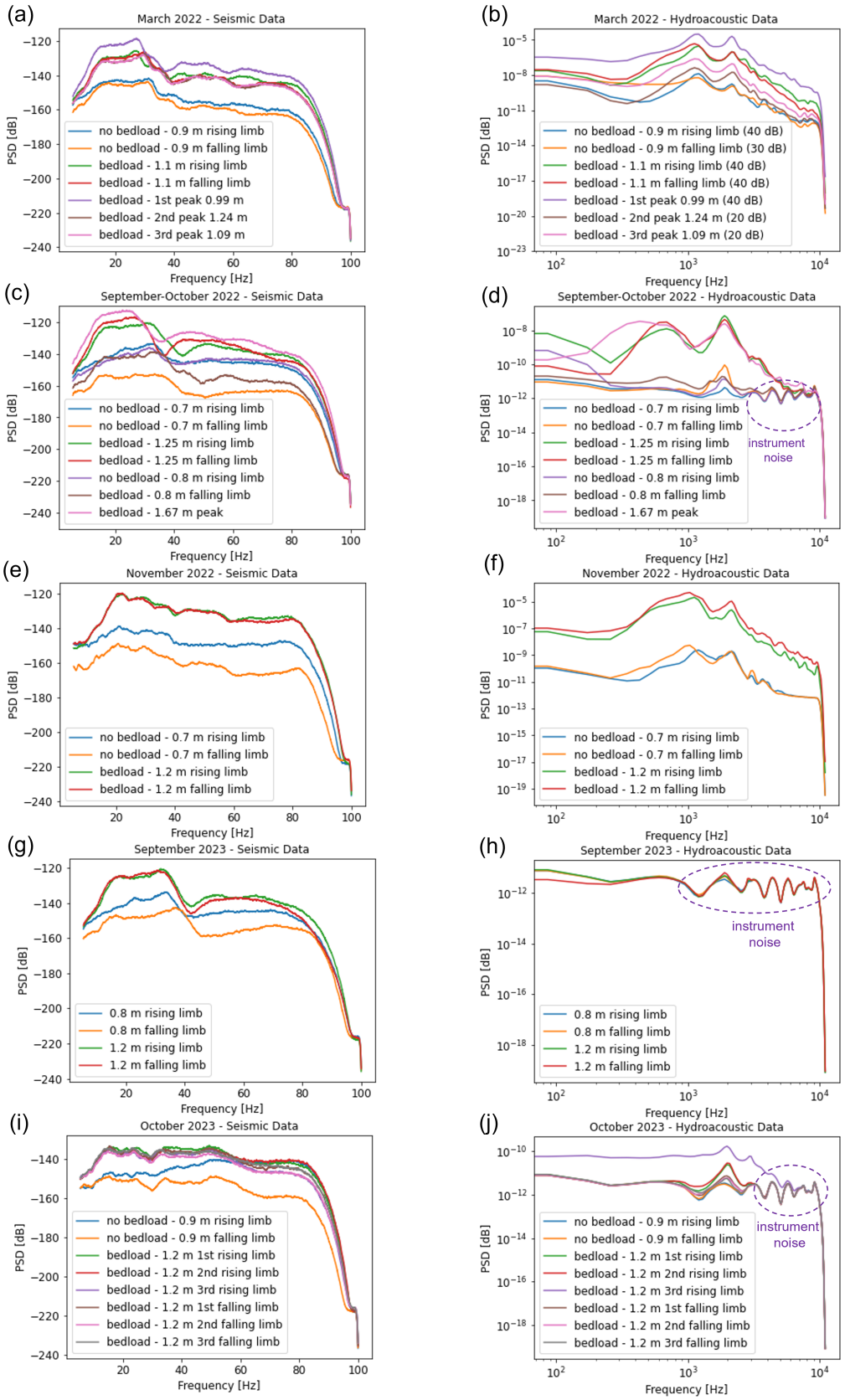


Figure 4.19: Seismic and hydroacoustic Power Spectral Density (PSD) plots during the five selected high flow events showing the frequency content of the signals during periods when bedload is and is no being transported. The line colours for each event correspond to the dot colours in Figure 4.18. The hydroacoustic data for the March 2022 event in (b) is labelled with the gain value the data logger recorded at.

showing preferentially higher power levels, thereby complicating direct comparisons between the signals. This only occurred for the recordings during the March 2022 event.

During the September-October 2022 event the hydroacoustic classifications revealed that there was difference in bedload entrainment thresholds on the rising and falling limb of the event with bedload transport identified at 0.8 m on the falling limb but not on the rising limb. This behaviour is explored further in Chapter 5. Figure 4.19c and d include variations in the power of the seismic and hydroacoustic data across water levels on the rising and falling limb at which bedload transport did and did not occur, as well as at the peak of the event. The seismic signals at the lower water levels (0.7 m and 0.8 m) have less strong signals than at the higher water levels (1.25 m and 1.67 m), with lower water levels showing a dominant frequency peak at around 20-40 Hz (Figure 4.19c). The seismic signals on the rising limb (blue and purple lines) are higher than those on the falling limb, and may be a result of the broadband signals prior to the large increase in water level (Figure 4.6). The seismic signal of bedload at 0.8 m on the falling limb (brown line) has greater power than that for no bedload at 0.7 m on the falling limb (orange line) with an additional small peak in power at around 50-60 Hz. The signals at 1.25 m on both the rising and falling limbs and at the event peak are very similar with two broad peaks at 10-30 Hz and 40-60 Hz. Looking at the hydroacoustic data in Figure 4.19d, there is a similar pattern observed to the seismic data with the bedload transport at larger water levels (green, red and pink lines) showing stronger hydroacoustic signals than those at lower water levels when bedload was not being transported. Interestingly, the period of bedload transport at 0.8 m on the falling limb is very similar to the periods of no bedload transport. All hydroacoustic signals reveal a bimodality with two peaks at around 800 Hz and 2000 Hz, with the peaks being more pronounced for the bedload transport signals at higher water levels. At very high frequencies all signals align and follow an oscillating pattern. This has been interpreted to be instrument noise as discussed earlier based on the audible high frequency clicking sounds that can be heard.

The November 2022 event reveals similar seismic and hydroacoustic data to the previous two events analysed with the periods of bedload transport resulting in stronger signals in both sets of data (Figure 4.19e and f). The seismic data for this event again shows that the seismic power when no bedload transport is occurring on the rising limb (blue line) is greater than when no bedload transport is occurring on the falling limb (orange line) (Figure 4.19e). When bedload is being transported at 1.2 m on the rising and falling limbs the seismic power is in very good agreement. There is not such a clear change in the dominant seismic frequencies between the water levels as the red, green and orange lines show a peak at around 20-30 Hz and a smaller peak at 40-60 Hz. The blue line for no bedload transport on the rising limb doesn't reveal the 40-60 Hz increase in seismic power, but this may be a result of the masking by the broadband signals present prior to the increase in water levels. In Figure 4.19f there is a clear distinction between the hydroacoustic signals when bedload is being transported and when bedload is not being transported, with bedload resulting in stronger signals. The bimodality observed in the September-October 2022 data is also visible here in all lines plotted, with a broader lower frequency peak for the bedload transport periods.

For the September 2023 event, although it was difficult to decipher the hydroa-

coustic data audibly due to instrument noise, it was still possible. However, when plotted as frequency versus power, the instrument noise dominated (Figure 4.19h) and does not show any useful information about the individual signals. The seismic data, however, shows good agreement with the previous three events (Figure 4.19g). The seismic signals during the periods of bedload transport on the rising and falling limbs (red and green lines) are in good agreement with each other and are at higher power than periods where no bedload transport was observed. We see again that the power of the signal on the rising limb when no bedload transport was occurring (blue line) is greater than on the falling limb (orange line). All lines show a dominant peak at around 10-35 Hz, with an additional smaller peak only during periods of bedload transport (green and red lines) at around 45-80 Hz.

The final event analysed in October 2023 consisted of three water level peaks. I therefore chose to plot the PSD values for periods of no bedload transport prior to the first peak and after the third peak, as well as for periods of bedload transport during the rising and falling limbs of all three peaks (Figure 4.19i and j). Although the frequency content of the seismic signals at the chosen water levels are very similar with peaks around 10-30 Hz and 40-60 Hz (Figure 4.19i), there are some variations in the seismic power. The water levels at which bedload is being transported results in a stronger seismic signal at around -140 dB, whereas when no bedload is occurring on the falling limb of the event (orange line) the power is around -150 dB. When no bedload is being transported on the rising limb (blue line) the seismic power at frequencies of less than around 40 Hz is similar to when no bedload is being transported on the falling limb (orange line). However, at frequencies greater than 40 Hz the power during the rising limb increases and is then consistent with the seismic power observed for periods of bedload transport. This is most likely a result of the streaky high frequency broadband signals observed prior to the rise in water levels of the event (Figure 4.9). The seismic signals recorded at the maximum water levels of the three peaks of this event are all in very close agreement with each other. In Figure 4.19j, the PSD values of the hydroacoustic data are not very informative as the signals are strongly influenced by the instrument noise that is also audibly observed in the sound files. Subtle sounds of pebble movements can be heard when listening to the files but these small variations are masked in the plotted data by the instrument noise.

4.3.5.1 Comparison summary of seismic and hydroacoustic frequency content

The seismic data for each of the events revealed distinct frequency patterns that correlated strongly with periods of bedload transport identified through the hydroacoustic recordings. Hydroacoustic data were used to classify periods of bedload transport and non-transport audibly, and these classifications guided the selection of seismic data for analysis. During periods of bedload transport, seismic signals consistently displayed two peaks: a dominant peak at 10-30 Hz and an additional peak at 40-60 Hz, which was absent during periods of no transport. This two-peak signature was observed across all events highlighting the consistency of seismic data in detecting bedload movement, but was least noticeable in the smaller events. Seismic power also increased significantly at higher water levels (above 0.8-1.1 m) and showed subtle variations, such as stronger signals during the rising limbs of events.

Where the hydroacoustic data were distinguishable from instrument noise, they

resembled the seismic data, with two prominent peaks during bedload transport and a single peak during periods of no transport. However, issues like instrument noise and inconsistent gain settings in some events limited the usefulness of the hydroacoustic data for direct comparisons. Despite these challenges, where the hydroacoustic signal frequency content closely aligned with the seismic data, it emphasised the use of seismic monitoring for sediment transport. This strong correlation between hydroacoustic classifications and seismic signatures demonstrates the effectiveness of integrating both methods for detecting and analysing bedload transport in dynamic river systems.

4.4 Discussion and Conclusion

4.4.1 Distinction between bedload and turbulence induced signals

It is clear from Figures 4.3 - 4.17 that the geophones located adjacent to the river can record distinct river-induced seismic signals, with changes in seismic power coinciding with changes in water levels. Additionally, these geophones have been found to record other sources of seismic waves, such as distant earthquakes, as shown in Appendix E. The continuous strong frequency band observed in the river-induced seismic spectrograms, which is present in all events at generally around 15-40 Hz, is consistent with the estimated dominant turbulence-induced frequencies (10-50 Hz) from the 'eseis' package model outputs as well as with the results of previous seismic bedload studies, such as Tsai et al. (2012), Schmandt et al. (2013), and Coviello et al. (2018). Additionally this frequency range was observed to be a consistent peak in the seismic PSD data shown in Figure 4.19 across all five events at site W_07. Therefore, this band in the River Feshie seismic data has been interpreted as the signal from river turbulence (Figure 4.20). The fact that the power in this band also increases as the water level begins to rise above a certain value and decreases once the water level drops below the same value, reaffirms the signal as a result of turbulence as seismic noise from turbulence is expected to increase linearly with water level (Burtin et al., 2008; Hsu et al., 2011; Turowski et al., 2015).

The observed high power signal in the spectrograms along with the PSD plots at 40-80 Hz are in agreement with the outputs of the 'eseis' package model (Figure 4.2) which suggested bedload-dominant signals would be around 40+ Hz. The strong signal at 40-80 Hz which is only present during increased water levels is consistent with the results of previous studies, such as Gimbert et al. (2014), Barrière et al. (2015), and Coviello et al. (2018), in which bedload-induced seismic signals were found to be in the range of 10-80 Hz. From Figure 4.3 and 4.20 we can see that this band is active over a shorter duration than the turbulence band, starting and stopping at higher water levels than the strong turbulence signal. We therefore interpret this band to be the result of bedload-induced seismic noise. This higher frequency signal was observed in the data for all geophone sites during all events (Figures 4.5-4.17).

Although we have estimated frequency ranges in which the two processes dominate, there is a clear overlapping of the turbulence and bedload signals at 40-60 Hz (Figure 4.20). This complicates the differentiation of the two processes, making it challenging to identify a clear onset of bedload transport. In addition, the

gradual decrease in seismic power in the bedload signal over the falling limb of the hydrographic events doesn't provide a clear point that bedload motion is stopped. Therefore, calculating bedload fluxes from seismic data alone would be challenging. The delay from when the water level begins to rise to the estimated onset of bedload transport as shown in Figure 4.20, is due to the river having to reach a certain level in order the surpass the threshold of bedload entrainment. This threshold value can be affected by many factors such as the grain sizes of bedload particles present (Batalla and Martín-Vide, 2001), armouring and imbrication of pebbles on the river bed (An et al., 2018; Gomez and Soar, 2022), and the concentration of suspended sediment in the flow (Rickenmann, 1991; Quick et al., 2023). The estimated similar threshold of motion on the rising and falling limb suggests that there is no significant armouring effect and that the entrainment of particles is related to the rising water levels. These thresholds are explored further in Chapter 5 with the use of further hydroacoustic data analysis. However, Figure 4.20 includes an introduction to the use of hydroacoustic data to help in identifying the onset and cessation of bedload motion. The peach coloured arrow indicates the full duration of bedload transport as observed by listening to the audio files. It is similar to the rough estimate of bedload transport from the frequency content of the seismic signals in Figure 4.20b. Hydroacoustic data could prove a useful tool in confirming the occurrence of bedload transport, aiding in the analysis of seismic signals.

In addition to the expected frequency content of the seismic signals related to bedload and turbulence estimated by the eseis' package models, the model outputs also indicated that seismic power should be around -160 dB to -150 dB for water levels of 0.8 m with geophones positioned approximately 20 m from the river. For the highest water levels of around 1.6 m at the same distance, the expected seismic power is around -140 dB. The seismic PSDs shown in Figure 4.19 align closely with these estimates from the eseis' model, with water depths of 0.7-0.8 m at geophone W_07 (about 19 m from the river channel thalweg) resulting in seismic power around -150 dB, and water levels of 1.2 m or higher yielding seismic power of approximately -140 dB.

The high power broadband signals that occur periodically throughout the monitoring period, but are most concentrated in the few hours prior to the increase in water level, closely resemble the characteristics of signals from wind and rain as found by many studies, including Burtin et al. (2011), Roth et al. (2016), Dean (2018) and Rindraharisaona et al. (2022). Rainfall and wind were identified to exhibit similar seismic signal characteristics with short durations and broad frequencies in the range of 10-100 Hz (Burtin et al., 2011; Burtin et al., 2013; Dietze et al., 2017) with some studies finding signals as low as 2 Hz and others observing signals up to 500 Hz (Roth et al., 2016; Rindraharisaona et al., 2022). Wind and rain produce signals with overlapping characteristics which makes it difficult to differentiate them. Rindraharisaona et al. (2022) additionally found that the burial depth of the seismic sensors has an impact on the amplitude of the seismic signals from rain observed as does the soil type, with greater signal attenuation with increasing burial depth and larger soil grain sizes. The clustered signals prior to the increases in water level in the data in this chapter are most likely dominated by rainfall as, in the absence of snowmelt, rain must necessarily precede rising water levels. There is a lag between the rainfall and the increased water levels which is most likely a result of infiltration effects and surface runoff in the catchment. However, due to the Feshie catchment

having impermeable headlands and high rates of surface runoff from saturated peaty soils, the river responds relatively quickly to the input of rain water.

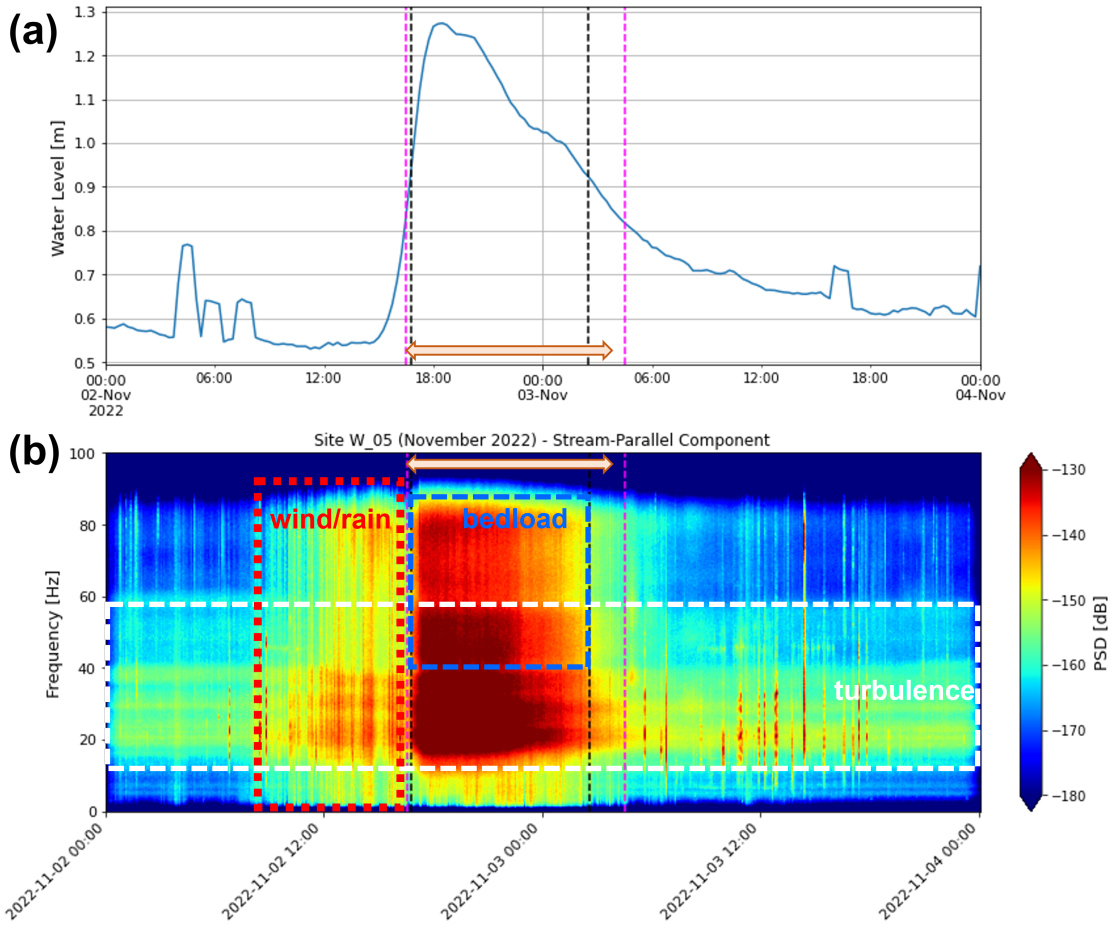


Figure 4.20: Same figure used for Figure 4.3 with labels highlighting the interpreted sources of the different seismic contributions to the signal. The bedload and turbulence frequencies are shown to overlap between 40 Hz and 60 Hz, as discussed in the text. The pale peach arrows highlight the period of observed bedload transport from the hydroacoustic audio files.

These general characteristics were evident in the recordings from all geophone sites, though the clarity of the distinction between bedload and turbulence varied by site, and wind and rain signals were stronger at some locations. Typically, the turbulence signal was observed between 10 Hz and 40 Hz, with slight variations at sites like W_03 and W_05. Additionally, the bedload signal generally extended from the upper end of the turbulence range, with some overlap, reaching up to around 70-85 Hz depending on the site.

4.4.2 Site and event comparisons

It was observed in Figures 4.5-4.17 that there is more variability in the signals between the sites for the same event than there is between the events recorded at the same site, i.e. inter-site variability is greater than inter-event variability. Although the signals of different events at one site varied slightly from each other, this was due to the nature of the high flow event such as the magnitude and duration. The overall characteristics at one site remained similar across multiple events, such as the abrupt onsets and gradual terminations of the interpreted bedload transport

signal and the dominant frequencies of bedload (40-80 Hz) and turbulence (15-40 Hz). However, when comparing the variability between sites for a single event there is a large variation in the seismic signal characteristics.

Since the distance between the river and the river-adjacent geophone sites are all less than 30 m, going by the R 'eseis' package model outputs it would be expected that there would not be a significant change in the power and frequency of the recorded signals. Slight changes in distance may cause small variations in these signals but they would not be expected to be significant. This was observed in the data with all geophone sited close to the river showing broadly similar seismic signal characteristics in terms of frequency and power (Figures 4.5-4.9). The frequency ranges of the interpreted bedload and turbulence signals were broadly similar across all sites within 30 m of the river, but those sites located slightly further back from the river (i.e. W_04, E_04, E_08) recorded weaker high frequency signals with the bedload component only reaching maximum frequencies of around 70-75 Hz rather than 80-85 Hz (Figures 4.12, 4.16 and 4.17). This is consistent with the 'eseis' package model estimations and the attenuation analysis from the seismic refraction survey (section 3.2.5) where the seismic power and frequency decreases as the distance between the source and receiver increases. Site E_06, the control site, provides further evidence of this amplitude and frequency attenuation effect with distance since the site is located approximately 300 m from the river. From the 'eseis' package model it was expected that the signal from the river would drop in power to around -180 dB to -160 dB and the peak frequency of both the turbulence and bedload signals would shift down to 5-10 Hz and 10-20 Hz, respectively. From the spectrograms of the seismic data at site E_06 (Figure 4.10) it is clear that the geophone records very little evidence of a clear river-induced signal and that the local meteorological signals dominate this site. The distance the waves have had to travel through the earth has filtered them and caused attenuation of the signals by the time they reach the geophone. This emphasises the use of this site as a control site, as it records minimal river-induced ground vibrations.

W_03 showed the noisiest signal of all sites with evidence of resonant frequency bands, and is probably due to the site locality (Figure 4.11). It is interpreted that the very steep slopes composed of loose glacial till with a very thin layer of soil on top could increase the scattering of seismic waves as well as cause resonant frequencies due to the vibration of the till deposits. Despite the effect of topography on ground motion not being very well understood, Geli et al. (1988) found that on hill tops there was a significant amplification with respect to the base and that hill sides show very complex amplification-deamplification patterns of seismic signals. Sites W_04 and W_05 provide a good opportunity to analyse the effects of elevation above the river bed on the recorded seismic signals, since W_04 is at a similar horizontal distance from the river but is at a greater elevation. Unfortunately, there was only one event in which both these sensors recorded: the September-October 2022 event. In this event it appears that there is a generally stronger signal with stronger higher frequencies recorded at W_05 than W_04, but other than that the signals look very similar (Figure 4.6). The reduced seismic power and high frequency signal at W_04 could be due to attenuation of the signal or scattering effects due to topographical features, however without further analysis over multiple events it is hard to conclusively say.

Comparing the sites that are located on the flat floodplain close to the river

(W_05, W_07, E_03, E_04, E_08) against those located up steep banks (W_03, W_04) it appears that there are generally clearer distinct interpreted turbulence and bedload frequency bands at those sites on flatter ground. This is particularly clear for sites E_04, W_05 and W_07 during the September-October 2022 event (Figure 4.6) where there is a distinction between a roughly 15-40 Hz frequency band and a 40-80 Hz frequency band, particularly in the stream-parallel and stream-perpendicular components. This may likely be a result of a more direct path from source to sensor without abrupt slopes and boundary layers to influence signal scattering. Unfortunately, due to a lack of events in which all geophones were recording it is hard to provide a deeper analysis of the influence of the elevation of the sensor above the river bed on the seismic signals observed. From the data that is available, it would appear that geophones located close to the river (within approximately 30 m) on flat ground with a thick soil layer, like W_05, W_07, E_04 and E_08, provide the signals with the clearest distinct frequency bands and may be best suited for differentiating the turbulence and bedload induced seismic signals.

Interestingly, sites W_03, E_04 and E_08 showed the strongest meteorological signals from wind and rain. These three sites were located among taller vegetation and small trees, which would be expected to increase the signals from wind (Johnson et al., 2019) due to wind-induced motion in the vegetation propagating into the ground, but decrease the signal from rain due to the ground surface being protected by a canopy layer (Dietze et al., 2017). On this note the wind signals would be expected to be more dominant in the horizontal directions due to the swaying nature of vegetation and the longitudinal profile of wind (Johnson et al., 2019), and rain would be expected to have greater vertical dominance due to the vertical direction of rainfall as a result of gravity (Bakker et al., 2022). This was not observed in this data, and generally the vertical component was weaker than the horizontal components at all sites across all events. Even at control site E_06, the signals were weakest in the vertical direction. However, even in the areas where it was more open and not surrounded by trees and shrubs, the ground was still covered by heather or tall hummocky grass which creates a barrier for rain to reach the ground surface, possibly dampening the signal (Dietze et al., 2017). This may also influence the strength of the horizontal wind signals recorded due to the swaying of small shrubbery (Johnson et al., 2019).

4.4.3 Remaining challenges in seismic monitoring of bedload transport

There still remains challenges in interpreting bedload-induced seismic data due to the interference of other sources of seismic noise such as turbulence, wind, rain and anthropogenic signals, which overlap the frequencies of bedload transport. This makes it very difficult to identify a clear bedload-induced signal and accurately record the onset and termination of bedload motion, meaning much of the fluvial seismology work remains partially subjective. Combining seismic measurements with other methods of monitoring bedload transport, such as hydroacoustics, to provide independent evidence of bedload motion would be beneficial to overcome this challenge. Additionally, current seismic bedload transport studies have primarily focused on the analysis of the vertical component of signals due to the assumption that the dominant waves produced by bedload impacts will be Rayleigh waves which

include a vertical directional component (Tsai et al., 2012). However, the results here show that there is some richness in the horizontal data that may shed some light on specific transport processes at play or provide more accurate estimates of bedload fluxes. These challenges will be addressed in the following two chapters in which I look at the use of combining independent hydroacoustic and seismic measurements to monitor bedload entrainment thresholds, and analyse the differences in the three directional components to identify whether one contains a stronger bedload transport signal than the others.

Chapter 5

Inferring bedload transport thresholds through seismic and hydroacoustic recordings

The content presented in this chapter has been accepted into the scientific journal Earth Surface Processes and Landforms (ESPL): Matthews, B., Naylor, M., Sinclair H., Black, A., Williams, R., Cuthill, C., Gervais, M., Dietze, M., Smith, A. (2024). Sounding out the river: Seismic and hydroacoustic monitoring of bedload transport. Article DOI: 10.1002/esp.5940. The manuscript has been reviewed and is currently being prepared for publication. The accepted manuscript is included in Appendix F.

To overcome some uncertainty in identifying the onset and arrest of bedload transport from the seismic data as presented in chapter 4, here independent hydroacoustic analysis of the occurrence of bedload transport is used. The material in this chapter has been edited from the accepted manuscript in Appendix F. This research was conducted in collaboration with the named co-authors. Fieldwork and data collection was carried out over the course of my PhD (2020-2024) by myself, with assistance from mainly Mark Naylor, Hugh Sinclair, and Matt Gervais. Additional fieldwork support was provided by Richard Williams, Michael Dietze and Calum Cuthill, with several others attending odd days of fieldwork, either for personal or professional interest. All data processing and analysis was conducted by myself with guidance from my supervisors. I took the lead on the manuscript writing and wrote the initial draft, with subsequent comments and edits made by co-authors. Additional data and analysis is included in this chapter that was not included in the paper due to length restrictions for ESPL and in an aim to keep the paper more focused. I believe it is important analysis for the story of my thesis and so have included the information in this section. An in-depth site overview, fieldwork and data processing is not given here as these are described in depth in Chapter 3. All figures in the published manuscript are included in this chapter along with some extra figures to complement the additional analysis included here.

5.1 Introduction

The dynamic nature of sediment movement in river systems makes monitoring and measuring the transport of coarse bedload challenging, particularly as rivers erode,

aggrade and shift their course. One of the key challenges lies in accurately measuring the onset of entrainment of bedload in the water column, and the mobilisation of larger-scale bedforms such as braid bars. Variations in entrainment thresholds are determined by metrics such as particle shape and size distribution (Wilcock and Crowe, 2003; Jain et al., 2021), bedforms (Church et al., 1998), sediment cohesion (Kothyari and Jain, 2008), and changes in grain size between the bed surface and subsurface where coarse sediment may act to armour the river bed (Lisle and Madej, 1992; Jain et al., 2021). Using flume tank experiments it has been demonstrated that variations in these characteristics respond to durations and frequencies of moderate to peak discharge conditions (Ockelford et al., 2019; Luo et al., 2023). The grain-size distribution may be modified at the bed surface by winnowing of finer grains resulting in the formation of an armoured surface layer of coarser grains (Pitlick et al., 2009; Gomez and Soar, 2022). This armouring modifies the onset of bedload entrainment complicating the relationship between the measured grain-size distribution and the entrainment threshold. A further complication to the measurement of bedload transport are hysteresis patterns, where sediment transport rates do not have a linear scaling with the flow conditions (Bogen, 1980). Armouring is an example of a process that could result in hysteresis in bedload transport as it may increase the threshold for sediment motion on the bed causing the rising and falling limbs of a flood hydrograph to have different threshold entrainment values. The mobilisation of coarse bedload can also be influenced by the suspended sediment concentration at the sediment water interface (Rickenmann, 1991; An et al., 2018). Suspended sediment loads are commonly higher during the rising limb of flood hydrographs that also results in different entrainment thresholds on either side of a flood. Such non-linear and thresholded behaviour makes it difficult to predict the timings and intensity of bedload transport. Another potential factor driving hysteresis is the history of large events that reshape the riverbed and modify the critical shear stress for subsequent events (Turowski et al., 2011; Masteller et al., 2019). The variables determining entrainment thresholds, as mentioned above, are also reflected in the variation of dimensionless critical shear stress values for median grain sizes across different settings (e.g. Buffington and Montgomery, 1997).

Addressing these challenges requires innovative site and reach-scale measurement techniques, geomorphological and hydrological field observations, and sediment transport modelling to gain a more comprehensive understanding of bedload transport dynamics, and the interplay between sediments, flow dynamics, and riverbed characteristics. However, since coarse bedload is mobilised when rivers are at high flow, logistical challenges are introduced when using many measurement techniques. Traditional methods of monitoring bedload transport in rivers, such as sediment sampling, sediment traps, grain size analysis and flow measurements, have typically relied on direct field measurements and observations. However, these approaches come with several limitations: sediment sampling and flow measurements can be labour-intensive, time-consuming, and difficult at high flows, while sediment traps (although continuous in measurement) are prone to errors due to bedload particles bouncing over or around the traps, and are subject to damage during high flows (Brasington et al., 2003; Bunte et al., 2004; Bunte and Abt, 2005; Thorne, 2014). These traditional methods struggle to capture the full complexity and natural dynamics of bedload transport, as they are typically performed during mild hydrologic events, over short timescales, and during daylight hours. They also gen-

erally only measure at a single point in space, while bedload transport occurs along cross-sections with potentially variable transport at individual points in space. As a result, they may not provide sufficiently representative data needed for effective river management, infrastructure design, or understanding sediment transport patterns. Engineers often use numerical models or empirical equations as alternatives to traditional methods for forecasting bedload transport (Geay et al., 2020). However, simplification of these empirical equations relative to complexities of natural bedload transport processes in rivers, and the challenge of estimating grain size distribution, entrainment thresholds, and bed morphology among other factors, results in considerable uncertainties in the sediment transport estimates (Dey, 2014; Downs et al., 2016).

Modern technologies and advanced measurement techniques are increasingly being employed to address these limitations and provide more precise insights into bedload transport dynamics. Several recent studies have explored the potential for seismic sensors (such as geophones) to be used to monitor environmental and geomorphic processes (e.g. Burtin et al., 2008; Roth et al., 2016; Dietze and Gimbert, 2019; Lagarde et al., 2021). Geophones, which are typically used for seismic studies, have important applications in the field of bedload transport monitoring. Previously, geophones have been strategically deployed in riverbeds or on river banks to capture the ground vibrations caused by bedload particles interacting with the river bed. These vibrations can be analysed to estimate the timings, intensity and frequency of bedload transport in rivers. This innovative use of geophones provides a non-intrusive and continuous monitoring method that overcomes some limitations associated with traditional bedload measurement techniques, facilitating the monitoring of bedload transport under conditions that were previously not possible (Burtin et al., 2010). Geophones record a range of environmental signals that are filtered by their passage through the earth. The potential sources for these signals include precipitation, wind, tides, traffic, turbulent motion in rivers, and the impact of bedload on riverbeds (Wilcock et al., 1999; Burtin et al., 2008; Rindraharisaona et al., 2022). Previous studies have focused on the frequency characteristics of seismic energy to discriminate different sources of seismic noise (Burtin et al., 2008; Burtin et al., 2014; Gimbert et al., 2014). The key discrimination for river induced seismic signals is between coarse bedload transport and water turbulence. It has been suggested that bedload transport induces broadband higher frequency seismic waves than the continuous signal from river turbulence (Schmandt et al., 2013; Gimbert et al., 2014; Vore et al., 2019).

By correlating the bedload induced seismic data with river discharge, crucial insights have been gained into the dynamics of sediment transport and how it responds to variations in hydraulic characteristics. Many studies found a hysteretic relationship between these parameters which has been interpreted to be evidence of bedload transport, as significant hysteresis is not expected in the relationship between river stage and turbulence (Burtin et al., 2008; Hsu et al., 2011; Schmandt et al., 2013; Turowski et al., 2013; Roth et al., 2014; Chao et al., 2015; Roth et al., 2016; Roth et al., 2017), and sediment motion during flood events is often characterised by different transport rates on rising and falling limbs (Mao, 2012). As outlined above, factors like particle size, shape and bed structure can influence the initiation of bedload transport in rivers, such that sediment entrainment thresholds may vary relative to changes in flow conditions. Bedload transport may even

continue after the water level has begun to decrease, or may initiate and cease at different levels, since it takes time for particles to be entrained or re-deposited based on the local hydraulic conditions. Additionally, threshold effects due to contact and friction cohesion can influence particle movement, requiring higher shear stresses to initiate transport and causing lagged responses in sediment mobilisation, leading to complex and hysteretic transport dynamics. The interpretation of hysteresis in bedload transport data has become a foundational assumption for many fluvial seismic studies, with some studies reporting a clockwise pattern of hysteresis where bedload transport peaks before the peak in water level, and some recording an anticlockwise pattern where the peak in water level occurs prior to the peak in bedload transport. Clockwise patterns are associated with readily available sediments, often due to increased sediment supply from upstream sources, which enhances transport capacity and allows sediment to be mobilised earlier in the event (Reid et al., 1985; Kuhnle, 1992; Hassan et al., 2006; Gaeuman, 2010; Mao, 2012; Mao et al., 2014), while anticlockwise patterns are thought to be caused by processes that increase sediment supply after a flood peak or from the formation of armour layers, which restrict sediment availability (Reid et al., 1985; Kuhnle, 1992; Lee et al., 2004; Mao et al., 2014). Factors such as changes in bed packing can either cause clockwise or anticlockwise hysteresis, depending on whether it makes material more exposed or less available for transport. These previous studies have shed light on the invaluable use of geophones for bedload monitoring purposes, however they generally had little independent data to constrain when bedload was being transported. Additionally, the reliability of hysteresis interpretations in previous studies are difficult to prove due to partial or total lack of in situ information.

In order to test some of these assumptions used in interpreting geophone data, we combine geophones with hydrophones to independently classify when coarse bedload is transported. Hydrophones are typically used to detect and record underwater sound, making them particularly useful for applications in the fields of marine biology, underwater communication, and sonar systems (Ballance et al., 2023; Bountourakis et al., 2023). In contrast to geophones, hydrophones can record all particle collisions within the local river channel – collisions between particles and the bed, as well as inter-particle collisions. However, it is more logistically difficult to deploy them routinely as they have to be placed within a river water column for the duration of the measurements, thus requiring careful methodological approach and appropriate housing to protect the instrument during high flow events. On an event-by-event basis they can provide independent data to validate the seismic bedload transport information obtained from geophones and to test whether hysteresis in the relationship between the fluvial seismic signal and water level is in fact a fingerprint of bedload transport.

Here, we use co-located hydrophones to test the application of geophones in characterising the onset of coarse bedload transport, and the presence of hysteresis during the passage of a flood hydrograph. Our study determines bedload mobilisation thresholds and evaluates the influence of antecedent events through independent seismic and hydroacoustic characterisations. By integrating seismic, water level, and hydroacoustic data we aim to gain insights into bedload transport thresholds, examine hysteresis patterns, and shed light on the intricate relationship between flowing water and sediment. Our analysis focuses on a relatively stable section of the gravel-bed River Feshie (Figure 5.1) and analyses seismic signals from the three largest

flow events in 2022. This enables the consistency of bedload transport entrainment thresholds to be examined and explored, and the effects of antecedent events on the thresholds observed. Our findings will contribute to more informed decision-making in river systems management and environmental protection, by constraining entrainment thresholds and hence enabling calculations and model estimations of sediment mobility in the channels.

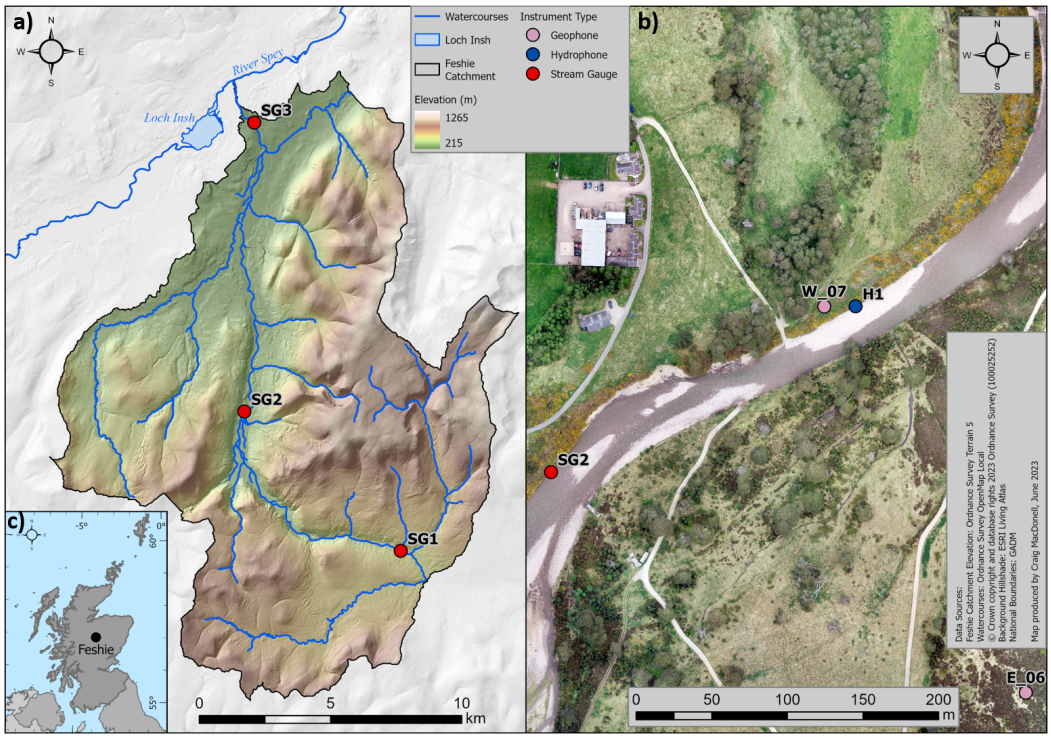


Figure 5.1: Maps of the River Feshie fieldsite at the (a) catchment scale showing the three stream gauge sites, (b) reach scale showing the sites of instruments used in this study, and (c) national scale. Photos of the field deployments can be found in Chapter 3.

In the late 1970s a stream gauge was maintained in the same stretch as our study site by Ferguson and Werritty (1983) and recorded a mean flow of 3-4 m^3s^{-1} with regular floods reaching 20-30 m^3s^{-1} and the largest floods recorded exceeded 100 m^3s^{-1}. A stream gauge that is currently located approximately 12 km downstream at Feshiebridge (SG3 in Figure 5.1), maintained by SEPA (Scottish Environment Protection Agency), records the same variable flow regime with peak flows exceeding 100 m^3s^{-1} and a maximum of 260 m^3s^{-1}, likely due to the more confined channel and increased tributary input along the river. From flow data over the last 7 years at Feshiebridge (SG3) (Figure 5.2) it can be seen that there are generally larger flows occurring during winter and spring. Flow patterns of 2022 were generally similar to previous years with low flows during summer and larger peaked flows in spring, autumn and winter. Summer flows in 2022 were particularly low, and were bounded by large events in early spring and autumn. The largest event of 2022, which we use for this analysis, peaked at around 138 m^3s^{-1}. Prior to this there had only been six other peaks that exceeded this level over the 7 years (Figure 5.2); the largest of these occurring in December 2015 as a result of Storm Frank that caused widespread flooding across much of Scotland, Northern England and Wales (Barker et al., 2016).

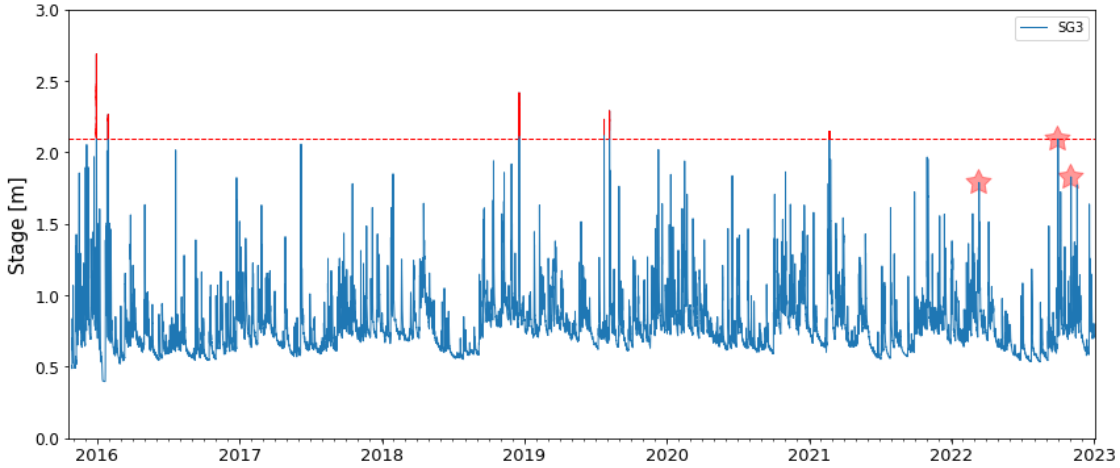


Figure 5.2: Stage measurements from SEPA stream gauge at SG3 from 27th October 2015 to 31st December 2022. Red stars mark the three largest events in 2022 that are analysed in this study. Red line marks the water level of the largest event in 2022, with peaks that have previously exceeded this value also marked in red.

5.2 Methods

5.2.1 Data collection

5.2.1.1 Stream gauge data

This study uses water level (stage) measurements recorded at three stream gauge sites on the River Feshie. To measure water level at our study site, we deployed a LiDAR (Light Detection and Ranging) water level sensor on the remains of a footbridge at site SG2 which takes repeat measurements of the distance to the water surface every 5 minutes. Using this data combined with channel geometry measurements, we have been able to convert to discharge values, however we will be using stage data in this analysis as it is more accurate measured data. We also have access to water level and discharge data collected every 15 minutes at stream gauges SG1 and SG3, located approximately 10km upstream and downstream of our site (Figure 5.1). These data are managed by Dr Andrew Black (University of Dundee) and SEPA, respectively. We use the SEPA data as the historic record since our local sensor has only been operational since the end of 2020.

The three events analysed in the published manuscript occurred on the 11th - 14th March 2022 (three successive peaks with a maximum water level of 1.27 m at SG2), 30th September - 1st October 2022 (one peak with a maximum water level of 1.69 m at SG2, a roughly once-in-a-year event), and 2nd - 3rd November 2022 (one peak with a maximum water level of 1.30 m at SG2). These events are herein referred to as the 'March 2022 event', the 'September-October 2022 event', and the 'November 2022 event', respectively. The March 2022 event follows a series of snowmelt cycles that caused three repeated peaks in water level, resulting from rainfall on snow combined with snowmelt and reaches a peak discharge of 84 m^3s^{-1} at the SEPA station SG3. The larger September-October 2022 event is of a shorter duration and occurs following intense precipitation in the catchment that coincides with the tailend of Hurricane Fiona that hit Canada in mid-late September 2022, resulting in peak discharge of 131 m^3s^{-1} at SG3. The November 2022 event is an early winter storm with similar magnitude to the March 2022 event, however it occurs as a result of high rainfall alone, reaching peak discharge at 90 m^3s^{-1}. The three peaks

in the first event allow us to test the consistency of the onset of bedload, the second event allows us to explore the impact of a large event on these thresholds of motion, and the final event allows us to explore the new behaviour of the river after a large event. Thus combining data from successive high flow events demonstrates how the technique can be used to make inferences about the effects of antecedent events on the mobilisation of bedload.

In addition to the three events of 2022 analysed in the ESPL manuscript, here I include the analysis of some 2023 data which was collected and analysed after the manuscript was initially submitted. 2023 was a quiet year hydrologically speaking with only a couple high flow events occurring. Here, I include the analysis of the largest event of the year that occurred on the 7th - 9th October, described in detail in Chapter 4. This event was larger than the March and November 2022 events of 2022 but approximately 20cm smaller at the peak than the September-October 2022 event of 2022 (recorded at SG2). However, the single event comprised of three successive peaks of increasing magnitude (see Figure 4.1), similar to the March 2022 event although this event was not a result of snowmelt or rain on snow - this was a rainfall induced event. Since the water levels remained high between the peaks and did not return to the levels prior to the first peak, all three were included in one event. The first peak occurred at 08:45 on the 7th October 2023 peaking at 1.28 m, the second peak occurred at 20:15 on the 7th October peaking at 1.34 m, and the third and largest peak occurred at 08:30 on the 8th October peaking at 1.49 m. Due to it being solely a rainfall induced high flow event the hydrograph has quite a steep rising limb and a more gradual falling limb following the largest peak. Having this additional event in 2023 allows us to compare the threshold of transport and nature of sediment transport with the successive 2022 events.

5.2.1.2 Seismic and hydroacoustic data

This study integrates seismic and hydroacoustic data to study the mobilisation and transport of bedload along a short (∼100 m) stretch of the River Feshie (Figure 5.1). We use the co-located stream gauge sensor (SG2) to analyse the water level dependence of the seismic and hydroacoustic data.

For all events, we compare data from 3-component PE6B (4.5Hz) geophones connected to Digos DataCube loggers recording at a sampling rate of 200 Hz (additional details can be found in Chapter 3). The geophone data is continuously recorded. The geophones are buried in soil at approximately 10 cm depth (base of instrument to surface), levelled and oriented with the North-South (horizontal) component aligned along the downstream river direction. For the 2022 events we directly compare two geophones. The geophone at site W_07 is located within approximately 5 m of the river and 1 m above the base level water surface. It is well sited to record a strong river signal as the small source-to-sensor distance minimises the attenuation of high frequencies, which is important for this study as we are wanting to resolve frequencies of bedload transport (Figure 5.1). The other geophone at site E_06 is located approximately 300m from the river as a control site to characterise other sources of environmental noise, such as precipitation and wind as the impact of rain on the ground and the movement of vegetation by wind can be recorded by geophones (Dean, 2018; Rindraharisaona et al., 2022). Both sites have similar geology with high-velocity Moinian schist bedrock overlain by low-velocity glacial till. Signals which are common to both W_07 and E_06 we identify as non-

river environmental noise, and this approach allows us to confirm that the relatively high broadband noise level prior to the water rising is due to hydrometeorological noise. Generally, seismic bedload studies have used the vertical component of seismic waves as, due to the impact direction of bedload on the river bed, it was assumed that the emitted seismic waves would be best represented by Rayleigh waves with strong vertical displacements (Tsai et al., 2012; Dietze et al., 2019). Here, we present the analysis of the stream-parallel component. This was chosen because, although using the vertical and the stream-perpendicular components for the analysis gave similar results, the vertical component tended to be noisier due to its susceptibility to rain interference (as discussed in Chapter 4) and theoretically the stream-parallel component should give the strongest river-related signal (Roth et al., 2016). This idea is explored further in Chapter 6. The area is anthropogenically very quiet with little traffic on the estate roads, and so there is minimal interference from these sources. The geophones are expected to record both the interaction of turbulence in the water with the bed and direct collisions of particles with the bed. It has previously been found that seismic waves emitted from bedload collisions resulted in higher frequencies than those from turbulence, with bedload generally found to occur in the range of 30-60 Hz and turbulence around 1-20 Hz (Tsai et al., 2012; Gimbert et al., 2014; Dietze and Gimbert, 2019).

Unfortunately, during the October 2023 event the control site E_06 had failed to record this event due to battery failure and therefore we do not have any control site data to identify periods of rainfall, but using analysis for the manuscript as baseline we are able to identify visually when these occur. Site W_07 which was used for the manuscript analysis did record, but due to the river bursting it's banks and the battery being flooded the instrument stopped working during the falling limb of the event. Thankfully, it took several hours for this effect to come into force with the battery running on residual power and so the instrument stopped recording in the early hours of the 9th October once the peak in water level had started to subside and it was already well into the falling limb. It is unclear why it flooded and stopped recording during this event but was still recording during the September-October 2022 event despite that one being larger. We were now using a new type of battery so perhaps it was more susceptible to water entering the internals of the battery. We use this site though for this analysis to compare to that found in the paper. We also include the data from two other sites, E_03 and E_04, as they are in a similar setting to W_07 on the flat flood plain. However, E_03 is located on the east bank approximately 52 m from the main channel and 10 m from a side channel that is only active during very high flows (as evidenced from timelapse imagery and visual observations), and E_04 is located about 27 m from the river on the east bank and in trees.

To independently characterise the bedload motion recorded within the study site, we deployed a hydrophone (Jez Riley French D-series) within the river at site H1 connected to our own Raspberry Pi logger, to record the hydroacoustic signal of turbulence and bedload motion. In previous hydroacoustic studies hydrophones have been deployed in metal pipes or attached to metal plates embedded in the river bed (Barrière et al., 2015), attached to the bottom of boats or river surveying equipment such as river boards (Geay et al., 2020), or attached to man-made infrastructure, such as bridges or metal frames (Belleudy et al., 2010), however these were logistically unfeasible in our study site. Instead, the hydrophone was mounted within

a roughly 40 kg (0.4 m x 0.3 m x 0.3 m) granite block with a hollow cylindrical core of diameter 0.2 m in order to protect it from damage by direct impacts from mobile material The hydrophone block is located approximately 5 m downstream of the geophone at site W_07 and 40cm from the river bank (Figure 5.1). The recording system is built using a PiZero, a Witty Pi for scheduling and a HiFiBerry DAC+ADC Pro sound card (sampling at 44.1 kHz); due to the size of the datafiles, we record a 30 second sample every 15 minutes. Data are recorded at two different gains of 30 dB and 40 dB to manage potential issues of data quality. In addition to measuring collisions between particles and the bed, like geophones, hydrophones also record collisions of particles in suspension. The hydroacoustic data is used as a complementary data set to the seismic data to confirm the occurrence and timing of bedload motion.

5.2.2 Data processing and analysis

We preprocess the seismic data, as described in Chapter 3, Section 3.4.1, by removing the instrument response through ObsPy using information provided by Digos on the specific instrument used. We then apply a bandpass filter in the frequency domain (between 4.5 Hz and 99 Hz) to the data prior to deconvolution to remove the frequencies most affected by the instrument itself. The data is then detrended to remove the mean trend of the signal using ObsPy. We computed the power spectral density (PSD) using Welch's method (Welch, 1967) with a 1-minute window and no overlap, to quantify the variation in seismic power as a function of time and frequency, which we compare to water level. In order to isolate the bedload signal, the standard methodology is to then average the PSD over the relevant frequency bands (Tsai et al., 2012; Bakker et al., 2020; Lagarde et al., 2021). This frequency range is typically around 30-60 Hz with turbulence found to be approximately 1-20 Hz (Tsai et al., 2012; Gimbert et al., 2014; Dietze and Gimbert, 2019). This approach allows us to compute the PSD for the seismic energy recorded within the frequency range commonly associated with the appearance of bedload transport. The data is plotted as a visual representation of the frequencies of the signal over time as a spectrogram and then as a time varying PSD plot to show the temporal change in seismic power over the chosen frequency bands.

The raw hydroacoustic data contains a lot of information about the processes occurring in the river. There is a distinct audible signal from turbulence (gurgling), smaller grain sizes being transported (tinkling and tapping), and larger grain sizes being transported (thudding and knocking), which can be used to manually classify the dominant process. Audio file snippets will be included in the online published version of the manuscript for this work (Appendix F). For the duration of each of the three high flow events from 2022 and the one event from 2023 considered here, the 30 second hydroacoustic recordings taken every 15 minutes were manually categorised by whether bedload was being transported and whether it was not. The recordings were categorised as 'Bedload Transport' if they were dominated by moving pebbles with more than 10 pebble hits over a 5 second window, however if there was only the occasional pebble movement ($\simeq$10 per 5 seconds) and it was dominated by turbulence noises the files were classified as 'No Bedload Transport'. The categorisation into the larger and smaller grains being transported is a bit more ambiguous as it relied on an audible identification of a change in frequency, and more work could be done

to look at the frequency characteristics of the hydroacoustic data. This will be likely explored further by the wider 'Sounding Out The River' project team with their recent deployments in Nepal. For this study, the same researcher processed all the hydroacoustic data to minimise errors in the categorisation and listened to the full 30 seconds recordings during the hydrograph peaks of interest. At low water levels ($\sim$ 0.6 m) the hydrophones are exposed and therefore don't record any river related signals so categorisation at these water levels are excluded from our analysis. Categorising the hydroacoustic data provides independent evidence of when bedload is being transported that we can overlay on the seismic analysis to test the thresholds of entrainment for coarse bedload and whether bedload transport and hysteresis in the PSD are directly related.

Unfortunately, due to unknown reasons the hydroacoustic data during the October 2023 event had a lot of instrument noise affecting the recorded signals, as described in Chapter 4. This noise dominated the signals during moderate flows and, despite trying to edit and amplify the signals, those recordings were not useful. However, the hydrophone appeared to record clearer signals during low-moderate flows when the sensor was only just covered by water and during high flows when there was bedload movement. This is most likely because the sloshing turbulence within the block at low water levels created a lot of noise that essentially 'drowned out' the instrument noise (although still loud), and at high flows the loud sound from pebble movement is sufficient enough to be heard over the instrument noise. Although pebble movement could be heard, it is unclear whether the first evidence of pebble movement is in fact the first occurrence of pebble movement, as movement of a smaller volume of sediment may have had a weaker signal that was overpowered by the instrument sound. Despite this, the recordings that were decipherable have been included in this analysis.

The water level data collected on-site was corrected for the height of the sensor above the riverbed to provide approximate water depth measurements, assuming the river bed was fixed. All stream gauge data, including that accessed from gauges SG1 and SG3, were linearly interpolated and resampled to one-minute intervals so that they could be combined with the geophone data that was analysed in minute long windows. Since the water level hydrographs during a high flow event are fairly smooth it is easy to interpolate between the 15 minute samples. This also provided us much more richness in the data, as resampling the geophone data to 15 minute intervals to match the original stream gauge data sample rate would potentially miss important information from the propagating flood waves.

5.3 Results

The results compare the co-located geophone and hydrophone data at site W_07 and H1, respectively, and geophone data collected at a control site approximately 300 m away from the river (E_06) for the 2022 events, and river sites E_03 and E_04 for the 2023 event. This comparative analysis is supported by locally measured stream gauge data from SG2 (Figure 5.1c). The results discuss the river-induced seismic signals at the geophone sites, the observed transport thresholds over three successive high flow events, comparison to a similar scale event a year later, and the robustness of using hysteresis as a fingerprint of bedload transport.

5.3.1 Seismic signal characteristics

First we compare and contrast the geophone data recorded beside the river (W_07) and at the control site (E_06) in order to discriminate background environmental signals from those sourced from the river channel.

The water-level time series and spectrograms derived from the geophone data at each site are plotted in Figure 5.3 for two different events. The plots in each column have common time axes; the November 2022 event is not shown because the control site geophone E_06 was not recording at this time. Prior to the water rising, all the spectrograms show vertical broadband streaks of high amplitude (approximately -140 to -145 dB), which correspond to the periods of rain that necessarily precede the water level rising as we observed no snowmelt-only hydrological events (Figure 5.3 (c-f)). Similarly, when the water level is dropping, it is likely that there will be less rain at the site, and fewer vertical streaks on the spectrogram, as the water level would not be dropping if there was still significant rain across the catchment. This assumption does not necessarily hold true for large catchments as local conditions may vary from catchment wide conditions, such as rainfall patterns, however our interpretation makes this assumption due to the relatively small catchment size. Some of these streaky broadband signals could also be a result of wind but it is difficult to differentiate the two without further meteorological data as they tend to have similar characteristics and occupy similar frequency bands (Rindraharisaona et al., 2022).

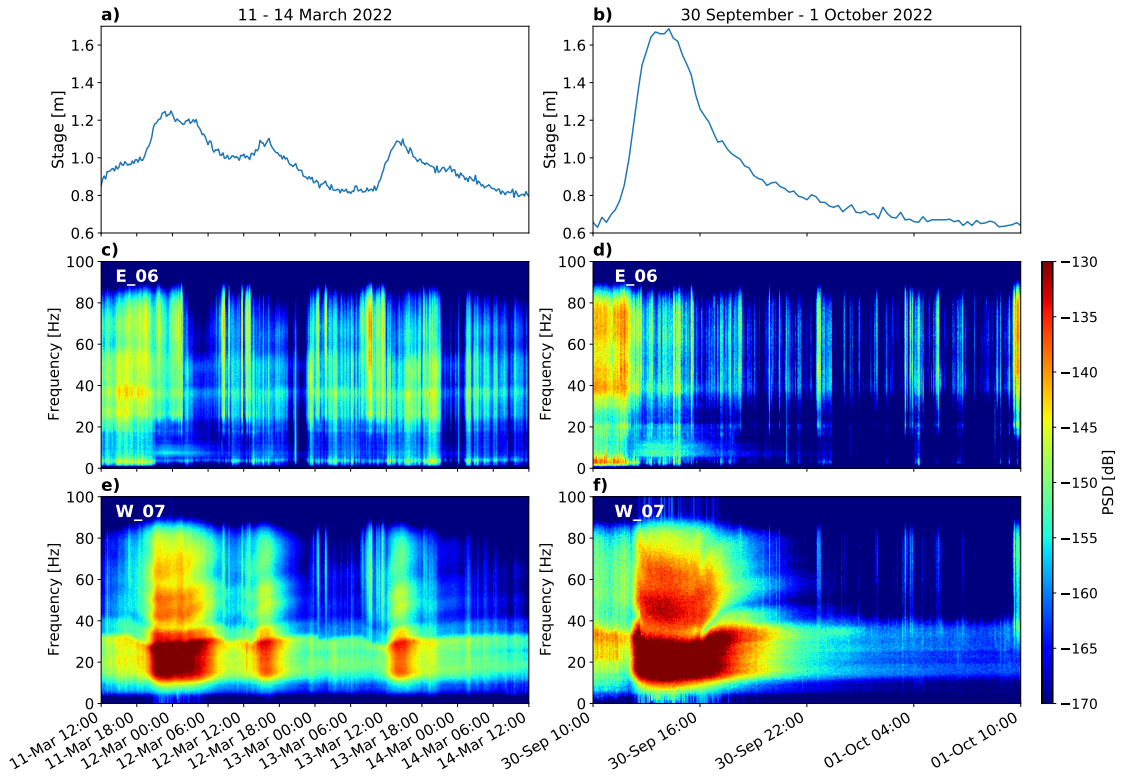


Figure 5.3: Data for two distinct high flow events in March and September-October 2022, one in each column. Included in this plot are; (a, b) the time-series of the water level at SG2, (c, d) the spectrograms of the geophone data (in 1 minute windows) at the control site to highlight environmental noise such as wind and rain, and (e, f) the spectrograms of the geophones at the river site which is dominated by signals of turbulence and sediment transport.

In contrast to the control site we see that the PSD time-series measured at the river bank station, W_07, evolves as the water level changes. During periods

of base level flow, when the water is low, the greatest power is recorded within a frequency range of approximately 5-35 Hz and is continuous, even during low flows prior to and following the large events, which suggests this is the background river signal (turbulence); this feature is absent at the control site. This value is slightly higher than those found in previous studies (as previously discussed in the 5.2 Section) but is most likely a result of site characteristics. The values here are in agreement with the results of preliminary use of the eseis model (Figure 4.2) in that it is estimated that the turbulence signal would dominate up to around 40 Hz (with slight variations depending on the water levels). The sudden onset of higher frequency (40-80 Hz) high power seismic signals at W_07 recorded during the peak of the flood waves suggests that there is a separate signal in addition to that derived from turbulence. During the highest water levels, these high power bands extend to higher frequencies, up to around 85 Hz, but once the river level drops back down towards base levels these higher frequency signals become less dominant. These high power, high frequency signals are also absent from the control site, thus enforcing the interpretation that these are river related signals, but the hydroacoustic data will help clarify this. During the peaks there is a dip in the lower frequency of the higher frequency band (around 40 Hz) which dips into the constant lower frequency band below 40 Hz. This is particularly noticeable on the September-October 2022 event. The dip occurs shortly after the initial power increase and then rectifies itself as the high power frequency above 40 Hz begins to subside.

The signals recorded from the October 2023 event share many characteristics with those observed in the 2022 events. There is an increase in seismic power corresponding to an increase in water level at all sites (Figure 5.4). Sites E_03 and W_07 show a clear constant signal at lower frequencies with an injection of higher frequency noise above approximately 40 Hz for both sites during the peaks of the hydrograph. E_04 appears to have a constant signal that spans a larger frequency range (5 - 60 Hz) and no clear additional high frequency signal during the event peaks. However, the seismic power within the 5 - 60 Hz band does show increases corresponding to peaks in the water level. W_07 shows the clearest separation of the two frequency bands, with the dip in frequency that was observed in the September-October 2022 event present in the second and third peaks getting larger with greater water levels. This dip is not present in the signals from sites E_03 and E_04.

These comparisons allow us to identify the seismic signals that are induced by river-related processes, and specifically those induced by bedload transport, which are then used throughout the rest of this study to analyse transport thresholds and patterns. These interpretations are also introduced in Chapter 4.

Having documented the fingerprints of different physical processes within the time-frequency domain (Figure 5.3), we simplify the analysis by focusing on the 30-80 Hz band, as previous studies (e.g. Burtin et al., 2008; Roth et al., 2016; Turowski et al., 2015) have found that bedload transport produces signals at higher frequencies than turbulence, which going by our interpretation from Figure 5.3 and the analysis in Chapter 4 would be >30 Hz. This is also in agreement with the findings from running the eseis model in Chapter 4, Section 4.3.1. Specifically, in minute long windows shown in the spectrogram, we average the values of the power over the 50 to 60 Hz range for three distinct high flow events to calculate a single scalar value at each time, which we refer to as the average power spectral density (aPSD) in the coming plots (See Section 5.2: Data processing and analysis). This

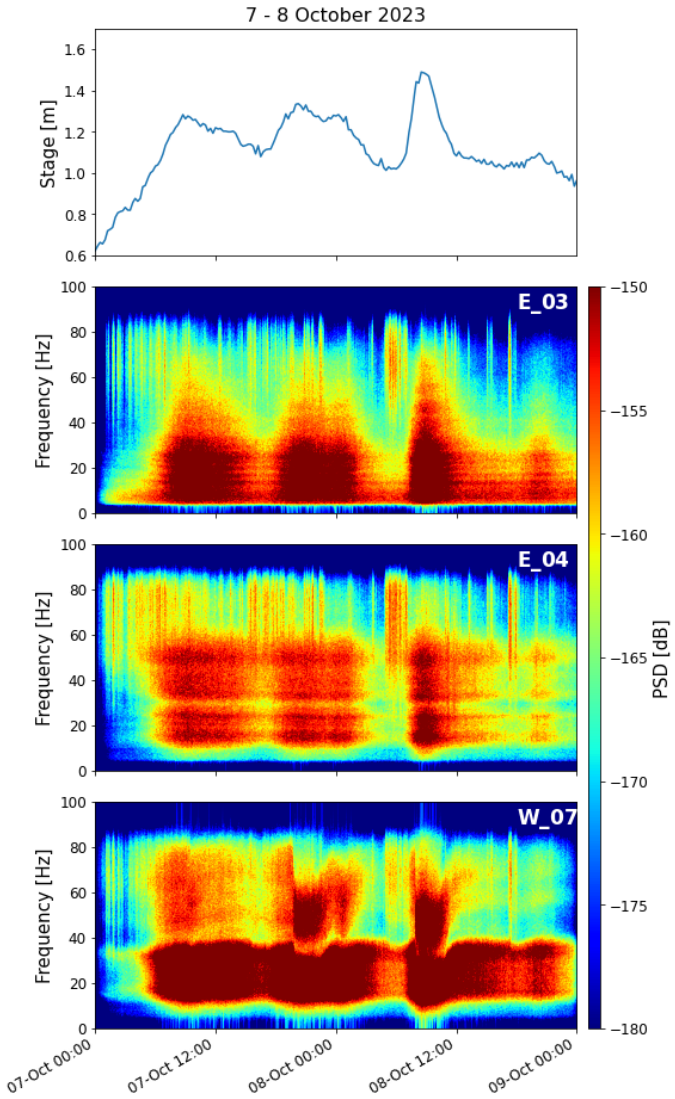


Figure 5.4: Seismic power variations in frequency and time during the high flow event in October 2023 at sites E_03, E_04, W_07.

narrower frequency range was chosen as there was less influence from meteorological and turbulence seismic signals, making the bedload transport the strongest signal observed for those frequencies.

The aPSDs calculated using the selected frequency band of 50-60 Hz highlight the use of site E_06 as a control site and the strength of the river-induced seismic signals recorded at W_07, E_04 and E_03. At the control site the PSD is dominated by the contributions from the broadband intermittent meteorological (wind and rain) signal. Consequently the aPSD shows a large amount of scatter that is independent of the water level (Figure 5.5 a,b). In contrast, the aPSD at the sites beside the river mirror the variations in water level for all events, showing a close parallel between the two (Figure 5.5 c-e and Figure 5.6). The meteorological noise is still visible at all sites, particularly E_03 and W_07, prior to the hydrological peaks, but the river-induced seismic noise is dominant above base water levels ($\sim$ 0.90 - 1.10 m) as turbulence increases and bedload begins to mobilise.

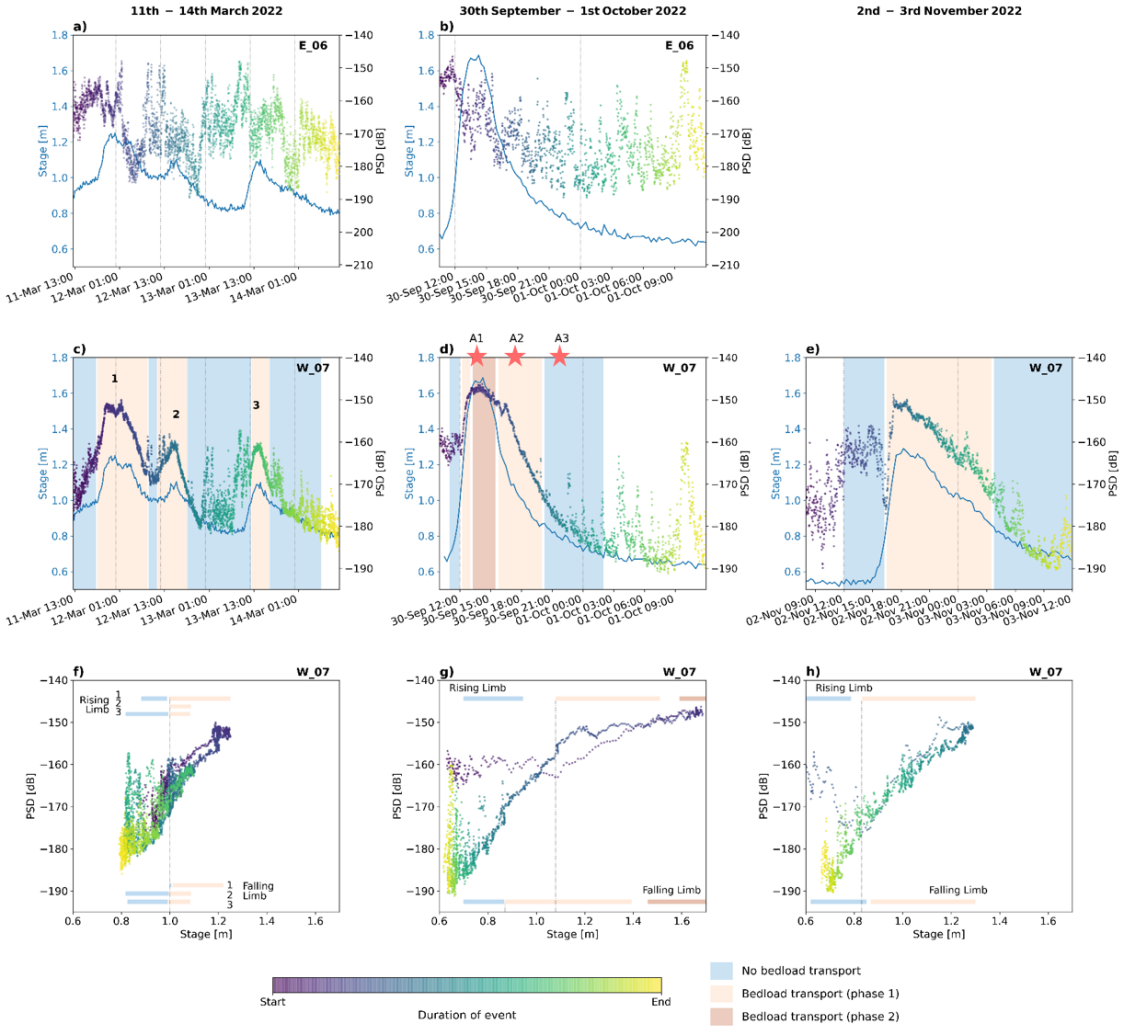


Figure 5.5: Plots summarising the time series of the water level (blue line) and seismic power averaged over the frequency range 50-60 Hz (points coloured by time) for the three largest flow events in 2022. Each column displays a different event showing; (a, b) the aPSD and water level timeseries' for the control site highlighting the environmental noise around the water level peaks, (c, d, e) the aPSD timeseries for the river site layered on top of the independent classification of bedload transport activity using the hydroacoustic data (white shading shows gaps in the data or when the hydrophone was exposed, blue shows periods where the hydrophone records only turbulence, peach shows when bedload transport starts (phase 1) and beige shows when there is an audible shift to lower frequencies on the hydrophone interpreted to be mobilisation of larger grains during bedload transport (phase 2)), (f, g, h) the PSD versus stage relationship with the hydrophone bedload transport classifications shown as bars for the rising and falling limbs of the hydrological peaks. Red stars in d) show the timings of the hydrophone recordings included in Audio 1-3 in the published manuscript, labelled A1, A2 and A3.

5.3.2 Bedload transport characteristics

5.3.2.1 Entrainment thresholds of coarse bedload

Using the hydrophone data, we classify whether bedload is being transported, independently of the geophone data, and include this information on the water-level versus aPSD plot (peach and beige shaded regions in Figure 5.5 c-e and Figure 5.4, with blue shading for when only turbulence was observed and white regions when the hydrophone was exposed out the water). All four of the high flow events discussed here resulted in the mobilisation of bedload during the peaks in water level, with the peach colour, labelled 'Bedload transport (phase 1)' indicating the movement of bedload material. During the largest of the three 2022 events (the September-October 2022 event) there was also an audible shift in frequency of the

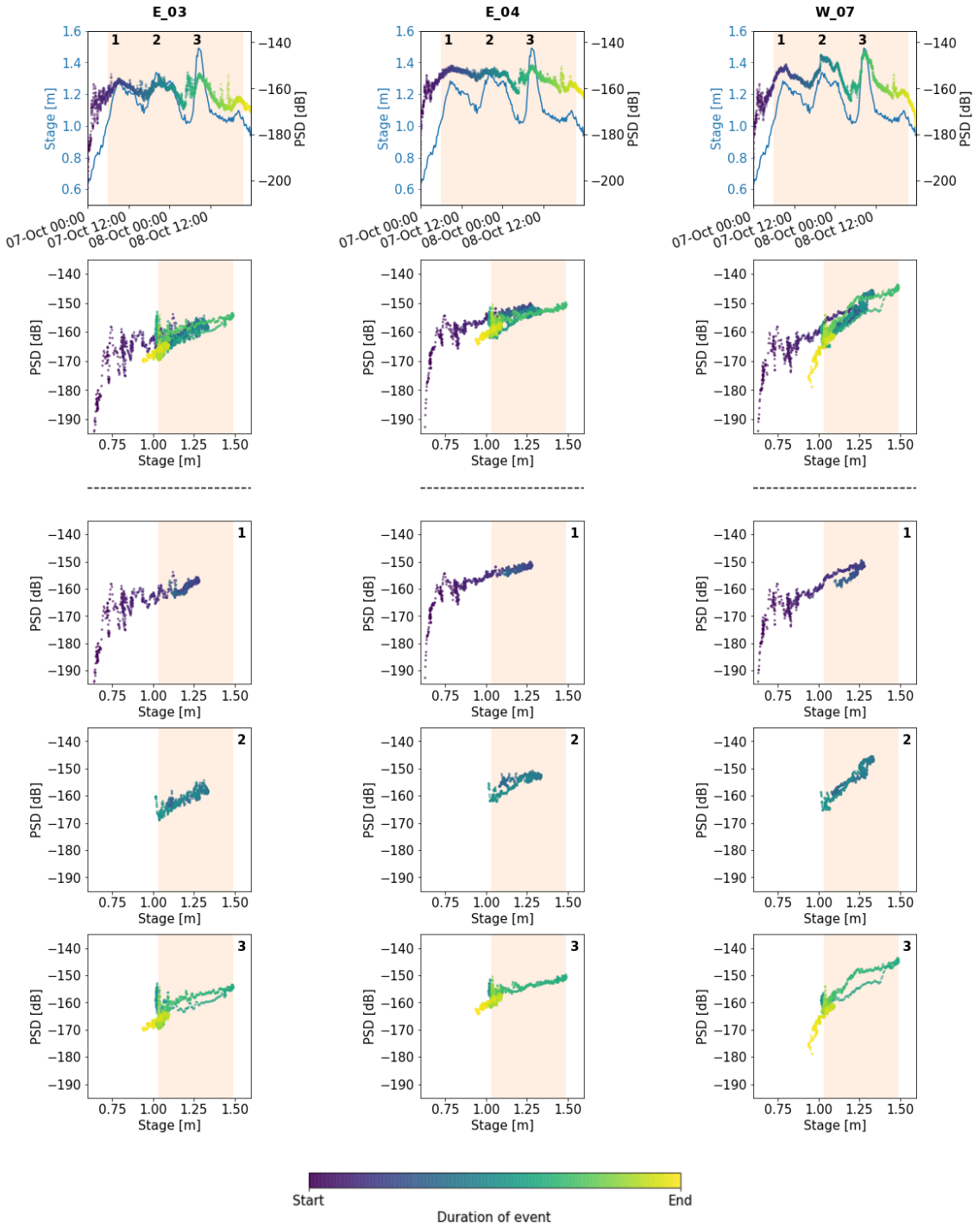


Figure 5.6: aPSD variations against time and water level for the October 2023 event at the three selected sites, E_03, E_04, and W_07. The peach shading indicates the periods of bedload transport as categorised in the hydroacoustic data. The first row shows the aPSD over time (coloured dots) overlain on the hydrograph (blue line). The black numbers indicate the three peaks of the event. The second row shows the aPSD against stage for the full duration of the event, and the following three rows show the aPSD versus stage for each of the three consecutive peaks, labelled in the top right corner of each panel.

recordings at the highest water level (>∼ 1.50 - 1.60 m), which is shown in the beige colour and labelled 'Bedload transport (phase 2)' in Figure 5.5d at the peak of the event, which lasted approximately 135 minutes. Recordings during the two transport phases and the turbulence phase highlight the audible changes during these processes. This audible frequency drop in the hydroacoustic data coincides with a shift to lower frequencies in the geophone data seen in Figure 5.3f, where the lower

frequency end of the high amplitude seismic power dips from about 40 Hz to around 30 Hz at the same time as the peak of the hydrograph and then rises back up following the peak. The gaps between the hydroacoustic categorisations in Figure 5.5 c-h are due to the 15 minute hydroacoustic sampling interval resulting in a range of water level at which mobilisation of coarse bedload starts. Here, this water level range is greater during the rising limb than the falling limb (Figure 5.5f-h) due to the rapid rate of increase in water level relative to the quarter-hourly hydrophone recordings compared to the gradually waning falling limb. Similar features would be observed in a rapidly decreasing flow, however this was not the case in the events analysed here.

Further, we can compare the timing of onset of bedload transport with the water level at that time to explore any systematic changes in the threshold for motion and arrest across the events. Figures 5.5 and 5.7 reveals that bedload mobilisation during the moderate scale March 2022 event consistently starts and stops at a water level of ∼1.00 m. This is the case across all three daily peaks, labelled 1-3 in Figures 5.5c and 5.7b and c. However, during the largest September-October 2022 event it is observed that coarse bedload transport initiates at between 0.95 m and 1.08 m, accounting for the uncertainty in the sampling period of the hydroacoustic data. The previously mentioned audible drop in frequency of the hydroacoustic data occurs between 1.50 m and 1.59 m and continues throughout the peak (at 1.69 m) and falling limb and stops at around 1.39 - 1.44 m, labelled 'Bedload transport (phase 2)' in Figure 5.5 and 5.7. At this point on the falling limb the audible frequency increases to similar to the initial mobilisation and bedload transport is sustained until the water level drops to ∼0.87 m. The September-October 2022 event therefore had coarse bedload mobilisation initiating at ∼1.00 m on the rising limb and ceasing at ∼0.87 m on the falling limb. The third event in November is much like the early March 2022 event in that the mobilisation of bedload starts and stops at the same level on the rising and falling limb of the hydrograph. However, for this event the entrainment threshold is now followed through from the September event at ∼ 0.79 - 0.87 m. For the October 2023 event (Figure 5.6) the initiation and cessation of bedload transport occurred at the same value at the start and end of the transport period at 1.01-1.03 m on the rising limb and 1.00-1.03 m on the falling limb (accounting for the 15 minute uncertainty in hydroacoustic recording gaps). However, as mentioned previously there may be some uncertainty in these observations due to instrument recording noise. It was evident that transport continuously occurred throughout the three peaks of this event, with no noticeable shift in the audible frequency of hydroacoustic recordings at any point over the 39.75 hours of transport. This period of transport has been marked on the plots from each of the three sites during the October 2023 event, however since the hydrophone was located adjacent to site W_07 we can only accurately relate the transport occurrence to that site.

5.3.2.2 Seismic power versus water level hysteresis relationships

Now consider the water-level versus aPSD plots for the 50-60 Hz frequency band in Figure 5.5 f-h, Figure 5.6, and Figure 5.7a. These allow us to test the validity of the assumption that hysteresis in the water level versus PSD is a reliable fingerprint of bedload transport. As noted above, bedload transport occurred during all three events which was evidenced through the hydroacoustic data. Looking at the water level versus aPSD plots it is clear that both the March 2022 and November 2022

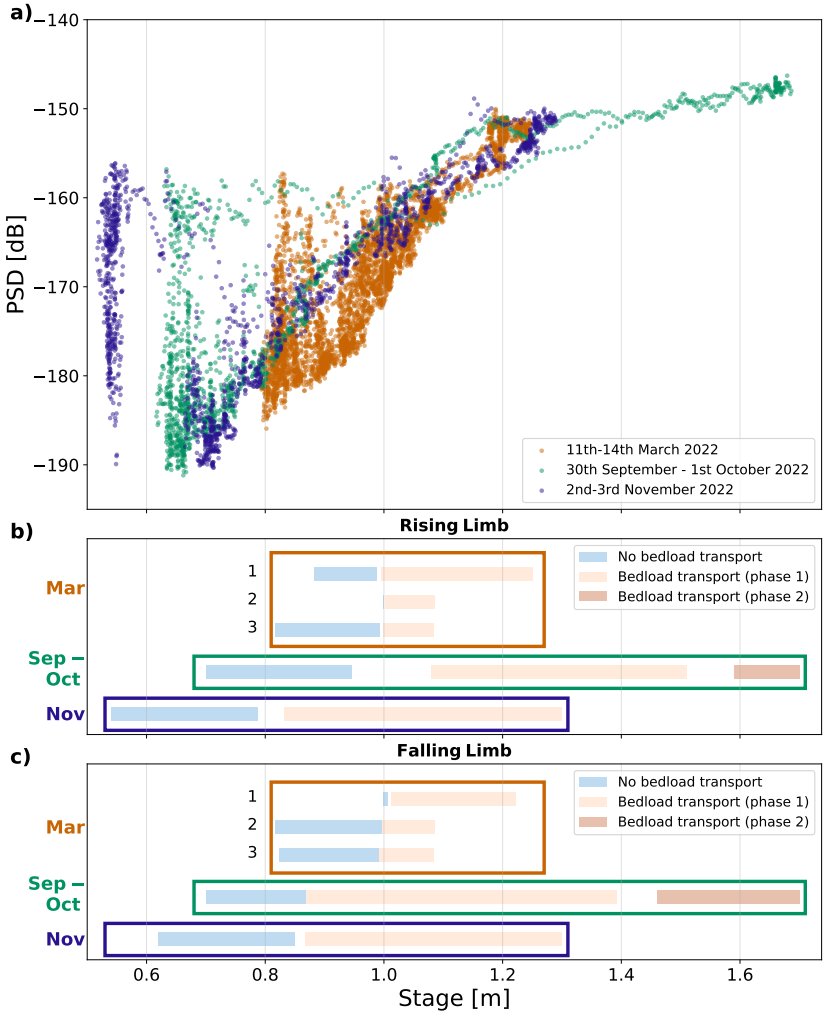


Figure 5.7: (a) Superposition of the PSD versus water level relationships for three distinct high flow events to enable a clearer comparison of the similarities and differences between each event. (b) Bedload activity transitions from independent interpretation of hydroacoustic data that occurred on the rising limbs of flood peaks for all three events; note that for the March and September events bedload started being transported at a water level of ∼1.00-1.10 m whilst transport during the November 2022 event initiated at a water level of ∼0.80 m. (c) Bedload activity transitions from independent interpretation of hydroacoustic data that occurred on the falling limbs flood peaks for all three events; note that for the March 2022 event bedload stopped being transported at a water level of ∼1.00 m whilst the arrest of bedload transport occurred at ∼0.85 m for the September and November 2022 events.

events have relatively linear relationships and show no signs of hysteresis despite independent evidence from the hydroacoustic data that bedload was actively being transported. They also show very similar gradients of aPSD against water level for both the rising and falling limbs, suggesting that the nature of coarse bedload transport is similar for both events. In contrast, the aPSD analysed over the 50-60 Hz range in the larger September-October 2022 event does exhibit some anticlockwise hysteresis, but only between ∼ 1.00 m and 1.40 m. In addition the slope of the aPSD versus water level is lower at higher water levels (Figure 5.5g). Until around 12:00 on the 30th September (at water levels $<$ 1.00 m), the aPSD is relatively constant at around -160 dB for this event whilst the precipitation dominates the signal, as evidenced in Figure 5.5 d and discussed above in section 5.3: Comparison of the river site with the non-fluvial control site. Once the water level reaches ∼1.00-1.10 m, the aPSD starts to rise at a similar gradient to the other two events (gradient $= \theta_{PSD} = 43$) but at slightly lower PSD values (Figure 5.5f and h; Figure 5.7). This occurs at a very similar entrainment threshold to what was observed through

the hydroacoustic data, discussed above. At around 1.40 m the aPSD has risen to approximately -148 dB, and now levels off slightly ($\theta_{PSD} = 7.5$). One possible cause for a levelling off like this could be due clipping of the waveforms when the recorded signal exceeds the upper limit of the geophones recording range, resulting in a loss of data. However, this is not the case here and the observed behaviour is real (Figure 5.8). This much lower gradient is sustained up to the peak of the event and continues with the falling limb until ∼1.15 m, at which point the gradient returns similar to the original gradient ($\theta_{PSD} = 50$). This sustained lower gradient lasts longer on the falling limb than the rising limb, which can also be seen on the aPSD timeseries in Figure 5.5d where the aPSD remains close to peak levels for a short time after the peak even once the water level has begun to decrease.

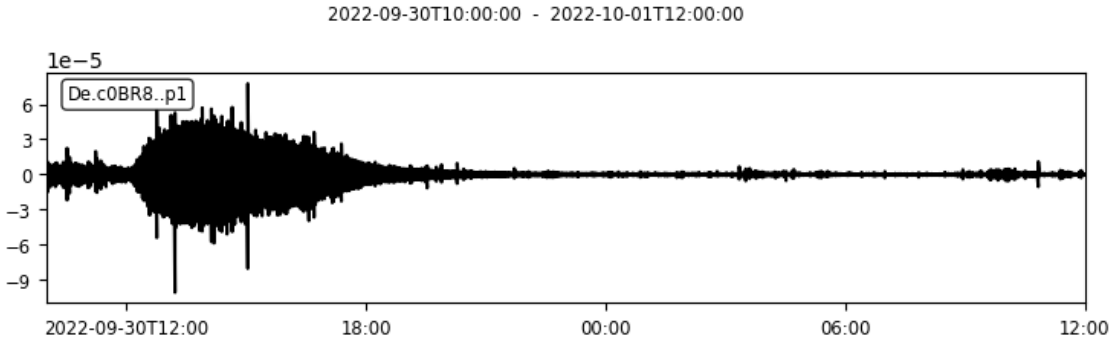


Figure 5.8: Waveform of the north-south component at site W_07 during the September-October 2022 event demonstrating the saturation in the PSD at high water levels is not because of clipping of the waveform amplitudes.

The October 2023 event, like the March 2022 event, consisted of three successive hydrological peaks that were classified as one event. The second row of Figure 5.6, shows the relationship between seismic power and water level across the full duration of the event, however it is difficult to decipher any patterns due to the overlapping data. I therefore separated the three peaks into their own panels in the subsequent rows of the figure, labelled accordingly in the top right corner of the plots and coloured by time across the full duration of the event. As mentioned earlier, the hydroacoustic classifications are only really accurate for site W_07, however we have included it here as an indication since the sites are within relatively close proximity to each other. The first peak of this event shows a small degree of this (clockwise) looping hysteretic relationship at site W_07, but not at E_03 or E_04 (Figure 5.6). The second peak shows very little variation in seismic power at the same water levels on the rising and falling limb at any site. The third peak again shows hysteretic loops but this time at W_07 and E_03, and the loops are anticlockwise closely resembling the characteristics of the September-October 2022 event. The third loop also showed the overlapping/clustering lines (linear relationship) of the rising and falling limb at water levels above ∼ 1.40 - 1.45 m at sites E_03 and W_07. There is a noticeable gradient change ($\theta_{PSD} = 13$ to $\theta_{PSD} = 55$) for site W_07 at approximately 1.20 m on the falling limb of the third peak matching the gradient change in the September-October 2022 event. Although less noticeable there is a similar gradient change at around 1.20 m at site E_03. Although there was an increase in seismic power at E_04 during the duration of the event, it shows less correlation with water level over the three peaks. This results in the seismic power versus water level relationship to be fairly flat and linear. However, as discussed in Chapter 4 this site is very susceptible to wind signals which may dominate the

recording at this site essentially smoothing out the river-related signal.

In summary, the initial entrainment threshold that was observed in March 2022 dropped by about 15-20% (∼1.00 m to ∼ 0.80-0.85 m) following the September-October 2022 event peak and this new lower threshold was maintained for the subsequent November high flow event. The March and November 2022 events show no hysteresis whereas the larger September-October 2022 event shows a degree of anticlockwise hysteresis for water levels between ∼ 1.00 m and 1.40 m (when bedload transport is observed to initiate), and then behaves linearly at water levels above 1.40 m. Although the third peak of the October 2023 event resembled the September-October 2022 event, the threshold behaviour was similar to that of the March and November 2022 events where the threshold was the same on the rising and falling limbs, and was the same threshold as the March 2022 event. Unfortunately, due to the noise from meteorological signals at the initial stages of the high flow events, it is difficult to identify any features in the seismic data that would indicate the initial transport of the coarse bedload, which is why the hydroacoustic data has proven very useful in this analysis.

5.3.2.3 Bedload transport hysteresis observed using offset stream gauge data

So far we have looked at the relationship between water level and seismic power using local stream gauge measurements from our co-located LiDAR stream gauge sensor. However, it is not always possible to acquire co-located stream gauge data to where seismic measurements are being conducted. Therefore, here we compare the hysteretic relationships observed if we were to use water level data collected from the two additional stream gauge datasets we have access to. These being SG1 and SG3, located approximately 10km upstream and downstream of our site (Figure 5.1) which both record quarter-hourly data. These data are managed by Dr Andrew Black (Dundee University) and the Scottish Environment Protection Agency (SEPA), respectively.

From Figure 5.9, it is evident that using offset stream gauges induces patterns of hysteresis that are not present when using co-located measurements. Using the stream gauge data from SG1 upstream of our site results in preferential anticlockwise hysteresis patterns for all three 2022 events, with a weaker relationship during the March 2022 event. Using the downstream gauge SG3, however, results in clear clockwise hysteresis for all three events.

5.4 Discussion

5.4.1 Seismic characteristics

As mentioned, all sites record clear river-induced signals for all events, however the shift to lower frequencies during the peak of the events at W_07 is interesting. It is unclear what causes this behaviour, which is not seen at other sites. Here, I hypothesise on the potential causes for a drop in frequency during the peak of the events.

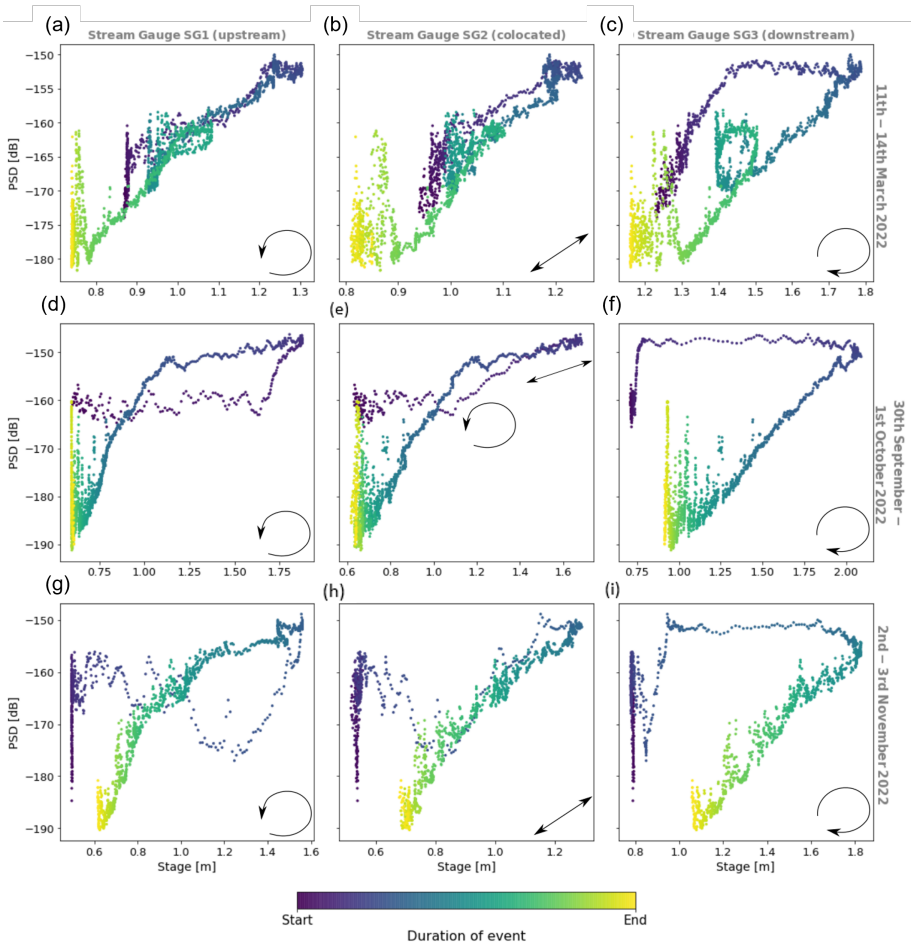


Figure 5.9: Hysteresis patterns produced when using offset and co-located water level and seismic measurements for all three 2022 events. (a, d, g) When using upstream water level measurements relative to the seismic measurements an anticlockwise hysteresis is apparent. (b, e, h) A generally more linear relationship is observed when using co-located measurements, however the larger September-October 2022 event shows a more complicated behaviour with a degree of hysteresis at intermediate water levels and a linear relationship at high water levels. (c, f, i) Using downstream water level measurements relative to seismic measurements results in clear clockwise hysteresis for all three events.

Transport likely begins in the main channel as sediment from upstream is flushed through. However, once the water level reaches around 1.2 m, the bar adjacent to W_07 becomes submerged, exposing the bar material to transport. Since the secondary material transported is closer to the geophone, any observed frequency shift would more likely result in an increase in frequency rather than a decrease, as the proximity to the sensor reduces attenuation. It is possible that the frequency dip observed may correlate with the 'eseis' model in Figure 4.2, which suggests that as water levels—and consequently bedload flux—increase, the transition from turbulence-dominated to bedload-dominated signals shifts to lower frequencies. Initial hypotheses included the possibility of the sensor getting 'wet feet,' changes in site properties, standing waves, or a grain size signal. However, given the relatively smooth nature of this stretch and the homogeneous gravel-cobble sized particles, standing waves seem unlikely. Timelapse photos of the channel adjacent to W_07 before and after the September-October 2022 event (Figure 3.11) indicate a change in grain sizes, with larger grains deposited after this event. This could be linked to the frequency shift observed. Nonetheless, since the frequency dip was also noted in the lowest peak of the October 2023 event, with no corresponding audible change

in frequency from the hydroacoustics, it suggests that grain size variations may not be a factor here. Further analysis or seismic refraction surveys could provide more insight, but this is beyond the scope of this thesis.

5.4.2 Bedload entrainment threshold variability

From seismic and hydroacoustic measurements at our field site in the alluvial River Feshie, it is clear that we can record information on the mobilisation of coarse bedload. One key finding is that the coarse bedload transport threshold, and hence bed strength, depends on the recent history of larger discharge events. We believe that the largest event observed in 2022 leaves disordered material on the surface of the bed that is easier to re-mobilise than it was prior to the large event (Jain et al., 2021). We interpret the change in entrainment threshold as a consequence of changes in the grain structure and sorting on the river bed (Jain et al., 2021) with greater deposition of unsorted material; this is consistent with the very rapid fall in water level inhibiting the bed to find a stable form (Luo et al., 2023). It was also visually observed that there was no significant change to the width of the channel or the elevation of the bed. The water depth at which entrainment was initiated changed by ∼15 cm, but the bed elevation is unlikely to have changed by this amount, therefore this is unlikely to have had an effect on the thresholds observed. The water depths at which entrainment was initiated in all analysed events fall within the ranges predicted using commonly used Shields stress values (0.03–0.06) in Section 3.2.4, as shown in Figure 3.23. Therefore, these results are consistent with the typical ranges observed in previous studies on Shields stress thresholds.

We hypothesise that, in the absence of a further large flow event like the September-October 2022 event, over cycles of moderate scale events, such as snow melt cycles or moderate rainfall events like the March and November 2022 events, the bed will progressively regain its strength as the clasts locally reorganise and the water level threshold for mobility will again rise to a higher value (Ockelford et al., 2019; Luo et al., 2023). This hypothesis is supported by the observation that in the initial March 2022 event, the daily rainfall plus snowmelt cycles were just sufficient to initiate the motion of bedload at their peak suggesting that these moderate events have helped the system find a more stable configuration over time. Since events of a similar size to the March and November 2022 events are expected to happen approximately once every 5-6 months, the river will undergo somewhat frequent local sorting of material before a large approximately one in one year event like the September-October 2022 event breaks through the sorted material and causes large amounts of resorting.

Since 2023 was a hydrologically quiet year we can't easily examine the threshold variabilities across subsequent events. However, from Figure 4.1d it can be seen that there were a few smaller events that occurred in September 2023 and may have reached the threshold for motion. These moderate flows may have cause some small local reorganisation of grains in the channel, strengthening the bed in doing so and raising the threshold back up to around 1 m water depth by the time this October 2023 event occurred.

5.4.3 Hysteresis patterns observed using collocated measurements

Prior to this study, hysteresis in the water-level versus seismic PSD plot was viewed as an indicator of bedload transport processes, with a signal driven purely by turbulence expected to show little to no hysteresis (Burtin et al., 2008; Hsu et al., 2011; Turowski et al., 2015). In our study bedload was transported in all four events, but hysteresis in the high frequency signal only occurred in the two largest events when using co-located stream gauge data from SG2; thus using hysteresis alone as an indicator of bedload transport is insufficient to detect transport events. Our findings are in agreement with Roth et al. (2017) who found that hysteresis may not be an effective measure of bedload transport as they identified that the seismic power tracks more closely to the changing water levels than the sediment transport rates measured using impact plate geophones. In our field site, as a conservative estimate, we saw hysteresis emerge for high flow events which exceeded water levels in excess of 1.30 m whilst the actual bedload mobilisation threshold varied between 0.85 m-1.00 m.

We also see a levelling off of the PSD for water levels above 1.20 m. Here, we interpret this to be most likely caused by the presence of a sheet flow of granular material, which would make it difficult to increase the frequency and magnitude of collisions with the bed (Palucis et al., 2018), thus reducing the seismic power measured in the high frequencies with increasing water level. We believe that although there will be a limit on the grain-to-bed interactions during granular sheet flow, there will likely be increased grain-to-grain interaction which is possible to record with the hydroacoustics. These behaviours have been seen in studies looking at force fluctuations from debris flows. Work by Allstadt et al. (2020) and Piantini et al. (2022) measured fluctuating basal and shear stresses and observed that the forces were limited by the thickness of the flow. In rivers this effect would depend on the solid concentration of the flow (Piantini et al., 2023). At low sediment concentrations particles are agitated and inter-particle collisions occur, but at high sediment concentrations transported particles mainly interact through long-lasting contact, therefore reducing the force on the riverbed (Piantini et al., 2023). Piantini et al. (2023) additionally saw a negative relationship between seismic power exerted on the bed and solid concentration of the flow, along with suppressed hysteresis patterns. Therefore the decrease in seismic power observed over the falling limb of the larger events could be due to damping events caused by the development of a sediment layer at the base of a thick sediment flow or concentrated mobile sediment layer (McCoy et al., 2013; Kean et al., 2015; Piantini et al., 2022). Additionally, force fluctuations have been found to be controlled by bed roughness, in which bedload particles impact the river bed as they encounter bed roughness elements (Farin et al., 2014; Lai et al., 2018). Piantini et al. (2023) observed a negative relationship between these parameters. Further analysis into the frequency characteristics of hydroacoustic data would potentially shed some light on this, however this work was outwith the scope of this thesis. Under this scenario, due to the reduced grain-to-bed interactions, measurable with geophones, studies which attempt a mass balance based on hysteresis are likely to underestimate the total bedload transported (e.g. Chao et al., 2015) and the construction of a mass balance using geophones alone will struggle at high flow rates; a proper analysis of bedload flux will need to consider

such non-linearity.

In conjunction with the expected hysteresis at high frequencies, previous studies have suggested that analysing the low frequency band (<∼1-30 Hz, e.g. Burtin et al., 2008; Chao et al., 2015; Dietze and Gimbert, 2019) can effectively isolate the turbulence signal. By focusing on this frequency range, it was believed that hysteresis would not be observed in the water-level versus PSD plot (Tsai et al., 2012). However, findings from this study challenge these assumptions, especially in relation to the largest event analysed. Contrary to expectations, hysteresis is also observed in the lower frequency range, as shown in Figure 5.10. This adds complexity to distinguishing between turbulence and bedload seismic signals, potentially leading to inaccurate estimations of bedload transport fluxes. However, this analysis may be complicated by the fact that bedload and turbulence can occupy overlapping frequency ranges, and therefore discrimination of the frequency bands of interest is very important to avoid contamination of the data. Findings by Turowski et al. (2013) and Roth et al. (2017), also suggest that water turbulence can in some cases be the dominant source of seismic noise with the energy transmitted to geophones by bedload being much smaller than the energy of the water. Therefore, hysteresis that is observed may in fact be related to the changing discharge rather than the occurrence of bedload transport.

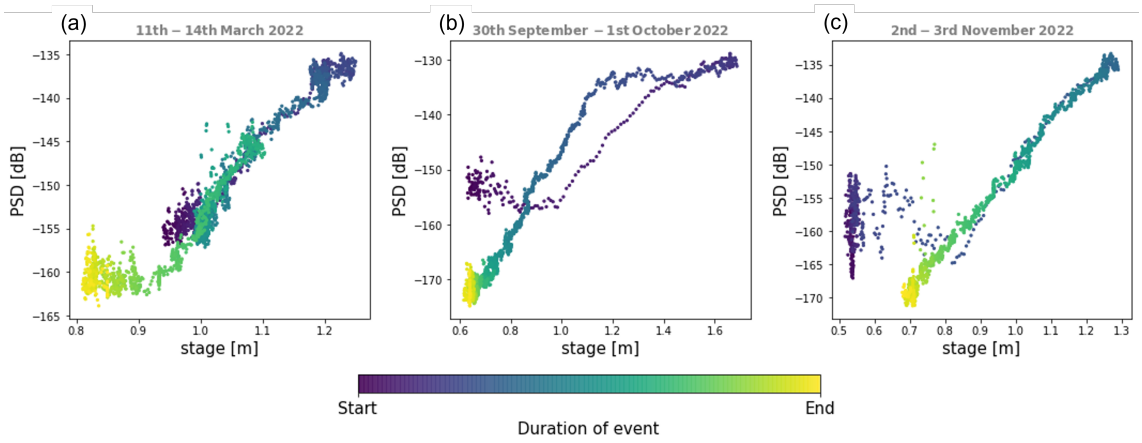


Figure 5.10: SG2 water level versus PSD summed over 20-30 Hz for the N-S component at site W_07 for all three 2022 events. This reveals a similar behaviour to the higher frequency band in Figure 5.5.

5.4.4 Hysteresis patterns observed using offset seismic and stream gauge measurements

Previous studies commonly combined the seismic PSD with stream gauge timeseries to test for a hysteresis in the mean seismic power, analysed over the frequency range relevant to bedload processes. However, any temporal lead or lag in the water level timeseries at the stream gauge station, compared to what the water is actually doing at the geophone site, will result in apparent hysteresis due to a temporal offset of similar shaped curves (Figure 5.11). Thus, when the sensors are not co-located, there is a risk that a hysteresis may be introduced as an artefact and hence bedload transport miscellaneously claimed. We provide a demonstration of this artefact in the Figure 5.9 where we compare the mean PSD plots for the moderate sized events, which show no hysteresis using the co-located stream gauge, against mean PSD plot

generated using stream gauge data that is from permanent stations around 10km downstream and 10km upstream of our fieldsite (Figure 5.1). Many studies that have used offset measurements have made an attempt to correct for the offset (i.e. Hsu et al., 2011; Schmandt et al., 2013; Chao et al., 2015), however there are many uncertainties in these corrections which do not account for local variability in water levels or sediment availability.

Some studies have opportunistically used seismometers that are located at distance from the river. If a seismometer is located at some distance from the river, it will be difficult to construct the water-level vs mean PSD plot as the seismometer will be averaging the seismic sources over a relatively long stretch of the river (Cook and Dietze, 2022) whereas the stream gauge is measuring at a point location. Consequently, the use of seismometers further from the river smooths the pulsating nature of bedload transport (Lagarde et al., 2021; Cook and Dietze, 2022) and under the scenario of transport migrating with the pulse of high water, the bedload transport would appear more sustained than if it had been measured beside the river (Figure 5.11). A further complication is that high frequencies, which are those most informative of bedload transport, are preferentially attenuated over large distances (Schmandt et al., 2013; Gimbert et al., 2014; Lagarde et al., 2021).

We believe it to be a more robust experimental design to co-locate a stream gauge sensor in our study reach. Having co-located water level and seismic observations, means this effect is negligible in our study as geophone W_07 is located approximately 5 m from the river and thus is integrating over a small area.

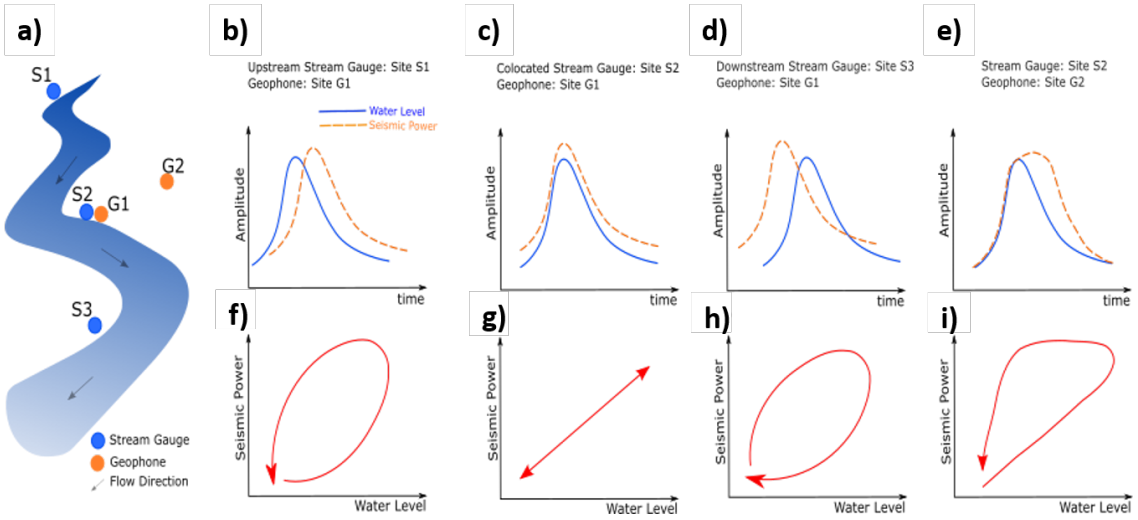


Figure 5.11: Examples of sources of hysteresis in the relationship between water level and seismic power. When the stream gauge and geophone are offset (a), hysteresis will be introduced as an artefact of the temporal offset even when the form of the seismic power and water level curves are the same. If water level is measured upstream of the seismic data an anticlockwise hysteresis pattern will occur (b, f). If water level and seismic measurements are co-located, no hysteresis will be observed (c, g). If water level is measured downstream of the seismic measurements then a clockwise hysteresis pattern will occur (d, h). Changes in the shape of the seismic power curve with respect to the water level curve as a result of increased source-to-sensor distance for the seismic data can also result in a hysteretic relationship (e, i).

Looking forwards, long-term monitoring on this reach would allow us to observe a series of successive events with varying durations. This would provide us with a more comprehensive understanding of the factors influencing the threshold for bedload mobilisation. In particular, we could assess whether the bedload mobilisation threshold is primarily influenced by the magnitude of high flow events, the duration

of individual events or the periods between events. Furthermore, the relationship between these dynamics, the arrangement of the riverbed structure, and the calculation of the entrainment threshold parameter, Shields stress, could be explored.

5.5 Conclusions

Developing a clear, robust methodology for understanding and digitally monitoring bedload transport and fluxes is fundamental for informing engineering and flood risk models, particularly with the concerns regarding the increased extreme event occurrence as a result of climate change. The use of seismic sensors is a key step forward and provides the opportunity to monitor bedload transport in previously inaccessible conditions, however it is clear that care has to be taken when developing the methodological design. Combining seismic data with other measurement techniques such as hydroacoustic data, as done in this study, allows the independent interpretation of the mobilisation of bedload which can inform a more accurate analysis of the seismic signal from bedload transport. By studying three successive high flow events, we test for variations in the flow conditions in an alluvial river that characterise the onset and termination of particle entrainment, thereby exploring the presence of hysteresis in seismic data as a fingerprint of coarse bedload transport. Through the use of hydroacoustic data to independently characterise bedload transport, our study found that bedload transport occurred during all three events but that mobilisation initiated and terminated at different water levels. Notably, these entrainment thresholds were influenced by preceding events, with a discernible drop of approximately 15 - 20 % following the largest of the three events. Our study also reveals that while hysteresis in seismic data, in relation to water level, can sometimes be indicative of bedload transport, it is not a definitive requirement. It was also observed that a single transport event in October 2023 exhibited similar thresholds of motion and hysteresis patterns as the 2022 events. These findings emphasise the need to enhance our understanding of the factors that influence the occurrence of bedload transport, particularly in climate change-affected rivers. Being able to accurately distinguish between distinct seismic signals associated with bedload transport and water turbulence is crucial, and will enable us to improve our ability to estimate bedload transport fluxes and gain deeper insights into the complex dynamics of alluvial rivers impacted by climate change. Our study shows the value in combining seismic and hydroacoustic data for long-term digital monitoring of bedload transport and suggests the possibility that this combination of data will allow us to identify different granular flow regimes in the field. Routine monitoring with such digital systems enables us to understand the systematic evolution in the onset of bedload transport and will be of direct use in calibrating widely used flood and bedload transport engineering models.

Chapter 6

Comparison of the directional components of the river-induced seismic signals

The geophones used for this PhD record in three orthogonal components, as described in Chapter 3. The North-South component was oriented with the downstream direction of the river, thus providing us with a stream-parallel component and subsequently a stream-perpendicular component (the East-West component), along with the vertical component. As discussed in Chapter 2, the majority of previous fluvial seismology studies, including the developed numerical models by Tsai et al. (2012) and Gimbert et al. (2014), have assumed the majority of bedload transport information resides in the Rayleigh waves and so have focused on the analysis of a single component, typically the vertical component. This assumption was built into the 'eseis' package by Dietze (2018a), which was analysed in Chapter 4. In Chapter 4, I presented the signals recorded in all three components and briefly described the differences in the signals. I then went on to use only the stream-parallel component in the analysis in Chapter 5 and the published manuscript (Appendix F). In this chapter, I will test the assumption that the bedload transport signal is predominantly composed of Rayleigh waves by looking for changes in the relative amplitudes of the horizontal (stream-parallel and stream-perpendicular) and vertical components. Given that turbulence and the impact of bedload impose different forcings on the bed of the river, we might expect this difference to be evident in the geophone data where such forcings are referred to as 'source effects'.

6.1 Introduction

6.1.1 Seismic wave types

Monitoring seismic waves is crucial for understanding earthquakes and the Earth's internal structure. They can be classified into two wave types: body waves and surface waves (Stein and Wysession, 1991). Body waves traverse the Earth's inner layers, with Primary (P) waves and Secondary (S) waves being the two main types. P-waves are compressional, moving particles back and forth in the direction of wave travel, and are the fastest seismic waves, capable of traveling through both solid and liquid layers. S-waves are shear waves, moving particles perpendicular to the

wave's direction, slower than P-waves, and can only travel through solids (Stein and Wysession, 1991).

Surface waves, which travel along the Earth's surface, are typically more destructive due to their larger amplitude and lower frequency compared to body waves. They tend to arrive after body waves and can be categorised into two main types: Love waves and Rayleigh waves (Stein and Wysession, 1991) (Figure 6.1). Love waves cause horizontal ground motion, moving in a plane perpendicular to the direction of propagation. These waves result in horizontal shearing of the ground, which can severely damage structures, especially those that are not designed to withstand lateral forces. Love waves travel faster than Rayleigh waves but are confined to the Earth's surface (Stein and Wysession, 1991). Rayleigh waves have a more complex motion, moving in an elliptical pattern that involves both vertical and horizontal displacements in the vertical plane. Their movement is similar to that of ocean waves, rolling along the ground and causing the ground to move both up and down, as well as side to side. This rolling motion can cause significant damage to buildings and infrastructure by shaking them in multiple directions simultaneously.

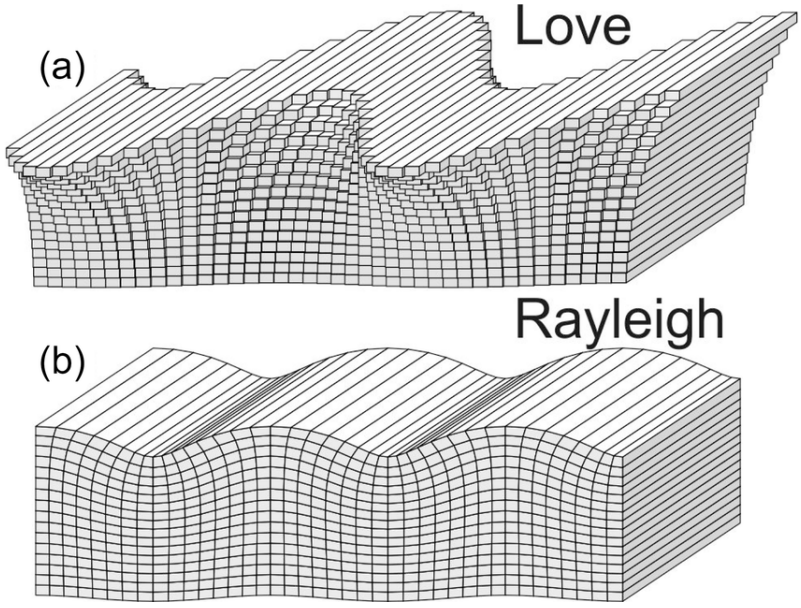


Figure 6.1: Ground displacement associated with (a) Love and (b) Rayleigh waves (Shearer, 2009; Burtin et al., 2016).

Seismic signals consist of both body and surface waves, which can be distinguished by their unique characteristics, such as relative magnitudes and polarizations. Surface waves, characterised by their lower frequency and larger amplitude, are especially powerful in shallow seismic events, leading to significant destruction despite their slower arrival compared to body waves. Shallow earthquakes generate stronger surface waves, while deeper earthquakes produce weaker ones. Understanding the behavior and characteristics of these waves is crucial for interpreting seismograms, assessing the impact of earthquakes, and developing building codes and construction practices aimed at mitigating damage during seismic events.

6.1.2 River-induced seismic signals

Seismic sensors, or seismometers, installed on the ground are capable of recording signals generated by various surface and near-surface processes that induce force

fluctuations, creating elastic waves that propagate through the surrounding medium. These processes encompass a wide range of natural events such as snow avalanches (Kishimura and Izumi, 1997), ocean storms (Gilmore, 1947), glacial activities (Ekström et al., 2003), and landslides (Kanamori and Given, 1982). Among these, fluvial processes are particularly significant, as demonstrated by Govi et al. (1993), who showed that such processes generate high-frequency (> 1Hz) ground vibrations that can be utilised for river monitoring.

The research by Govi et al. (1993) in a stream in the Gallina Valley, North West Italy, revealed that the average ground velocity near the stream closely correlated with the water level measured on the flood hydrograph. Moreover, they observed seismic energy peaks during the rising and falling limbs of the hydrograph signal, which were interpreted as the movement of coarse sediments. Since the early 21st century, numerous studies have corroborated the findings by Govi et al. (1993), identifying water flow (or turbulence) and sediment transport as the primary sources of river-induced ground motion.

In the past decade, seismic monitoring techniques have advanced significantly, from single sensor deployments to employing multiple sensors to analyse the spatial distribution of bedload movement (Schmandt et al., 2017). These methods also examine the spatial and temporal evolution of bedload transport by analysing phase delays between sensors (Burtin et al., 2010; Chao et al., 2015). These advancements have greatly enhanced our ability to monitor and understand fluvial processes through seismic data.

Seismic signals can be measured in three orthogonal directional components: North-South (N-S), East-West (E-W), and vertical. Each component of a seismic sensor captures different aspects of the signals, including the contributions from Rayleigh and Love waves. Rayleigh waves exhibit a strong vertical signal due to their elliptical polarization in the radial propagation direction, while Love waves vibrate purely in the transverse horizontal direction with no vertical component. Unlike Rayleigh waves, which only require a free surface, Love waves also depend on a waveguide to propagate.

Many of the previous fluvial seismology studies have focused on measuring seismic signals in only the vertical component, gathering information primarily about Rayleigh waves (e.g. Gaeuman, 2016). Others have recorded in all three components, though the majority of these studies have ultimately discarded the horizontal data, relying solely on the vertical component (e.g. Bakker et al., 2020). This approach assumes that horizontal forces are primarily driven by water flow processes, with shear stresses acting mostly parallel to the riverbed (Tsai et al., 2012), while bedload transport signals are more prominent in the vertical component. Idealised bedload transport motion associated with the saltation mode would impact the bed perpendicularly inducing a force normal to the riverbed preferentially generating Rayleigh waves (Barrière et al., 2015). Consequently, seismic bedload transport models (e.g. Tsai et al., 2012) discussed in earlier chapters have also focused exclusively on the vertical component, assuming the bedload signal is predominantly contained in Rayleigh waves. It is also important to note that the Rayleigh and Love wave components of the seismic signals will likely be influenced by path and site effects, which can alter the characteristics of the observed seismic signal.

However, these studies fail to account for the impacts of particles with the river bed in transport modes other than saltation, such as rolling or sliding, or the fact

that due to the flow of water particles are more likely to obliquely impact the river bed. A study by Roth et al. (2016) found that the horizontal components, especially the stream-parallel component, likely contain more information about bedload transport than the vertical component. Their research indicated that water discharge signals are strongest in the vertical and channel-parallel components, while bedload sediment transport predominantly causes ground motion in the channel-parallel direction at a seismometer located close to the river. Variations in transport modes, such as rolling and sliding, could be significant factors with the ability to generate horizontally polarised surface waves (Love waves) (Schmandt et al., 2013; Roth et al., 2016). Work by Schmandt et al. (2013) additionally found high power signals in the horizontal components in their data from Hance Rapid in Colorado where the horizontal and vertical spectra in the inferred signal from bedload transport were approximately equal. They briefly suggested that factors such as bed roughness and rolling or sliding transport mechanisms may contribute to the generation of Love waves. However, they do not go into detail about this and conclude their work by saying that Love and Rayleigh waves should be considered in bedload-flux seismic monitoring. In addition to the work by Roth et al. (2016) and Schmandt et al. (2013), Barrière et al. (2015) also found a strong river-induced seismic signal recorded in the horizontal components, however this time the horizontal signals resulted in a 10 dB increase in seismic power but a shift to approximately 10 Hz lower frequency content. Barrière et al. (2015) conclude their results based on the findings of Gimbert et al. (2014) and consider that the horizontal components are more sensitive to water flow processes than bedload transport. Although the mentioned studies have noted signals in the horizontal component, there has been limited exploration of its potential as a key method in fluvial seismology or seismic geomorphology.

6.1.3 HVSR method to understand site effects

An interesting method that is used within the field of earthquake seismology, particularly in engineering seismology, is the comparison of the proportion of horizontal seismic wave movement to vertical movement through what is referred to as the Horizontal-to-Vertical-Spectral-Ratio (HVSR or H/V). This is a passive method that is used to retrieve information about the shallow subsoil seismic properties (Guo et al., 2021; Xu and Wang, 2021). The method was first introduced by Nakamura (1989) for understanding site effects on seismic signals. It is calculated by finding the ratio between the horizontal and vertical components of a seismic signal from small ground vibrations. The simple method attracted a lot of attention for wide uses. HVSR is commonly used in engineering as it can be used to identify resonant frequencies of a site or of a building (Nakamura, 1989; Xu and Wang, 2021). This is particularly important in regions that are subject to regular seismic activity to ensure the buildings can withstand the shaking. The resonance frequency is the frequency that a material naturally vibrates at. The material amplifies incident waves with the same frequency upon contact. Seismic noise can excite the resonance and show as spikes in the frequency component of the signal at the resonant frequency. The resonance frequency is related to the layer thickness (depth to bedrock) and the average shear wave seismic velocity of the unconsolidated sediments, and therefore the HVSR can be used to determine to thickness or shear-wave velocity of the sediments that overly bedrock (Xu and Wang, 2021). It is also commonly used for

mineral exploration and for finding the shear-wave velocity structure of the near-subsurface. This is a passive method and so typically for these site explorations the focus is on using the seismic noise rather than an active seismic source, like an earthquake. When HVSR equals 1 at a particular frequency, it suggests that the ground motion in the horizontal direction is equal to the ground motion in the vertical direction at that frequency. This could be due to various factors, including the resonance of the site, the characteristics of the seismic waves, and the geological properties of the subsurface (Guo et al., 2021; Xu and Wang, 2021).

6.1.4 Chapter overview

It is clear that there needs to be more work looking at the comparison of the vertical and horizontal seismic signals acquired from near rivers when undertaking seismic bedload transport studies. Even though richness in the horizontal data has been identified in some previous studies (e.g. Schmandt et al., 2013; Barrière et al., 2015; Roth et al., 2016), in-depth comparisons of the vertical and horizontal signals have not been performed. In this chapter I test the applicability of the HVSR method for identifying the dominant component in bedload transport induced seismic signals, and whether this can shed light onto the transport processes occurring within the fluvial system. Although the HVSR is typically used for site characterisation within the field of engineering by analysing the frequency content, we are using it here to analyse the contributions of all three recorded components of a fluvial seismic signal over the duration of bedload transport events. This approach assumes that the ground response remains constant while the source varies, meaning that relative variations in the signals are more meaningful and informative than absolute values. In theory, based on work by Tsai et al. (2012) among others, the dominant wave type that would be generated by the assumed near-vertical component of force on the riverbed from saltating particles would be Rayleigh waves. Going by this assumption it would be expected that the seismic power in the horizontal components would be less than the vertical components when analysing a bedload-induced portion of the signal. Here I calculate the HVSR for a selection of key sites in the study reach over the two largest events recorded during the monitoring period in which we know bedload was being transported from the independent hydroacoustic data (Chapters 4 and 5). I share the results of the HVSR calculations and discuss the benefit of using this method and the dominance of directional components seen in the data recorded at the River Feshie.

6.2 Methods

6.2.1 Data

This chapter uses seismic, hydroacoustic and stream gauge data collected at the River Feshie study site as described in Chapter 3. All data used for this chapter has undergone the same processing steps as described in section 3.4. The seismic data instrument response has been removed from the data and the signal was converted into ground velocity values (units m/s). To analyse the frequency content of the signals the Fourier transform for the seismic spectra were calculated, as described in section 3.4.1. Example Fourier spectra for all three components (plotted as spec-

trograms) have been shown and described in detail in Chapter 4, section 4.3.2. The hydroacoustic data has had minimal processing as the recordings are saved as sound files that can be loaded directly into audio software. The stream gauge data used for this site, like the previous two data chapters, was recorded with the LiDAR sensor at SG2 (Figure 3.1). The distance from the sensor to the water surface was recorded once every 15 minutes in units of centimetres. Processing involved correcting for the depth of the water as described in section 3.4.2, converting to units of metres, and performing a rolling mean with a ten minute window to the data to smooth out erroneous spikes.

The two largest events captured (the September-October 2022 and October 2023 event as described in Chapter 4) are used for the work in this chapter to compare the directional dominance of seismic signals across two high flow bedload transport events. These two events also provide two different styles of high flows, with the September-October 2022 event consisting of a single peak in water levels and the October 2023 event consisting of three increasing peaks. Both events had local stream gauge data as well as hydroacoustic data. However, the hydrophone data was contaminated by a lot of instrument noise during the October 2023 event, particularly at moderate flows, which reduced the certainty in the independent identification of bedload transport initiation and cessation. As described in Chapters 4 and 5, the instrument noise dominated at moderate flows but once bedload was being transported these signals could be heard over the instrument noise. A start and end of bedload transport has been estimated using the data that was available, however there is uncertainty whether these reflect the actual first and last occurrence of bedload movement.

Not all of the eight geophones recorded during each of the selected events (Figure 6.2). I chose to perform the HVSR analysis on three common sites between the events (E_04, W_04, and W_07), as well as an additional site for each event. I included site W_05 for the September-October 2022 event as the initial HVSR analysis revealed that it had an unusual signal compared to the other sites. Site E_03 was included for the October 2023 event as it showed a strong initial HVSR signal. This site was not deployed until March 2023 and therefore could not be included for the September-October 2022 event. Although W_03 was recording for both events it is not included in the analysis in this chapter as from the work in Chapter 4 it was clear that this site was hardest to interpret with noisier signals and potentially stronger observed site effects.

6.2.2 Calculating HVSR of river-induced seismic signals

In simplified terms the HVSR is calculated as the amplitude of the horizontal component (H) divided by the amplitude of the vertical component (V) of a seismic signal ($\frac{H}{V}$). HVSR is proposed based on two assumptions: firstly, that its value is 1 at bedrock, i.e. horizontal and vertical waves travel the same (HVSR = $\frac{H}{V} = 1$); secondly, there is no amplification of the vertical component when the wave propagates from bedrock to the surface (Xu and Wang, 2021). However, assuming no vertical amplification is a simplification, as it may not hold true in environments where surface materials or complex subsurface structures influence seismic wave propagation.

Initial processing steps including converting from the default datalogger file type

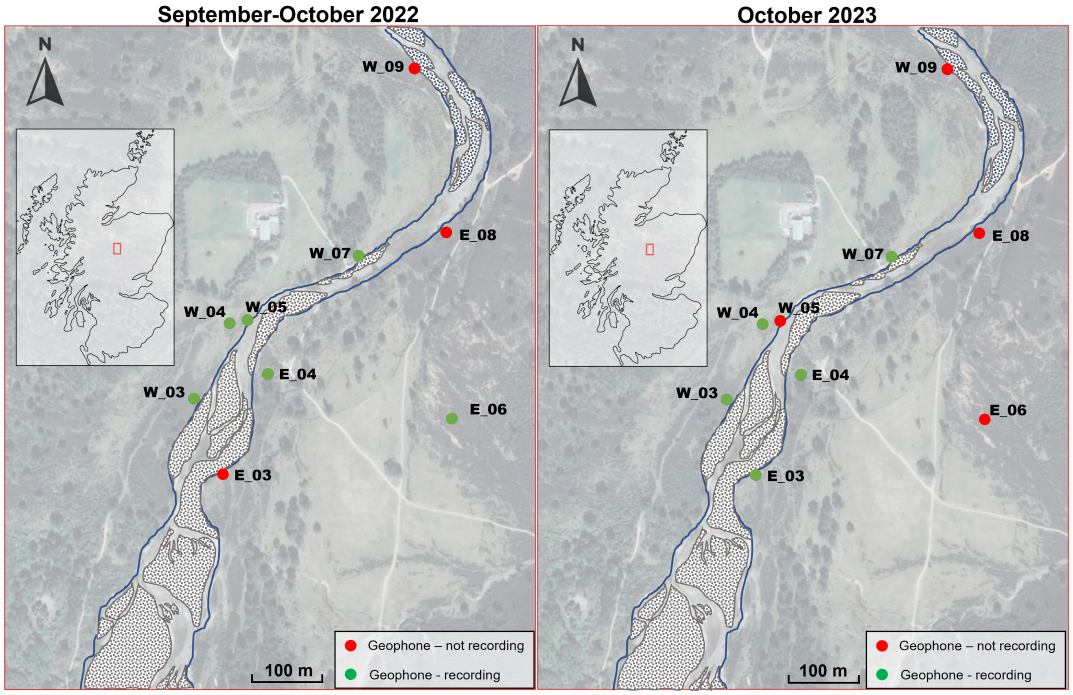


Figure 6.2: Map showing which geophone sites were recording during the events analysed in this chapter.

to miniSEED format and removing the instrument response were performed as described in Chapter 3, section 3.4. This data was subsequently divided into short time segments, and a Fast Fourier Transform (FFT) was applied to each segment to produce a series of spectra, or power spectral density (PSD) values. The geophones in this study recorded data in three components. As discussed in Chapters 3 and 4, the N-S component is aligned parallel to the river and the E-W component is aligned perpendicular to the river, thus providing information on the stream-parallel and stream-perpendicular signals. The components will be referred to a stream-parallel ($\parallel$) and stream-perpendicular ($\perp$) throughout this chapter. The HVSR calculation uses a single horizontal component and so I calculated the geometric mean of the stream-parallel and stream-perpendicular components PSD values in each time segment:

$$PSD_{av.}(f) = \sqrt{PSD_{\parallel}(f) \times PSD_{\perp}(f)} \tag{6.1}$$

where $PSD_{\parallel}(f)$ and $PSD_{\perp}(f)$ are the spectra in the time-frequency domain for the stream-parallel and stream-perpendicular components, respectively, and $PSD_{av.}(f)$ is the averaged horizontal component spectra in the frequency domain. The geometric mean was chosen as it is less sensitive to extreme values in the data and it maintains the consistency in the scales. This was performed on the Fourier spectra from the data processing steps, resulting in one 'averaged' horizontal Fourier spectrum. This 'averaged' horizontal component was then used the calculate the HVSR ($HVSR_{av.}$) by performing a simple division by the vertical component spectra (PSD_V):

$$HVSR_{av.} = \frac{PSD_{av.}}{PSD_V} \tag{6.2}$$

For this work, HVSR was calculated in the frequency and time domain as I was interested in analysing the frequency characteristics of this signal but also how this relationship varied with time over the hydrograph of a bedload transport event.

Additionally, I calculated the HVSR using just the stream-parallel or stream-perpendicular components (not averaging them) to identify whether there was a stronger signal in either horizontal direction:

$$HVSR_{\parallel} = \frac{PSD_{\parallel}}{PSD_V} \tag{6.3}$$

$$HVSR_{\perp} = \frac{PSD_{\perp}}{PSD_V} \tag{6.4}$$

where $HVSR_{\parallel}$ and $HVSR_{\perp}$ are the resulting HVSR spectra using the stream-parallel and stream-perpendicular components, respectively.

The HVSR spectra could then either be analysed for their frequency or time characteristics through plotting as a colour map image with axes of frequency and time and colour scale of HVSR value. This is similar to the spectrograms in Chapters 4 and 5 (e.g. Figure 4.3) but with the HVSR value as the colour scale instead of the seismic power. To gain a better understanding of the frequency characteristics of the site the HVSR could be plotted as a simple function of frequency. This is commonly used to identify site characteristics of the point location such as the resonance frequency. However, for this study we are interested in the temporal evolution of the HVSR during fluvial bedload transport events that can be observed and compared to the timeseries of stage data measured at SG2. Therefore, instead of calculating the HVSR as a function of frequency, I calculated it as a function of time, slicing for frequency bands of interest. By looking at the initial spectrograms of the three components of the data in Chapter 4 (shown further here), as well as using the analysis from Chapter 5, I identified the dominant frequency bands in the signals at each site. These selected bands are then used to subset the seismic data to analyse the contributions from the horizontal and vertical components in the two dominant fluvial processes. The HVSR values for these bands are calculated by averaging across the frequency range chosen.

6.3 Results

6.3.1 HVSR observations from seismic signals at the River Feshie using the averaged horizontal components

Here I discuss the resulting HVSR values for the chosen events and sites using the 'averaged' horizontal component. The specific characteristics of the seismic recordings in all three components for each site have been described in detail in Chapter 4, but I will give a brief overview of these signals again here.

All events show a weak constant signal throughout the plotted periods, generally at frequencies up to 40 Hz, which has been interpreted in earlier chapters to be the flow turbulence signal, which increases in seismic power as the water levels increase. Additionally, all sites show a higher frequency signal (typically greater than 40 Hz) present only during the higher water levels which, when compared with independent hydroacoustic data, has been interpreted as the signal from bedload transport in earlier chapters. The exact frequency content of these turbulence and bedload bands varies between site but with broadly similar limits. The frequency bands selected for the HVSR analysis are analysed for their characteristics in this section and interpreted in the discussion section.

The occurrence of bedload transport found from the hydroacoustic data are included in these figures as pale pink and beige blocks and dashed lines to compare to the HVSR outputs. These transport periods are described in detail in Chapter 5. To summarise: during the September-October 2022 event, two distinct phases of bedload transport were observed. These phases were distinguished by a shift in audible frequency and are classified as 'phase 1' (pale pink) and 'phase 2' (beige) transport. In contrast, the October 2023 event did not exhibit this frequency shift in the hydroacoustic data. As a result, it only has 'phase 1' transport.

6.3.1.1 September-October 2022 event

As shown in Figure 6.2, six geophones were recording during the September-October 2022 event, one being the control site E_06. As mentioned in section 6.2.1, sites E_04, W_04 and W_07 were chosen as the common sites between this event and the October 2023 event. Additionally, site W_05 is included for this event as it has been a key site for analysis throughout the rest of this thesis. All sites (E_04, W_04, W_05 and W_07) show a clear correlation between the seismic signal recorded in all three components and the change in water levels during the September-October 2022 event (Figures 6.3, 6.4, 6.5, and 6.6). There is a distinct increase in seismic power, shown by the red colours, during increased water levels. This increased seismic power spans frequencies of about 15-85 Hz.

E_04

Looking at the data in Figure 6.3e for site E_04, it is clear that the HVSR reveals some information about the event. There appears to be an increase in HVSR values (greater horizontal signal) from approximately 5-30 Hz and 40-60 Hz at the time of bedload transport initiation as found through the hydroacoustic data (pale pink dashed line in Figure 6.3e). There is an even stronger signal in the 40-60 Hz range that starts when the second phase of bedload transport occurs, which was interpreted in Chapter 5 to be when larger grain sizes were being transported. These high HVSR values slowly decrease as the water levels drop on the gradual falling limb of the hydrograph. The end of the transport period as identified from the hydroacoustics does not line up clearly with the end of the high HVSR values but since they decline slowly it is challenging to select an end point. Chapter 4 discussed these signals in more detail and explained how we selected different frequency bands for the analysis of bedload transport and turbulence signals. In the data for E_04 (Figure 6.3), there appears to be a distinct banding at 15-30 Hz and 35-55 Hz. This is seen in the signals in the lead up to the high water levels as well as faintly following the drop in water levels. This is likely a site effect due to the resonant frequency and scattering of waves in the substrate at this site. However, as discussed in Chapters 2 and 4 and shown through the increased frequency range of these bands during high flows in Figure 4.17, there are likely bedload and turbulence signals that can be distinguished by dominant frequency ranges but challenged by overlapping frequencies (Figure 4.3).

For the analysis of how the HVSR values vary over the duration of the event we have chosen the frequency ranges of 15-35 Hz and 40-60 Hz as they show distinct signatures in the 'averaged' HVSR values in Figure 6.3e. Figure 6.3f shows the 'averaged' HVSR values across the 15-35 Hz and 40-60 Hz frequency ranges. These values have been smoothed out using a rolling mean with a 10 minute window. This reveals a sharp increase in both the lower frequency and higher frequency signal

at the same time as bedload movement is first identified in the hydroacoustic data (12:00-12:15 on the 30th September 2022). Both these HVSR values are lower prior to the event than in the low water levels following the peak. However, the low frequency signal appears to actually begin rising around 11:30, shortly after the water levels have just begun to rise. It continues to rise sharply until the start of the second transport phase and just before the peak in water level, at which point it begins to fall and the horizontal signal becomes weaker. This decrease in HVSR, although quite quick, is less steep that the rising limb and continues to fall until around 18:00 and then remains constant over the remainder of the falling limb of the hydrograph. At no point the 15-35 Hz band drops below the HVSR = 1 line, illustrating a strong horizontal dominance of the river-induced seismic signal.

As already mentioned the 40-60 Hz HVSR shows a strong increase from just below 1 (where the vertical signal dominates over the horizontal signal) that coincides with the initiation of bedload transport from the hydracoustic data. This ratio generally increases very sharply up until around 14:00 on the 30$^{\text{th}}$ September, at which point the values begin the level off and remain fairly constant at around HVSR = 6.5. This coincides with the peak of the hydrograph and the transport of the larger grains. However, this HVSR value does not decrease with the falling limb of the hydrograph but remains at this level until around 19:00 shortly before the end of bedload mobilisation before gradually returning towards base levels over the course of the remaining 17 hours plotted. Other than a dip prior to the rising limb and a couple irregular dips following the high water levels, the bedload HVSR does not drop below the HVSR = 1 line, again showing a very strong horizontal seismic signal.

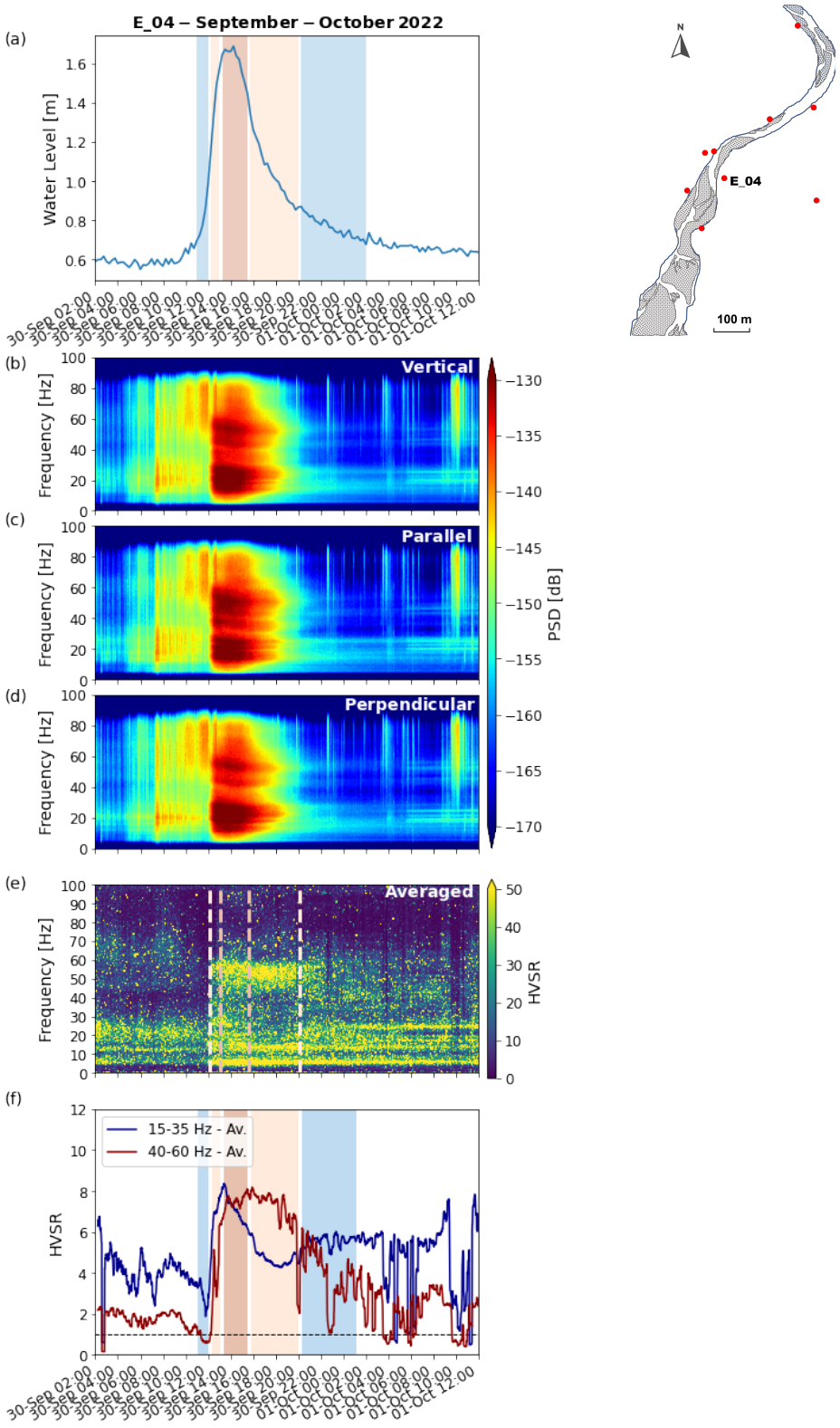


Figure 6.3: (a) Hydrograph from local stream gauge (SG2), with three plots showing the spectrograms of the seismic signal recorded at site E_04 during the September-October 2022 event in (b) the vertical component, (c) the stream-parallel component, and (d) the stream-perpendicular component. (e) The resulting HVSR values in frequency and time using the 'averaged' horizontal component and the vertical component. (f) The 'averaged' HVSR in the 15 - 35 Hz and the 40 - 60 Hz frequency ranges. The pale pink and beige blocks in (a) and (f) correspond to the hydroacoustically observed periods of bedload transport as described in Chapter 5, with the dashed lines of corresponding colour in (e) indicating the onset and arrest of these transport phases. The inset map on the right shows the location of this site in relation to the other geophone sites in the study reach.

W_04

Site W_04 shows some similarities in the HVSR for the two frequency bands as E_04, with an increase in both during the high water levels. However, W_04 shows a much weaker HVSR for the lower frequency band. From the spectrograms the lower frequency range was selected as around 10-60 Hz but for the HVSR calculation I selected a smaller range that included the strongest portion of the signal (15-35 Hz). In Figure 6.4e this frequency range shows no distinct change in HVSR values as the water levels begin to rise. This is also evidenced in Figure 6.4f, where the 'averaged' 15-35 Hz HVSR sits close to HVSR = 1 prior to the increase in water level and only increases up to around HVSR = 2 during the event. However, this increase does coincide with the increase in water level. This slightly increased value of HVSR remains constant throughout the peak of the event and only very gradually begins to decrease once bedload transport has stopped (according to the hydroacoustic data).

In comparison, the higher frequency signal, which dominates at around 60-80 Hz in Figure 6.4, shows a strong correlation between HVSR, water level and hydroacoustic data. Figure 6.4e shows a strong increase in HVSR for the 60-80 Hz frequency range that coincides with the onset of bedload transport from the hydroacoustic data. These values remain strong over the duration of the hydrographic peak and over the bedload transport period before showing a gradual decrease over the remainder of the falling limb of the hydrograph following the cessation of bedload transport. Figure 6.4f highlights this behaviour, showing a very sharp increase in HVSR that coincides with the onset of bedload transport as identified with the hydroacoustic data. Prior to this increase the 60-80 Hz HVSR was near a value of 1. Similar to E_06, this sharp increase continues until just before the peak of the hydrograph at which point the second phase of bedload transport begins. Again this HVSR value remains fairly constant over the peak of the event and throughout the period of bedload transport before dropping fairly quickly at the end of the transport period at around 19:30 on the 30th September. However, unlike E_04 there is a slight dip in the HVSR value during the transport of the larger grains (darker beige colour in Figure 6.4f). Following the transport of bedload, the HVSR gradually decreases back towards HVSR = 1.

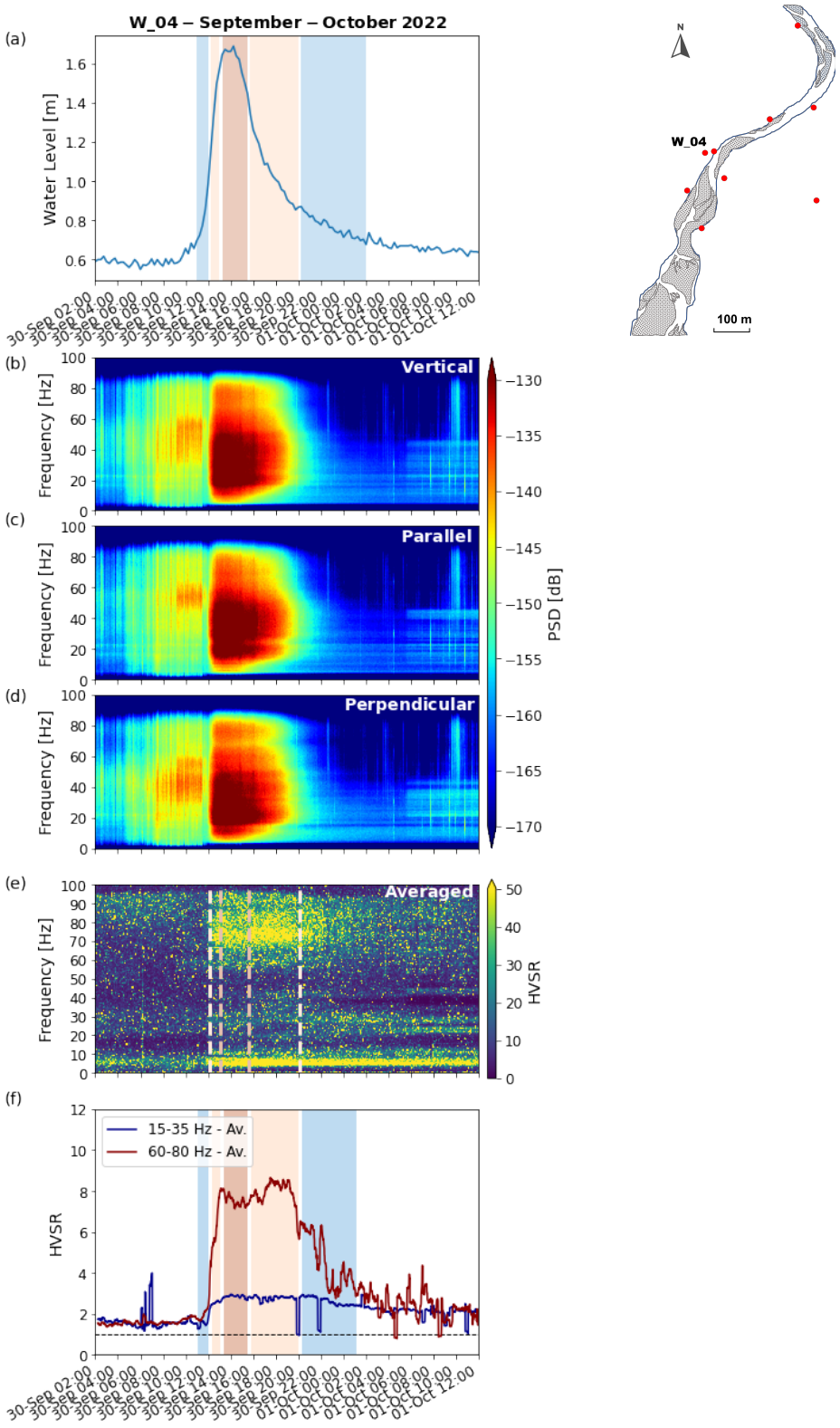


Figure 6.4: (a) Hydrograph from local stream gauge (SG2), with three plots showing the spectrograms of the seismic signal recorded at site W_04 during the September-October 2022 event in (b) the vertical component, (c) the stream-parallel component, and (d) the stream-perpendicular component. (e) The resulting HVSR values in frequency and time using the 'averaged' horizontal component and the vertical component. (f) The 'averaged' HVSR in the 15 - 35 Hz and 60 - 80 Hz frequency ranges. The pale pink and beige blocks in (a) and (f) correspond to the hydroacoustically observed periods of bedload transport as described in Chapter 5, with the dashed lines of corresponding colour in (e) indicating the onset and arrest of these transport phases. The inset map on the right shows the location of this site in relation to the other geophone sites in the study reach.

W_05

The spectrograms (Figures 6.5b-d) of site W_05 show very similar signals to those of the previous two sites discussed, with a sharp increase in seismic power in two frequency bands (15-40 Hz and 40-80 Hz) as the water level begins to rise and bedload transport (as identified from the hydroacoustic classifications) initiates. However, the horizontal and vertical signals are very similar in seismic power particularly for the higher frequency range of 40-80 Hz resulting in a very different HVSR signal than sites E_04 and W_04 (Figure 6.5e). Here the HVSR values for the lower frequency (15-40 Hz) band is much stronger than for the 40-80 Hz band, however both show fairly constant values over the course of the full period plotted. Although the HVSR values for the two frequency bands are quite different, there is no obvious change in HVSR in Figure 6.5e as the water level increases for either band. For the HVSR analysis over time frequencies of 20-30 Hz and 50-60 Hz were selected from within the larger distinct HVSR band identified in Figure 6.5e. Figure 6.5f shows that the 20-30 Hz signal has much higher HVSR values than the 50-60 Hz signal starting at around HVSR = 6 prior to the change in water level. Following the increase in water level and initiation of bedload transport from the hydroacoustic data, the HVSR value for the 20-30 Hz band drops slightly over the course of the transport period reaching HVSR value of around 2.8. As the transport period comes to an end and water levels continue to fall, the 20-30 Hz HVSR begins to rise again, but it does not stay constant at around HVSR = 6 like prior to the event; it instead slowly drops back down to around 4. The 50-60 Hz HVSR shows a similar drop as bedload transport starts at around 12:00 on the 30th September, however the value is consistently below HVSR = 1 throughout the whole plotted period. Once the HVSR value drops to around 0.4 it remains at this level and doesn't rise back up to the levels observed before the water level rise.

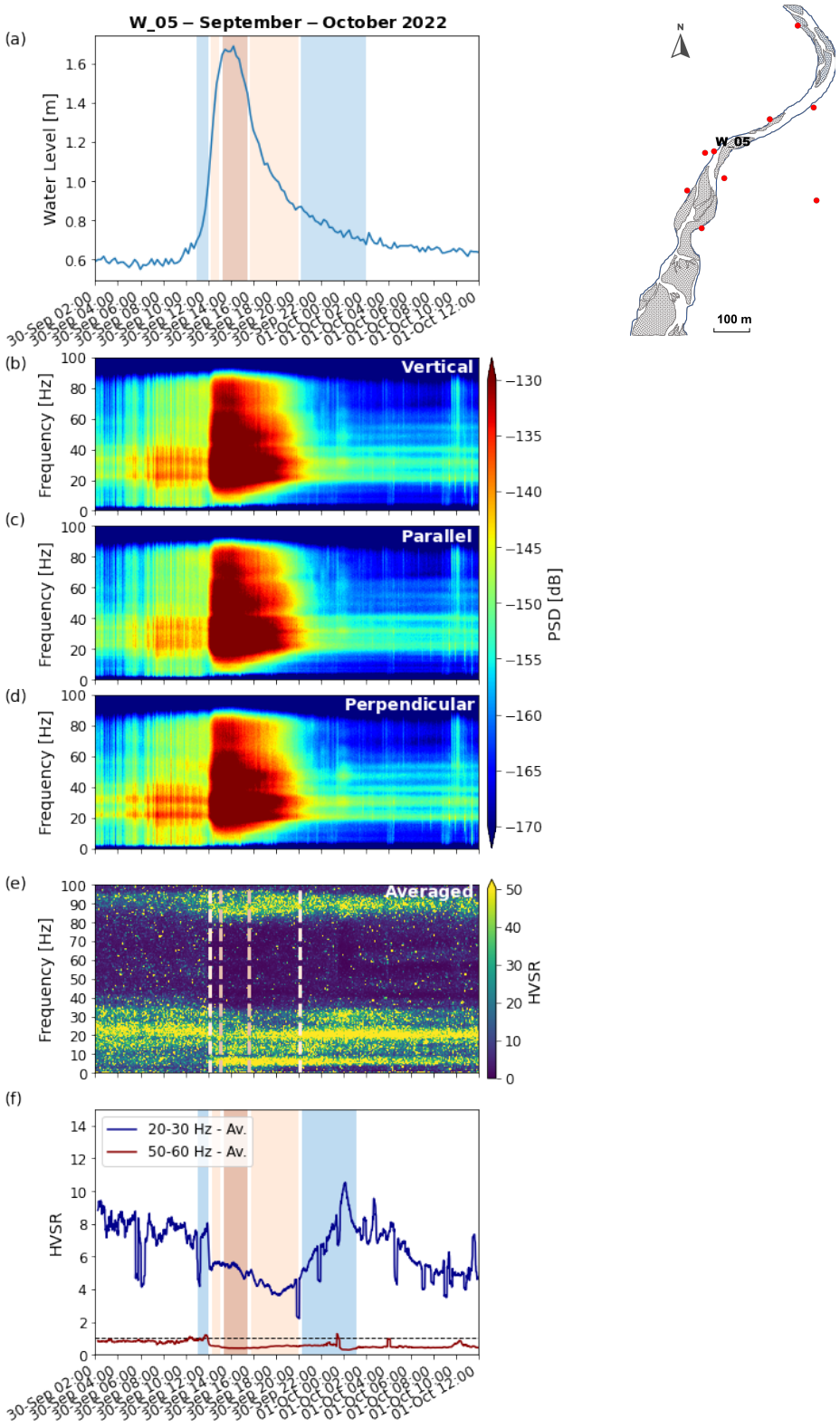


Figure 6.5: (a) Hydrograph from local stream gauge (SG2), with three plots showing the spectrograms of the seismic signal recorded at site W_05 during the September-October 2022 event in (b) the vertical component, (c) the stream-parallel component, and (d) the stream-perpendicular component. (e) The resulting HVSR values in frequency and time using the 'averaged' horizontal component and the vertical component. (f) The 'averaged' HVSR in the 20 - 30 Hz and 50 - 60 Hz frequency ranges. The pale pink and beige blocks in (a) and (f) correspond to the hydroacoustically observed periods of bedload transport as described in Chapter 5, with the dashed lines of corresponding colour in (e) indicating the onset and arrest of these transport phases. The inset map on the right shows the location of this site in relation to the other geophone sites in the study reach.

W_07

As discussed in Chapters 4 and 5, the spectrograms of seismic data (Figure 6.6 b-c) recorded during the September-October 2022 event at site W_07 reveal an interesting frequency shift in all three components during the peak period of bedload transport, which is not visible on the other sites. Figure 6.6e also reveals this frequency shift in the calculated HVSR. There appears to be two dominant frequency bands here, 5-40 Hz and a 70-80 Hz band that drops to 40-65 Hz during the peak of the event, that both experience this frequency shift. The sharp dip in frequencies in both bands coincides well with the rising water levels and the onset of bedload transport from the hydroacoustic data. The dip from 70 Hz to 40 Hz begins at the first pale pink dashed line and returns to around 70-80 Hz following the cessation of bedload transport (second pink dashed line). Two frequency bands within these were chosen to subset the HVSR data: 15-30 Hz and 40-80 Hz. Figure 6.5f shows that generally the 15-30 Hz signal has a greater HVSR than the 40-80 Hz signal, except for during the peak of the transport event. The 15-30 Hz HVSR increases as water levels begin to rise at the start of the event but dip sharply during the peak of the hydrograph at which point transport phase 2 is occurring. The HVSR value increases following this intense transport period and continues fairly constant throughout the remaining 26 hours. The 'averaged' 40-80 Hz HVSR shows an very clear response to the two phases of bedload transport. Prior to the increase in water levels the 40-80 Hz HVSR is very constant at around 2. It then begins to increase as the water levels rise and the transport of bedload initiates. As the transition between the two bedload transport phases occur the 40-80 Hz HVSR dramatically increases from around 4 to 12 in a 30 minute period. It continues to experience a gradual increase up to 14 during the second phase of bedload transport, before very rapidly dropping back down to a value of 4 at the point at which it transitions back to the first phase of bedload transport. From here the HVSR very gradually decreases back towards a value of 2 by 02:00 on the 1st October over the falling limb of the high flow event.

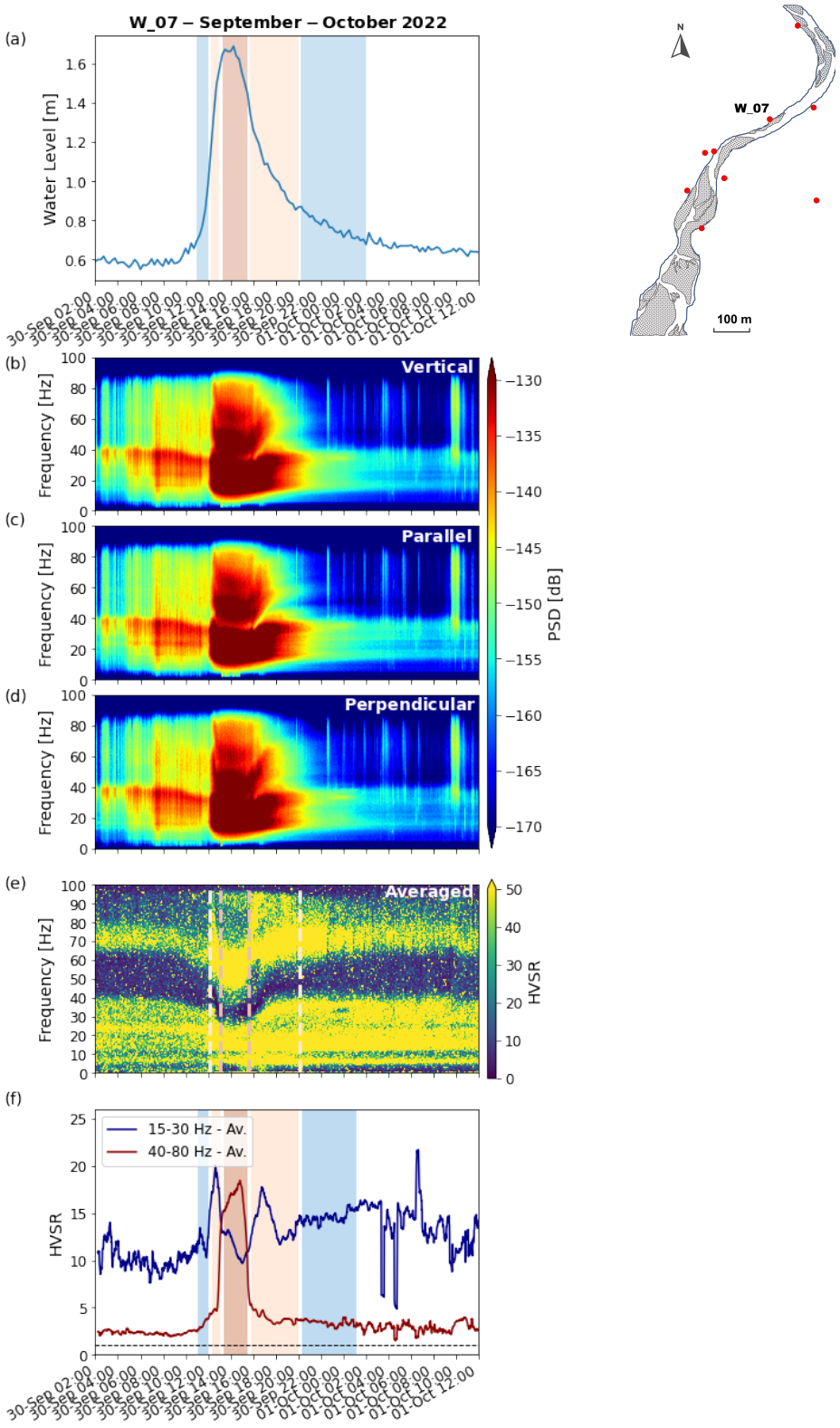


Figure 6.6: (a) Hydrograph from local stream gauge (SG2), with three plots showing the spectrograms of the seismic signal recorded at site W_07 during the September-October 2022 event in (b) the vertical component, (c) the stream-parallel component, and (d) the stream-perpendicular component. (e) The resulting HVSR values in frequency and time using the 'averaged' horizontal component and the vertical component. (f) The 'averaged' HVSR in the 15 - 30 Hz and 40 - 80 Hz frequency ranges. The pale pink and beige blocks in (a) and (f) correspond to the hydroacoustically observed periods of bedload transport as described in Chapter 5, with the dashed lines of corresponding colour in (e) indicating the onset and arrest of these transport phases. The inset map on the right shows the location of this site in relation to the other geophone sites in the study reach.

6.3.1.2 October 2023 event

During the October 2023 event five geophones successfully recorded data as shown in Figure 6.2. The three common sites with the September-October 2022 event (E_04, W_04, and W_07) along with the additional site of E_03 are analysed for this event. This section will discuss the seismic signals and calculated HVSR values for each of these sites in detail. Further in depth analysis and interpretations of these spectrograms are included in Chapter 4. Overall, all four sites show clear correlations between the seismic signals recorded in all three components and the change in water level (Figures 6.7a-d, 6.8a-d, 6.9a-d, 6.10a-d). There is a distinct increase in seismic power, shown by the deep red colours, during increased water levels. This increased seismic power spans frequencies of about 15-85 Hz for E_04, W_04 and W_07, but extends as low as 5 Hz at E_03. All events show a constant signal at frequencies of up to 60 Hz throughout the plotted periods, which increases in seismic power as the water levels increase. Additionally, all sites show a higher frequency signal present only during the higher water levels. The occurrence of bedload transport found from the hydroacoustic data are included in these figures as pink and beige blocks and dashed lines to compare to the HVSR outputs. As discussed in Chapters 4 and 5, the hydroacoustic data recorded during the October 2023 event is contaminated by a lot of instrument noise, particularly at moderate flows, and thus made the identification of transport initiation and cessation more challenging. However the period where bedload particles could be distinguished in the recordings is included for this event to give an indication of the start and stop of bedload motion.

E_03

E_03 shows a constant signal throughout the full duration plotted at around 5-20 Hz in the spectrograms (Figure 6.7b-d). This signal has power of around -150 dB to -145 dB at low water levels and increases significantly to greater than -130 dB during the water level peaks in the hydrograph in Figure 6.7a. During these hydrographic peaks the frequency range of the high power seismic signal extends up to around 70 Hz, which undulates with changing water levels over each of the three peaks. The spectrograms of the recordings at this site look fairly similar for each of the three components, but with the stream-parallel component showing the strongest signal at 5-30 Hz.

The calculated HVSR values for this site (Figure 6.7e) show one very strong band at 5-10 Hz and a weaker and broader band at 20-60 Hz. The high HVSR values at 5-10 Hz are constant over the full three days plotted. The 20-60 Hz range, however, shows some correlations with the peaks in the hydrograph. Here we see lower HVSR values prior to the first peak in water level and then subsequent increases in the HVSR values over the duration of the three individual peaks. From Figure 6.7e it is hard to identify any obvious connections between the hydroacoustic derived bedload transport initiation and cessation (dashed lines) and the changes in HVSR values in either frequency band. For the lower frequency signal, a frequency band of 5-15 Hz was selected as this included a portion of the constant high HVSR signal up to 10 Hz along with a portion of the constant low HVSR values at 10-15 Hz. Additionally, the 50-60 Hz band was selected as it showed the strongest signal within the 20-60 Hz band mentioned earlier. Figure 6.7f, shows that there is a very small correlation with the bedload transport period and the HVSR variations for the frequency band of 5-15 Hz. The HVSR value for this band starts at around

HVSR = 2 and gradually rises to around HVSR = 4 during the first peak in water level. It then undulates back and forth of HVSR = 3-4 over the following two water level peaks before returning back to HVSR = 2 at 12:00 on 9th October when water levels reach 0.77 m. This undulation in values does not appear to coincide with the water level peaks, and therefore doesn't appear to show a correlation with changing water levels. The 50-60 Hz HVSR is on average much greater than the 5-15Hz HVSR starting at 4 and increasing up to 8 during the three peaks in water level. There is a clear increase in HVSR after 06:00 on the 7th October which coincides with when the first bedload motion was recorded on the hydrophone, although as mentioned above these recordings were interrupted by instrument noise and so these transport thresholds are estimates. There are then two subsequent peaks in HVSR that occur at the same time as the increased water levels, however the peak in HVSR for all three peaks occurs after the peak in water levels during the falling limbs of the hydrograph. The 50-60 Hz HVSR returns back to around 4 at 06:00 on the 9th October when water levels reach 0.87 m.

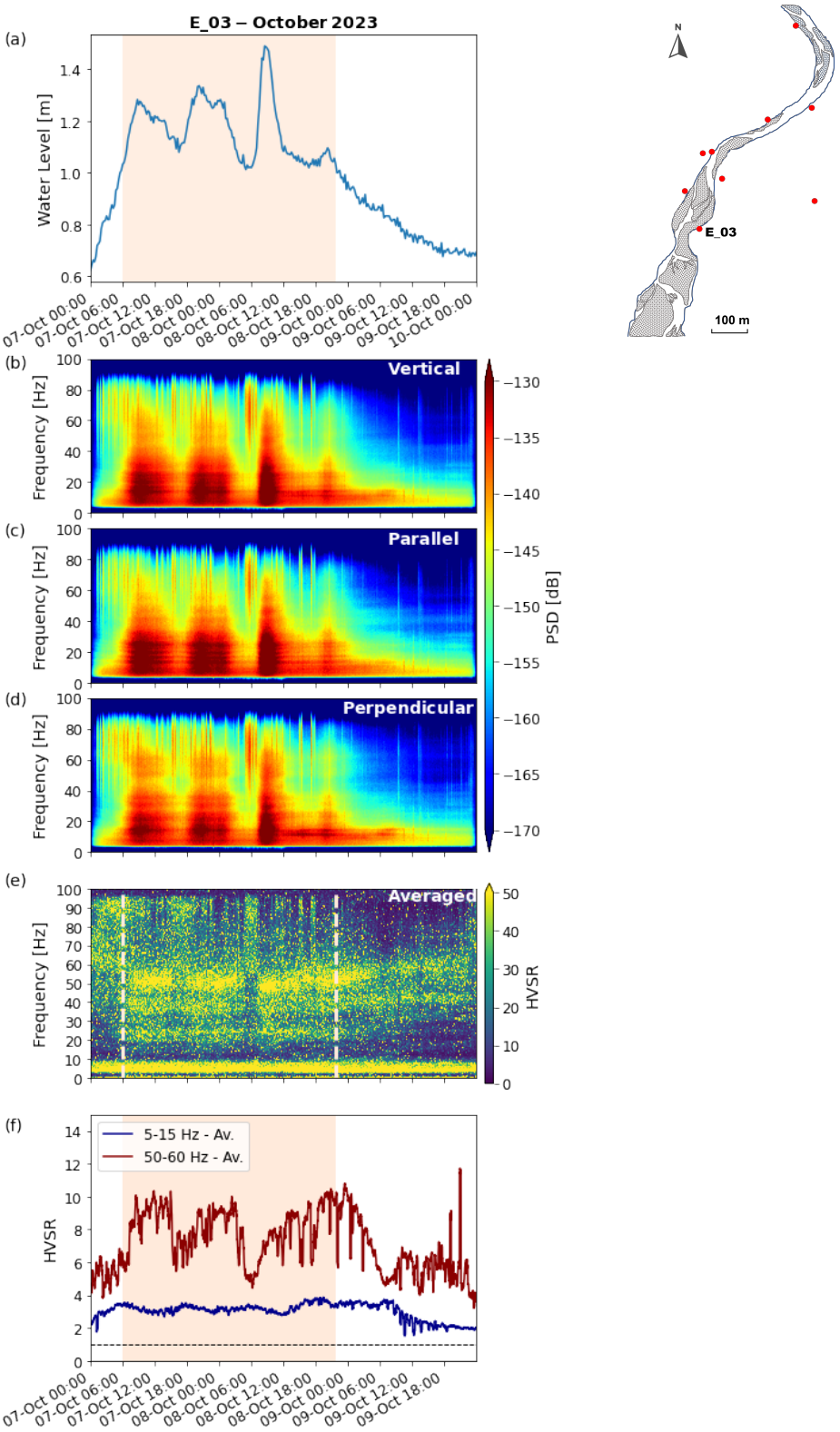


Figure 6.7: (a) hydrograph from local stream gauge (SG2), with three plots showing the spectrograms of the seismic signal recorded at site E_03 during the October 2023 event in (b) the vertical component, (c) the stream-parallel component, and (d) the stream-perpendicular component. (e) The resulting HVSR values in frequency and time using the 'averaged' horizontal component and the vertical component. (f) The 'averaged' HVSR in the 10 - 15 Hz and 50 - 60 Hz frequency ranges. The pale pink blocks in (a) and (f) correspond to the hydroacoustically observed periods of bedload transport as described in Chapter 5, with the dashed lines of corresponding colour in (e) indicating the onset and arrest of bedload transport. The inset map on the right shows the location of this site in relation to the other geophone sites in the study reach.

E_04

Similar to the September-October 2022 event, E_04 shows strong seismic power at 10-70 Hz that coincides with the three peaks in water level of the October 2023 event (Figure 6.8a-d). This occurs at two distinct frequency bands, 15-35 Hz and 40-60 Hz, with the lower frequency band also showing a faint continuous signal even during low flows. All three components show a similar signal with the stream-parallel component exhibiting the strongest power across the two bands.

The HVSR values shown in Figure 6.8e and f, similar to site E_03, show a correlation with the three peaks in water level particularly at frequencies of 40-60 Hz. The initial increase in HVSR in this band occurs shortly after the estimated onset of bedload transport from the hydroacoustic data. There are also evident drops in HVSR between the hydrograph peaks in this frequency range. Following the approximate end of bedload transport at 21:45 on the 8th October, the HVSR value at 40-60 Hz gradually decreases. The HVSR values in the 15-35 Hz band shows a fairly constant signal across the full three day duration with no obvious variations coinciding with the changes in water level. Figure 6.8f highlights this, showing that the 'averaged' HVSR at 15-35 Hz is around a value of 4 throughout the entire three days. There is a slight increase in this value prior to the first water level peak and then very small increased HVSR values (up to a value of 5) during the three water level peaks. The 'averaged' HVSR at 40-60 Hz shows a stronger correlation with the hydrograph with an increase from below HVSR = 1 up to around HVSR = 14 over the three water level peaks. The initial increase in HVSR occurs coincidentally with the onset of bedload transport estimated from the hydroacoustic data. The estimated end of bedload transport does not align with any abrupt changes in HVSR for the 4-60 Hz range, instead the HVSR shows a gradual decrease over the falling limb of the hydrograph only approaching values of HVSR = 1 again towards the very end of the recording period.

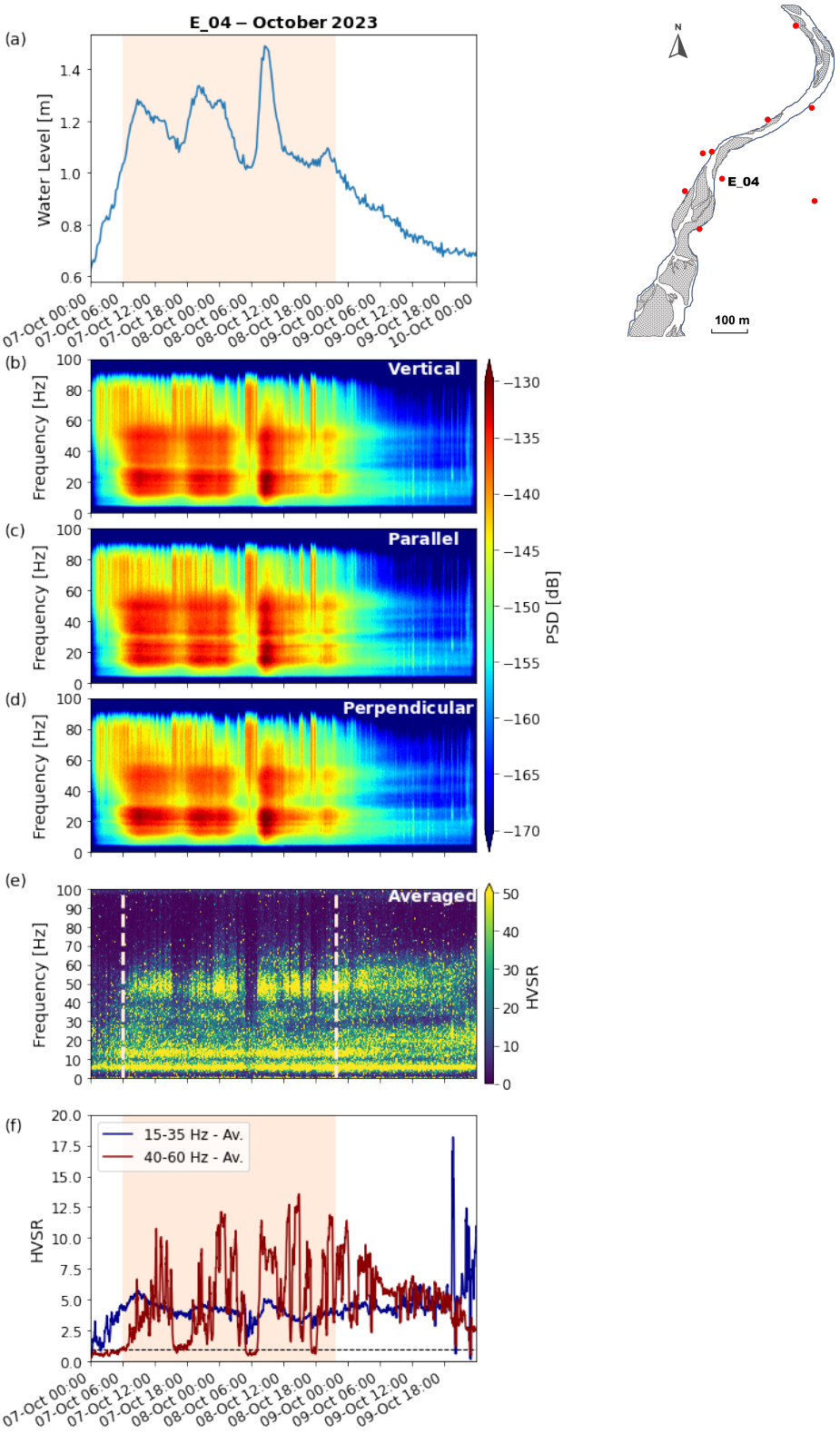


Figure 6.8: (a) hydrograph from local stream gauge (SG2), with three plots showing the spectrograms of the seismic signal recorded at site E_04 during the October 2023 event in (b) the vertical component, (c) the stream-parallel component, and (d) the stream-perpendicular component. (e) The resulting HVSR values in frequency and time using the 'averaged' horizontal component and the vertical component. (f) The 'averaged' HVSR in the 15 - 35 Hz and 60 - 80 Hz frequency ranges. The pale pink blocks in (a) and (f) correspond to the hydroacoustically observed periods of bedload transport as described in Chapter 5, with the dashed lines of corresponding colour in (e) indicating the onset and arrest of bedload transport. The inset map on the right shows the location of this site in relation to the other geophone sites in the study reach.

W_04

At W_04 there is a clear banding of seismic signals observed in the spectrograms of all three components with one higher frequency band (60-80 Hz) and one lower frequency band (15-50 Hz) (Figure 6.9b-d). All three components visually show very similar seismic power and frequency characteristics, and all three show good correlation between increased seismic power and increased water level.

The HVSR values plotted in frequency and time (Figure 6.9e) show similar bands to the spectrograms however the higher frequency band shows increased HVSR values at 65-80 Hz band and the lower frequency band shows much smaller values. There is the addition of a very strong HVSR band at 5-8 Hz, but since this was not present in the spectrograms this is likely not a river-induced signal. Unlike the lower frequency band, the 65-80 Hz band shows some correlation with changing water levels, with slightly decreased values between the water level peaks. This is further evidenced in Figure 6.9f where we see the average HVSR across the 15-35 Hz band exhibiting a very constant value of around 3 throughout the entire three day period with no fluctuations with changing water levels. The HVSR averaged over 60-80 Hz shows a stronger correlation with changing water levels showing an increase from around 2 to 10 during the three water level peaks, with a large dip in HVSR between the second and third water level peak. The increases in HVSR are not as clearly defined and correlated with water levels as was observed for site E_03. The initial increase in the 60-80 Hz HVSR coincides with the estimated onset of bedload transport from the hydroacoustic data, however the HVSR does not show an abrupt decrease coinciding with the estimated arrest of bedload transport from the hydroacoustic data. Instead the HVSR shows a gradual decrease back down to a value of 3 over the 26 hours following the estimated end of bedload transport.

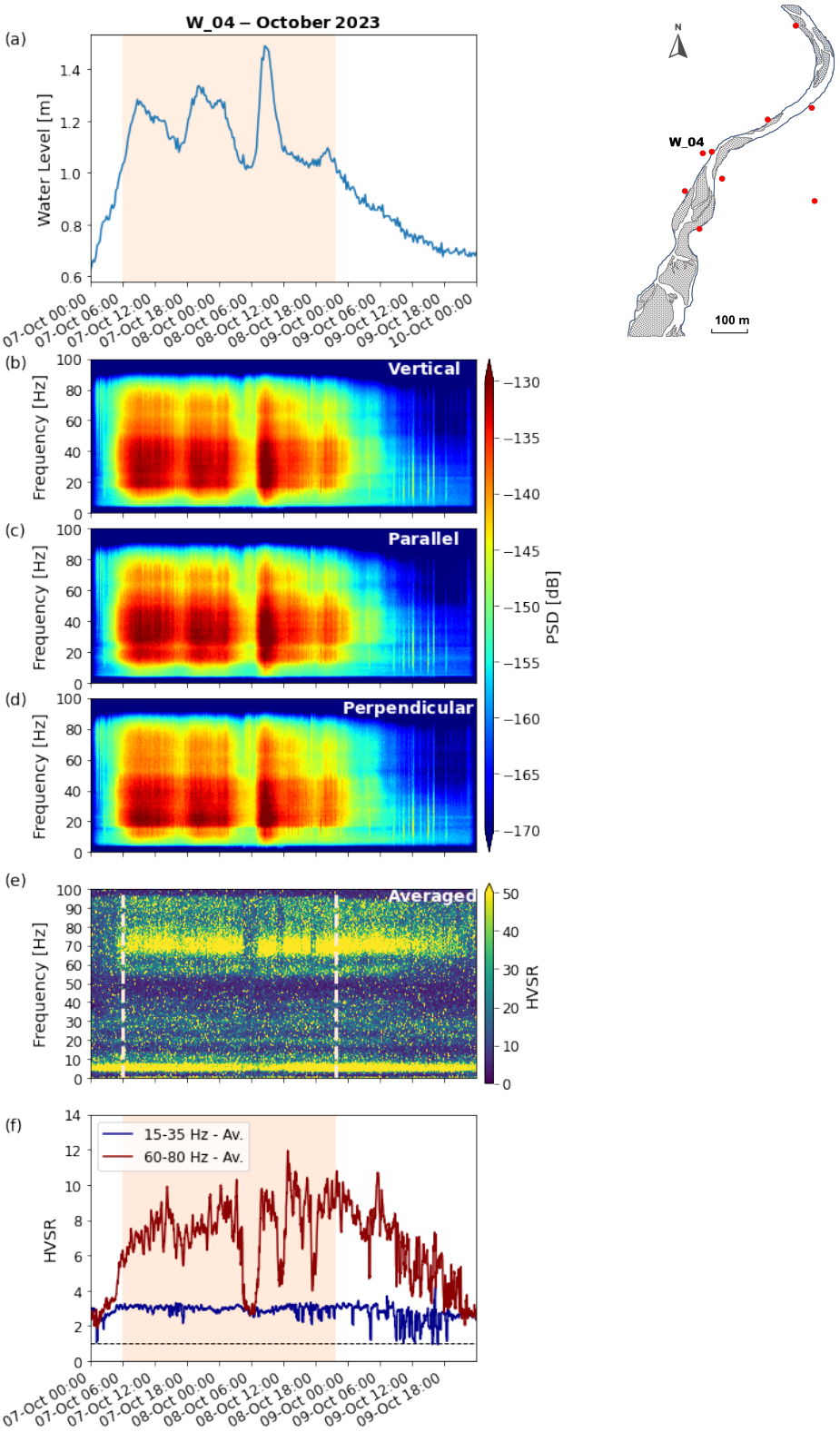


Figure 6.9: (a) hydrograph from local stream gauge (SG2), with three plots showing the spectrograms of the seismic signal recorded at site W_04 during the October 2023 event in (b) the vertical component, (c) the stream-parallel component, and (d) the stream-perpendicular component. (e) The resulting HVSR values in frequency and time using the 'averaged' horizontal component and the vertical component. (f) The 'averaged' HVSR in the 15 - 35 Hz and 60 - 80 Hz frequency ranges. The pale pink blocks in (a) and (f) correspond to the hydroacoustically observed periods of bedload transport as described in Chapter 5, with the dashed lines of corresponding colour in (e) indicating the onset and arrest of bedload transport. The inset map on the right shows the location of this site in relation to the other geophone sites in the study reach.

W_07

Similar to what was observed for the September-October 2022 event, W_07 again shows a correlation between increase seismic power in two frequency bands and the changing water levels and identified bedload transport from hydroacoustic data (Figure 6.10a-d). This site again shows the interesting frequency shift in the data during the water level peaks as observed in the September-October 2022 event. As discussed in more detail in Chapter 4, this frequency shift is most noticeably observed in the second and third peaks of the October 2023 event, which are also the larger two peaks. Visually observed in the spectrogram, the seismic signals look very similar in all three components in terms of their amplitude and frequency characteristics.

The HVSR values as a function of frequency and time reveal the same two distinct bands as can be observed in the spectrograms, 15-40 Hz and 40-80 Hz (Figure 6.10e). The three event peaks can be seen on the HVSR data with increases in the 40-80 Hz band during the increased water levels, particularly noticeable in the 40-70 Hz range. The initial increase in HVSR at around 06:00 on the 7th October coincides with the estimated onset of bedload transport from the hydroacoustic data. The HVSR values from 5-40 Hz appear to remain fairly constant throughout the monitored period other than when the frequency shift caused a dip in power at 30-40 Hz. Taking a subsection of these bands where the HVSR variations are clearest (20-35 Hz and 50-70 Hz) Figure 6.10f shows that the average HVSR in the lower frequency signal is generally higher than the average HVSR in the higher frequency band. This is true except for during the two larger water level peaks in which we observe the frequency shift in the spectrograms. At this point the HVSR values for the 50-70 Hz band increase significantly, and the HVSR values for the 20-35 Hz band decrease. Throughout the full period the 20-35 Hz HVSR hovers around 10-15 with dips down to around 5 during the second and third water level peaks. Other than this there is no obvious correlation between the 20-35 Hz HVSR and changing water levels. The 50-70 Hz HVSR begins at a value of 2.5 and increases up to around 7.5 during the first peak, 15 during the second peak and 29 during the final peak in water level. There is a slight decrease in HVSR value for the 50-70 Hz band between each of the peaks, but most distinct between the larger second and third peaks. The increase in HVSR during the second and third peaks are very abrupt with a similarly abrupt decrease as water levels drop.

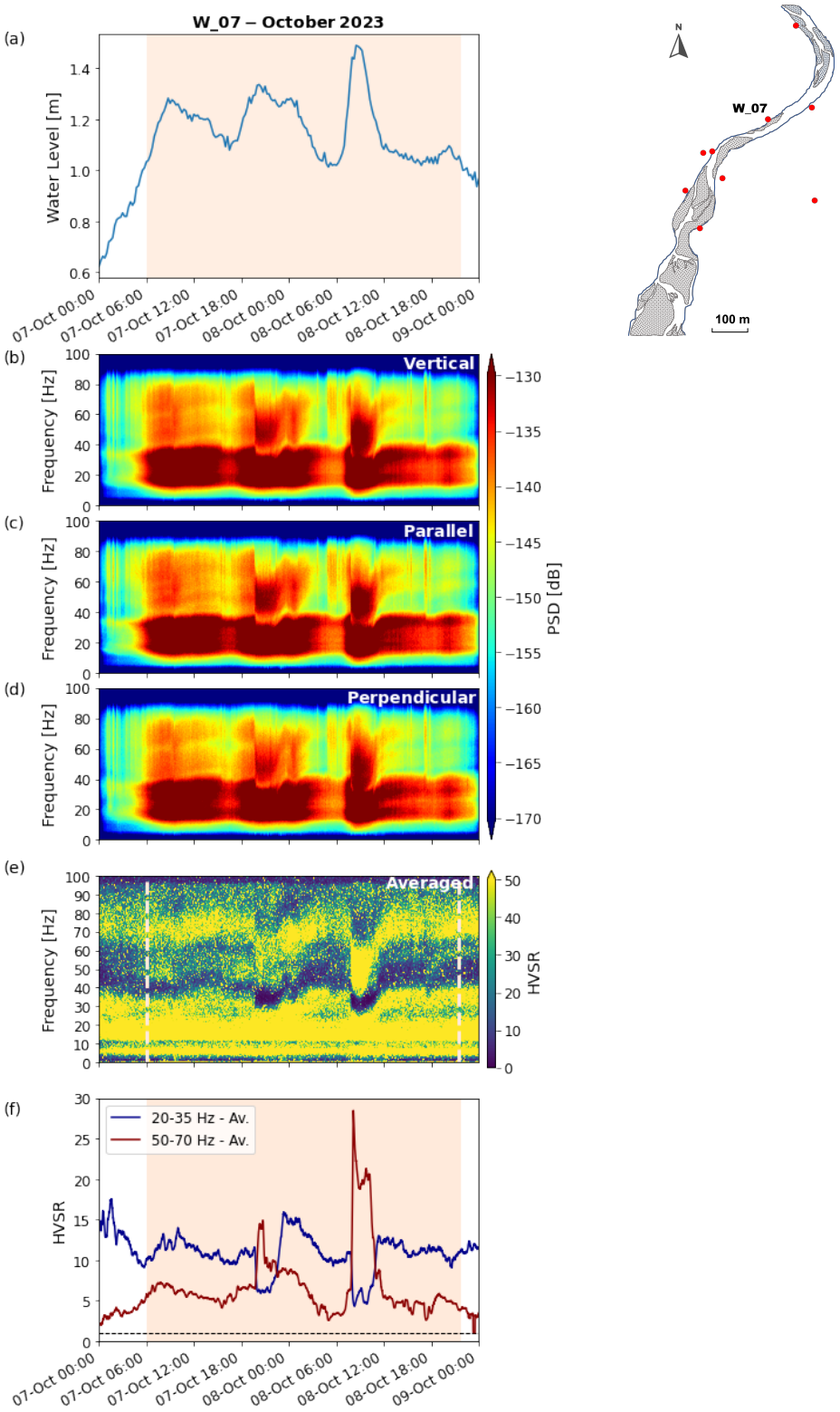


Figure 6.10: (a) hydrograph from local stream gauge (SG2), with three plots showing the spectrograms of the seismic signal recorded at site W_07 during the October 2023 event in (b) the vertical component, (c) the stream-parallel component, and (d) the stream-perpendicular component. This site only recorded until 09:00 on the 9th October. (e) The resulting HVSR values in frequency and time using the 'averaged' horizontal component and the vertical component. (f) The 'averaged' HVSR in the 20 - 35 Hz and 50 - 70 Hz frequency ranges. The pale pink blocks in (a) and (f) correspond to the hydroacoustically observed periods of bedload transport as described in Chapter 5, with the dashed lines of corresponding colour in (e) indicating the onset and arrest of bedload transport. The inset map on the right shows the location of this site in relation to the other geophone sites in the study reach.

6.3.2 Comparing the HVSR values using the stream-parallel and stream-perpendicular components

In the previous figures the HVSR was calculated using an 'averaged' horizontal component found through calculating the geometric mean of the stream-parallel and stream-perpendicular components. It was clear that the 'averaged' horizontal component was in general much stronger than the vertical component, resulting in high HVSR values. To identify if there is a stronger stream-parallel or stream-perpendicular signal from river-induced seismic noise, in this section I analyse the HVSR calculated using the stream-parallel and stream-perpendicular components individually (as shown in Equations 6.3 and 6.4), referred to as 'stream-parallel HVSR' and 'stream-perpendicular HVSR'. For this analysis I use the three common sites that recorded during both the September-October 2022 and October 2023 events (E_04, W_04 and W_07).

6.3.2.1 September-October 2022 event

E_04

As already mentioned, the 'averaged' HVSR for site E_04 shows a strong correlation with increasing water levels and periods of bedload transport in both the selected high (40-60 Hz) and low (15-35 Hz) frequency ranges (Figure 6.11a-b). The stream-parallel HVSR and stream-perpendicular HVSR (Figure 6.11c-d) values resemble that of the 'averaged' HVSR (Figure 6.11b), with increases occurring in both the frequency bands coinciding with the increases in water level and onset of bedload transport from the hydroacoustic data. The stream-parallel HVSR shows a stronger signal in general for both frequency bands with very distinct onsets. The stream-perpendicular HVSR on the other hand shows a much weaker signal with a much less obvious onset on the rising limb.

Figure 6.11e shows the HVSR values averaged over the two frequency bands (15-35 Hz and 40-60 Hz) for all three HVSR variations. It is clear that at low flows, the three HVSR values for both 15-35 Hz and 40-60 Hz are in close agreement with each other and with the 15-35 Hz signals showing stronger power than the 40-60 Hz signals. Around 12:00 on the 30th September the HVSR values in the two frequency bands increase for all three HVSR variations. The 15-35 Hz HVSR using the stream-perpendicular component is stronger during the increased water levels than the stream-parallel HVSR, but both show very similar characteristics in that they reach their peak at around 13:30 on the 30th at the transition point between the two transport phases identified through the hydroacoustic data analysis in Chapter 5. They both decrease at a similar rate over the falling limb of the hydrograph and return to similar levels once the transport of bedload has ceased. The 40-60 Hz HVSR on the other hand is stronger in the stream-parallel HVSR than the stream-perpendicular HVSR. Both show an abrupt increase in value coinciding with increased water levels and when bedload transport is estimated to have initiated using the hydroacoustic data, but the stream-parallel HVSR reaches a value of around 10 and the stream-perpendicular HVSR only increases to around 6. They maintain these levels during the transport periods before decreasing back down to similar values during the falling limb of the hydrograph once bedload transport has stopped.

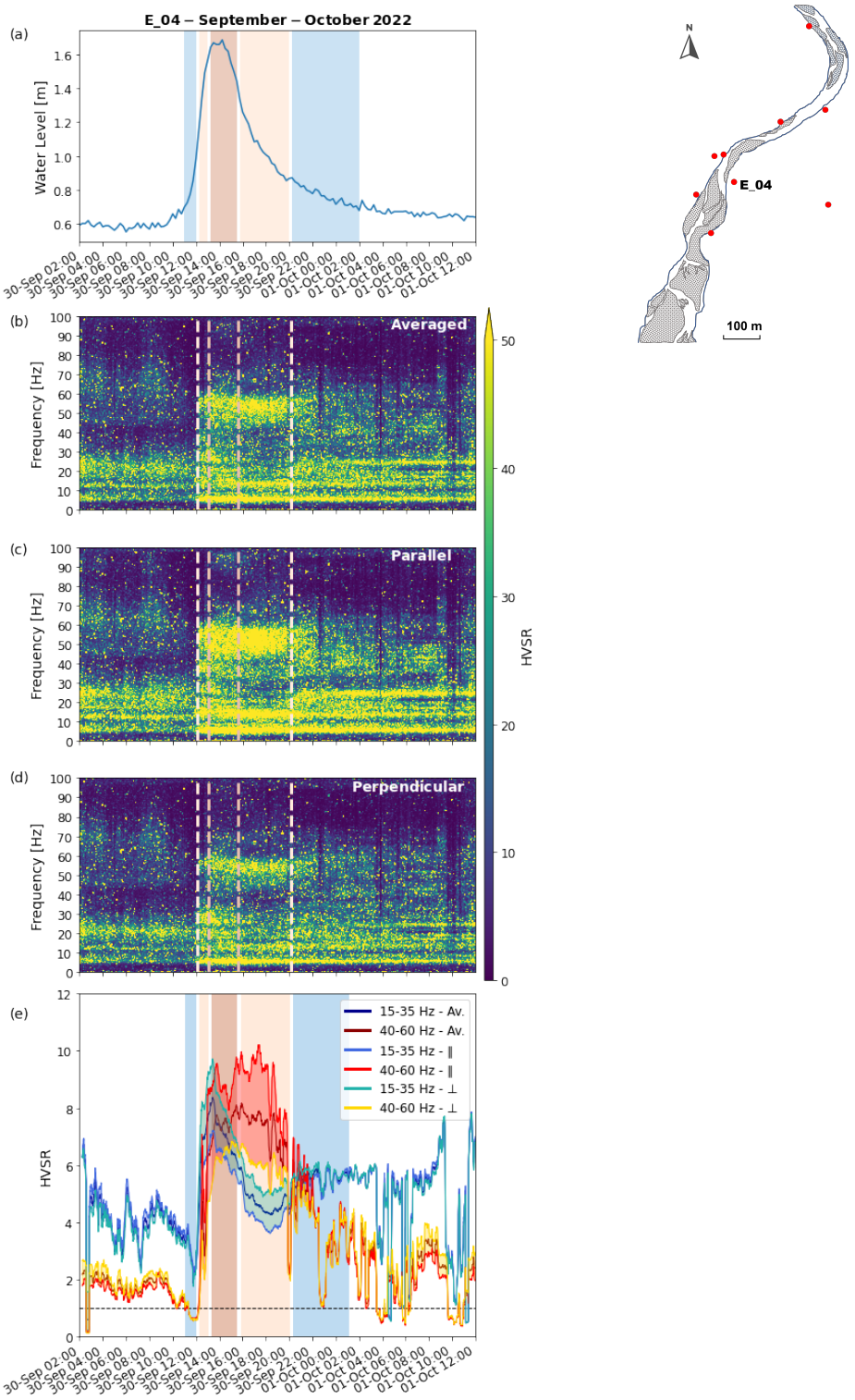


Figure 6.11: Data from geophone site E_04 during the September-October 2022 event. (a) Hydrograph from local stream gauge (SG2). The resulting HVSR values in time and frequency using (b) the 'averaged' horizontal component, (c) the stream-parallel component, and (d) the stream-perpendicular component. (e) The HVSR values averages across the 15 - 35 Hz and 40 - 60 Hz frequency ranges in the three calculated HVSRs - labelled 'Av.' for the 'averaged' component, '∥' for the stream-parallel component, and '⊥' for the stream-perpendicular component. The two frequency ranges have been colour filled with the colour of the greatest HVSR to show which component is strongest. The pale pink and beige blocks in (a) and (e) correspond to the hydroacoustically observed periods of bedload transport as described in Chapter 5, with the dashed lines of corresponding colour in (b)-(d) indicating the onset and arrest of bedload transport. The inset map on the right shows the location of this site in relation to the other geophone sites in the study reach.

W_04

The stream-parallel HVSR and stream-perpendicular HVSR at W_04 are very similar in terms of their magnitudes, frequency characteristics and timings (Figure 6.12c-d). The resulting 'averaged' HVSR therefore displays very similar characteristics to using the stream-parallel and stream-perpendicular components. As found in Chapter 4 and discussed in reference to Figure 6.4, there are two dominant frequency bands in the seismic power data in the spectrograms of 15-35 Hz and 60-80 Hz. In the HVSR figures (Figure 6.12b-d) there are high values above 60 Hz that coincide with the increased water level and the initiation of bedload transport as found in the hydroacoustic data. There is a much more gradual decrease of the HVSR values above 60 Hz during the falling limb of the hydrograph following the cessation of bedload transport from the hydroacoustic data. The HVSR values within the 15-35 Hz range is much more consistent through the monitored period with no obvious fluctuations in response to changing water levels.

Figure 6.12e shows the HVSR values averaged over the two frequency bands (15-35 Hz and 60-80 Hz) for all three HVSR variations. At low water levels prior to the hydrograph peak the HVSR values for both frequency bands sit around 1.5-2. At the exact time that bedload transport was estimated to initiate in the hydroacoustic recordings, the bedload HVSR values rapidly increase up to approximately HVSR = 6 and continue to rise to a value of 8-9 by the start of the second transport phase. It highlights the high HVSR and strong dominance of horizontal signals in the higher frequency (60-80 Hz) seismic data. The stream-parallel and stream-perpendicular HVSR values are very similar with the stream-parallel signal being stronger throughout the majority of the event. There is a slight dip in the stream-parallel HVSR value down to just below 8 during the second transport phase before it increases again towards the end of the full transport period. At this point the stream-perpendicular signal sees a slight increase, becoming stronger than the stream-parallel component for a short time. At the point that bedload was observed to stop moving from the hydroacoustic data, the HVSR values drop abruptly down to a value of around 6, and then gradually decrease back towards base levels of HVSR = 2 over the course of the falling limb of the hydrograph. The HVSR at 15-35 Hz shows less correlation with changing water levels and the periods of bedload transport. The values remained fairly constant at around 1-2 for the stream-parallel HVSR and 2-3 for the stream-perpendicular HVSR, with a slight increase in both values at 12:00 on 30th September coinciding with the increasing water levels. This increased level is maintained for all HVSR values over the duration of the high water levels. The 15-35 Hz stream-parallel HVSR shows a gradual decrease following the cessation of bedload transport over the falling limb of the hydrograph, but the stream-parallel HVSR maintained the value of around 3 for the 16 hours following the return to just turbulence.

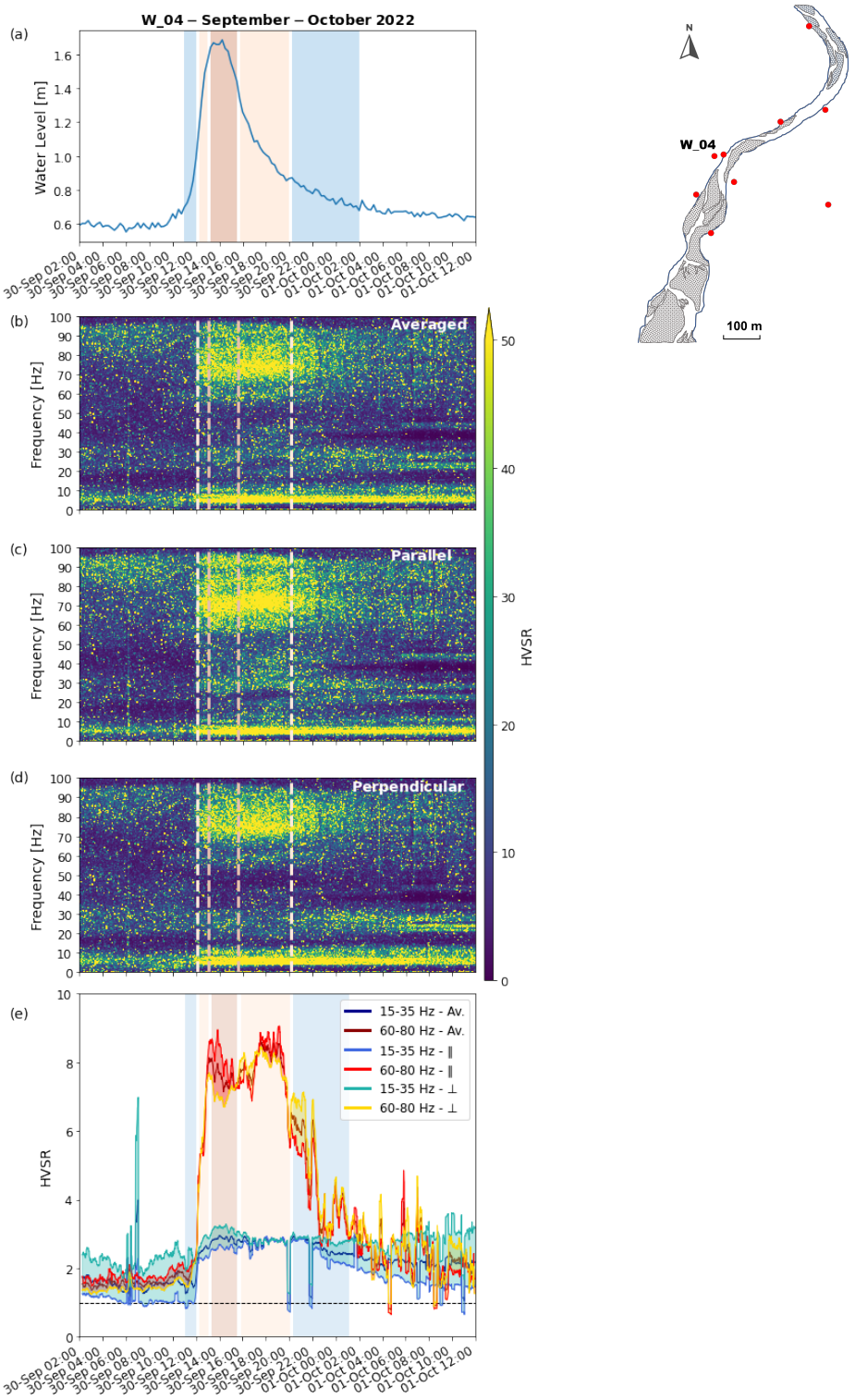


Figure 6.12: Data from geophone site W_04 during the September-October 2022 event. (a) Hydrograph from local stream gauge (SG2). The resulting HVSR values in time and frequency using (b) the 'averaged' horizontal component, (c) just the stream-parallel component, and (d) just the stream-perpendicular component. (e) The 'averaged' HVSR in the 15 - 35 Hz and 60 - 80 Hz frequency ranges in the three calculated HVSRs - labelled 'Av.' for the 'averaged' component, '∥' for the stream-parallel component, and '⊥' for the stream-perpendicular component. The two frequency ranges have been colour filled with the colour of the strongest HVSR to show which component is dominant. The pale pink and beige blocks in (a) and (e) correspond to the hydroacoustically observed periods of bedload transport as described in Chapter 5, with the dashed lines of corresponding colour in (b)-(d) indicating the onset and arrest of bedload transport. The inset map on the right shows the location of this site in relation to the other geophone sites in the study reach.

W_07

As discussed earlier in this chapter, there are again two distinct frequency bands (15-30 Hz and 40-80 Hz) observed in the seismic power signals at site W_07 in Figures 6.6b-d that are similar in all three components. The HVSR value using the stream-parallel component is very similar in characteristics to the stream-perpendicular HVSR, resulting in the 'averaged' HVSR showing very similar results to both. Both the stream-parallel HVSR and the stream-perpendicular HVSR show a strong correlation with changing water levels and periods of bedload transport identified through independent hydroacoustic measurements, as discussed above. The frequency shift which is characteristic of data collected at this site is still visible in all HVSR calculations.

Figure 6.13e shows that the HVSR values using the 'averaged' components and the stream-parallel and stream-perpendicular individual components are initially of very similar values for both frequency bands. In the 15-30 Hz band the HVSR varies around 10-15 with the stream-parallel HVSR showing slightly higher values than the stream-perpendicular HVSR. As water levels begin to rise there is a rapid increase in the 15-30 Hz HVSR values, particularly for the stream-parallel HVSR which is now a lot stronger than the stream-perpendicular signal, showing that there is a large stream-parallel directional component in the lower frequency river-induced seismic data. All three average HVSR values for the 15-30 Hz band experience a dip during the second phase of bedload transport, as bedload transport becomes more intense and potentially larger grains are mobilised (discussed in Chapter 5, Appendix F). These then rise again following the transition back to phase 1 of bedload transport before reducing back down to around HVSR = 12 - 15, which is roughly maintained for the remainder of the selected period.

The 40-80 Hz HVSR values behave quite differently to the 15-30 Hz HVSR values. The stream-parallel and stream-perpendicular HVSR are very similar in the 10 hours prior to the increased water levels, remaining very constant at around HVSR = 2. This shows more similar horizontal to vertical signals than was observed for the 15-30 Hz band, but still with stronger horizontal components. There is a very gradual increase in all 40-80 Hz HVSR values as water levels begin to rise from about 0.7 - 1.4 m and the initial stages of bedload transport begin. However, once the second stage of bedload transport occurs (beige colours in Figure 6.13) the 40-80 Hz HVSR values increase significantly from 5 to around 15-20, with the stream-parallel HVSR showing marginally the highest values. These high HVSR values are sustained over the course of the period of intense bedload transport (phase 2), but following this the values drop drastically back down to around 5 and then gradually decrease further over the course of the falling limb of the hydrograph.

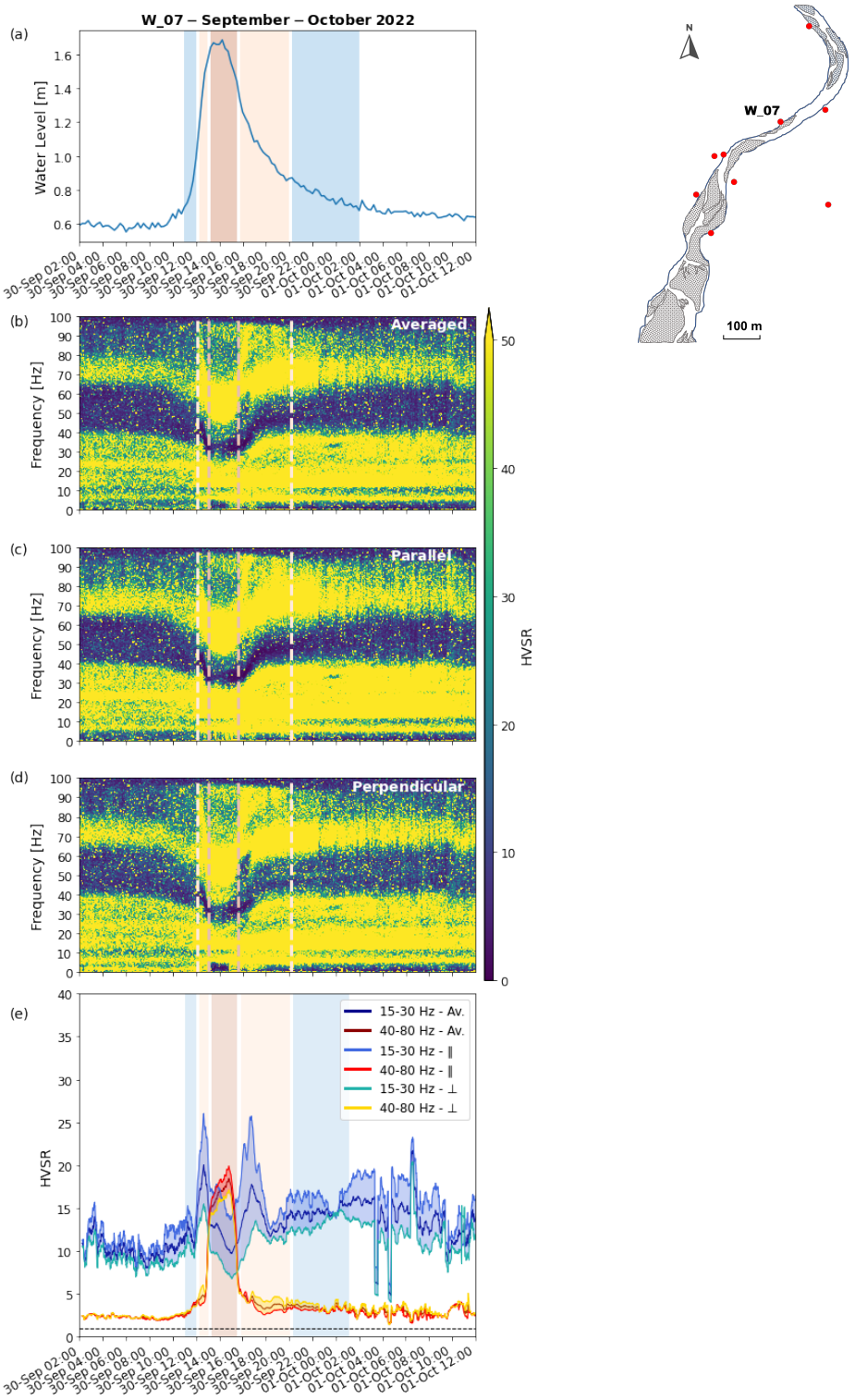


Figure 6.13: Data from geophone site W_07 during the September-October 2022 event. (a) Hydrograph from local stream gauge (SG2). The resulting HVSR values in time and frequency using (b) the 'averaged' horizontal component, (c) just the stream-parallel component, and (d) just the stream-perpendicular component. (e) The 'averaged' HVSR in the 15 - 30 Hz and 40 - 80 Hz frequency ranges in the three calculated HVSRs - labelled 'Av.' for the 'averaged' component, '∥' for the stream-parallel component, and '⊥' for the stream-perpendicular component. The two frequency ranges have been colour filled with the colour of the strongest HVSR to show which component is dominant. The pale pink and beige blocks in (a) and (e) correspond to the hydroacoustically observed periods of bedload transport as described in Chapter 5, with the dashed lines of corresponding colour in (b)-(d) indicating the onset and arrest of bedload transport. The inset map on the right shows the location of this site in relation to the other geophone sites in the study reach.

6.3.2.2 October 2023 event

E_04

As already mentioned, the three peaks in water level of the October 2023 event are visible in the 'averaged' horizontal component HVSR of the seismic data from site E_04, especially in the higher frequency signal. In Figure 6.14b-d we can see that the three methods of calculating HVSR show very similar results with distinct increases around 40-60 Hz in the bedload signal coinciding with increases in water level and less obvious correlations in the lower frequency (20-30 Hz) band used in the earlier section. The onset of the high HVSR during the rising limb of the first water level peak appear to coincide with the estimated initiation of bedload transport from the hydroacoustic data, however there is no clear relationship between the two on the falling limb.

In Figure 6.14e, we can see that the HVSR values for the 20-30 Hz signal start at around 2 and increase to between 4 and 7 during the increased water levels. This increase happens for both the stream-parallel and stream-perpendicular HVSR and occurs in the three hours prior to the identified onset of bedload motion from the hydroacoustic data. The 20-30 Hz HVSR values remain fairly constant at around 4-7 throughout the remainder of the monitored period with only very slight fluctuations in response to changes in water level during the three peaks of the event. The stream-perpendicular HVSR is consistently stronger than the stream-parallel HVSR for the 20-30 Hz band.

In contrast, the HVSR values for the 45-60 Hz band show very variable values over the duration of the event, but very similar values between the stream-parallel and stream-perpendicular HVSRs. Both the stream-parallel and stream-perpendicular HVSR show a sharp increase in HVSR from around 1 to 14 coinciding with the initial onset of bedload motion from the hydroacoustic data and three peaks broadly coinciding with the peaks in water level. Each subsequently larger water level peak results in larger HVSR values. Between each water level peak the HVSR values drop back down to a value of around 1. In general, although hard to see due to the erratic nature of the HVSR values, it appears that the stream-parallel HVSR is higher than the stream-perpendicular HVSR, especially during the peaks of the event, for the 45-60 Hz band.

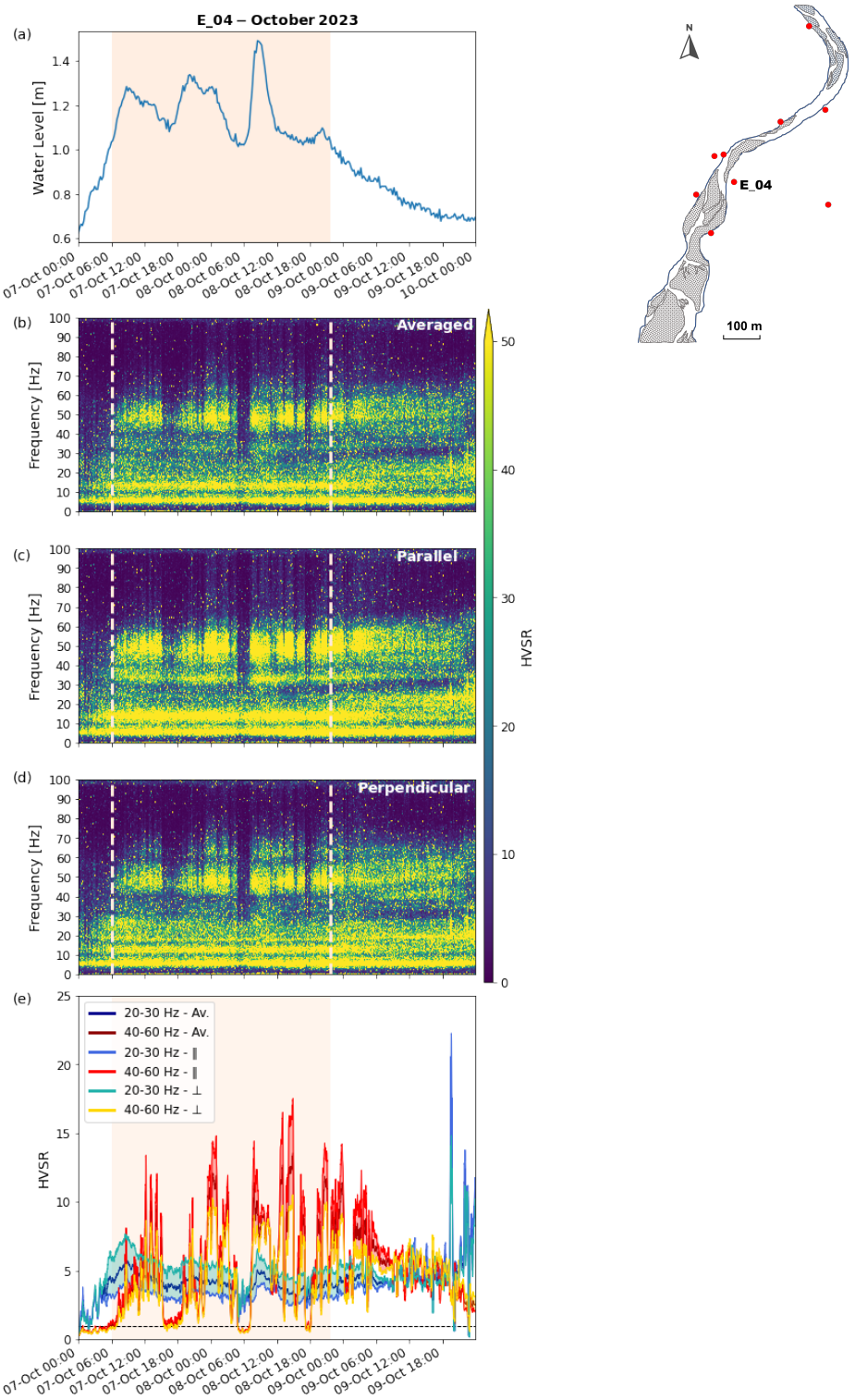


Figure 6.14: Data from geophone site E_04 during the October 2023 event. (a) Hydrograph from local stream gauge (SG2). The resulting HVSR values in time and frequency using (b) the 'averaged' horizontal component, (c) just the stream-parallel component, and (d) just the stream-perpendicular component. (e) The 'averaged' HVSR in the 20 - 30 Hz and 40 - 60 Hz frequency ranges in the three calculated HVSRs - labelled 'Av.' for the 'averaged' component, '∥' for the stream-parallel component, and '⊥' for the stream-perpendicular component. The two frequency ranges have been colour filled with the colour of the strongest HVSR to show which component is dominant. The pale pink and beige blocks in (a) and (e) correspond to the hydroacoustically observed periods of bedload transport as described in Chapter 5, with the dashed lines of corresponding colour in (b)-(d) indicating the onset and arrest of bedload transport. The inset map on the right shows the location of this site in relation to the other geophone sites in the study reach.

W_04

As discussed earlier there are two distinct frequency bands observed in the spectrograms of the seismic power, however they are less clear in the calculated HVSR values in frequency and time (Figure 6.9). These bands were selected as 15-35 Hz and 60-80 Hz. The higher frequency band has strong HVSR values, while the lower frequency band doesn't show a consistent strong or weak HVSR.

In Figure 6.15b-d, it can be seen that the stream-parallel and stream-perpendicular HVSR values of the 60-80 Hz band are more similar at the start of the event than at the end of the event. This is also seen in Figure 6.15e. For this band the HVSR values increase as water levels begin to rise and bedload transport is observed to initiate from the hydroacoustic sound files. There is not a clear link to the changing water levels, however a significant dip appears in the HVSR for this frequency band during the dip between the second and third water level peaks. The 60-80 Hz HVSR slowly decreases following the cessation of bedload transport, until reaching a value of around 3 again by midnight on the 9^{th} October. Throughout the event the stream-perpendicular HVSR is greater than the stream-parallel HVSR for the 60-80 Hz band. In the 15-35 Hz band the stream-parallel and stream-perpendicular HVSRs are very similar throughout the full period. They also show no correlation with changing water levels, remaining very constant at around HVSR = 3.

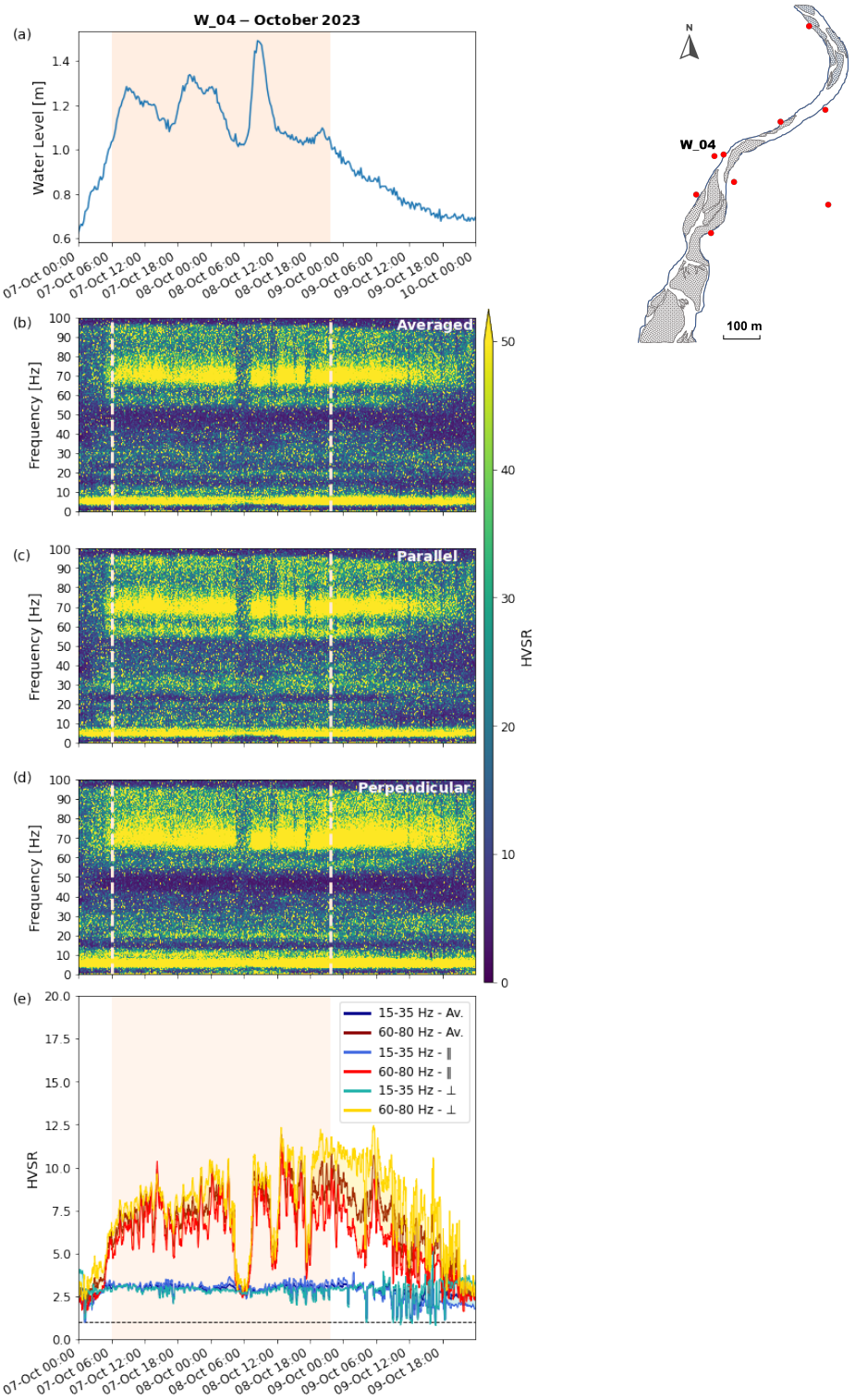


Figure 6.15: Data from geophone site W_04 during the October 2023 event. (a) Hydrograph from local stream gauge (SG2). The resulting HVSR values in time and frequency using (b) the 'averaged' horizontal component, (c) just the stream-parallel component, and (d) just the stream-perpendicular component. (e) The 'averaged' HVSR in the 15 - 35 Hz and 45 - 60 Hz frequency ranges in the three calculated HVSRs - labelled 'Av.' for the 'averaged' component, '∥' for the stream-parallel component, and '⊥' for the stream-perpendicular component. The two frequency ranges have been colour filled with the colour of the strongest HVSR to show which component is dominant. The pale pink and beige blocks in (a) and (e) correspond to the hydroacoustically observed periods of bedload transport as described in Chapter 5, with the dashed lines of corresponding colour in (b)-(d) indicating the onset and arrest of bedload transport. The inset map on the right shows the location of this site in relation to the other geophone sites in the study reach.

W_07

At site W_07 the HVSR values calculated using the stream-parallel and stream-perpendicular components are visually very similar in Figures 6.16 b-d. All three show high values in the 20-35 Hz and 50-70 Hz frequency bands selected earlier along with the frequency shift during the second and third water level peaks, as described in the previous two chapters and earlier in this chapter. In the frequency range of 50-70 Hz there appears to be increased HVSR using both the stream-parallel and stream-perpendicular components coinciding with the three water level peaks in the hydrograph. Since the geophone at site W_07 failed to record after 00:00 on the 9^{th}, the durations of these HVSR plots are shorter than at the previous two sites mentioned. The lower frequency band (20-35 Hz) shows fairly constant HVSR values across the event, with slight dips coinciding with the two larger water level peaks.

Looking at the HVSR values averaged over the 20-35 Hz and 50-70 Hz ranges, it can be seen that the stream-parallel component is strongest for both. The 20-35 Hz HVSR is generally larger than the 50-70 Hz HVSR and shows a small degree of correlation with changing water level. Unlike the other sites, this site shows a reduction in 20-35 Hz HVSR values during the water level peaks, specifically the second and third peaks. The 50-70 Hz HVSR on the other hand shows a much stronger correlation with the hydrograph peaks, with increasing HVSR peaks for each subsequently increasing water level peak.

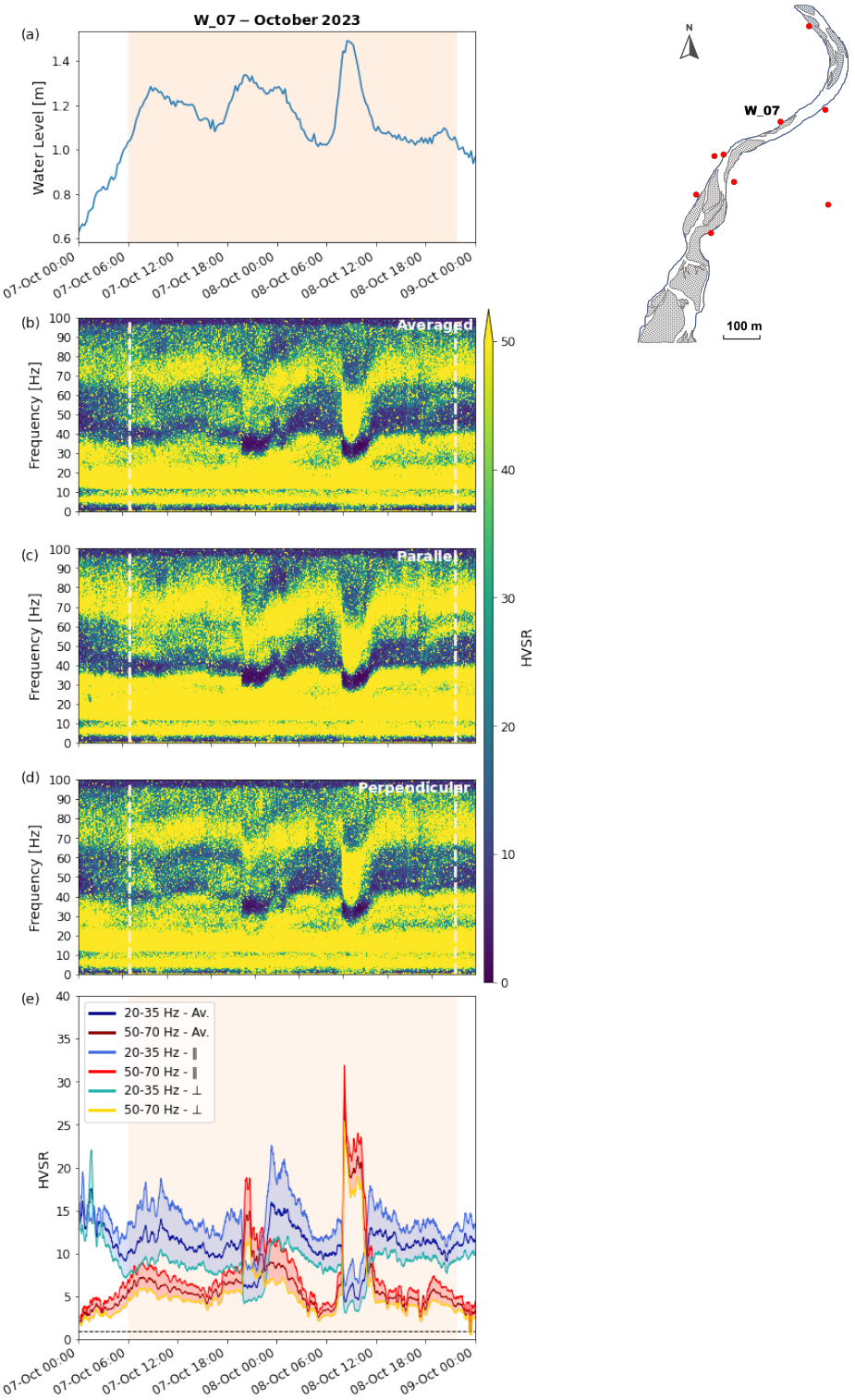


Figure 6.16: Data from geophone site W_07 during the October 2023 event. (a) Hydrograph from local stream gauge (SG2). The resulting HVSR values in time and frequency using (b) the 'averaged' horizontal component, (c) just the stream-parallel component, and (d) just the stream-perpendicular component. (e) The 'averaged' HVSR in the 20 - 35 Hz and 50 - 70 Hz frequency ranges in the three calculated HVSRs - labelled 'Av.' for the 'averaged' component, '∥' for the stream-parallel component, and '⊥' for the stream-perpendicular component. The two frequency ranges have been colour filled with the colour of the strongest HVSR to show which component is dominant. The pale pink and beige blocks in (a) and (e) correspond to the hydroacoustically observed periods of bedload transport as described in Chapter 5, with the dashed lines of corresponding colour in (b)-(d) indicating the onset and arrest of bedload transport. The inset map on the right shows the location of this site in relation to the other geophone sites in the study reach.

6.3.3 Frequency analysis of calculated HVSR

To compare with the outputs of the turbulence and bedload models included in the R 'eseis' package developed by Dietze (2018a) (discussed in more detail in Chapters 3 and 4), I attempted to plot the frequency content of the HVSR during periods of no bedload transport and bedload transport as identified through the manual listening and categorisation of the hydroacoustic files. Due to the highly varied nature of the HVSR data, I had to run a moving average through the data and apply a normalisation to the data in order to compare the frequency content between the selected periods. Due to the averaging of the data, the plots are not very smooth and appear quite angular. However, they do provide an indication of the dominant frequencies in the signals. Since the data is not overly informative I have chosen to include it for site W_07 only for both the September-October 2022 and October 2023 events. The selected water levels match those in the PSD figures (Figure 4.18) in Chapter 4. For the two events I have separated the periods when there was no mobilisation of bedload and the periods where there was bedload transport. As can be seen in Figure 6.17, the periods when no bedload was moving in the September-October 2022 event show a strong HVSR signal around 15-30 Hz. The periods of bedload transport, however, show two distinct peaks in HVSR at around 10-40 Hz and 50-80 Hz. In the October 2023 event there is a similar structure to the signals when bedload is and is not being transported (Figure 6.18). The periods without bedload motion show a single peak in HVSR at around 10-30 Hz, whereas the periods with bedload movement show two distinct peaks again at around 10-25 Hz and 40-80 Hz.

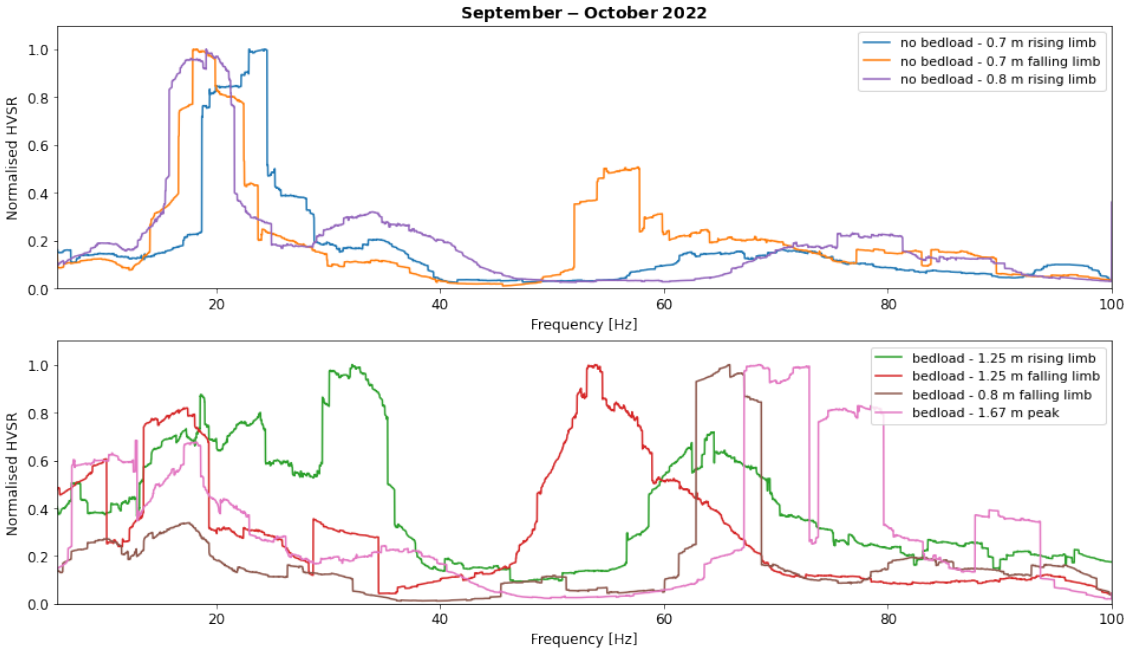


Figure 6.17: Frequency content of the HVSR signals at site W_07 during the September-October 2022 event for periods when there was (a) no bedload motion and (b) bedload transport inferred from the hydroacoustic data.

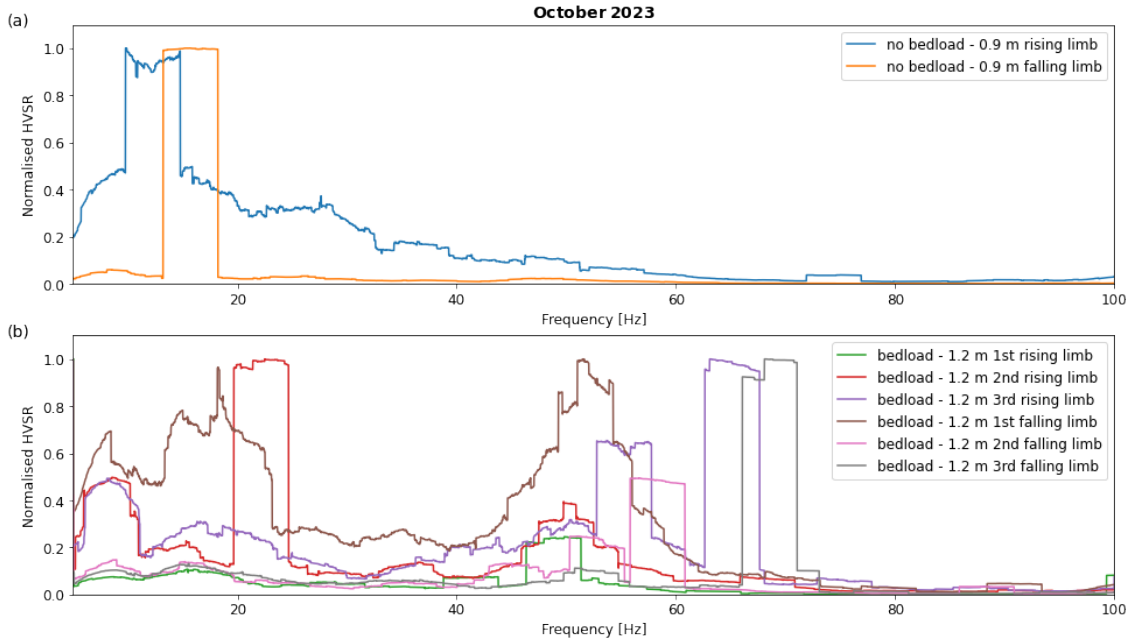


Figure 6.18: Frequency content of the HVSR signals at site W_07 during the October 2023 event for periods when there was (a) no bedload motion and (b) bedload transport inferred from the hydroacoustic data.

6.3.4 Results Summary

HVSR using averaged horizontal component

The HVSR data using the averaged horizontal component revealed consistent patterns across both the September-October 2022 and October 2023 events, but also some key differences.

The HVSR data from the four sites (E_04, W_04, W_05, and W_07) during the September-October 2022 event revealed distinct seismic patterns with two main frequency bands. The lower-frequency band (up to 40 Hz) was linked to flow turbulence, while the higher-frequency band (above 40 Hz) was associated with bedload transport. At E_04 and W_05, the HVSR signals showed a stronger high-frequency response, which tended to increase with rising water levels and was more closely linked to periods of bedload transport identified by hydroacoustics than the lower-frequency signal. In contrast, W_07 displayed a stronger low-frequency HVSR response than high-frequency HVSR. W_05 showed a decrease in power in both frequency bands during periods of increased water levels and bedload transport, indicating a different seismic response compared to the other sites.

For the October 2023 event, the HVSR signals from E_03, E_04, W_04, and W_07 displayed a similar pattern to the September-October 2022 event, with an increase in HVSR signal strength correlating with rising water levels. The October 2023 event was marked by three water level peaks, visible in the HVSR signals across all four sites. While E_03, E_04, and W_04 all showed a stronger high-frequency signal, W_07 displayed a stronger low-frequency HVSR than high-frequency HVSR, similar to the September-October 2022 event. However, during the two larger water level peaks, the higher-frequency response at W_07 became more prominent, showing a shift from its generally stronger low-frequency response observed throughout the rest of the event.

HVSR using stream-parallel and stream-perpendicular components

The comparison of HVSR values using the stream-parallel and stream-perpendicular components reveals some key similarities and differences across sites and events. In general, the stream-parallel component tends to show stronger HVSR signals, particularly at higher frequencies (above 40 Hz), while the stream-perpendicular component typically exhibits weaker signals, especially in the lower frequency ranges (up to 40 Hz).

For the September-October 2022 event, at site E_04, both components show similar patterns in response to increasing water levels and bedload transport occurrence, with the stream-parallel HVSR generally stronger at high frequencies, and the stream-perpendicular HVSR stronger at low frequencies. Similarly, at W_05, the stream-parallel HVSR is stronger at high frequencies, while the stream-perpendicular HVSR is stronger at low frequencies. In contrast, W_07 shows a stronger stream-parallel HVSR across both high and low frequencies, but the low-frequency stream-parallel signal is stronger than the high-frequency stream-parallel signal apart from during the very peak in water level when 'phase 2' bedload transport occurs.

For the October 2023 event, E_04 showed stronger stream-parallel signals at higher frequencies and stronger stream-perpendicular signals at lower frequencies. At W_04, the stream-perpendicular HVSR was dominant at higher frequencies, with similar strength between stream-parallel and stream-perpendicular signals at lower frequencies. There was also less clear correlation to water levels and bedload transport compared to the September-October 2022 event. In contrast, W_07 displayed stronger stream-parallel signals across both high and low frequencies with the lower-frequency HVSR signal being stronger in power than the higher frequency signal.

6.4 Discussion

From the analysis in this chapter of the contributions from the three orthogonal directional components in the river-induced seismic signals it is clear that generally there was the presence of two frequency bands that showed varying characteristics. These typically correlated, to a degree, with changing water levels and identified periods of bedload transport from the manually categorised hydroacoustic data, as well as the threshold effects of the bedload transport component. Although the exact frequency values of these bands varied between events and sites, on the whole they occurred below 40 Hz and above 40 Hz. The results in Figures 6.17 and 6.18 show that there were two peaks in the power of the HVSR signals at around 10-40 Hz and 45-80 Hz. When analysing the data for periods when bedload was and was not being transported it was observed that two peaks at these frequencies were present for periods of bedload movement, but only the 10-40 Hz peak was present for periods without bedload motion. Since turbulence will be present whether bedload is or is not being transported the associated signal would be expected to be present at all times. Therefore, the lower frequency band observed is attributed to be the turbulence signal since it is present when bedload motion is both present and not. These frequency values are in good agreement with those found through the analysis in Chapter 4 and the outputs of using the 'eseis' package bedload and turbulence models (Dietze, 2018a). Figure 4.19 in Chapter 4 revealed a strong peak in the seismic power at around 10-40 Hz during periods of just turbulence and periods where both turbulence and bedload transport was present. Additionally, for periods of bedload transport another smaller peak was observed at around 40-80 Hz. The outputs from the models included in the R 'eseis' packaged estimated the turbulence signal to generally result in peaks at around 5-50 Hz, and the bedload signal to dominate from around 30-40 Hz and above. These values are all in close agreement with those found in this chapter and thus for this discussion I will refer to the lower frequency band as the turbulence signal and the higher frequency band as the bedload signal.

6.4.1 Are there stronger horizontal or vertical signals in river-induced seismic signals?

On the whole, the HVSR values for the interpreted turbulence and bedload signals are consistent across the sites and events all within an order of magnitude. However, slight variations may be a result of site characteristics, such as the topographic slope or substrate material, or the processes occurring within the immediate stretch of the river. Various site characteristics can affect the HVSR observed, such as soft soil deposits (lower shear velocities), presence of the water table (saturated soils), depth of soil layers, site geometry, local topography, and site specific geological conditions (Guo et al., 2021; Xu and Wang, 2021). From the refraction survey results in section 3.2.5 it suggests a velocity structure at the site comprising dry soil overlying glacial till, with slightly higher-velocity weathered bedrock beneath. This structure likely results in the impedance contrast necessary for a Love wave waveguide. The glacial till likely serves as the low-velocity layer relative to the weathered bedrock, facilitating the trapping and resonance of Love waves, as indicated by the high H/V ratios. Although there is no evidence of a water table effect, the dry conditions of

the upper soil and the velocity contrast at the till-bedrock interface offer a credible explanation for the observed seismic response.

From the HVSR results in section 6.3.1, it is clear that in general the horizontal seismic wave components dominate the signals from the River Feshie study site. This is true for both turbulence- and bedload-induced seismic waves in all sites shown in this chapter, except site W_05 which shows a vertical dominance for the bedload signal but a horizontal component dominance for the turbulence signal. Additionally, site W_05 sees a reduction in the value of the HVSR during the high water level event when bedload is being transported in both the turbulence and bedload signals, where all other sites see a general increase in both signals during the events. Without further testing it is hard to decipher why this characteristic is only seen at site W_05. I hypothesise that this may be related to the site's unique characteristics, as it is closer to the river than the others but raised a few metres above it. As described in Chapter 3, this site although only about 2 m from the river's edge is located on a flat ledge of the steep river bank approximately 2-3 m above the river. There is a possibility that the elevation of this site is causing a dominance in the Rayleigh waves through the amplification of Rayleigh waves near topographic features as found by Sánchez-Sesma and Campillo (1993). Undertaking active seismic surveys at each geophone site would have revealed information about the seismic characteristics expected, but unfortunately time and logistics did not permit this.

W_07 also shows an interesting signal as was described in Chapters 4 and 5, where it experiences a frequency shift predominantly in the bedload-induced signal during the peak of the event. This is observed in all three components and the resulting HVSR. This could be the result of an increased grain size of transported material at the highest flows which induces a lower frequency of sound (Tsai et al., 2012; Gimbert et al., 2014; Lagarde et al., 2021), a potential change in the transport mechanism which could also be linked to changing grain size (Roth et al., 2016; Lagarde et al., 2021), or it may be linked to the presence of a granular sheet flow (Palucis et al., 2018; Piantini et al., 2023) as discussed in Chapter 5. Since this shift is present in the October 2023 event when there was no noticeable change in frequency in the hydroacoustic recordings at peak flows, it is assumed that grain size is not the key factor causing this behaviour. However, further analysis of these signals could reveal more information on this. If the underwater camera had been working during this time, it could have also revealed if there were in fact larger grains mobilised during the event peak. Although there was no footage available of the pebbles in motion, images that were captured by the underwater camera before and after the large September-October 2022 event (included in Chapter 3) reveal a change in the grain sizes present on the river bed with significantly increased grain sizes visible following the event.

The general increased horizontal power in the bedload-induced seismic signals, suggests that there is a strong horizontal directional component associated with the movement of bedload. Previous studies assumed that due to the vertical impacts from saltating particles, the vertical signals would be strongest, therefore focusing on the Rayleigh wave signals (e.g. Tsai et al., 2012). Although saltating particles do impact the river bed with a strong vertical directionality, due to them also being affected by the flow of water they actually impact the riverbed at angles much different from normal to the bed (Schmandt et al., 2013; Roth et al., 2016). This induces

seismic signals with a combination of horizontal and vertical motion. Additionally, if particles are travelling along the riverbed through rolling or sliding motion there will most likely be a very strong horizontal direction (dominance of Love waves) to the seismic waves with a potentially smaller vertical contribution (Schmandt et al., 2013; Roth et al., 2016). In the presence of large boulders, saltating particles could also impact the upstream sides of these boulders additionally inducing horizontally polarized waves (Roth et al., 2016). Previously, the vertical motion has been used in bedload transport studies, capturing some aspects of bedload transport but not the complete picture. Clearly, in an alluvial setting like the River Feshie, the horizontal components contain a significant portion of the bedload transport seismic signal and should be considered in future fluvial seismology studies.

In addition to the two frequency bands observed in the seismic data that have been interpreted as the signals of turbulence and bedload transport, strong broadband seismic noise was observed prior to the increased water levels in all high flow events. This was also discussed in detail in Chapters 4 and 5. These signals have been interpreted to be a meteorological signal, specifically of rain which necessarily precedes increased river levels in the absence of snowmelt or lake outbursts (which is not applicable to this catchment) (Dean, 2018; Rindraharisaona et al., 2022). These rain and wind signals cause significant noise in the lead up to an event, often extending over the rising limb of a hydrograph of particularly large events with sustained rainfall input or occurring intermittently throughout a single event composed of multiple water levels peaks. Since the seismic frequencies produced by rain and wind significantly overlap those produced by river processes, such as turbulence and bedload transport, they contaminate the river-induced seismic signals making it challenging to identify the onset and thresholds of bedload motion with changing water levels (Bakker et al., 2022; Rindraharisaona et al., 2022). This effect could be seen in Figure 5.5 in Chapter 5, where the relationship between the averaged PSD and water levels is affected during the rising water levels. In that chapter, this affected the identification of hysteretic relationships between water level and seismic power which has previously been used to provide information on the presence of bedload transport and on the different transport processes at play. The River Feshie data is notably influenced by rain signals due to its small catchment area, making it susceptible to local rainfall. This means significant water level increases from localised upstream rainfall are unlikely without local rainfall to the stretch of interest. The HVSR technique effectively removes these rain signals. This is evident by the abrupt onset of high HVSR values that correspond directly with increased water levels, rather than showing the broadband signals leading up to the event. This pattern is particularly noticeable at monitoring site E_04 and W_04, and is observed across multiple water level peaks such as in the October 2023 event. Figure 6.14 shows a decrease in HVSR values in between successive water level peaks, especially in the bedload-induced signal at site E_04. This could be due to the significant vertical signal commonly associated with rainfall-induced seismic noise that typically occupies frequencies similar to those of bedload transport signals (Dean, 2018; Bakker et al., 2022; Rindraharisaona et al., 2022). Otherwise, as seen in Chapter 4 of this thesis, the meteorological signals have very similar vertical and horizontal components, meaning that performing a ratio calculation of the two will result in a value close to zero. This can be seen clearest in the bedload HVSR values in this chapter as the wind and rain signals in the spectrograms dominate more of the

high frequency signals. In the majority of sites included in this chapter the bedload HVSR is near to, and sometimes below, HVSR = 1 prior to the rise in water levels and onset of bedload transport, thus showing the similar strength of horizontal and vertical signals. During the falling limb of the events and shortly after water levels have returned to base values, the HVSR does not reach as low values as before, thus reinforcing that this is a signal from rain.

6.4.2 Do river processes induce stream-parallel or stream-perpendicular seismic signals?

While it is evident that the horizontal components of river-induced seismic signals are typically stronger than the vertical component, particularly for bedload-induced signals, determining the dominant horizontal direction can provide insights into the complex transport processes in an alluvial mountain river like the Feshie. By comparing the HVSR calculated using either the stream-parallel or stream-perpendicular horizontal component, it has been found that the stream-parallel signal generally dominates in the bedload-induced noise. This pattern was observed at sites E_04 and W_07 during both the September-October 2022 and October 2023 events, as well as at site W_04 during the September-October 2022 event. Although particle movement is three-dimensional in rivers, at high flows the force of the water would likely cause pretty uniform downstream motion. The data from this chapter clearly suggests that the downstream signal is dominant for the bedload portion of the signal. This dominance in the downstream direction (stream-parallel component) may be due to the oblique directionality of particle impacts with the bed downstream or particles rolling or sliding in the flow direction (Schmandt et al., 2013; Roth et al., 2016).

In contrast, the HVSR of the turbulence signal shows more variation. Site E_04 exhibits a stronger stream-perpendicular signal during both the September-October 2022 and October 2023 events, while W_07 shows a stronger stream-parallel signal during both events. For W_04, the relationship varies between events: the stream-parallel and stream-perpendicular signals are very similar during the October 2023 event, but the stream-perpendicular signal is strongest during the September-October 2022 event. The reasons for these variations in the HVSR values of bedload-induced signals between the two horizontal components are unclear, but I hypothesise that site effects may play a role. W_04 and E_04 are farther from the channel than W_07, yet E_04 and W_07 are both on flat floodplains, while W_04 is elevated above the riverbed. Without detailed seismic refraction surveys at each site, it is challenging to confirm if the observed signal variations are characteristic of the sites and what they reveal about wave propagation at these locations.

6.4.3 HVSR method implications on seismic bedload transport studies

This work clearly demonstrates a strong horizontal component in river-induced seismic signals, particularly due to bedload transport processes. Most previous studies on bedload transport seismology have focused solely on the vertical signal component, assuming that the bedload-induced signal is mainly contained within Rayleigh waves (e.g. Tsai et al., 2012; Gimbert et al., 2014). Consequently, fundamen-

tal methods in fluvial seismology and developed seismic bedload transport models often deal only with the vertical component, with some studies deploying single (vertical) component seismic sensors (e.g. Hsu et al. (2011)). Based on these findings, studies that have recorded data in three components but only utilised the vertical component should consider reanalysing the data using the horizontal components for comparison, and any new studies should also adopt this approach. This could enhance seismic models by incorporating all directional components, especially for detailed transport process analysis. Developing three-component analysis may also improve experimental designs by accounting for site characteristics and target processes. Since HVSR is commonly used in engineering seismology to understand site characteristics, it could help compare signals from geophones in different catchments and substrates, such as soil versus bedrock, providing insights into signal variations due to site placement. Utilising all components that contain important information about bedload and turbulent motion in rivers provides more accurate data to forecast the effects of flood events, such as the volume of sediments mobilised.

6.5 Conclusion

Previous studies in fluvial seismology, as well as those examining seismic signals induced by wind and rain, typically focus on the vertical components of recorded seismic signals. This focus stems from the assumption that Rayleigh waves, which involve both vertical and horizontal motion, dominate the signals from fluvial processes such as bedload transport. However, this thesis presents data from the River Feshie that demonstrate a strong horizontal component for both turbulence and bedload-induced signals, with a particular dominance in the stream-parallel direction for bedload transport signals. This dominance is likely due to particle impacts with the riverbed in the downstream direction, driven by flow direction and gravity preferentially inducing Love waves. HVSR calculations applied to river-induced seismic data effectively identify the onset of bedload transport by filtering out rain signals that precede water level rises. This approach simplifies the analysis of seismic power variations in frequency and/or time, which was previously complicated by rain signals.

This study also explores the complex factors that can influence both horizontal and vertical signals during high flow conditions accompanied by bedload mobilisation, and advances our current methods for monitoring bedload transport. Observing a high Horizontal-to-Vertical Spectral Ratio (HVSR) at high frequencies likely indicates the presence of bedload; however, the behavior of bedload movement during these periods is complex and non-uniform.

Future research should focus on investigating the directional components of river-induced seismic noise, starting with controlled flume experiments and then extending these methods to natural rivers, analysing the wave polarizations. This approach could enhance current seismic methods for bedload transport by incorporating signals from Love waves in addition to Rayleigh waves. Such advances would provide a more comprehensive understanding of fluvial processes and improve seismic monitoring techniques. Additionally, these improvements can contribute to enhanced flood models and more accurate sediment flux estimations.

Chapter 7

Discussion

Monitoring bedload transport is crucial for understanding river dynamics, sediment budgets, and managing riverine and coastal environments (Reid et al., 1985; Hoey and Sutherland, 1991; Lisle, 1995). Over recent decades, monitoring methods have advanced significantly from direct sampling to indirect passive monitoring using seismic sensors. Since the initial findings by Govi et al. (1993) that fluvial processes generate high-frequency ground vibrations, several studies have confirmed that these vibrations can be used to monitor rivers. It was found that river-induced ground vibrations are primarily caused by water flow turbulence and sediment impacting the river bed. An observed hysteresis pattern in the relationship between seismic power and changing water discharge or flow depth has been a key influence on the identification of bedload transport (e.g. Burtin et al., 2008; Hsu et al., 2011; Schmandt et al., 2013; Barrière et al., 2015). However, accurately distinguishing between bedload and turbulence-induced seismic signals, as well as other environmental noise, remains challenging. Various studies have demonstrated the potential of using seismic sensors for bedload transport monitoring in high-altitude, steep mountain catchments, although lower catchments with more anthropogenic noise pose challenges. Bedload signals depend on factors like grain size, channel slope, and water discharge, making smaller rivers and flatter catchments more difficult to monitor accurately (Tsai et al., 2012; Barrière et al., 2015). Understanding the characteristics of seismic signals from river-induced ground vibrations is crucial for interpreting the signals and understanding the potential of seismic monitoring for such processes.

This thesis has addressed some of the uncertainties identified in previous work, opening up avenues for future work to better constrain the use of seismic sensors as a bedload transport monitoring tool. The main data chapters in this thesis (Chapters 4, 5 and 6) explore three key themes. Chapter 4 analyses the recorded signals across multiple events and all seismic sensor sites from the study reach and interprets the signals from turbulence and bedload transport, with reference to a seismic model that aims to differentiate the expected signals from the two processes. This chapter reveals that the signals from turbulence and bedload transport are quite hard to differentiate as they tend to occupy overlapping frequency bands, as do other environmental sources of noise. It is then difficult to identify an onset of bedload transport to allow bedload flux estimations or the accurate spatial monitoring of bedload motion. Chapter 5 takes the interpretations from Chapter 4 and combines them with hydroacoustic measurements, which provide an independent identification

of the mobilisation of bedload transport. I used this data combination to assess the behaviour of the seismic signal in a high and low frequency band to determine if there was in fact a strong bedload transport signal. This work revealed that the seismic power relates to changing water levels; however, it is challenging with seismics alone to identify bedload signals. Using hydroacoustic data revealed that the previously used hysteretic relationship between seismic power and water level for bedload transport analyses may not be effective as it is not a necessary condition. Additionally, we found a relationship between the magnitude and duration of events and the hysteresis patterns observed and the thresholds of particle entrainment. Finally, Chapter 6 delves deeper into the differences in the signals observed in the three measured components revealing that the horizontal components contained a significant portion of the river-induced signals, with the stream-parallel component generally showing stronger bedload signal and the turbulence signal showing more variation in the dominant directional component.

In this section, I summarise key discussion points, challenges encountered during this research, suggest potential directions for future work to address unresolved issues identified in this PhD, and discuss the wider implications of this work.

7.1 Interpreting river-induced seismic signals

The recent advances in monitoring bedload transport using seismic sensors have proven to be invaluable. These sensors allow for continuous data collection without the logistical challenges of traditional methods or the uncertainties associated with numerical models. However, this research is still in the proof-of-concept stage, relying heavily on the models developed by Tsai et al. (2012) and Gimbert et al. (2014).

Although there is general agreement among fluvial seismology studies that seismic signals from turbulence generate seismic noise with a lower peak frequency than those from bedload transport, the overlapping frequency ranges of these two processes complicate signal discrimination. Typically, turbulence is observed at frequencies below 20 Hz, while bedload transport is observed at frequencies above 10-15 Hz (Schmandt et al., 2013; Gimbert et al., 2014). However, these exact values vary depending on factors such as the subsurface composition and velocity structure at the site, the distance between the source and the sensor, and the specifications of the instruments used. From the results of using the R 'eseis' package turbulence and bedload models (Figure 4.19), it was shown that the expected seismic spectrums for the River Feshie study reach had a peak at around 5-40 Hz for the turbulence-induced signal and 40 Hz and above for the bedload-induced signal. However, these estimated spectra overlapped considerably highlighting the difficulty in separating the two processes. It should also be noted that the bedload and turbulence models do not account for site effects, and these signals will therefore overprint on top of the modelled outputs.

The work in this thesis demonstrates that seismic sensors deployed on or near riverbanks can effectively record river-induced seismic signals. However, distinguishing between the signals of water turbulence and bedload transport using seismic data alone remains largely speculative. Many studies have noted a hysteresis in the relationship between water level or flow discharge and seismic power, attributing this to seismic noise generated by mobilised bedload. This interpretation is based on

initial findings by Govi et al. (1993), which showed that changes in water level or river discharge correlated with changes in seismic power. Less pronounced hysteresis in lower frequency signals compared to high frequency signals has contributed to the interpretation that discharge and bedload transport generate seismic signals in different frequency ranges (e.g., Schmandt et al., 2013; Gimbert et al., 2014).

From the seismic data presented in this thesis from the River Feshie, comparisons with hydroacoustic data reveal that hysteresis in seismic power versus water level data is not necessarily required for bedload transport to occur. The hysteresis patterns of the large September-October 2022 event show a strong correlation with identified transport periods from the hydroacoustic data and changes in transport regime and/or grain sizes at the highest water levels. However, the smaller water level peaks in other events either show no hysteresis or minimal hysteresis at higher water levels around 1.1-1.2 m, despite independent evidence of bedload motion at water levels around 0.8+ m. Therefore, interpreting bedload transport using the hysteresis relationship is not sufficient for all transport events and does not provide accurate timings of bedload motion initiation and cessation, which are necessary for bedload flux calculations. The hydroacoustic data proved very useful in aiding the identification of periods of bedload transport.

A significant challenge in interpreting bedload entrainment thresholds using seismic data alone is the contamination of river-induced data by other environmental sources of seismic noise, such as wind and rain. As discussed in Chapter 2, wind and rain occupy overlapping frequency ranges with those observed for bedload transport. Since rain typically precedes increases in water levels in a river (in the absence of snowmelt or dam/lake outbursts), there is generally a strong broadband signal leading up to increased water levels and subsequent bedload mobilisation. This complicates the identification of the onset of bedload motion.

7.2 Importance of hydroacoustic measurements

As highlighted in the previous section, the hydroacoustic data collected at the River Feshie was extremely valuable for identifying bedload motion in the channel. While the seismic sensors recorded signals from turbulence, bedload transport, and other environmental sources—often occupying overlapping frequency bands—distinguishing the bedload signal alone proved very challenging. Manually listening to the hydroacoustic files was the most effective method for pinpointing the start and end of bedload transport. However, there was some discrepancy in determining the onset and, more specifically, the cessation of transport. In a large event within a flashy catchment like the River Feshie, the rising limb of the hydrograph is typically very sharp, resulting in an abrupt onset of bedload motion once the entrainment threshold is exceeded. However, the more gradual falling limbs make it difficult to pinpoint the exact moment of bedload transport cessation. This identification is challenging and subject to uncertainties and interpretation by the observer.

Our research has demonstrated that hydroacoustic measurements can potentially provide insights into the general grain sizes being transported in the River Feshie, as larger particles are expected to induce lower frequencies (Geay et al., 2017). This inference aligns with findings from seismic studies and the output of the 'eseis' models, where seismic power increases with increasing grain size (Tsai et al., 2012). However, accurately estimating the mobilised grain sizes remains challenging with-

out independent measurements, despite the development of approximate numerical relationships by Tsai et al. (2012) and others.

Hydroacoustic data can be analysed similarly to seismic data by identifying peak frequencies in the signal. A challenge encountered in this thesis was that the deployment method might have caused a strong bimodality in the signal, observable even at low water levels with no bedload transport. However, the ability to manually listen to the audio files provides a dual interpretation potential, making hydroacoustic data easier to handle and interpret than seismic data. Analysing the frequency content of the hydroacoustic data revealed similar patterns to the seismic data with increased power for increased discharge. Unfortunately, unlike seismic data, hydroacoustic signals do not convey information about the directionality of the sound waves traveling through the water from source to receiver.

This work underscores the importance of having independent measures of bedload transport, especially in the early stages of fluvial seismology research on any river. Independent measurement can be achieved through various methods, with continuous indirect methods being the most effective as they provide measurements over the same duration as seismic data. Using sediment traps to independently measure bedload flux and compare with seismic data has proven useful in previous studies (Schmandt et al., 2017; Bakker et al., 2020; Lagarde et al., 2021). However, sediment traps have limitations due to their size and the fact that they only provide measurements over a combined duration (usually a single event) and not for each timestamp. This approach fails to offer information on the initiation and cessation of bedload transport or the mobilisation of different grain sizes at varying water levels unless active measurements are performed throughout an event, which can be dangerous. Continuous, indirect methods such as hydroacoustics can overcome these limitations.

Depending on the research requirements, either seismic or hydroacoustic measurements, or a combination of both, can be useful. For instance, if the goal is to identify the timings of bedload transport, hydroacoustics may provide the necessary data and can inform a spatial narrative with an array of hydrophones along a channel. However, for more in-depth analysis of wave directionality and the specific processes producing the signals, an integrated system of seismic and hydroacoustic measurements would likely be most effective.

7.3 Directional components of river-induced seismic signals

The research presented in this thesis raises an intriguing question about whether both Rayleigh and Love waves should be considered in fluvial seismology. As discussed in Chapter 6, most previous studies attempting to monitor bedload transport using seismic measurements have assumed that Rayleigh surface waves are the primary waves excited by sediment transport due to the relatively vertical impacts of particles with the riverbed (e.g., Burtin et al., 2016; Goodling et al., 2018). Rayleigh waves move with both vertical and horizontal motion, while Love waves are polarised only in the horizontal plane. Consequently, the vertical signal from river-induced ground motion has been used to identify the presence of Rayleigh waves and thus the occurrence of bedload transport. The seismic models developed by Tsai et al. (2012)

and Gimbert et al. (2014), which are widely used in fluvial seismology research, apply this assumption and have not undergone extensive quantitative testing.

The work in this thesis reveals that for the signals recorded at the River Feshie, there is considerable richness in horizontally propagating seismic waves. Notably, there is a strong stream-parallel component in what is interpreted to be the bedload transport signal. This behaviour was discussed by Roth et al. (2016) and briefly mentioned by Schmandt et al. (2013), suggesting that obliquely impacting saltating particles, as well as those moving through rolling and sliding, could induce horizontally polarised waves, particularly in the stream-parallel direction. Without further testing, it is difficult to conclusively determine the cause of the stream-parallel signals at the River Feshie, but the suggestions by Schmandt et al. (2013) and Roth et al. (2016) appear plausible for our setting. In contrast, the interpreted water turbulence signals show some variance, but generally, the horizontal components are stronger than the vertical component, with the stream-perpendicular signal showing the strongest signal at most sites and events.

7.4 PhD challenges

During the work for this thesis, I encountered several methodological and logistical limitations. Here are some of the main limitations I faced:

1. **Data Collection and Analysis Responsibilities**: As part of a wider research project funded by NERC, I was central to most data collection and analysis efforts for methodologies that would be used in my thesis and by the wider project. At the start of my PhD, we deployed a variety of measurement instruments at the field site and collected data from them. This required me to familiarise myself with many new techniques and independently develop skills to manage and process all the data. Some measurement methods, such as ADCP measurements and underwater photographs, did not yield as much useful data as initially hoped. Had this been known beforehand, it could have saved significant time. However, the diversity of measurement methods proved beneficial in this long-term monitoring study, providing options for data selection and enhancing the narrative of my thesis.

2. **Accurate ADCP Measurements**: Unfortunately, we did not manage to acquire accurate ADCP measurements at the study site due to the unpredictable nature of high-flow events and the logistical challenges of mobilising a small team to the River Feshie on short notice. Accurate discharge measurements local to our site would have been useful for the PhD analysis. However, the water stage measurements collected with locally deployed stream gauge sensors provided sufficient data to analyse the trends of interest.

3. **Fieldwork Coordination**: Conducting fieldwork in such a beautiful catchment was a fantastic experience. However, the distance to the site made it challenging to coordinate team members for routine monitoring trips. Implementing near real-time monitoring would have alleviated some limitations by making data easily accessible for analysis as events occurred. Despite this, routine maintenance trips would still have been necessary. Calum Cuthill made

progress in developing low-cost seismic sensors for near real-time monitoring, but telemetering data from all geophone sites in a remote catchment with limited signal proved challenging.

4. **Instrument Deployment Challenges**: Deploying instruments presented several challenges. Some equipment, such as data loggers, were expensive, requiring careful consideration of geophone placement to avoid flood damage. The development of low-cost sensors, as initiated by Calum Cuthill, would have been advantageous, minimising financial loss if equipment was damaged or lost. Additionally, the heaviness of some equipment made deployment difficult and raised safety concerns, especially when transporting batteries to geophone and hydrophone sites across uneven terrain and through the river.

7.5 Future work

The key results from this thesis, and challenges and limitations faced, present new opportunities and research pathways for future fluvial seismology research. I summarise these key opportunities below:

1. **Complementary Continuous Monitoring Methods**: This work has highlighted the benefits of using complementary continuous monitoring methods to identify bedload transport occurrences. Specifically, this research utilised hydroacoustic measurements, but additional methods could also be applied. Hydroacoustics provide continuous data that can be analysed for frequency characteristics similar to seismic data. Moreover, manual listening to hydroacoustic recordings can confirm bedload transport occurrences. Deploying multiple hydrophones along a river stretch could also provide a spatial understanding of bedload transport patterns. While site and funding limitations prevented us from implementing this approach in our study, future research should consider using multiple sensors over longer river stretches to ensure comprehensive data collection.

2. **Hydrophone Deployment Setup**: Our deployment setup may have caused a bimodality in the hydrophone signal due to interference from wave propagation in the hollowed-out block. To better understand the effect of the deployment method, testing could be performed through controlled experiments to determine the frequency characteristics of different sources of noise, such as pebble drops or water turbulence.

3. **Horizontal and Vertical Seismic Components**: This PhD highlights the importance of analysing both horizontal and vertical seismic signal components adjacent to rivers for studying bedload transport and turbulence. Identifying the surface wave types that are excited by water turbulence and bedload transport is important to help identify the dominant mechanisms generating seismic waves in both the turbulence and bedload components. Future fluvial seismology studies should consider which directional components are most useful for their specific research goals. While simple bedload transport detection might be achieved with vertical component sensors, analysing both components will likely yield more accurate data for studies focused on specific fluvial processes

or spatial-temporal patterns of bedload transport. Given the widespread use of the seismic models by Tsai et al. (2012) and Gimbert et al. (2014) in bedload studies, these models should be further developed to include horizontal signal components. This enhancement would provide more accurate estimations of seismic signatures associated with turbulence and bedload, as well as improve inversions for bedload flux.

4. **Testing in Diverse Settings**: It would be valuable to test the findings of this thesis in various settings with different characteristics and scales. For instance, assessing transport thresholds and hysteresis patterns or the horizontal-to-vertical spectral ratio in a bedrock channel versus an alluvial channel, or in larger and smaller alluvial and bedrock settings. A University of Edinburgh PhD student, Eliana Toro Paz, who started in September 2023, aims to apply some methodologies from this PhD to rivers in Nepal, providing an opportunity to validate these findings in a significantly different environment.

5. **Low-Cost Seismic Systems for Real-Time Monitoring**: Developing low-cost seismic systems for near-real-time monitoring would be particularly beneficial for remote or distant research sites. This would alleviate logistical challenges and improve data management. Research such as Eliana's PhD work would benefit from such a system, allowing for remote monitoring and timely data analysis, reducing the dependency on infrequent field trips.

6. **Timelapse Imagery as a Proxy for Water Level**: Timelapse imagery from the channel banks, collected during this PhD, was effective in identifying channel evolution and correlating high flow event timings with stream gauge data. Early in the project, there were discussions about the possibility of using timelapse imagery as a proxy for water level in study sites where deploying local stream gauge sensors might be difficult. Although this idea was proposed as a potential project for a Master's dissertation, it did not come to fruition. Nevertheless, this concept could be worth exploring, especially for remote, inaccessible channels such as bedrock gorges that lack the infrastructure for attaching stream gauge sensors.

7. **Underwater Cameras for Grain Size Analysis**: The use of underwater cameras to gather information on mobilised grain sizes could complement this field of research. While cameras have been used to study stationary seafloor and riverbed grain sizes (e.g. Stevens et al., 2023), using them to monitor moving particles has not been extensively explored. A potential setup could involve a camera pointing perpendicular to the riverbed over a uniformly gridded surface, capturing images of particles during transport events. These images could then be analysed for grain size using the grid squares for scale. However, I can see many limitations this method may face such as damage during large events, visibility issues in turbid waters, and the need for regular maintenance to keep the grid visible and free from sediment.

7.6 Wider implications

Through the work presented in these chapters, this thesis contributes significantly to the field of fluvial seismology by identifying weaknesses in previous studies and laying the groundwork for future research on innovative approaches to the analysis and monitoring of bedload transport. The significance of monitoring bedload transport cannot be overstated. Accurate forecasting and management of sediment transport are essential for understanding river morphology, maintaining habitat quality, and ensuring infrastructure stability (Reid et al., 1985; Lisle, 1995; Roth et al., 2017). By enhancing monitoring techniques through the integration of seismic and hydroacoustic methods, we can achieve a more comprehensive understanding of these processes, thereby supporting more effective river management and preservation strategies. This work opens up opportunities for broader fluvial seismology research by using three-component analysis for a more thorough understanding of transport processes.

Enhanced bedload transport monitoring methods, particularly continuous techniques like seismic and hydroacoustic measurements, could significantly improve our understanding of sediment motion and flux in regions prone to channel switching, such as the lower Himalayas. These regions frequently experience substantial flood events due to channel switching, which can dramatically alter the landscape and pose serious risks to communities and infrastructure (Pal et al., 2020). Effective monitoring of these processes can provide critical data for forecasting and managing such events, allowing for the development of robust flood management strategies. By continuously tracking sediment movement, we can identify patterns and triggers for channel switching, thereby improving our ability to anticipate and mitigate the impacts of floods.

Sediment transport by rivers can be highly erosive, damaging infrastructure like bridges and embankments, which are particularly vulnerable to sediment-induced scour. Scour is the removal of sediment around bridge foundations or embankments, which can undermine the stability of these structures and lead to catastrophic failures (Prendergast and Gavin, 2014). Continuous bedload transport monitoring using seismic sensors could enhance our understanding of how sediment transport affects bridge scour compared to the erosive power of water alone. By distinguishing between the effects of sediment and water, engineers can design more resilient structures and implement targeted mitigation measures. Moreover, analysing the duration of transport events and the effects of different grain sizes is crucial, as the impact on infrastructure can vary significantly depending on these factors (Prendergast and Gavin, 2014). Hydroacoustics could also potentially play a significant role in this analysis by being deployed to structures to study turbulence and bedload patterns, providing real-time data that can inform maintenance and repair strategies, ultimately extending the lifespan of infrastructure.

Additional in-stream infrastructure such as hydropower plants can both affect and be affected by sediment transport patterns in rivers. Sediment accumulation can reduce the efficiency of hydropower stations by clogging turbines and reducing reservoir capacity, while sediment scouring can damage the hydropower infrastructure (Thapa et al., 2015). Conversely, the construction of dams and other hydropower infrastructure can disrupt the natural flow of sediment, affecting downstream ecosystems and river morphology (Tomczyk et al., 2022). Continuous monitoring using

seismic and hydroacoustic methods could provide valuable insights into these interactions, facilitating the design of hydropower stations that can either endure sediment motion or reduce their impact on natural sediment transport patterns. By understanding sediment dynamics, hydropower operators can implement measures to manage sediment more effectively, such as optimised sediment flushing schedules and the design of sediment bypass systems.

More specifically, this work opens up opportunities for ongoing research in the River Feshie catchment. As discussed in Chapter 1, the River Feshie catchment is currently undergoing ambitious rewilding initiatives designed to restore native woodlands and enhance the overall biodiversity of the area (Turnbull, 2016; Gullett et al., 2023). This comprehensive restoration effort aims not only to revitalise natural habitats but also to create a resilient ecosystem capable of adapting to environmental changes. Understanding the implications of sediment transport within this context is crucial. By studying sediment dynamics, researchers can gain valuable insights into how sediment movement influences the ecological balance of the river and its surrounding habitats. These insights are essential for effective ecosystem monitoring, providing critical information to assess and mitigate the impacts of sediment transport on aquatic life, riparian vegetation, and overall ecosystem health.

Additionally, woody debris presents significant challenges in catchments such as the Feshie, where it can profoundly impact river channel morphology and hydrological processes. Continuous monitoring of sediment movement and channel flow using advanced techniques like seismic and hydroacoustic methods holds promise for shedding light on this complex research area. By deploying these methods, researchers can gather continuous data on sediment dynamics and channel morphology, offering valuable insights into how woody debris influences flow patterns and sediment transport. Hydroacoustics, in particular, can play a crucial role by monitoring the turbulent conditions generated by large woody debris, providing detailed information on flow dynamics and sediment interactions.

Advancements in continuous sediment monitoring technologies could potentially enhance the numerical models of the Feshie, enabling a more detailed exploration of the impacts associated with changing land use and climate. Changes in land use, influenced by initiatives like the rewilding project aimed at increasing native vegetation, can significantly alter how the river responds to climate change. This may include stabilising banks, reducing sediment input into the channel, and enhancing water filtration into the riverbed. Another PhD candidate at the University of Edinburgh has already made progress in this area, developing initial numerical models that incorporate the thresholds of sediment entrainment found through the seismic and hydroacoustic analysis in this thesis, along with the related fluxes. This integrated sediment and hydrology model, utilising CAESAR-Lisflood, has proven effective in refining default parameters, thereby increasing the relevance and applicability of results specific to the Feshie catchment. These advancements have the potential to enhance the accuracy of bedload flux calculations by integrating data from field measurements, seismic observations, hydroacoustic analyses, and numerical sediment modeling techniques.

Overall, continuous sediment monitoring can be used to evaluate the effectiveness of sediment reduction actions in the catchment and guide adaptive sediment management strategies. This comprehensive approach to monitoring and analysing

sediment transport has far-reaching implications for river management, infrastructure protection, and ecological preservation.

Chapter 8

Conclusions

The overarching theme of this thesis was to explore the seismic signals recorded in the River Feshie catchment to understand the signal differentiation between the two key fluvial processes that cause ground vibrations: flow turbulence and bedload transport. My findings presented in Chapters 4, 5 and 6 and discussed in Chapter 7, contribute to the existing body of research around fluvial seismology outlined in Chapter 2.

Chapter 4 examines the effectiveness of geophones in recording seismic waves induced by processes within the River Feshie channel in Scotland and investigates the feasibility of distinguishing between flow turbulence and bedload transport using seismic data. Chapter 5 employs hydroacoustic measurements to independently verify bedload transport occurrences, enhancing understanding of recorded seismic signals and bedload transport dynamics during significant flow events. Chapter 6 delves into the variations in river-induced seismic signals across three directional components, evaluating whether bedload transport or flow turbulence predominantly induces specific surface waves. Below I present the main conclusions drawn from these thesis chapters and provide overall concluding remarks.

Chapter 4: Site and event variations in river-induced seismic characteristics

This chapter serves as the foundational analysis for the subsequent research chapters, focusing on the variations in recorded river-induced ground vibrations between sites and events. It successfully examines the capability of geophones to capture seismic signals from the River Feshie in all three directional components. The analysis highlights the complexities involved in differentiating between the frequency bands associated with flow turbulence and bedload transport using seismic data alone. This challenge underscores the necessity of integrating complementary monitoring methods to independently verify and interpret bedload transport occurrences. Additionally, this chapter reveals that the signals recorded at a single site across multiple events are generally very consistent. However, greater variability in the signals arise between different sites as a result of varying site characteristics. This implies that the site effects are dominant, and the source effects are more subtle in comparison.

Moving forward, the thesis proposes expanding the analysis to include additional data sources, such as hydroacoustic measurements, to enhance the reliability and accuracy of bedload transport identification. By combining these methods, the study aims to refine the understanding of how different fluvial processes manifest in seis-

mic signals, ultimately contributing to more robust methodologies for monitoring river dynamics and sediment transport.

Chapter 5: Inferring bedload transport thresholds through seismic and hydroacoustic recordings
Building upon the findings of Chapter 4, which demonstrated the challenges in interpreting bedload transport signals from seismic data, this chapter highlights the significance of integrating seismic measurements with other continuous methods like hydroacoustics. The thesis establishes hydroacoustic measurements as a robust independent tool for monitoring bedload transport, complementing the analysis using seismic data. Analysis of hydroacoustic recordings during bedload transport events unveiled insights into the characteristics of seismic signatures associated with bedload transport processes. Specifically, it highlighted that the entrainment thresholds of bedload particles in the River Feshie were influenced by the magnitude and duration of high flow events. Large events were observed to weaken an established armour layer that was developed gradually over successive smaller flows and deposit unsorted material during rapid falling water levels, thereby facilitating easier mobilisation of particles in subsequent events. Additionally, the combined analysis of hydroacoustic and seismic data revealed that the commonly observed hysteresis relationship between seismic power and water level, often used as an indicator of bedload transport (as discussed in Chapters 2 and 5), is not consistently observed during periods of bedload transport. Its presence appears to depend on the magnitude of the hydrological events or water levels encountered, and is not a universal characteristic across all bedload transport events.

Chapter 6: Comparison of the directional components of the seismic signals
Chapter 4 demonstrated the successful recording of river-induced seismic signals in all three directional components: stream-parallel, stream-perpendicular, and vertical. Previous studies suggested that the vertical component carried the strongest bedload transport signal. However, Chapter 6 of this thesis challenges this notion by revealing a significant presence of horizontal signals. Specifically, the stream-parallel component exhibited the strongest signal across the frequency band associated with bedload transport, while interpreted turbulence-dominated frequencies were observed strongest in both the stream-parallel and stream-perpendicular directions. The exact reasons for these signal characteristics are not definitively known and require further investigation. It is possible that the dominance of stream-parallel signals during bedload transport events is due to particles rolling and sliding downstream, or from oblique impacts of particles on the riverbed. These findings underscore the importance of analysing horizontally polarised waves in river-induced ground vibrations, particularly with the availability of low cost three-component seismic sensors. Such analysis could potentially aid in distinguishing between turbulence and bedload-induced signals in future studies.

This thesis advances the field of fluvial seismology by demonstrating the effective use of seismic sensors for monitoring river processes, including bedload transport.

It addresses the challenges of distinguishing bedload transport signals from other noise sources, such as turbulence and rain, by advocating for the integration of complementary datasets. This approach enhances signal identification and accuracy.

Moreover, the research underscores the importance of considering horizontally-induced seismic waves in bedload transport monitoring and flux estimations. By incorporating these horizontal components, we can achieve a more precise understanding of seismic signatures related to both turbulence and bedload, ultimately leading to better estimations of bedload flux.

In summary, this thesis not only builds upon existing fluvial seismology research but also opens new avenues for more accurate and comprehensive monitoring of river processes. The insights gained from this work significantly contribute to our understanding of sediment transport in rivers, a key factor in river channel evolution. This understanding is essential for managing and forecasting flood risks, particularly as climate change is expected to increase the frequency and severity of flood events in many regions worldwide. These advances are crucial for developing effective river management strategies and mitigating the impacts of climate change on flood risk.

Bibliography

Allstadt, K. E., Farin, M., Iverson, R. M., Obryk, M. K., Kean, J. W., Tsai, V. C., Rapstine, T. D., and Logan, M. (2020). "Measuring Basal Force Fluctuations of Debris Flows Using Seismic Recordings and Empirical Green's Functions". en. In: *Journal of Geophysical Research: Earth Surface* 125.9, e2020JF005590. ISSN: 2169-9011. DOI: 10.1029/2020JF005590. URL: https://onlinelibrary.wiley.com/doi/abs/10.1029/2020JF005590 (visited on 04/19/2024).

An, C., Parker, G., Hassan, M., and Fu, X. (2018). "Can magic sand cause massive degradation of a gravel-bed river at the decadal scale? Shi-ting River, China". In: *Geomorphology* 327. DOI: 10.1016/j.geomorph.2018.10.026.

Apsley, D. (n.d.). *Bed-Load Sediment Transport Formulae*. URL: https://personalpages.manchester.ac.uk/staff/david.d.apsley/hydraulics/bedload.pdf.

Ashida, K. and Bayazit, M. (1973). "Influence of Vertical Motion on Initiation of Sediment Movement". In: *Proceedings of the 15th Congress of the International Association for Hydraulic Research*. Delft, Netherlands, pp. 475–484. (Visited on 06/26/2024).

Ashida, K. and Michue, M. (1972). "Study on hydraulic resistance and bed-load transport rate in alluvial streams". In: *Journal of Civil Engineering* 206, pp. 59–69.

Attal, M., Mudd, S., Hurst, M., Weinman, B., Yoo, K., and Naylor, M. (2015). "Impact of change in erosion rate and landscape steepness on hillslope and fluvial sediments grain size in the Feather River Basin (Sierra Nevada, California)". In: *Earth Surface Dynamics* 3, pp. 201–222. DOI: 10.5194/esurf-3-201-2015.

Babiński, Z. (2005). "The relationship between suspended and bed load transport in river channels". en. In: *Sediment Budgets I*. Vol. 291. Foz do Iguaçu, Brazil: IAHS.

Badoux, A., Andres, N., and Turowski, J. M. (2014). "Damage costs due to bedload transport processes in Switzerland". English. In: *Natural Hazards and Earth System Sciences* 14.2. Publisher: Copernicus GmbH, pp. 279–294. ISSN: 1561-8633. DOI: 10.5194/nhess-14-279-2014. URL: https://nhess.copernicus.org/articles/14/279/2014/ (visited on 06/26/2024).

Bakker, M., Gimbert, F., Geay, T., Misset, C., Zanker, S., and Recking, A. (2020). "Field Application and Validation of a Seismic Bedload Transport Model". en. In: *Journal of Geophysical Research*, p. 22.

Bakker, M., Legout, C., Gimbert, F., Nord, G., Boudevillain, B., and Freche, G. (2022). "Seismic modelling and observations of rainfall". In: *Journal of Hydrology* 610, p. 127812. ISSN: 0022-1694. DOI: 10.1016/j.jhydrol.2022.127812. URL: https://www.sciencedirect.com/science/article/pii/S0022169422003870 (visited on 06/07/2024).

Ballance, L. T., Pitman, R. L., Barlow, J., Pusser, T., DeAngelis, A. I., Hayslip, C., Irvine, L., Steel, D., Baker, C. S., Gillies, D., Baumann-Pickering, S., Trickey, J. S., and Gisborne, B. (2023). "Acoustic recordings, biological observations, and genetic identification of a rare(?) beaked whale in the North Pacific: Mesoplodon carlhubbsi". en. In: *Marine Mammal Science*. ISSN: 1748-7692. DOI: 10.1111/mms.13059. URL: https://onlinelibrary.wiley.com/doi/abs/10.1111/mms.13059 (visited on 10/30/2023).

Barker, L., Hannaford, J., Muchan, K., Turner, S., and Parry, S. (2016). "The winter 2015/2016 floods in the UK: a hydrological appraisal". en. In: *Weather* 71.12. _eprint: https://onlinelibrary.wiley.com/doi/pdf/10.1002/wea.2822, pp. 324–333. ISSN: 1477-8696. DOI: 10.1002/wea.2822. URL: https://onlinelibrary.wiley.com/doi/abs/10.1002/wea.2822 (visited on 10/20/2023).

Barman, A. (2023). *Seismic Refraction Survey – Determine Classification And Thickness Of Various Soil Layer*. en-US. Running Time: 142 Section: Foundation. URL: https://civilhex.com/seismic-refraction-survey/ (visited on 06/27/2024).

Barrière, J., Oth, A., Hostache, R., and Krein, A. (2015). "Bed load transport monitoring using seismic observations in a low-gradient rural gravel bed stream: Seismic monitoring of bedload transport". en. In: *Geophysical Research Letters* 42.7, pp. 2294–2301. ISSN: 00948276. DOI: 10.1002/2015GL063630. URL: http://doi.wiley.com/10.1002/2015GL063630 (visited on 10/28/2020).

Batalla, R. J. and Martín-Vide, J. P. (2001). "Thresholds of particle entrainment in a poorly sorted sandy gravel-bed river". In: *CATENA* 44.3, pp. 223–243. ISSN: 0341-8162. DOI: 10.1016/S0341-8162(00)00157-0. URL: https://www.sciencedirect.com/science/article/pii/S0341816200001570 (visited on 06/06/2024).

Belleudy, P., Valette, A., and Graff, B. (2010). "Monitoring of bedload in river beds with an hydrophone: first trials of signal analyses". en. In: *Dittrich, Andreas; Koll, Katinka; Aberle, Jochen; Geisenhainer, Peter (Hg.): River Flow 2010*. URL: https://hdl.handle.net/20.500.11970/99836.

Bertoldi, W., Zanoni, L., Miori, S., Repetto, R., and Tubino, M. (2009). "Interaction between migrating bars and bifurcations in gravel bed rivers". en. In: *Water Resources Research* 45.6. ISSN: 1944-7973. DOI: 10.1029/2008WR007086. URL: https://onlinelibrary.wiley.com/doi/abs/10.1029/2008WR007086 (visited on 06/26/2024).

Best, J. (1988). "Sediment transport and bed morphology at river channel confluences". In: *Sedimentology* 35, pp. 481–498.

Bogen, J. (1980). "The hysteresis effect of sediment transport systems". In: *Norsk Geografisk Tidsskrift - Norwegian Journal of Geography* 34.1. Publisher: Routledge _eprint: https://doi.org/10.1080/00291958008545338, pp. 45–54. ISSN: 0029-1951. DOI: 10.1080/00291958008545338. URL: https://doi.org/10.1080/00291958008545338 (visited on 10/30/2023).

Boundary Layer — Definition & Characteristics (2024). en-us. URL: https://www.nuclear-power.com/nuclear-engineering/fluid-dynamics/boundary-layer/ (visited on 07/08/2024).

Bountourakis, V., Elvander, F., and Pulkki, V. (2023). *Using optimal mass transport in bearing-time records for underwater target localization and tracking*.

Brasington, J., Langham, J., and Rumsby, B. (2003). "Methodological sensitivity of morphometric estimates of coarse fluvial sediment transport". en. In: *Geomorphology* 53.3, pp. 299–316. ISSN: 0169-555X. DOI: 10.1016/S0169-555X(02)00320-3. URL: https://www.sciencedirect.com/science/article/pii/S0169555X02003203 (visited on 02/01/2023).

Brasington, J., Rumsby, B. T., and Mcvey, R. A. (2000). "Monitoring and modelling morphological change in a braided gravel-bed river using high resolution GPS-based survey". en. In: p. 18.

Brodsky, E. E., Roeloffs, E., Woodcock, D., Gall, I., and Manga, M. (2003). "A mechanism for sustained groundwater pressure changes induced by distant earthquakes". en. In: *Journal of Geophysical Research: Solid Earth* 108.B8. _eprint: https://onlinelibrary.wiley.com/doi/pdf/10.1029/2002JB002321. ISSN: 2156-2202. DOI: 10.1029/2002JB002321. URL: https://onlinelibrary.wiley.com/doi/abs/10.1029/2002JB002321 (visited on 06/26/2024).

Brogan, W. L. (1962). "Hertz impact between a surface and a mass-spring-mass system". In: *International Journal of Mechanical Sciences* 4.2, pp. 115–127. ISSN: 0020-7403. DOI: 10.1016/S0020-7403(62)80034-4. URL: https://www.sciencedirect.com/science/article/pii/S0020740362800344 (visited on 07/17/2024).

Brown, C. B. (1950). "Sediment Transport". In: *Engineering Hydraulics*. Ed. by H. Rouse. Chapter: 12. Wiley.

Buffington, J., Montgomery, D., and Greenberg, H. (2004). "Basin-scale availability of salmonid spawning gravel as influenced by channel type and hydraulic roughness in mountain catchments". In: *Canadian Journal of Fisheries and Aquatic Sciences* 61.11. Publisher: NRC Research Press, pp. 2085–2096. ISSN: 0706-652X. DOI: 10.1139/f04-141. URL: https://cdnsciencepub.com/doi/10.1139/f04-141 (visited on 06/26/2024).

Buffington, J. M. and Montgomery, D. R. (1997). "A systematic analysis of eight decades of incipient motion studies, with special reference to gravel-bedded rivers". en. In: *Water Resources Research* 33.8, pp. 1993–2029. ISSN: 1944-7973. DOI: 10.1029/96WR03190. URL: https://onlinelibrary.wiley.com/doi/abs/10.1029/96WR03190 (visited on 03/27/2024).

Bunte, K. and Abt, S. R. (2005). "Effect of sampling time on measured gravel bed load transport rates in a coarse-bedded stream". In: *Water Resources Research* 41.11. DOI: https://doi.org/10.1029/2004WR003880. URL: https://agupubs.onlinelibrary.wiley.com/doi/10.1029/2004wr003880 (visited on 10/30/2023).

Bunte, K., Abt, S. R., Potyondy, J. P., and Ryan, S. E. (2004). "Measurement of Coarse Gravel and Cobble Transport Using Portable Bedload Traps". EN. In: *Journal of Hydraulic Engineering* 130.9. Publisher: American Society of Civil Engineers, pp. 879–893. ISSN: 0733-9429. DOI: 10.1061/(ASCE)0733-9429(2004)130:9(879). URL: https://ascelibrary.org/doi/10.1061/%28ASCE%290733-9429%282004%29130%3A9%28879%29 (visited on 10/30/2023).

Bunte, K., Swingle, K., and Abt, S. (2007). *Guidelines for Using Bedload Traps in Coarse-Bedded Mountain Streams: Construction, Installation, Operation, and Sample Processing*. DOI: 10.13140/2.1.3912.3847.

Burtin, A., Bollinger, L., Vergne, J., Cattin, R., and Nábělek, J. L. (2008). "Spectral analysis of seismic noise induced by rivers: A new tool to monitor spa-

tiotemporal changes in stream hydrodynamics". en. In: *Journal of Geophysical Research* 113.B5. ISSN: 0148-0227. DOI: 10.1029/2007JB005034. URL: http://doi.wiley.com/10.1029/2007JB005034 (visited on 10/28/2020).

Burtin, A., Cattin, R., Bollinger, L., Vergne, J., Steer, P., Robert, A., Findling, N., and Tiberi, C. (2011). "Towards the hydrologic and bed load monitoring from high-frequency seismic noise in a braided river: The "torrent de St Pierre", French Alps". en. In: *Journal of Hydrology* 408.1-2, pp. 43–53. ISSN: 00221694. DOI: 10.1016/j.jhydrol.2011.07.014. URL: https://linkinghub.elsevier.com/retrieve/pii/S0022169411004562 (visited on 10/28/2020).

Burtin, A., Hovius, N., McArdell, B. W., Turowski, J. M., and Vergne, J. (2013). "Seismic constraints on dynamic links between geomorphic processes and routing of sediment in a steep mountain catchment". en. In: *Earth Surface Dynamics Discussions* 1.1, pp. 783–816. ISSN: 2196-6338. DOI: 10.5194/esurfd-1-783-2013. URL: https://esurf.copernicus.org/preprints/1/783/2013/ (visited on 10/28/2020).

Burtin, A., Hovius, N., McArdell, B. W., Turowski, J. M., and Vergne, J. (2014). "Seismic constraints on dynamic links between geomorphic processes and routing of sediment in a steep mountain catchment". en. In: *Earth Surface Dynamics* 2.1, pp. 21–33. ISSN: 2196-632X. DOI: 10.5194/esurf-2-21-2014. URL: https://esurf.copernicus.org/articles/2/21/2014/ (visited on 10/28/2020).

Burtin, A., Hovius, N., and Turowski, J. (2016). "Seismic monitoring of torrential and fluvial processes". In: *Earth Surface Dynamics* 4. DOI: 10.5194/esurf-4-285-2016.

Burtin, A., Vergne, J., Rivera, L., and Dubernet, P. (2010). "Location of river-induced seismic signal from noise correlation functions: Location of river seismic signal". en. In: *Geophysical Journal International* 182.3, pp. 1161–1173. ISSN: 0956540X. DOI: 10.1111/j.1365-246X.2010.04701.x. URL: https://academic.oup.com/gji/article-lookup/doi/10.1111/j.1365-246X.2010.04701.x (visited on 10/28/2020).

Cao, Z. and Carling, P. A. (2002). "Mathematical modelling of alluvial rivers: reality and myth. Part 1: General review". In: *Water & Maritime Engineering IS4* 3, pp. 207–219.

Chao, W.-A., Wu, Y.-M., Zhao, L., Tsai, V. C., and Chen, C.-H. (2015). "Seismologically determined bedload flux during the typhoon season". en. In: *Scientific Reports* 5.1, p. 8261. ISSN: 2045-2322. DOI: 10.1038/srep08261. URL: http://www.nature.com/articles/srep08261 (visited on 10/28/2020).

"Sediment Transport" (2008). en. In: *Open-Channel Flow*. Ed. by M. H. Chaudhry. Boston, MA: Springer US, pp. 453–477. ISBN: 978-0-387-68648-6. DOI: 10.1007/978-0-387-68648-6_16. URL: https://doi.org/10.1007/978-0-387-68648-6_16 (visited on 06/26/2024).

Cheng, N.-S. (2004). "Analysis of bedload transport in laminar flows". en. In: *Advances in Water Resources* 27.9, pp. 937–942. ISSN: 03091708. DOI: 10.1016/j.advwatres.2004.05.010. URL: https://linkinghub.elsevier.com/retrieve/pii/S0309170804001009 (visited on 06/26/2024).

Church, M. (2006). "Bed Material Transport and the Morphology of Alluvial River Channels". In: *Annual Review of Earth and Planetary Sciences* 34.1. _eprint: https://doi.org/10.1146/annurev.earth.33.092203.122721, pp. 325–354. DOI: 10.

1146/annurev.earth.33.092203.122721. URL: https://doi.org/10.1146/annurev.earth.33.092203.122721 (visited on 04/12/2021).

Church, M., Hassan, M. A., and Wolcott, J. F. (1998). "Stabilizing self-organized structures in gravel-bed stream channels: Field and experimental observations". en. In: *Water Resources Research* 34.11, pp. 3169–3179. ISSN: 1944-7973. DOI: 10.1029/98WR00484. URL: https://onlinelibrary.wiley.com/doi/abs/10.1029/98WR00484 (visited on 03/10/2023).

Cook, K. L., Andermann, C., Gimbert, F., Adhikari, B. R., and Hovius, N. (2018). "Glacial lake outburst floods as drivers of fluvial erosion in the Himalaya". In: *Science* 362.6410. Publisher: American Association for the Advancement of Science, pp. 53–57. DOI: 10.1126/science.aat4981. URL: https://www.science.org/doi/10.1126/science.aat4981 (visited on 10/31/2022).

Cook, K. L. and Dietze, M. (2022). "Seismic Advances in Process Geomorphology". In: *Annual Review of Earth and Planetary Sciences* 50.1, pp. 183–204. DOI: 10.1146/annurev-earth-032320-085133. URL: https://doi.org/10.1146/annurev-earth-032320-085133 (visited on 08/25/2022).

Coviello, V., Capra, L., Vázquez, R., and Márquez-Ramírez, V. H. (2018). "Seismic characterization of hyperconcentrated flows in a volcanic environment". en. In: *Earth Surface Processes and Landforms* 43.10, pp. 2219–2231. ISSN: 1096-9837. DOI: 10.1002/esp.4387. URL: https://onlinelibrary.wiley.com/doi/abs/10.1002/esp.4387 (visited on 06/07/2024).

Cowan, W. L. (1956). "Estimating hydraulic roughness coefficients". In: *Agricultural Engineering* 37.7, pp. 473–475.

Dean, T. (2018). "The seismic signature of rain". en. In: *ASEG Extended Abstracts* 2018.1, pp. 1–8. ISSN: 2202-0586. DOI: 10.1071/ASEG2018abP068. URL: https://www.tandfonline.com/doi/full/10.1071/ASEG2018abP068 (visited on 12/06/2022).

Dell'Agnese, A., Mao, L., and Comiti, F. (2014). "Calibration of an acoustic pipe sensor through bedload traps in a glacierized basin". en. In: *CATENA* 121, pp. 222–231. ISSN: 0341-8162. DOI: 10.1016/j.catena.2014.05.021. URL: https://www.sciencedirect.com/science/article/pii/S0341816214001568 (visited on 05/31/2021).

Dey, S. (2014). *Fluvial Hydrodynamics*. en. GeoPlanet: Earth and Planetary Sciences. Berlin, Heidelberg: Springer Berlin Heidelberg. ISBN: 978-3-642-19061-2 978-3-642-19062-9. DOI: 10.1007/978-3-642-19062-9. URL: http://link.springer.com/10.1007/978-3-642-19062-9 (visited on 11/20/2020).

Diaz, J., Ruiz, M., Udina, M., Polls, F., Martí, D., and Bech, J. (2023). "Monitoring storm evolution using a high-density seismic network". en. In: *Scientific Reports* 13.1. Number: 1 Publisher: Nature Publishing Group, p. 1853. ISSN: 2045-2322. DOI: 10.1038/s41598-023-28902-8. URL: https://www.nature.com/articles/s41598-023-28902-8 (visited on 02/27/2024).

Dietze, M. (2018a). *'eseis' - a comprehensive R software toolbox for environmental seismology*. URL: https://doi.org/10.5880/GFZ.5.1.2018.001.

Dietze, M. (2018b). "The R package "eseis" – a software toolbox for environmental seismology". In: *Earth Surface Dynamics* 6, pp. 669–686. DOI: 10.5194/esurf-6-669-2018.

Dietze, M. and Gimbert, F. (2019). "The seismic view on sediment laden ephemeral flows – modelling of ground motion data for fluid and bedload dynamics in the Arroyo de los Piños". en. In: p. 10.

Dietze, M., Lagarde, S., Halfi, E., Laronne, J. B., and Turowski, J. M. (2019). "Joint Sensing of Bedload Flux and Water Depth by Seismic Data Inversion". en. In: *Water Resources Research* 55.11, pp. 9892–9904. ISSN: 1944-7973. DOI: https://doi.org/10.1029/2019WR026072. URL: https://agupubs.onlinelibrary.wiley.com/doi/abs/10.1029/2019WR026072 (visited on 02/26/2021).

Dietze, M., Losee, J., Polvi, L., and Palm, D. (2020). "A seismic monitoring approach to detect and quantify river sediment mobilization by steelhead redd-building activity". en. In: *Earth Surface Processes and Landforms* 45.12. _eprint: https://onlinelibrary.wiley.com/doi/pdf/10.1002/esp.4933, pp. 2840–2849. ISSN: 1096-9837. DOI: https://doi.org/10.1002/esp.4933. URL: https://onlinelibrary.wiley.com/doi/abs/10.1002/esp.4933 (visited on 02/26/2021).

Dietze, M., Turowski, J. M., Cook, K. L., and Hovius, N. (2017). *Spatiotemporal patterns and triggers of seismically detected rockfalls*. en. preprint. Physical: Geomorphology (including all aspects of fluvial, coastal, aeolian, hillslope and glacial geomorphology). DOI: 10.5194/esurf-2017-20. URL: https://esurf.copernicus.org/preprints/esurf-2017-20/esurf-2017-20.pdf (visited on 10/31/2022).

Dingle, E. H. and Venditti, J. G. (2023). "Experiments on Gravel-Sand Transitions: Examination of Washload Deposition". en. In: *Journal of Geophysical Research: Earth Surface* 128.7, e2023JF007116. ISSN: 2169-9011. DOI: 10.1029/2023JF007116. URL: https://onlinelibrary.wiley.com/doi/abs/10.1029/2023JF007116 (visited on 07/08/2024).

Downs, P. W., Soar, P. J., and Taylor, A. (2016). "The anatomy of effective discharge: the dynamics of coarse sediment transport revealed using continuous bedload monitoring in a gravel-bed river during a very wet year: Dynamics of coarse sediment transport using continuous monitoring". en. In: *Earth Surface Processes and Landforms* 41.2, pp. 147–161. ISSN: 01979337. DOI: 10.1002/esp.3785. URL: http://doi.wiley.com/10.1002/esp.3785 (visited on 10/28/2020).

Du Boys, P. (1879). "Le Rhône et les rivières à lit affouillable – Étude du régime du Rhône et de l'action exercée par les eaux sur un lit à fond de graviers indéfiniment affouillable". In: *Annales des Ponts et Chaussées* 49, pp. 141–195. URL: https://www.sid.ir/paper/600573/en (visited on 06/26/2024).

Einstein, H. (1950). "The Bed-Load Function for Sediment Transportation in Open Channel Flows". In: URL: https://www.semanticscholar.org/paper/The-Bed-Load-Function-for-Sediment-Transportation-Einstein/7f9d8f5699e%2068821d27baf02f890cd0b6a02c0ec (visited on 06/24/2024).

Ekström, G., Nettles, M., and Abers, G. A. (2003). "Glacial Earthquakes". In: *Science* 302.5645. Publisher: American Association for the Advancement of Science, pp. 622–624. DOI: 10.1126/science.1088057. URL: https://www.science.org/doi/10.1126/science.1088057 (visited on 06/17/2024).

Farin, M., Mangeney, A., and Roche, O. (2014). "Fundamental changes of granular flow dynamics, deposition, and erosion processes at high slope angles: Insights from laboratory experiments". en. In: *Journal of Geophysical Research: Earth Surface* 119.3, pp. 504–532. ISSN: 2169-9011. DOI: 10.1002/2013JF002750. URL:

https://onlinelibrary.wiley.com/doi/abs/10.1002/2013JF002750 (visited on 06/07/2024).

Ferguson, R. I., Ashmore, P. E., Ashworth, P. J., Paola, C., and Prestegaard, K. L. (1992). "Measurements in a Braided River chute and lobe: 1. Flow pattern, sediment transport, and channel change". en. In: *Water Resources Research* 28.7, pp. 1877–1886. ISSN: 1944-7973. DOI: https://doi.org/10.1029/92WR00700. URL: https://agupubs.onlinelibrary.wiley.com/doi/abs/10.1029/92WR00700 (visited on 04/06/2021).

Ferguson, R. I. and Werritty, A. (1983). "Bar Development and Channel Changes in the Gravelly River Feshie, Scotland". en. In: *Modern and Ancient Fluvial Systems*. Oxford, UK: Blackwell Publishing Ltd., pp. 181–193. ISBN: 978-1-4443-0377-3 978-0-632-00997-8. DOI: 10.1002/9781444303773.ch14. URL: http://doi.wiley.com/10.1002/9781444303773.ch14 (visited on 10/28/2020).

Gaeuman, D. (2010). "Mechanics of Bedload Rating Curve Shifts and Bedload Hysteresis in the Trinity River, California". en. In.

Gaeuman, D. (2016). "Seismic Monitoring of Bedload Transport in a Large Gravel-bed River". In: URL: https://www.usbr.gov/research/projects/detail.cfm?id=5561.

Gaeuman, D. and Jacobson, R. B. (2007). "Field Assessment of Alternative Bed-Load Transport Estimators". EN. In: *Journal of Hydraulic Engineering* 133.12. Publisher: American Society of Civil Engineers, pp. 1319–1328. ISSN: 0733-9429. DOI: 10.1061/(ASCE)0733-9429(2007)133:12(1319). URL: https://ascelibrary.org/doi/abs/10.1061/%28ASCE%290733-9429%282007%29133%3A12%281319%29 (visited on 11/10/2021).

Geay, T., Belleudy, P., Gervaise, C., Habersack, H., Aigner, J., Kreisler, A., Seitz, H., and Laronne, J. B. (2017). "Passive acoustic monitoring of bed load discharge in a large gravel bed river". en. In: *Journal of Geophysical Research: Earth Surface* 122.2, pp. 528–545. ISSN: 2169-9011. DOI: https://doi.org/10.1002/2016JF004112. (Visited on 05/31/2021).

Geay, T., Zanker, S., Misset, C., and Recking, A. (2020). "Passive Acoustic Measurement of Bedload Transport: Toward a Global Calibration Curve?" en. In: *Journal of Geophysical Research: Earth Surface* 125.8. ISSN: 2169-9003, 2169-9011. DOI: 10.1029/2019JF005242. (Visited on 11/20/2020).

Geli, L., Bard, P.-Y., and Jullien, B. (1988). "The effect of topography on earthquake ground motion: A review and new results". In: *Bulletin of the Seismological Society of America* 78, pp. 42–63. DOI: 10.1785/BSSA0780010042.

Gilmore, M. H. (1947). "Tracking Ocean Storms with the Seismograph". en. In: Section: Bulletin of the American Meteorological Society. DOI: 10.1175/1520-0477-28.2.73. URL: https://journals.ametsoc.org/view/journals/bams/28/2/1520-0477-28_2_73.xml (visited on 06/17/2024).

Gilvear, D., Cecil, J., and Parsons, H. (2000). "Channel change and vegetation diversity on a low-angle alluvial fan, River Feshie, Scotland". en. In: *Aquatic Conservation: Marine and Freshwater Ecosystems* 10.1, pp. 53–71. ISSN: 1099-0755. DOI: 10.1002/(SICI)1099-0755(200001/02)10:1<53::AID-AQC348>3.0.CO;2-4. (Visited on 01/27/2023).

Gimbert, F., Fuller, B., Lamb, M., Tsai, V., and Johnson, J. (2019). "Particle transport mechanics and induced seismic noise in steep flume experiments with accelerometer-embedded tracers". en. In: *Earth Surface Processes and Land-*

forms 44.1. _eprint: https://onlinelibrary.wiley.com/doi/pdf/10.1002/esp.4495, pp. 219–241. ISSN: 1096-9837. DOI: https://doi.org/10.1002/esp.4495. URL: https://onlinelibrary.wiley.com/doi/abs/10.1002/esp.4495 (visited on 02/05/2021).

Gimbert, F., Tsai, V., and Lamb, M. (2014). "A physical model for seismic noise generation by turbulent flow in rivers". en. In: *Journal of Geophysical Research: Earth Surface* 119.10, pp. 2209–2238. ISSN: 21699003. DOI: 10.1002/2014JF003201. URL: http://doi.wiley.com/10.1002/2014JF003201 (visited on 10/28/2020).

Gomez, B. and Church, M. (1989). "An assessment of bed load sediment transport formulae for gravel bed rivers". en. In: *Water Resources Research* 25.6, pp. 1161–1186. ISSN: 00431397. DOI: 10.1029/WR025i006p01161. URL: http://doi.wiley.com/10.1029/WR025i006p01161 (visited on 10/28/2020).

Gomez, B. and Soar, P. J. (2022). "Bedload transport: beyond intractability". In: *Royal Society Open Science* 9.3. Publisher: Royal Society, p. 211932. DOI: 10.1098/rsos.211932. URL: https://royalsocietypublishing.org/doi/10.1098/rsos.211932 (visited on 10/30/2023).

Goodling, P. J., Lekic, V., and Prestegaard, K. (2018). "Seismic signature of turbulence during the 2017 Oroville Dam spillway erosion crisis". English. In: *Earth Surface Dynamics* 6.2. Publisher: Copernicus GmbH, pp. 351–367. ISSN: 2196-6311. DOI: 10.5194/esurf-6-351-2018. URL: https://esurf.copernicus.org/articles/6/351/2018/ (visited on 07/16/2024).

Govi, M., Maraga, F., and Moia, F. (1993). "Seismic detectors for continuous bed load monitoring in a gravel stream". In: *Hydrological Sciences Journal* 38.2. Publisher: Taylor & Francis _eprint: https://doi.org/10.1080/02626669309492650, pp. 123–132. ISSN: 0262-6667. DOI: 10.1080/02626669309492650. URL: https://doi.org/10.1080/02626669309492650 (visited on 06/17/2024).

Gullett, P. R., Leslie, C., Mason, R., Ratcliffe, P., Sargent, I., Beck, A., Cameron, T., Cowie, N. R., Hetherington, D., MacDonell, T., Moat, T., Moore, P., Teuten, E., and Hancock, M. H. (2023). "Woodland expansion in the presence of deer: 30 years of evidence from the Cairngorms Connect landscape restoration partnership". en. In: *Journal of Applied Ecology* 60.11, pp. 2298–2308. ISSN: 1365-2664. DOI: 10.1111/1365-2664.14501. URL: https://onlinelibrary.wiley.com/doi/abs/10.1111/1365-2664.14501 (visited on 11/02/2023).

Guo, Z., Aydin, A., Huang, Y., and Xue, M. (2021). "Polarization characteristics of Rayleigh waves to improve seismic site effects analysis by HVSR method". In: *Engineering Geology* 292, p. 106274. ISSN: 0013-7952. DOI: 10.1016/j.enggeo.2021.106274. URL: https://www.sciencedirect.com/science/article/pii/S0013795221002854 (visited on 04/22/2024).

Harrelson, C. C., Rawlins, C. L., and Potyondy, J. P. (1994). "Stream channel reference sites: An illustrated guide to field technique". en. In: *Gen. Tech. Rep. RM-245. Fort Collins, CO: U.S. Department of Agriculture, Forest Service, Rocky Mountain Forest and Range Experiment Station. 61 p.* 245. DOI: 10.2737/RM-GTR-245. URL: https://www.fs.usda.gov/research/treesearch/20753 (visited on 05/15/2024).

Hassan, M. A., Egozi, R., and Parker, G. (2006). "Experiments on the effect of hydrograph characteristics on vertical grain sorting in gravel bed rivers". en. In: *Water Resources Research* 42.9. ISSN: 1944-7973. DOI: https://doi.org/10.

1029/2005WR004707. URL: https://agupubs.onlinelibrary.wiley.com/doi/abs/10.1029/2005WR004707 (visited on 12/03/2020).

Hauer, C., Leitner, P., Unfer, G., Pulg, U., Habersack, H., and Graf, W. (2018). "The Role of Sediment and Sediment Dynamics in the Aquatic Environment". en. In: *Riverine Ecosystem Management: Science for Governing Towards a Sustainable Future*. Ed. by S. Schmutz and J. Sendzimir. Cham: Springer International Publishing, pp. 151–169. ISBN: 978-3-319-73250-3. DOI: 10.1007/978-3-319-73250-3_8. URL: https://doi.org/10.1007/978-3-319-73250-3_8 (visited on 06/04/2024).

Hodge, R., Brasington, J., and Richards, K. (2009). "In situ characterization of grain-scale fluvial morphology using Terrestrial Laser Scanning". en. In: *Earth Surface Processes and Landforms* 34.7, pp. 954–968. ISSN: 1096-9837. DOI: 10.1002/esp.1780. URL: https://onlinelibrary.wiley.com/doi/abs/10.1002/esp.1780 (visited on 05/27/2024).

Hoey, T. B. and Sutherland, A. J. (1991). "Channel morphology and bedload pulses in braided rivers: a laboratory study". en. In: *Earth Surface Processes and Landforms* 16.5, pp. 447–462. ISSN: 01979337, 10969837. DOI: 10.1002/esp.3290160506. URL: http://doi.wiley.com/10.1002/esp.3290160506 (visited on 10/28/2020).

Hsu, L., Finnegan, N. J., and Brodsky, E. E. (2011). "A seismic signature of river bedload transport during storm events". en. In: *Geophysical Research Letters* 38.13. ISSN: 00948276. DOI: 10.1029/2011GL047759. URL: http://doi.wiley.com/10.1029/2011GL047759 (visited on 10/28/2020).

Jain, R., Tschisgale, S., and Fröhlich, J. (2021). "Impact of shape: DNS of sediment transport with non-spherical particles". en. In: *Journal of Fluid Mechanics* 916. Publisher: Cambridge University Press, A38. ISSN: 0022-1120, 1469-7645. DOI: 10.1017/jfm.2021.214. URL: https://www.cambridge.org/core/journals/journal-of-fluid-mechanics/article/impact-of-shape-dns-of-sediment-transport-with-nonspherical-particles/0B3ED0C2B19C84AB97EB83F7362389A8 (visited on 05/31/2023).

Jerolmack, D. J. and Paola, C. (2010). "Shredding of environmental signals by sediment transport". en. In: *Geophysical Research Letters* 37.19. ISSN: 00948276. DOI: 10.1029/2010GL044638. URL: http://doi.wiley.com/10.1029/2010GL044638 (visited on 10/28/2020).

Johnson, C. W., Meng, H., Vernon, F., and Ben-Zion, Y. (2019). "Characteristics of Ground Motion Generated by Wind Interaction With Trees, Structures, and Other Surface Obstacles". en. In: *Journal of Geophysical Research: Solid Earth* 124.8, pp. 8519–8539. ISSN: 2169-9356. DOI: 10.1029/2018JB017151. URL: https://onlinelibrary.wiley.com/doi/abs/10.1029/2018JB017151 (visited on 06/07/2024).

Kanamori, H. and Given, J. W. (1982). "Analysis of long-period seismic waves excited by the May 18, 1980, eruption of Mount St. Helens—A terrestrial monopole?" en. In: *Journal of Geophysical Research: Solid Earth* 87.B7, pp. 5422–5432. ISSN: 2156-2202. DOI: 10.1029/JB087iB07p05422. URL: https://onlinelibrary.wiley.com/doi/abs/10.1029/JB087iB07p05422 (visited on 06/17/2024).

Kasprak, A., Brasington, J., Hafen, K., Williams, R. D., and Wheaton, J. M. (2019). "Modelling braided river morphodynamics using a particle travel length framework". en. In: *Earth Surface Dynamics* 7.1, pp. 247–274. ISSN: 2196-632X. DOI:

10.5194/esurf-7-247-2019. URL: https://esurf.copernicus.org/articles/7/247/2019/ (visited on 10/28/2020).

Kean, J. W., Coe, J. A., Coviello, V., Smith, J. B., McCoy, S. W., and Arattano, M. (2015). "Estimating rates of debris flow entrainment from ground vibrations". en. In: *Geophysical Research Letters* 42.15, pp. 6365–6372. ISSN: 1944-8007. DOI: 10.1002/2015GL064811. URL: https://onlinelibrary.wiley.com/doi/abs/10.1002/2015GL064811 (visited on 06/07/2024).

Kishimura, K. and Izumi, K. (1997). "Seismic Signals Induced by Snow Avalanche Flow". en. In: *Natural Hazards* 15.1, pp. 89–100. ISSN: 1573-0840. DOI: 10.1023/A:1007934815584. URL: https://doi.org/10.1023/A:1007934815584 (visited on 06/17/2024).

Kostaschuk, R., Best, J., Villard, P., Peakall, J., and Franklin, M. (2005). "Measuring flow velocity and sediment transport with an acoustic Doppler current profiler". In: *Geomorphology*. Fluid Flow and Sediment Transport Process in Geomorphology 68.1, pp. 25–37. ISSN: 0169-555X. DOI: 10.1016/j.geomorph.2004.07.012. URL: https://www.sciencedirect.com/science/article/pii/S0169555X04002879 (visited on 06/26/2024).

Kothyari, U. C. and Jain, R. K. (2008). "Influence of cohesion on the incipient motion condition of sediment mixtures". en. In: *Water Resources Research* 44.4. _eprint: https://onlinelibrary.wiley.com/doi/pdf/10.1029/2007WR006326. ISSN: 1944-7973. DOI: 10.1029/2007WR006326. URL: https://onlinelibrary.wiley.com/doi/abs/10.1029/2007WR006326 (visited on 03/10/2023).

Kuhnle, R. A. (1992). "Bed load transport during rising and falling stages on two small streams". en. In: *Earth Surface Processes and Landforms* 17.2, pp. 191–197. ISSN: 1096-9837. DOI: https://doi.org/10.1002/esp.3290170206. URL: https://onlinelibrary.wiley.com/doi/abs/10.1002/esp.3290170206 (visited on 12/03/2020).

Lagarde, S., Dietze, M., Gimbert, F., Laronne, J. B., Turowski, J. M., and Halfi, E. (2021). "Grain-Size Distribution and Propagation Effects on Seismic Signals Generated by Bedload Transport". en. In: *Water Resources Research* 57.4. ISSN: 1944-7973. DOI: https://doi.org/10.1029/2020WR028700. URL: https://agupubs.onlinelibrary.wiley.com/doi/abs/10.1029/2020WR028700 (visited on 05/31/2021).

Lai, V. H., Tsai, V. C., Lamb, M. P., Ulizio, T. P., and Beer, A. R. (2018). "The Seismic Signature of Debris Flows: Flow Mechanics and Early Warning at Montecito, California". en. In: *Geophysical Research Letters* 45.11, pp. 5528–5535. ISSN: 1944-8007. DOI: 10.1029/2018GL077683. URL: https://onlinelibrary.wiley.com/doi/abs/10.1029/2018GL077683 (visited on 06/07/2024).

Lajeunesse, E., Malverti, L., and Charru, F. (2010). "Bed load transport in turbulent flow at the grain scale: Experiments and modeling". en. In: *Journal of Geophysical Research: Earth Surface* 115.F4. ISSN: 2156-2202. DOI: 10.1029/2009JF001628. URL: https://onlinelibrary.wiley.com/doi/abs/10.1029/2009JF001628 (visited on 06/26/2024).

Lamb, M. P., Dietrich, W. E., and Venditti, J. G. (2008). "Is the critical Shields stress for incipient sediment motion dependent on channel-bed slope?" en. In: *Journal of Geophysical Research: Earth Surface* 113.F2. ISSN: 2156-2202. DOI: 10.1029/2007JF000831. URL: https://onlinelibrary.wiley.com/doi/abs/10.1029/2007JF000831 (visited on 09/16/2021).

Le Guern, J., Rodrigues, S., Geay, T., Zanker, S., Hauet, A., Tassi, P., Claude, N., Jugé, P., Duperray, A., and Vervynck, L. (2020). "Relevance of acoustic methods to quantify bedload transport and bedform dynamics in a large sandy-gravel-bed river". en. In: *Earth Surface Dynamics* 9.3, pp. 423–444. ISSN: 2196-632X. DOI: 10.5194/esurf-9-423-2021. URL: https://esurf.copernicus.org/articles/9/423/2021/ (visited on 06/26/2024).

Lee, K. T., Liu, Y.-L., and Cheng, K.-H. (2004). "Experimental investigation of bedload transport processes under unsteady flow conditions". en. In: *Hydrological Processes* 18.13, pp. 2439–2454. ISSN: 1099-1085. DOI: https://doi.org/10.1002/hyp.1473. URL: https://onlinelibrary.wiley.com/doi/abs/10.1002/hyp.1473 (visited on 12/03/2020).

Lekić, V., Matas, J., Panning, M., and Romanowicz, B. (2009). "Measurement and implications of frequency dependence of attenuation". In: *Earth and Planetary Science Letters* 282.1, pp. 285–293. ISSN: 0012-821X. DOI: 10.1016/j.epsl.2009.03.030. URL: https://www.sciencedirect.com/science/article/pii/S0012821X09001800 (visited on 07/08/2024).

Lisle, T. E. and Madej, M. A. (1992). "Spatial variation in armouring in a channel with high sediment supply". en. In: *Dynamics of gravel-bed rivers*, pp. 277–293.

Lisle, T. E. (1995). "Particle Size Variations Between Bed Load and Bed Material in Natural Gravel Bed Channels". en. In: *Water Resources Research* 31.4, pp. 1107–1118. ISSN: 1944-7973. DOI: https://doi.org/10.1029/94WR02526. URL: https://agupubs.onlinelibrary.wiley.com/doi/abs/10.1029/94WR02526 (visited on 03/30/2021).

Liu, C., Sui, J., and Wang, Z.-Y. (2008). "Sediment load reduction in Chinese rivers". In: *International Journal of Sediment Research* 23.1, pp. 44–55. ISSN: 1001-6279. DOI: 10.1016/S1001-6279(08)60004-9. URL: https://www.sciencedirect.com/science/article/pii/S1001627908600049 (visited on 06/26/2024).

Luo, M., Jiang, Y., Wang, S., Liu, X., and Huang, E. (2023). "The effect of stress history on fluctuation of bedload transport rate and bed topography in gravel-bed streams". en. In: *Journal of Hydrology* 616, p. 128732. ISSN: 00221694. DOI: 10.1016/j.jhydrol.2022.128732. URL: https://linkinghub.elsevier.com/retrieve/pii/S0022169422013026 (visited on 06/01/2023).

Mao, L. (2012). "The effect of hydrographs on bed load transport and bed sediment spatial arrangement". en. In: *Journal of Geophysical Research: Earth Surface* 117.F3. ISSN: 2156-2202. DOI: https://doi.org/10.1029/2012JF002428. URL: https://agupubs.onlinelibrary.wiley.com/doi/abs/10.1029/2012JF002428 (visited on 11/30/2020).

Mao, L., Dell'Agnese, A., Huincache, C., Penna, D., Engel, M., Niedrist, G., and Comiti, F. (2014). "Bedload hysteresis in a glacier-fed mountain river". en. In: *Earth Surface Processes and Landforms* 39.7, pp. 964–976. ISSN: 1096-9837. DOI: https://doi.org/10.1002/esp.3563. URL: https://onlinelibrary.wiley.com/doi/abs/10.1002/esp.3563 (visited on 11/30/2020).

Masteller, C. C., Finnegan, N. J., Turowski, J. M., Yager, E. M., and Rickenmann, D. (2019). "History-Dependent Threshold for Motion Revealed by Continuous Bedload Transport Measurements in a Steep Mountain Stream". en. In: *Geophysical Research Letters* 46.5, pp. 2583–2591. ISSN: 1944-8007. DOI: 10.1029/2018GL081325. URL: https://onlinelibrary.wiley.com/doi/abs/10.1029/2018GL081325 (visited on 03/27/2023).

McCoy, S. W., Tucker, G. E., Kean, J. W., and Coe, J. A. (2013). "Field measurement of basal forces generated by erosive debris flows". en. In: *Journal of Geophysical Research: Earth Surface* 118.2, pp. 589–602. ISSN: 2169-9011. DOI: 10.1002/jgrf.20041. URL: https://onlinelibrary.wiley.com/doi/abs/10.1002/jgrf.20041 (visited on 06/07/2024).

McDowell, P. W., Barker, R. D., Butcher, A. P., Culshaw, M. G., Jackson, P. D., McCann, D. M., Skipp, B. O., Matthews, S. L., and Arthur, J. C. R. (2002). *Geophysics in engineering investigations*. en. Geological Society of London. ISBN: 978-1-86239-381-3. DOI: 10.1144/GSL.ENG.2002.019. URL: https://pubs.geoscienceworld.org/gsl/books/book/1516/Geophysics-in-engineering-investigations (visited on 06/20/2024).

Meunier, P., Métivier, F., Lajeunesse, E., Mériaux, A., and Faure, J. (2006). "Flow pattern and sediment transport in a braided river: The "torrent de St Pierre" (French Alps)". en. In: *Journal of Hydrology* 330.3-4, pp. 496–505. ISSN: 00221694. DOI: 10.1016/j.jhydrol.2006.04.009. URL: https://linkinghub.elsevier.com/retrieve/pii/S0022169406002058 (visited on 06/26/2024).

Meyer-Peter, E. and Müller, R. (1948). "Formulas for bed-load transport". In: Madrid.

Misset, C., Recking, A., Legout, C., Bakker, M., Bodereau, N., Borgniet, L., Cassel, M., Geay, T., Gimbert, F., Navratil, O., Piegay, H., Valsangkar, N., Cazilhac, M., Poirel, A., and Zanker, S. (2020). "Combining multi-physical measurements to quantify bedload transport and morphodynamics interactions in an Alpine braiding river reach". en. In: *Geomorphology* 351, p. 106877. ISSN: 0169555X. DOI: 10.1016/j.geomorph.2019.106877. URL: https://linkinghub.elsevier.com/retrieve/pii/S0169555X1930368X (visited on 10/28/2020).

Monsalve, A., Segura, C., Hucke, N., and Katz, S. (2020). "A bed load transport equation based on the spatial distribution of shear stress – Oak Creek revisited". English. In: *Earth Surface Dynamics* 8.3. Publisher: Copernicus GmbH, pp. 825–839. ISSN: 2196-6311. DOI: 10.5194/esurf-8-825-2020. URL: https://esurf.copernicus.org/articles/8/825/2020/ (visited on 07/14/2023).

Nakamura, Y. (1989). "A METHOD FOR DYNAMIC CHARACTERISTICS ESTIMATION OF SUBSURFACE USING MICROTREMOR ON THE GROUND SURFACE". In: *Railway Technical Research Institute, Quarterly Reports* 30.1. ISSN: 0033-9008. URL: https://trid.trb.org/View/294184 (visited on 06/17/2024).

Nielsen, P. (1992). "Coastal bottom boundary layers and sediment transport." In: *World Scientific* 4.

NRFA (2024). *8013 - Feshie at Feshie Bridge*. URL: https://nrfa.ceh.ac.uk/data/station/meanflow/8013 (visited on 05/28/2024).

Ockelford, A., Woodcock, S., and Haynes, H. (2019). "The impact of inter-flood duration on non-cohesive sediment bed stability". en. In: *Earth Surface Processes and Landforms* 44.14, pp. 2861–2871. ISSN: 1096-9837. DOI: 10.1002/esp.4713. URL: https://onlinelibrary.wiley.com/doi/abs/10.1002/esp.4713 (visited on 03/06/2023).

Pal, S., Mahato, S., and Bala, G. (2020). "Hydro-geomorphic consequences of avulsion susceptible zones along lower Mayurakshi river of eastern India". In: *Remote Sensing Applications: Society and Environment* 20, p. 100425. ISSN: 2352-9385.

DOI: 10.1016/j.rsase.2020.100425. URL: https://www.sciencedirect.com/science/article/pii/S2352938520303116 (visited on 07/16/2024).

Palucis, M. C., Ulizio, T., Fuller, B., and Lamb, M. P. (2018). "Intense Granular Sheetflow in Steep Streams". en. In: *Geophysical Research Letters* 45.11. _eprint: https://onlinelibrary.wiley.com/doi/pdf/10.1029/2018GL077526, pp. 5509–5517. ISSN: 1944-8007. DOI: 10.1029/2018GL077526. URL: https://onlinelibrary.wiley.com/doi/abs/10.1029/2018GL077526 (visited on 10/30/2023).

Parker, G., Seminara, G., and Solari, L. (2003). "Bed load at low Shields stress on arbitrarily sloping beds: Alternative entrainment formulation". en. In: *Water Resources Research* 39.7. ISSN: 1944-7973. DOI: 10.1029/2001WR001253. URL: https://onlinelibrary.wiley.com/doi/abs/10.1029/2001WR001253 (visited on 06/26/2024).

Petit, F., Houbrechts, G., Peeters, A., Hallot, E., Van Campenhout, J., and Denis, A.-C. (2015). "Dimensionless critical shear stress in gravel-bed rivers". In: *Geomorphology* 250, pp. 308–320. ISSN: 0169-555X. DOI: 10.1016/j.geomorph.2015.09.008. URL: https://www.sciencedirect.com/science/article/pii/S0169555X15301446 (visited on 06/28/2024).

Piantini, M., Gimbert, F., Korkolis, E., Rousseau, R., Bellot, H., and Recking, A. (2023). "Solid Concentration as a Main Proxy for Basal Force Fluctuations Generated by Highly Concentrated Sediment Flows". en. In: *Geophysical Research Letters* 50.1, e2022GL100345. ISSN: 0094-8276, 1944-8007. DOI: 10.1029/2022GL100345. URL: https://agupubs.onlinelibrary.wiley.com/doi/10.1029/2022GL100345 (visited on 04/19/2024).

Piantini, M., Gimbert, F., Bakker, M., Recking, A., and Nanni, U. (2022). "Using a dense seismic array to study fluvial processes in a braided river reach under flood conditions". en. In: *LHB*, p. 2053314. ISSN: 2767-8490. DOI: 10.1080/27678490.2022.2053314. URL: https://www.tandfonline.com/doi/full/10.1080/27678490.2022.2053314 (visited on 08/25/2022).

Pitlick, J., Cui, Y., and Wilcock, P. (2009). *Manual for Computing Bed Load Transport Using BAGS (Bedload Assessment for Gravel-bed Streams) Software*. Tech. rep.

PNSN (2024). *Site Effects*. en. URL: https://pnsn.org/outreach/earthquakehazards/site-effects (visited on 06/07/2024).

Prancevic, J. P. and Lamb, M. P. (2015). "Unraveling bed slope from relative roughness in initial sediment motion". en. In: *Journal of Geophysical Research: Earth Surface* 120.3, pp. 474–489. ISSN: 2169-9011. DOI: https://doi.org/10.1002/2014JF003323. URL: https://agupubs.onlinelibrary.wiley.com/doi/abs/10.1002/2014JF003323 (visited on 02/03/2021).

Prendergast, L. J. and Gavin, K. (2014). "A review of bridge scour monitoring techniques". In: *Journal of Rock Mechanics and Geotechnical Engineering* 6.2, pp. 138–149. ISSN: 1674-7755. DOI: 10.1016/j.jrmge.2014.01.007. URL: https://www.sciencedirect.com/science/article/pii/S167477551400016X (visited on 07/16/2024).

Quick, L., Creed, M. J., Sinclair, H. D., Attal, M., Borthwick, A. G. L., and Sinha, R. (2023). "Hyperconcentrated floods cause extreme gravel transport through the sandy rivers of the Gangetic Plains". en. In: *Communications Earth & Environment* 4.1. Publisher: Nature Publishing Group, pp. 1–12. ISSN: 2662-4435. DOI:

10.1038/s43247-023-00953-9. URL: https://www.nature.com/articles/s43247-023-00953-9 (visited on 06/06/2024).

Reid, I., Frostick, L. E., and Layman, J. T. (1985). "The incidence and nature of bedload transport during flood flows in coarse-grained alluvial channels". en. In: *Earth Surface Processes and Landforms* 10.1, pp. 33–44. ISSN: 1096-9837. DOI: 10.1002/esp.3290100107. URL: https://onlinelibrary.wiley.com/doi/abs/10.1002/esp.3290100107 (visited on 09/14/2021).

Rennie, C. D. and Villard, P. V. (2004). "Site specificity of bed load measurement using an acoustic Doppler current profiler". en. In: *Journal of Geophysical Research: Earth Surface* 109.F3. ISSN: 2156-2202. DOI: 10.1029/2003JF000106. URL: https://onlinelibrary.wiley.com/doi/abs/10.1029/2003JF000106 (visited on 06/26/2024).

Rheinheimer, D. and Yarnell, S. (2017). "Chapter 12 - Tools for Sediment Management in Rivers". en. In: *Water for the Environment*. Ed. by A. Horne, A. Webb, M. Stewardson, B. Richter, and M. Acreman. Elsevier, pp. 237–263. ISBN: 978-0-12-803907-6. DOI: 10.1016/B978-0-12-803907-6.00012-7. URL: https://linkinghub.elsevier.com/retrieve/pii/B9780128039076000127 (visited on 11/20/2020).

"Sediment Transport Dynamics in Rivers" (2020). In: *River Dynamics: Geomorphology to Support Management*. Ed. by B. L. Rhoads. Cambridge: Cambridge University Press, pp. 97–133. ISBN: 978-1-107-19542-4. DOI: 10.1017/9781108164108.005. URL: https://www.cambridge.org/core/books/river-dynamics/sediment-transport-dynamics-in-rivers/49D2771E8ECFA041876%20860212%20734D37B (visited on 06/26/2024).

Rickenmann, D., Turowski, J. M., Fritschi, B., Klaiber, A., and Ludwig, A. (2012). "Bedload transport measurements at the Erlenbach stream with geophones and automated basket samplers". en. In: *Earth Surface Processes and Landforms* 37.9, pp. 1000–1011. ISSN: 01979337. DOI: 10.1002/esp.3225. URL: http://doi.wiley.com/10.1002/esp.3225 (visited on 10/28/2020).

Rickenmann, D., Turowski, J. M., Fritschi, B., Wyss, C., Laronne, J., Barzilai, R., Reid, I., Kreisler, A., Aigner, J., Seitz, H., and Habersack, H. (2014). "Bedload transport measurements with impact plate geophones: comparison of sensor calibration in different gravel-bed streams". en. In: *Earth Surface Processes and Landforms* 39.7, pp. 928–942. ISSN: 01979337. DOI: 10.1002/esp.3499. URL: http://doi.wiley.com/10.1002/esp.3499 (visited on 10/28/2020).

Rickenmann, D. (1991). "Hyperconcentrated Flow and Sediment Transport at Steep Slopes". EN. In: *Journal of Hydraulic Engineering* 117.11. Publisher: American Society of Civil Engineers, pp. 1419–1439. ISSN: 0733-9429. DOI: 10.1061/(ASCE)0733-9429(1991)117:11(1419). URL: https://ascelibrary.org/doi/10.1061/%28ASCE%290733-9429%281991%29117%3A11%281419%29 (visited on 06/06/2024).

Rindraharisaona, E. J., Réchou, A., Fontaine, F. R., Barruol, G., Stamenoff, P., Boudevillain, B., Rigaud-Louise, F., and Delcher, E. (2022). "Seismic Signature of Rain and Wind Inferred From Seismic Data". en. In: *Earth and Space Science* 9.10. _eprint: https://onlinelibrary.wiley.com/doi/pdf/10. 1029/2022EA002328. ISSN: 2333-5084. DOI: 10.1029/2022EA002328. URL: https://onlinelibrary.wiley.com/doi/abs/10.1029/2022EA002328 (visited on 12/06/2022).

Roth, D., Brodsky, E., Finnegan, N., Rickenmann, D., Turowski, J., and Badoux, A. (2016). "Bed load sediment transport inferred from seismic signals near a river". en. In: *Journal of Geophysical Research: Earth Surface* 121.4, pp. 725–747. ISSN: 2169-9003, 2169-9011. DOI: 10.1002/2015JF003782. URL: https://onlinelibrary.wiley.com/doi/abs/10.1002/2015JF003782 (visited on 10/28/2020).

Roth, D., Finnegan, N., Brodsky, E., Cook, K., Stark, C., and Wang, H. (2014). "Migration of a coarse fluvial sediment pulse detected by hysteresis in bedload generated seismic waves". en. In: *Earth and Planetary Science Letters* 404, pp. 144–153. ISSN: 0012821X. DOI: 10.1016/j.epsl.2014.07.019. URL: https://linkinghub.elsevier.com/retrieve/pii/S0012821X14004695 (visited on 10/28/2020).

Roth, D., Finnegan, N., Brodsky, E., Rickenmann, D., Turowski, J., Badoux, A., and Gimbert, F. (2017). "Bed load transport and boundary roughness changes as competing causes of hysteresis in the relationship between river discharge and seismic amplitude recorded near a steep mountain stream". en. In: *Journal of Geophysical Research: Earth Surface* 122.5, pp. 1182–1200. ISSN: 21699003. DOI: 10.1002/2016JF004062. URL: http://doi.wiley.com/10.1002/2016JF004062 (visited on 11/16/2020).

Sánchez-Sesma, F. and Campillo, M. (1993). "Topographic effects for incident P, SV and Rayleigh waves". In: *Tectonophysics*. New horizons in strong motion: Seismic studies and engineering practice 218.1, pp. 113–125. ISSN: 0040-1951. DOI: 10.1016/0040-1951(93)90263-J. URL: https://www.sciencedirect.com/science/article/pii/004019519390263J (visited on 06/18/2024).

Schmandt, B., Aster, R. C., Scherler, D., Tsai, V. C., and Karlstrom, K. (2013). "Multiple fluvial processes detected by riverside seismic and infrasound monitoring of a controlled flood in the Grand Canyon". en. In: *Geophysical Research Letters* 40.18, pp. 4858–4863. ISSN: 0094-8276, 1944-8007. DOI: 10.1002/grl.50953. URL: https://onlinelibrary.wiley.com/doi/abs/10.1002/grl.50953 (visited on 10/28/2020).

Schmandt, B., Gaeuman, D., Stewart, R., Hansen, S., Tsai, V., and Smith, J. (2017). "Seismic array constraints on reach-scale bedload transport". en. In: *Geology* 45.4, pp. 299–302. ISSN: 0091-7613, 1943-2682. DOI: 10.1130/G38639.1. URL: https://pubs.geoscienceworld.org/geology/article/45/4/299-302/195340 (visited on 04/10/2024).

Schumm, S. (1977). *The fluvial system*. en. A Wiley-Interscience publication. New York: Wiley. ISBN: 978-0-471-01901-5.

SEPA (2024). *SEPA Time series data service (API)*. URL: https://timeseriesdoc.sepa.org.uk/ (visited on 05/28/2024).

Shearer, P. (2009). *Introduction to Seismology*. en. 2nd ed. ISBN: 9781316877111 Publisher: Cambridge University Press. Cambridge University Press. DOI: 10.1017/9781316877111. (Visited on 06/17/2024).

Shields, A. (1936). "Anwendung der Aehnlichkeitsmechanik und der Turbulenzforschung auf die Geschiebebewegung". PhD thesis. Mitteilungen der Preussischen Versuchsanstalt fur Wasserbau und Schiffbau, Berlin, Germany.

SHINE, P. (2022). *Seismic Methods*. en-US. URL: https://petroshine.com/seismic-methods/ (visited on 06/21/2024).

Singh, A., Wu, Z., Wilcock, P., and Foufoula-Georgiou, E. (2023). "Experimental Observations of Bedload Tracer Movement: Effects of Mixed Particle Sizes and Bedforms". en. In: *Water Resources Research* 59.5, e2022WR033114. ISSN: 0043-1397, 1944-7973. DOI: 10.1029/2022WR033114. URL: https://agupubs.onlinelibrary.wiley.com/doi/10.1029/2022WR033114 (visited on 06/26/2024).

Soar, P. J. and Downs, P. W. (2017). "Estimating bedload transport rates in a gravel-bed river using seismic impact plates: Model development and application". en. In: *Environmental Modelling & Software* 90, pp. 182–200. ISSN: 13648152. DOI: 10.1016/j.envsoft.2017.01.012. URL: https://linkinghub.elsevier.com/retrieve/pii/S1364815217300877 (visited on 10/28/2020).

Soulsby, C., Tetzlaff, D., Rodgers, P., Dunn, S., and Waldron, S. (2006). "Runoff processes, stream water residence times and controlling landscape characteristics in a mesoscale catchment: An initial evaluation". In: *Journal of Hydrology* 325.1, pp. 197–221. ISSN: 0022-1694. DOI: 10.1016/j.jhydrol.2005.10.024. URL: https://www.sciencedirect.com/science/article/pii/S0022169405005433 (visited on 05/27/2024).

Stark, K., Cadol, D., Varyu, D., Halfi, E., and Laronne, J. B. (2024). "Strengths and weaknesses of acoustic pipe microphone systems in ephemeral, sandy, gravel-bed rivers". en. In: *Earth Surface Processes and Landforms* 49.4, pp. 1383–1396. ISSN: 1096-9837. DOI: 10.1002/esp.5774. URL: https://onlinelibrary.wiley.com/doi/abs/10.1002/esp.5774 (visited on 03/27/2024).

Stein, S. and Wysession, M. (1991). *An Introduction to Seismology, Earthquakes, and Earth Structure*. Wiley-Blackwell. URL: https://www.wiley.com/en-us/An+Introduction+to+Seismology%2C+Earthquakes%2C+and+Earth+Structure-p-9780865420786 (visited on 06/17/2024).

Stevens, A. W., Hatcher, G. A., Dal Ferro, P., Dartnell, P., Warrick, J. A., Cohn, N., and Moritz, H. R. (2023). *Digital seafloor images, sediment grain size, bathymetry, and water velocity data from the lower Columbia River, Oregon and Washington, 2021*. DOI: 10.5066/P92U1KPY. URL: https://cmgds.marine.usgs.gov/data-releases/datarelease/10.5066-P92U1KPY/ (visited on 06/30/2024).

Syvitski, J. P. M. and Milliman, J. D. (2007). "Geology, Geography, and Humans Battle for Dominance over the Delivery of Fluvial Sediment to the Coastal Ocean". In: *The Journal of Geology* 115.1. Publisher: The University of Chicago Press, pp. 1–19. ISSN: 0022-1376. DOI: 10.1086/509246. URL: https://www.journals.uchicago.edu/doi/abs/10.1086/509246 (visited on 06/26/2024).

Thapa, B. S., Dahlhaug, O. G., and Thapa, B. (2015). "Sediment erosion in hydro turbines and its effect on the flow around guide vanes of Francis turbine". In: *Renewable and Sustainable Energy Reviews* 49, pp. 1100–1113. ISSN: 1364-0321. DOI: 10.1016/j.rser.2015.04.178. URL: https://www.sciencedirect.com/science/article/pii/S1364032115004517 (visited on 07/16/2024).

Thorne, P. D. (2014). "An overview of underwater sound generated by interparticle collisions and its application to the measurements of coarse sediment bedload transport". en. In: *Earth Surface Dynamics* 2.2, pp. 531–543. ISSN: 2196-632X. DOI: 10.5194/esurf-2-531-2014. URL: https://esurf.copernicus.org/articles/2/531/2014/ (visited on 10/28/2020).

Tomczyk, P., Wiatkowski, M., Gałka, B., and Gruss, Ł. (2022). "Assessing the Impact of a Hydropower Plant on Changes in the Properties of the Sediment of the Bystrzyca River in Poland". English. In: *Frontiers in Environmental Science*

10. Publisher: Frontiers. ISSN: 2296-665X. DOI: 10.3389/fenvs.2022.795922. URL: https://www.frontiersin.org/journals/environmental-science/articles/10.3389/fenvs.2022.795922/full (visited on 07/16/2024).

Tsai, V. C., Minchew, B., Lamb, M. P., and Ampuero, J.-P. (2012). "A physical model for seismic noise generation from sediment transport in rivers". en. In: *Geophysical Research Letters* 39.2. ISSN: 00948276. DOI: 10.1029/2011GL050255. URL: http://doi.wiley.com/10.1029/2011GL050255 (visited on 10/28/2020).

Turnbull, R. (2016). *Glenfeshie reborn - Rewilding a sporting estate*. en-GB. URL: https://treesforlife.org.uk/glenfeshie-reborn/ (visited on 06/14/2021).

Turowski, J. M., Badoux, A., and Rickenmann, D. (2011). "Start and end of bedload transport in gravel-bed streams". en. In: *Geophysical Research Letters* 38.4. ISSN: 00948276. DOI: 10.1029/2010GL046558. URL: http://doi.wiley.com/10.1029/2010GL046558 (visited on 10/28/2020).

Turowski, J. M., Böckli, M., Rickenmann, D., and Beer, A. R. (2013). "Field measurements of the energy delivered to the channel bed by moving bed load and links to bedrock erosion". en. In: *Journal of Geophysical Research: Earth Surface* 118.4, pp. 2438–2450. ISSN: 21699003. DOI: 10.1002/2013JF002765. URL: http://doi.wiley.com/10.1002/2013JF002765 (visited on 10/28/2020).

Turowski, J. M., Wyss, C. R., and Beer, A. R. (2015). "Grain size effects on energy delivery to the streambed and links to bedrock erosion". en. In: *Geophysical Research Letters* 42.6, pp. 1775–1780. ISSN: 0094-8276, 1944-8007. DOI: 10.1002/2015GL063159. URL: https://onlinelibrary.wiley.com/doi/abs/10.1002/2015GL063159 (visited on 10/28/2020).

Turowski, J. M., Yager, E. M., Badoux, A., Rickenmann, D., and Molnar, P. (2009). "The impact of exceptional events on erosion, bedload transport and channel stability in a step-pool channel". en. In: *Earth Surface Processes and Landforms* 34.12, pp. 1661–1673. ISSN: 1096-9837. DOI: https://doi.org/10.1002/esp.1855. URL: https://onlinelibrary.wiley.com/doi/abs/10.1002/esp.1855 (visited on 12/03/2020).

Van Rijn, L. (1984). "Sediment Transport, Part I: Bed Load Transport". In: *Journal of Hydraulic Engineering* 110.4, pp. 1431–1456.

Vore, M. E., Bartholomaus, T. C., Winberry, J. P., Walter, J. I., and Amundson, J. M. (2019). "Seismic Tremor Reveals Spatial Organization and Temporal Changes of Subglacial Water System". en. In: *Journal of Geophysical Research: Earth Surface* 124.2, pp. 427–446. ISSN: 2169-9011. DOI: 10.1029/2018JF004819. URL: https://onlinelibrary.wiley.com/doi/abs/10.1029/2018JF004819 (visited on 01/23/2023).

Welch, P. (1967). "The use of fast Fourier transform for the estimation of power spectra: A method based on time averaging over short, modified periodograms". In: *IEEE Transactions on Audio and Electroacoustics* 15.2. Conference Name: IEEE Transactions on Audio and Electroacoustics, pp. 70–73. ISSN: 1558-2582. DOI: 10.1109/TAU.1967.1161901. URL: https://ieeexplore.ieee.org/document/1161901 (visited on 11/10/2023).

Werritty, A. and Brazier, V. (1991). *The geomorphology, conservation and management of the River Feshie SSSI*. Tech. rep. Report for Nature Conservancy Council Rep.

Werritty, A. and Ferguson, R. I. (1980). "Pattern change in a Scottish braided river over 1, 30 and 200years". In: *Timescales in Geomorphology*. Ed. by R. A.

Cullingford, D. A. Davidson, and J. Lewin. Chichester: J. Wiley, pp. 53–68. ISBN: 978-0-471-27600-5.

Werritty, A. and McEwen, L. J. (1993). "Fluvial landforms and processes in Scotland". en. In.

Werritty, A. and McEwen, L. J. (2007). "Chapter 9: Eastern Grampian Mountains, Glen Feshie". In: *Geological Conservation Review*. Vol. 6: Quaternary of Scotland. URL: http://www.jncc.gov.uk/page-2731.

Wheaton, J. M., Brasington, J., Darby, S. E., Kasprak, A., Sear, D., and Vericat, D. (2013). "Morphodynamic signatures of braiding mechanisms as expressed through change in sediment storage in a gravel-bed river". en. In: *Journal of Geophysical Research: Earth Surface* 118.2, pp. 759–779. ISSN: 2169-9011. DOI: https://doi.org/10.1002/jgrf.20060. (Visited on 11/24/2020).

White, W. R., Milli, H., and Crabbe, A. D. (1973). *Sediment transport - an appraisal of available methods. Volume 1: summary of existing theories*. en. Tech. rep. The University of Manchester.

Wilcock, P. and Crowe, J. (2003). "Surface-based Transport Model for Mixed-Size Sediment". en. In: *Journal of Hydraulic Engineering* 129.2, pp. 120–128. ISSN: 0733-9429, 1943-7900. DOI: 10.1061/(ASCE)0733-9429(2003)129:2(120). URL: http://ascelibrary.org/doi/10.1061/%28ASCE%290733-9429%282003%29129%3A2%28120%29 (visited on 07/01/2021).

Wilcock, P. R. (2001). "Toward a practical method for estimating sediment-transport rates in gravel-bed rivers". en. In: *Earth Surface Processes and Landforms* 26.13, pp. 1395–1408. ISSN: 0197-9337, 1096-9837. DOI: 10.1002/esp.301. URL: https://onlinelibrary.wiley.com/doi/10.1002/esp.301 (visited on 07/14/2023).

Wilcock, W. S. D., Webb, S. C., and Bjarnason, I. T. (1999). "The effect of local wind on seismic noise near 1 Hz at the MELT site and in iceland". In: *Bulletin of the Seismological Society of America* 89.6, pp. 1543–1557. ISSN: 0037-1106. DOI: 10.1785/BSSA0890061543. URL: https://doi.org/10.1785/BSSA0890061543 (visited on 03/20/2023).

Wilson, K. (1996). "Bed-load transport at high shear stress". In: *Journal of Hydraulics Dvision* 92, pp. 49–59.

Wolman, M. G. (1954). "A method of sampling coarse river-bed material". en. In: *Eos, Transactions American Geophysical Union* 35.6, pp. 951–956. ISSN: 2324-9250. DOI: 10.1029/TR035i006p00951. URL: https://onlinelibrary.wiley.com/doi/abs/10.1029/TR035i006p00951 (visited on 10/20/2023).

Wyss, C. R., Rickenmann, D., Fritschi, B., Turowski, J., Weitbrecht, V., and Boes, R. (2014). "Bedload grain size estimation from the indirect monitoring of bedload transport with Swiss plate geophones at the Erlenbach stream". In: ISBN: 978-1-138-02674-2. DOI: 10.1201/b17133-255.

Xu, R. and Wang, L. (2021). "The horizontal-to-vertical spectral ratio and its applications". In: *EURASIP Journal on Advances in Signal Processing* 2021.1, p. 75. ISSN: 1687-6180. DOI: 10.1186/s13634-021-00765-z. URL: https://doi.org/10.1186/s13634-021-00765-z (visited on 12/07/2023).

Young, W. J. and Davies, T. R. H. (1991). "Bedload transport processes in a braided gravel-bed river model". en. In: *Earth Surface Processes and Landforms* 16.6. _eprint: https://onlinelibrary.wiley.com/doi/pdf/10.1002/esp.3290160603, pp. 499–511. ISSN: 1096-9837. DOI: https://doi.org/10.1002/esp.3290160603.

URL: https://onlinelibrary.wiley.com/doi/abs/10.1002/esp.3290160603 (visited on 04/06/2021).

Appendices

Appendix A

R 'eseis' Package Code

Code from the R 'eseis' package (Dietze, 2018b) used to model the turbulence and bedload seismic spectrums using a combination of field measured and default parameters.

```
## model the turbulence-related power spectrum
p_turbulence <- model_turbulence(d_s = 0.049, # mean sediment grain diameter
                      s_s = 0.42, # standard deviation of sediment
                           grain diameter
                      r_s = 2650, # sediment density
                      h_w = 1.6, # water level
                      w_w = 30, # river width
                      a_w = 0.0068, # river inclination
                      f = c(1, 100), # frequency range
                      r_0 = 20, # distance to the river
                      f_0 = 1, # Null frequency
                      q_0 = 20, # quality factor at f = 1 Hz
                      v_0 = 1295, # phase velocity
                      p_0 = 0.48, # power law variation coefficient
                      n_0 = c(0.6, 0.8), # Greens function estimates
                      res = 1000) # output resolution

## plot the turbulence power spectrum
plot_spectrum(data = p_turbulence,
              ylim = c(-200, -100))



## calculate bedload spectrum (i.e., fig. 1b in Tsai et al., 2012)
p_bedload <- model_bedload(d_s = 0.049, # mean sediment grain diameter
                           s_s = 0.42, # standard deviation of sediment
                                       grain diameter
                           r_s = 2650, # specific sediment density
                           q_s = 0.0009, # unit sediment flux
                           h_w = 1.6, # water level
                           w_w = 30, # river width
                           a_w = 0.0068, # river inclination
```

```
                            f = c(1, 100), # frequency range
                            r_0 = 20, # distance to the river
                            f_0 = 1, # Null frequency
                            q_0 = 20, # quality factor at f = 1 Hz
                            e_0 = 0, # exponent characterizing quality
                                       factor increase with frequency
                                       (dimensionless). "Reasonable
                                       value may be 0" (Tsai et al. 2012).
                            v_0 = 1295, # phase velocity
                            x_0 = 0.374, # exponent of the power law
                                           variation of Rayleigh wave
                                           velocities with frequency
                            n_0 = 1,
                            res = 1000), # output resolution
## plot the bedload power spectrum
plot_spectrum(data = p_bedload,
              ylim = c(-200, -100))
```

Appendix B

Active Seismic Survey

As mentioned in Chapter 3, we conducted an active seismic survey on the floodplain near geophone site W_07 to understand the subsurface structure of the study area. Ideally, we would have repeated the survey at multiple geophone sites to analyse seismic wave propagation characteristics in detail. However, due to time and logistical constraints, we focused on estimating just the subsurface velocity structure for my PhD work.

For the survey, we set up two main lines of wired seismic sensors as shown in Figure B.1; one parallel with the river channel and one perpendicular, crossing the river channel. Along each survey transect and perpendicular to the transects along the riverbank, we also deployed seismic nodes to compare with the wired geophone data. The parallel transect line was chosen to measure the propagation of seismic waves through the surface layer where the geophone was deployed. The perpendicular transect line aimed to capture information on how seismic signals propagate through the riverbed to the geophones located on the riverbanks. The yellow stars in Figure B.1 indicate the various shot locations where we used a sledgehammer striking a metal baseplate to generate seismic waves. Some shot locations were at the ends of the transect lines to measure the distance and speed of seismic waves traveling to each geophone along the line. Shot locations in the river (on the gravel bar) aimed to identify seismic signal propagation through the riverbed, reflecting the source of bedload-induced seismic signals within the channel. Although this aspect was not explored in my PhD, I am hopeful that the project team will further analyze the collected data.

The arrival times of seismic waves, recorded by each geophone during the shots, provide critical data for determining the subsurface velocity structure. To process and analyse this data, I utilised the Refrapy Python package, a tool specifically designed for seismic refraction data analysis that facilitates the processing, visualisation, and interpretation of seismic data.



Figure B.1: Seismic refraction survey setup at the River Feshie site, showing the geophone transect lines, the node locations, and the shot locations.

Appendix C

Grain Size Measurements

Table C.1: Grain sizes measured using Wolman count method adjacent to five geophone sites. Units [cm].

W_07 (bar) [cm]	**W_03 (bar)** [cm]	**E_04 (bar)** [cm]	**E_03 (bar)** [cm]	**W_05 (thalweg)** [cm]
2.2	8.1	1	0.6	2.7
3.1	1.5	3.6	0.8	1.8
1.6	4.7	6.3	0.4	6.3
8	6.5	8.9	1.1	4.9
3.4	1.4	4.2	1.6	1.1
9.8	7.2	1.1	4.6	3.2
0.8	1.7	15	5.6	12.6
3.9	12.4	4.7	3.7	10.5
2.4	12.4	3.2	4.2	3
3.8	0.4	0.4	1.2	1.6
8	11.3	4	1.2	2.1
1	10.4	7.8	1.1	7.1
8.7	0.5	6.7	3.4	3.5
2.5	2	3.9	1.8	7.5
2.5	7.4	1.9	1.9	11.4
0.6	1.4	12.5	6.6	15.3
9.4	1.5	3	2.9	7.8
10.6	2.7	11.6	6.3	4.4
4.1	1.5	0.2	1.4	14
1.4	9.8	4	2	8.9
2.8	2.8	5	3.5	3.8
3.2	1.9	4.6	1.1	3.6
6.9	0.2	8.5	5.9	5
0.7	4	8	1.8	3.2
6.4	1.3	3.6	4	6.4
0.5	0.7	6.3	4.9	7.8
1.7	6.1	5.5	4.3	1.8
8.4	4.3	1.7	2.1	2.2
0.6	9.2	10.3	3.9	9.4
5.2	12.1	1	0.1	2.7
2.9	0.3	6.1	2.9	5.1
16.3	1.4	15.5	1.3	6.2

4.8	6.8	8	1.7	11.4
5.6	4.5	3.8	4.1	6.7
10	10.2	4	6.1	11.6
0.9	11.5	0.6	3.8	4.9
1	5.6	4.4	9.2	3.8
4.8	6.2	0.7	13.3	16.2
3.3	2.7	9.5	3.2	14.6
1.4	5.7	0.2	6.2	7.2
3.4	4.8	2.8	1.4	9.8
2.7	7.6	15	0.7	13.1
3.2	6.2	4.2	0.9	3.2
1.6	5	2.2	1.7	8.8
1.6	2.8	0.4	1	2.4
0.4	5.1	10	3.1	10.4
9.2	4.6	3.8	4.4	5.3
5.6	3.9	19	1.6	13.3
0.8	3.6	5	5.1	8.4
3.4	0.7	3.2	1	5.8
3.3	0.2	1.8	5.3	1.3
4	1.5	11.3	2.1	9
6.9	6.6	12.6	2.2	3.3
4.2	5.7	3.7	0.4	10.4
2.1	15.2	1.3	1.2	1
0.6	5.8	6	3.7	0.9
5.5	4.9	5.7	10	1.4
12.4	3.4	3.6	3.2	0.9
6	0.8	11.8	5.8	3.1
0.9	3	1.9	6.4	1.3
3.3	0.5	1.8	3.3	3
8.8	0.3	2.4	1.1	3.9
4.3	4.3	1.5	1.7	8
7.3	7	0.3	1.8	6.7
3.9	2.5	0.2	1	5.2
6.1	3.8	4	1.1	1.3
5.8	8.2	1.8	2	2.4
7.8	2.3	12.4	2.6	2.2
2	7.6	8.5	11.3	9.8
0.4	1.8	3	10.4	9.4
8.7	0.6	12.8	4.3	10.3
10.7	10	1.3	2.6	6.6
3.2	5.1	3	3.3	1.8
7.3	2.4	3.5	3	8.1
0.8	6.4	0.5	4.8	3.2
3.9	0.4	10.5	4.4	1.6
8.5	8.5	0.9	3.5	6.2
7	0.5	4.7	2	2.4
5.8	2.4	6.4	0.9	1.1
8.8	1	9.5	2	4.1

2.9	1.4	0.5	2.9	1
16	5	2.5	1	2.2
3.9	4.9	4	3.4	9.8
0.6	2.4	5.1	2.4	3.6
5	3.8	0.1	5	2.2
0.7	0.9	4.1	1.6	3
4.7	8.8	9.4	1.1	
1	8.2	0.7	5.9	
7.3	16.9	2.6	1.9	
0.5	2.9	2.6	4.7	
5.6	4.4	3.3	1.6	
6.6	7.2	1.3	1.4	
8	4	3.1	1.3	
0.3	7.3	5.2	1.8	
8.8	3.6	3.8	1.3	
3	1.5	5.4	3.3	
10.9	6.4	2.2	3.7	
1.4	3.1	9.3	1.5	
2.9	7.3	0.8	4.8	
0.9	3.4	9.8	6.4	

Table C.2: Grain sizes measured using photographic analysis on gravel bar adjacent to site W_07.

Size [mm]	% Proportion	Size [mm]	% Proportion	Size [mm]	% Proportion
257.2065	100	144.9588	100	180.5995	100
253.8148	99	111.6789	99	179.4953	99
249.0551	98	104.226	98	126.8824	98
146.9252	97	85.91606	97	121.7215	97
144.0667	96	82.3412	96	115.5021	96
131.2475	95	78.33071	95	106.694	95
128.105	94	75.72538	94	96.00846	94
126.6583	93	74.41417	93	95.33442	93
110.9588	92	72.90223	92	94.62315	91
101.9464	91	72.8467	91	93.83331	90
96.95943	90	69.26758	90	90.11157	89
94.15781	89	67.50364	89	87.56012	88
88.26612	88	65.7995	88	87.01426	87
85.02307	87	65.23572	87	85.35188	86
83.34472	86	63.29668	86	77.48661	85
82.54052	85	61.98974	85	76.56444	84
78.89973	84	60.93053	84	71.37882	83
77.62786	83	60.43082	83	70.04727	82
75.70912	82	56.64241	82	69.54276	81
72.66712	81	52.73869	81	67.66949	80
67.47474	80	52.09803	80	67.07401	79
67.14694	79	51.01319	79	66.99544	78
66.6312	78	50.54765	78	63.14964	77
64.70372	77	48.95028	77	60.7057	76

63.21332	76	48.44203	76	57.09561	74
58.37933	75	48.20713	75	56.71517	73
55.38541	74	47.88253	74	56.48773	72
54.53312	73	47.19916	73	55.32158	71
52.2691	72	47.18635	72	51.91826	70
50.85737	71	46.22537	71	51.50887	69
49.70351	70	43.38086	70	50.1525	68
49.27518	69	43.36805	69	46.21573	67
49.2271	68	43.15877	68	45.98002	66
46.85382	67	42.88115	67	45.69882	65
46.28563	66	41.75787	66	45.6616	64
45.4989	65	40.41676	65	43.69735	63
45.16673	64	40.41249	64	41.74137	62
43.08191	63	39.75903	63	41.5801	61
42.81093	62	38.91763	62	41.35679	60
42.29081	61	38.42646	61	41.32371	59
42.25585	60	38.26844	60	40.36019	57
40.831	59	37.9353	59	37.36626	56
39.69899	58	34.76192	58	36.12982	55
38.75055	57	34.42878	57	35.66667	54
37.07658	56	33.92053	56	35.41028	53
36.72692	55	32.78443	55	33.71482	52
35.71729	54	32.76308	54	33.09453	51
34.66396	53	32.65203	53	32.31297	50
34.39297	52	31.51167	52	32.22613	49
33.50135	51	31.50739	51	31.56862	48
33.11673	50	29.99972	50	30.84081	47
33.0774	49	29.75627	49	30.4645	46
32.16829	48	29.54699	48	30.40661	45
32.16829	47	28.61164	47	30.19571	44
32.02406	46	28.59455	46	29.56301	43
31.26356	45	28.37246	45	28.99648	41
30.11407	44	28.03932	44	28.60363	40
30.08347	43	27.85993	43	27.44576	39
29.10007	42	26.94593	42	26.40367	38
28.75915	41	25.75859	41	25.86609	37
28.52751	40	25.58347	40	25.21685	36
27.86753	39	25.20335	39	23.93492	35
26.4252	38	24.89584	38	22.80599	34
26.05369	37	24.75917	37	21.92104	33
25.68656	36	24.55843	36	21.54473	32
25.34564	35	23.74266	35	19.60529	31
23.05977	34	23.15753	34	19.20417	30
21.37705	33	23.11909	33	18.6914	29
21.1323	32	23.11482	32	17.67826	28
21.00992	31	22.97815	31	17.55007	27
20.98806	30	22.91835	30	17.47977	26
19.53699	29	22.01716	29	17.46736	24

19.34468	28	20.16781	28	17.4012	23
18.38313	27	19.83894	27	17.38466	22
18.26512	26	19.45455	26	17.3433	21
18.17334	25	19.44173	25	16.54933	20
17.94606	24	18.70712	24	16.3343	19
17.57455	23	18.47221	23	16.10272	18
17.2992	22	17.87426	22	15.66025	17
17.20741	21	17.67353	21	14.96553	16
17.00199	20	17.45997	20	14.84974	15
16.66982	19	15.33727	19	14.705	14
16.57803	18	15.14508	18	14.61403	13
16.18904	17	14.80766	17	13.58848	12
16.15845	16	14.19264	16	13.43961	11
16.05792	15	13.22738	15	13.27834	10
15.54655	14	12.6209	14	12.45956	9
15.32802	13	12.43724	13	12.34377	7
14.97836	12	12.38172	12	12.02535	6
14.60248	11	11.65991	11	8.775034	5
14.19601	10	11.45918	10	8.733681	4
12.8542	9	10.79717	9	7.120928	3
12.08933	8	10.72029	8	3.820986	2
11.02726	7	10.69466	7	3.717604	1
8.771979	6	10.63487	6		
8.181935	5	10.36579	5		
7.827909	4	9.678156	4		
7.176676	3	9.52867	3		
6.057779	2	8.695819	2		
4.073485	1	7.124079	1		

Table C.3: Continuation of photographic grain sizes.

Size [mm]	% Proportion	Size [mm]	% Proportion	Size [mm]	% Proportion
186.8214	100	124.6012	100	198.8917	100
186.0221	99	124.046	99	157.1654	99
123.1102	98	123.1113	98	126.63	98
116.2607	97	118.3825	97	107.3212	97
115.4204	96	114.7086	96	105.1154	96
115.0925	95	110.4564	95	104.9851	95
111.5305	94	105.0335	94	102.6131	94
108.9809	93	101.7113	93	96.65154	93
105.759	92	100.9432	92	91.89399	92
98.27419	91	99.38854	91	90.47885	91
97.37651	90	98.7824	90	80.70318	90
92.90447	89	97.2925	89	80.6897	89
82.08713	88	93.3549	88	72.58075	88
80.82053	87	92.2259	87	70.51869	87
77.29947	86	87.55261	86	69.92119	86
75.23356	85	86.96035	85	69.64715	85

74.52033	84	85.10028	84	67.91754	84
74.15142	83	83.34664	83	67.66596	83
72.64297	82	82.94871	82	67.07744	82
72.28636	81	82.73124	81	65.249	81
68.20782	80	78.38184	80	61.98745	80
67.27325	79	77.23434	79	61.12938	79
67.056	78	76.66521	78	58.33505	78
66.27308	77	76.01743	77	57.22091	77
64.91631	76	76.00817	76	56.11576	76
64.66626	75	75.02724	75	55.69795	75
62.42	74	74.6432	74	55.35203	74
60.22702	73	74.43036	73	55.02408	73
57.96845	72	73.83347	72	54.4131	72
56.89451	71	73.80571	71	54.36368	71
56.58298	70	71.67265	70	54.36368	70
51.48379	69	69.76631	69	54.20644	69
51.38951	68	69.71542	68	53.58648	68
48.9219	67	69.69228	67	52.12193	67
46.59775	66	68.32731	66	50.1003	66
44.49085	65	66.63844	65	49.85771	65
43.62595	64	65.07451	64	49.81728	64
41.04767	63	64.39434	63	49.5028	63
40.77713	62	62.84891	62	48.73908	62
40.57218	61	59.96164	61	48.61329	61
40.09259	60	58.9437	60	48.44707	60
39.98602	59	58.22188	59	48.19549	59
39.87534	58	56.62556	58	47.16221	58
39.25639	57	56.50988	57	45.5539	57
39.08013	56	53.19693	56	45.05523	56
38.81779	55	51.33686	55	43.52329	55
38.75221	54	51.18417	54	40.64809	54
38.54726	53	48.31542	53	39.28238	53
38.50627	52	47.32523	52	38.56807	52
37.80533	51	46.84402	51	37.84029	51
36.96093	50	45.54845	50	37.20235	50
35.71073	49	43.85496	49	37.12598	49
35.57136	48	43.46629	48	36.77556	48
35.52627	47	40.35693	47	36.17806	47
35.20655	46	40.29215	46	35.00103	46
34.75156	45	38.3997	45	33.71618	45
32.29624	44	37.47892	44	33.1636	44
31.59121	43	34.61016	43	32.89405	43
31.50513	42	33.77267	42	31.73498	42
30.68122	41	33.50893	41	30.77359	41
30.20164	40	33.48579	40	29.62351	40
29.72205	39	33.2637	39	29.39889	39
29.27936	38	32.28739	38	27.21553	38
28.98833	37	31.75066	37	26.82918	37

28.88995	36	30.51524	36	26.58659	36
28.6932	35	30.27926	35	26.10589	35
28.2464	34	29.32147	34	25.71504	34
27.94717	33	28.85877	33	25.51737	33
27.79141	32	28.79862	32	24.92885	32
27.44709	31	28.21098	31	24.66829	31
26.71746	30	28.18785	30	24.33585	30
25.56154	29	27.82694	29	24.21006	29
25.07785	28	27.71589	28	22.11206	28
24.61056	27	26.97557	27	22.11206	27
24.4384	26	24.61116	26	20.48128	26
22.71271	25	22.18659	25	20.43187	25
22.61844	24	21.89046	24	19.62771	24
22.31511	23	21.58508	23	18.72023	23
21.60598	22	20.30339	22	16.92323	22
21.01572	21	20.01652	21	16.49195	21
19.98276	20	19.92398	20	15.94386	20
17.65451	19	18.73946	19	15.94386	19
16.05179	18	18.15183	18	15.64287	18
15.74027	17	16.46296	17	15.44969	17
15.55991	16	16.38893	16	14.52424	16
14.87127	15	15.82443	15	14.17831	15
14.71961	14	15.23217	14	13.98514	14
14.29331	13	14.79723	13	13.9492	13
12.60861	12	14.70006	12	13.67965	12
11.96096	11	13.8672	11	13.16301	11
9.677805	10	12.36342	10	12.54305	10
9.583527	9	11.84982	9	10.93923	9
8.280036	8	11.84982	8	10.08565	8
7.997203	7	10.28588	7	9.887982	7
7.751262	6	10.21185	6	9.268017	6
7.156903	5	9.860195	5	9.02093	5
6.402682	4	9.175395	4	8.71544	4
6.402682	3	5.316454	3	8.032581	3
5.94359	2	5.316454	2	5.081012	2
5.94359	1	4.543741	1	3.522116	1

Table C.4: Continuation of photographic grain sizes.

Size [mm]	% Proportion	Size [mm]	% Proportion	Size [mm]	% Proportion
138.7623	100	138.7297	100	141.1729	100
115.0679	99	124.4103	99	121.6829	99
110.5112	98	90.43402	98	104.3517	98
103.3931	97	88.62516	97	102.0761	97
85.35748	96	86.3574	96	101.4219	96
84.45974	95	82.32534	95	93.85674	95
82.51535	94	80.45856	94	91.5484	94
82.28986	93	77.40222	93	87.71208	93

81.68144	92	76.24383	92	84.24023	92
81.46445	91	73.97162	91	83.3711	91
80.46885	90	72.12712	90	81.9132	90
80.01785	89	69.56977	89	79.53478	89
72.37219	88	67.28865	88	78.60957	88
71.73824	87	65.36395	87	75.73584	87
69.84916	86	64.9897	86	74.13309	86
68.65785	85	63.75558	85	73.95085	85
65.90932	84	62.61502	84	73.8387	84
65.39025	83	61.42991	83	72.8621	82
61.09302	82	59.33591	82	72.39483	81
59.31881	81	58.43593	81	64.6334	80
58.68912	80	57.21518	80	62.74561	79
58.3062	79	56.28847	79	60.33915	78
57.29358	78	56.13254	78	58.52145	77
56.43414	77	55.83848	77	58.10557	76
54.40891	76	51.73959	76	53.83001	75
54.18766	75	50.22924	75	52.29268	74
53.70688	74	49.02631	74	50.71796	73
53.28992	73	48.57186	73	48.84887	72
52.77936	72	46.37094	72	48.29748	71
52.15818	71	44.86504	71	48.0031	70
51.71569	70	44.20565	70	47.86759	69
50.77541	69	43.6131	69	46.50782	68
50.00105	68	43.35914	68	45.90037	67
49.32881	67	42.59283	67	44.11538	66
48.38002	66	41.71513	66	43.56399	65
48.24812	65	41.6483	65	42.84906	64
45.75488	64	41.41217	64	39.19498	63
45.10391	63	41.15376	63	38.76509	62
45.10391	62	39.37163	62	37.91465	61
44.95925	61	38.68552	61	34.854	60
44.86139	60	38.31127	60	33.02228	59
44.85714	59	36.81874	59	32.48024	58
44.81459	58	36.24846	58	32.17652	57
44.40189	57	35.90985	57	30.45695	56
43.8658	56	33.24557	56	30.18125	55
43.07868	55	32.49708	55	29.82145	54
42.67023	54	31.93571	54	29.80743	53
41.01091	53	31.8867	53	29.77005	52
40.87476	52	31.41444	52	29.45231	51
39.71748	51	30.35407	51	28.44767	49
39.00695	49	30.25606	49	27.82619	48
38.19856	48	29.88626	48	27.77946	47
37.83266	47	28.86154	47	26.91033	46
37.7816	46	28.14424	46	26.43839	45
36.83706	45	28.13978	45	26.30288	44
34.11832	44	27.64524	44	24.97582	43

32.87595	43	26.78982	43	24.9104	42
30.45929	42	26.48686	42	24.67676	41
30.16997	41	25.70718	41	24.40107	40
29.2467	40	24.62454	40	23.46652	39
28.89782	39	24.16564	39	23.39176	38
28.38726	38	21.49245	38	22.91514	37
28.22132	37	21.01127	37	22.48524	36
26.52796	36	20.64594	36	22.11143	35
24.61335	35	20.24496	35	21.69088	34
21.27768	34	19.9019	34	19.41525	33
20.4778	33	19.27816	33	17.20037	32
20.2523	32	17.58068	32	17.08355	31
20.2523	31	17.56286	31	16.3733	30
19.60984	30	16.57823	30	16.3032	29
18.88655	29	16.4223	29	16.0976	28
17.76331	28	15.00996	28	15.8406	27
17.708	27	14.65354	27	15.8406	26
16.40181	26	14.11444	26	15.78453	25
15.54662	25	12.85359	25	14.74251	24
15.1254	24	12.0249	24	13.31732	23
14.22341	23	11.95361	23	13.09303	22
13.08316	22	11.86896	22	13.09303	21
13.01083	21	11.37888	21	12.9949	20
12.27902	20	10.8086	20	12.27997	19
11.8961	19	10.77741	19	12.16783	18
10.64097	18	10.23386	18	11.05104	16
10.57289	17	9.979909	17	10.90151	15
10.39845	16	9.378442	16	10.79871	14
9.139063	15	8.928455	15	10.65386	13
8.879527	14	8.79034	14	10.33611	12
8.203032	13	8.286889	13	9.948272	11
6.9479	12	7.507209	12	9.037087	10
6.169293	11	7.034945	11	8.971669	9
6.131001	10	6.861188	10	8.929614	8
5.450251	9	6.682975	9	8.784759	7
5.450251	8	6.682975	8	7.999738	6
4.816303	7	5.858741	7	7.401627	5
4.769501	6	5.529048	6	6.700715	4
4.144063	5	3.706824	5	5.719439	3
3.969621	4	3.706824	4	4.9204	2
3.969621	3	3.564253	3	4.54658	1
3.046354	2	3.515245	2		
2.722998	1	1.853412	1		

Table C.5: Mass of grain size classes from sieve measurements.

<1cm [kg]	1-2cm [kg]	2-4cm [kg]	4-8cm [kg]	8+cm [kg]	Sample Bag [kg]
28.96	18.18	23.54	21.46	45.67	2.34

Appendix D

Bedload Flux Calculations

I used a selection of widely used bedload flux calculations from various studies since 1948 to provide an overview of the sediment flux expected in the River Feshie study reach.

The range of constant parameters that are used in the following bedload flux equations are listed in Table D.1.

Table D.1: Parameters used in bedload flux calculations

Parameter	Value	Units
D_{50} (Wolman)	0.0384	m
D_{50} (Sieved)	0.035	m
Slope, S	0.0068	
Width, W	25	m
Sediment Density, ρ_s	2650	kg/m^3
Water Density, ρ_w	1000	kg/m^3
Density Ratio, s	2.65	
Gravitational acceleration, g	9.8	m^2/s

All equations output a value of dimensionless transport rate, ϕ, which could be converted into a bedload transport rate, q_b per metre width of the channel through:

$$\phi = \frac{q_b}{(g(s-1)D_{50}^3)^{\frac{1}{2}}} \tag{D.1}$$

where, g is gravitational acceleration constant, s is the ratio of sediment to water density, and D_{50} is the median grain size of the full distribution (van Rijn, 1984).

At first the dimensionless shear stress needs to be calculated by:

$$\tau^* = \frac{\tau}{(\rho_s - \rho_w)gD_{50}} > \tau_{cr}^* \tag{D.2}$$

where, $\tau = \rho_w ghS$. For the equations of Meyer-Peter and Müller (1948) and van Rijn (1984, Equation 22) the dimensionless transport rate (ϕ) can then be found using:

$$\phi = 8(\tau^* - \tau_{cr}^*)^{\frac{3}{2}} \tag{D.3}$$

These can be substituted into equation D.1 to convert the dimensionless transport rate (ϕ) to bedload flux (q_b) in $kg/m/s$. The parameter τ^*_{cr}, critical Shields stress, has varying values depending on the method used from previous studies. I use two different values of τ^*_{cr} from work by Meyer-Peter and Müller (1948) and van Rijn (1984):

Meyer-Peter and Müller (1948):

$$\tau^*_{cr} = 0.047 \tag{D.4}$$

van Rijn (1984, Equation 22):

$$\tau^*_{cr} = 0.056, \text{ if dimensionless grain size} > 150 \tag{D.5}$$

I additionally considered the formulae by Wilson (1996), Nielsen (1992), and Ashida and Michue (1972) for the dimensionless transport rate and substituted the values of ϕ into equation D.1:

Wilson (1996):

$$\phi = 12{\tau^*}^{\frac{1}{2}} \tag{D.6}$$

Nielsen (1992):

$$\phi = 12{\tau^*}^{\frac{1}{2}}(\tau^* - \tau^*_{cr}) \tag{D.7}$$

Ashida and Michue (1972):

$$\phi = 17(\tau^* - \tau^*_{cr})({\tau^*}^{\frac{1}{2}} - {\tau^*_{cr}}^{\frac{1}{2}}) \tag{D.8}$$

The above equations considered a singular grain size as representative of the full bedload mobilisation, so I have additionally included the calculations using the methods of Brown (1950) and Wilcock and Crowe (2003) that count for mixed sediment sizes.

Einstein (1950):

$$\phi = \begin{cases} 2.15F_{eb}e^{-\frac{0.391}{\tau^*}} & \text{if } 0.0025 \leq \tau^* \leq 0.2. \\ 40F_{eb}{\tau^*}^3 & \text{if } \tau^* > 0.2. \end{cases} \tag{D.9}$$

where,

$$F_{eb} = \left(\frac{2}{3} + \frac{36}{D_{50i}}\right)^{\frac{1}{2}} - \left(\frac{36}{D_{50i}}\right)^{\frac{1}{2}} \tag{D.10}$$

where D_{50i} is the median grain size within each grain size fraction.

Wilcock and Crowe (2003, Equation 2):

$$W_i = \frac{(s-1)gq_{bi}}{F_i u^3} \tag{D.11}$$

This equation can be used to find the volumetric transport rate of each grain size per unit width of the channel, q_{bi}, using the ratio of the density of water and sediment (s), gravity (g), grain size proportion (F_i), shear velocity ($u = \frac{\tau}{\rho_w}$), and a transport

parameter (W_i). Transport (W_i) is defined as two equations of the dimensionless shear ratio (τ/τ_{ri}):

$$W_i = \begin{cases} 0.002 \left(\frac{\tau}{\tau_{ri}}\right)^{7.5} & \text{if } \frac{\tau}{\tau_{ri}} < 1.35. \\ 14 \left(1 - \frac{0.894}{\sqrt{\frac{\tau}{\tau_{ri}}}}\right)^{4.5} & \text{if } \frac{\tau}{\tau_{ri}} \geq 1.35. \end{cases} \tag{D.12}$$

Where τ_{ri} is the reference shear stress for specific grain size class,

$$\tau_{ri} = \tau_{rm} \left(\frac{D_i}{D_{50}}\right)^b \tag{D.13}$$

This equation uses the median grain size for each size class (D_i), the median grain size for the whole distribution (D_{50}), the base reference shear stress for median grainsize (τ_{rm}) which is a function of sand content in percent (F_s), and a hiding factor which acts as a surrogate for fractional critical shear stress (b). b and τ_{rm} are defined as,

$$b = \frac{0.67}{1 + e^{1.5 - \frac{D_i}{D_{50}}}} \tag{D.14}$$

$$\tau_{rm} = 0.021 + 0.015 e^{(-20F_s)} \tag{D.15}$$

Appendix E

Additional Seismic Signals

As well as recording river- and meteorological-induced seismic signals, the geophones deployed in the River Feshie study reach also recorded other environmental signals. Here, I include the spectrograms of two examples of other signals recorded by the geophone at site W_07.

The River Feshie site, although away from main roads and in an anthropogenically quiet area, there are a number of estate buildings and vehicles that operate here. At least twice a day (when flows permit) estate vehicles cross the river ford adjacent to site W_07 to undertake deer stalking and other estate management duties. We regularly saw these vehicles crossing the river whilst undertaking field work. Figure E.1 shows the recorded signal by the geophone at site W_07 of an estate vehicle driving through the ford away from the geophone during a field visit on the 23rd March 2021. There is a slight increase in amplitude of the signal as seen in the waveform and the spectrogram as the vehicle approaches the river. The strongest signal occurs over less than a one-minute window in which there is increase power across the full frequency range, with the additional high power trace wiggling through frequency and time. This is interpreted to be a result of the agitation of the river bed by the vehicle, and the seismic signals as a result. The broadband high power signal stops at around 13:27, presumably when the vehicle reached the other side of the river channel. The high power wiggles continue over the following three minutes with gradually reducing power. These signals bounce around between about 60 Hz and 80 Hz. It is possible that this is the distant signal produced by the vehicle as it drives further away from the river.

In addition to the seismic signals produced by vehicle movement, our sensors successfully recorded the signal from a small magnitude 3.3 earthquake that struck the west of Scotland on the 16th November 2021, approximately 88 miles northwest of Glasgow and 11 miles northwest of a small town called Lochgilphead. The tremors were reported to have been felt as far as Edinburgh, 140 km away. Figure E.2 shows the very abrupt onset and high power of this signal, with the gradual decrease in power and frequency as the waves pass. This signal is unlike those observed for river-induced, or other environmental-induced, sources with the much sharper onset and high powers, masking the background river signal.

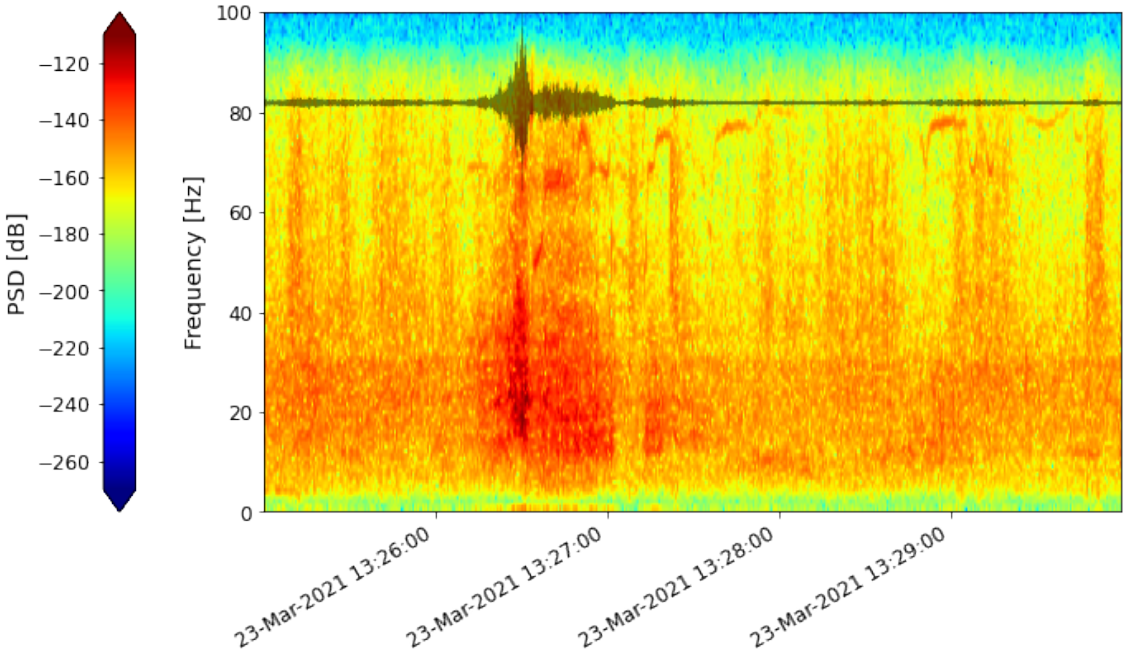


Figure E.1: Seismic signal at site W_07 of a vehicle driving through the ford away from the sensor.

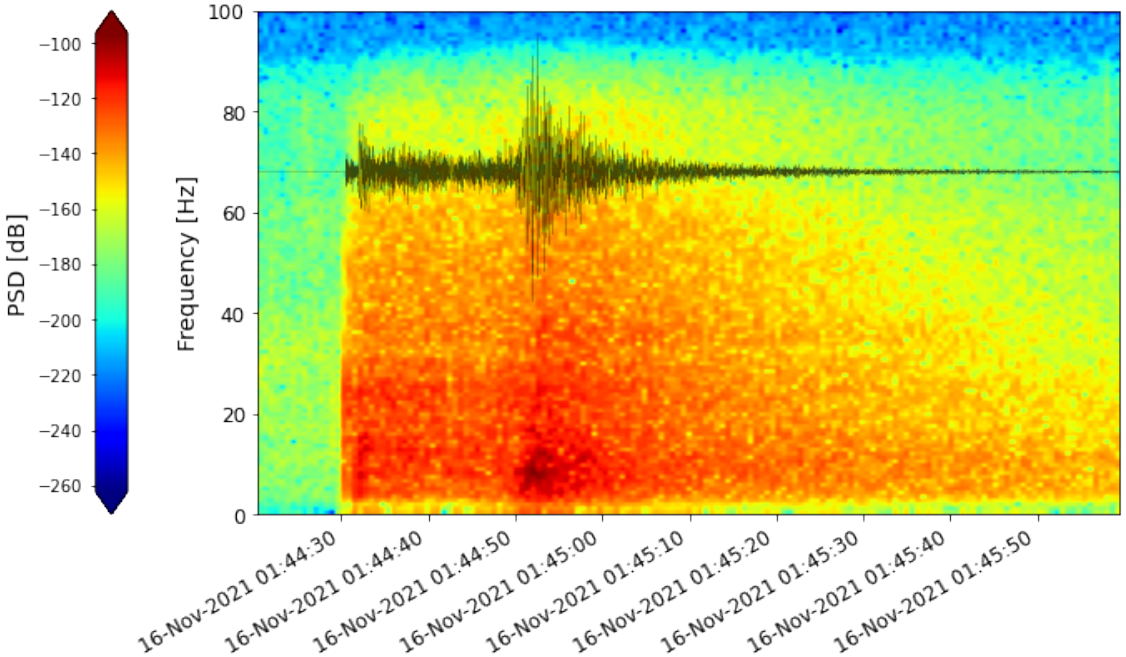


Figure E.2: Seismic signal at site W_07 of the magnitude 3.3 earthquake that struck the west of Scotland in November 2021.

Appendix F

ESPL manuscript of Chapter 5: Matthews et al. (2024)

As mentioned in Chapter 5, this appendix includes the manuscript text that is in the final stages of review with the Earth Surface Processes and Landforms journal (Article DOI: 10.1002/esp.5940). It has been through all stages of review and is currently waiting to be published. The manuscript makes reference to audio files which have been included in the journal submission, but are not possible to include in this thesis. I direct the reader to the ESPL paper once it is published to access the audio files.

Sounding out the river: Seismic and hydroacoustic monitoring of bedload transport

July 24, 2024

Abstract

Seismological observations provide a non-invasive and continuous means for indirectly measuring fluvial bedload transport. A significant challenge remains in independently characterising the seismic signature of bedload transport from other sources such as turbulence. We present a unique dataset from an alluvial Scottish river, combining seismic data and hydroacoustic measurements, to analyse bedload transport during three high flow events occurring within the same year. By studying three successive events, we assess the consistency of bedload transport thresholds in response to changing flow conditions, and explore the presence of hysteresis in seismic data versus water level as an indicator of coarse bedload transport. Through the use of hydroacoustic data to independently characterise bedload transport, our findings reveal that bedload transport occurred during all three events, but that the threshold for entrainment varied. These entrainment thresholds were influenced by antecedent events, with a drop of 15 - 20% of the threshold flow depth following the largest of the three events. In agreement with recent studies, we also found that hysteresis in the seismic versus water level data is not sufficient for identifying and analysing bedload transport: distinct hysteresis was only observed during the largest of the three events despite all events experiencing bedload transport as observed through the independent hydroacoustic data. Our work shows the value in combining independent datasets for long-term monitoring of bedload transport to understand the evolution in the thresholds of bedload motion, providing crucial information for effective river and land-use management in a changing climate with potentially impacted high flow events.

Keywords— river, bedload transport, entrainment threshold, fluvial geomorphology, environmental seismology

1 Introduction

Intensification of flood events linked to climate and land-use change poses significant threats to both infrastructure and ecosystems in many areas across the world. Climate change can drive increases in flood frequency and intensity, leading to increased transport of sediment and debris by rivers. Flooding and the transport of coarse gravelly bedload can benefit aquatic ecosystems, however increased magnitude and frequency of flooding could have profound ecological consequences, altering riverbed morphology, disturbing aquatic habitats and negatively impacting aquatic species (Hauer et al., 2018). The transport of bedload can also have significant impacts on infrastructure such as bridges and dams causing erosion and scour (Church, 2006; Turowski et al., 2011; Roth et al., 2017). Additionally, anthropogenic activities, including urban development, deforestation, channelisation and re-naturalisation for river management purposes, alter the patterns of bedload transport in rivers (Cox et al., 2021). Therefore, monitoring and understanding the timing and characteristics of coarse sediment mobilisation are crucial for predicting changes in channel morphology. This knowledge is essential for various applications, including designing and maintaining infrastructure to resist fluvial erosion, improving flood management, optimising sustainable water resource use, and preserving aquatic ecosystem health.

The dynamic and destructive nature of sediment movement in rivers makes monitoring and measuring the transport of coarse bedload challenging, particularly as rivers erode and aggrade their bed and shift their course. One of the key challenges lies in accurately measuring the onset of entrainment of bedload, and the continuous measurement of bedload transport in rivers. Variations in entrainment thresholds are influenced by factors such as particle shape and size distribution (Wilcock and Crowe, 2003; Jain et al., 2021), bedforms (Church et al., 1998), sediment cohesion (Kothyari and Jain, 2008), and changes in grain size between the bed surface and subsurface where coarse sediment may act to armour the river bed (Lisle and Madej, 1992; Jain et al., 2021). Tracer experiments that use pebbles loaded with accelerometers have demonstrated the complexity of entrainment thresholds with both clockwise and anticlockwise hysteresis between seismic power and streamflow during floods (Pretzlav et al., 2020). Using flume tank experiments it has been demonstrated that variations in bedload transport entrainment respond to durations and frequencies of moderate to peak discharge conditions, as a result of the river bed surface becoming more or less stable (Ockelford et al., 2019; Luo et al., 2023). The grain-size distribution may be modified at the bed surface by winnowing of finer grains resulting in the formation of an armoured surface layer of coarser grains (Pitlick et al., 2009; Gomez and Soar, 2022). This armouring modifies the onset of bedload entrainment complicating the relationship between the measured grain-size distribution and the entrainment threshold. A further complication to the measurement of bedload transport are hysteresis patterns, where sediment transport rates do not have a linear scaling with the flow conditions (Bogen, 1980). Armouring is an example of a process that could result in hysteresis

in bedload transport as it may increase the threshold for sediment motion on the bed causing the rising and falling limbs of a flood hydrograph to have different threshold entrainment values. The mobilisation of coarse bedload can also be influenced by the suspended sediment concentration at the sediment water interface (Rickenmann, 1991; An et al., 2018). Suspended sediment loads are commonly higher during the rising limb of flood hydrographs that also results in different entrainment thresholds on either side of a flood. Another potential driver of hysteresis relates to the history of large events that reorganise the bed and change the critical shear stress for subsequent events (Turowski et al., 2011; Masteller et al., 2019). The range of variables that determine entrainment thresholds as outlined above are also reflected in variations in dimensionless critical shear stress values of median grain sizes synthesised from a range of settings (e.g. Buffington and Montgomery, 1997).

Addressing the challenges of determining bedload entrainment thresholds for a given location requires innovative site and reach-scale measurement techniques. This facilitates a more comprehensive understanding of bedload transport dynamics, and the interplay between sediments, flow dynamics, and riverbed characteristics. However, since coarse bedload is mobilised when rivers are at high flow, logistical challenges are introduced when using many commonly used measurement techniques. Traditional methods of monitoring bedload transport in rivers, such as sediment sampling, sediment traps, grain size analysis and flow measurements, have typically relied on direct field measurements and observations and have been successfully used in a number of places, particularly in documenting the early motion of small grain sizes (Reid et al., 1985; Habersack et al., 2001; Bunte et al., 2004; Holmes, 2010). However, these approaches come with several limitations: sediment sampling and flow measurements can be labour-intensive, time-consuming, and difficult at high flows, while sediment traps (although continuous in measurement) are limited by the rapid filling of traps in high bedload transport rivers and the upper limit of grain sizes that can be measured as a result of the trap size. This limitation means they are less applicable to rivers with high sediment transport rates of large cobble to boulder sized bedload (Bunte et al., 2004; Bunte and Abt, 2005; Thorne, 2014). Non-continuous traditional methods struggle to capture the full complexity and natural dynamics of bedload transport, as they are typically performed during modest hydrologic events, over short timescales, and during daylight hours. Although some studies have used bedload samplers deployed across entire cross-sections of rivers (e.g. Dietze et al., 2019) these methods generally only measure at a single point in space, while bedload transport occurs along cross-sections with potentially variable transport at individual points in space. As a result, they may not provide sufficiently representative data needed for effective river management, infrastructure design, or understanding sediment transport patterns. Tracer grains have also enabled insight into these processes (e.g.Pretzlav et al., 2020), but are again challenging when large scale bedload movement is involved that disperses and buries the tracers long distances downstream. Engineers often use numerical

models or empirical equations as alternatives to traditional methods for predicting bedload transport (Geay et al., 2020). However, simplification of these empirical equations relative to complexities of natural bedload transport processes in rivers, and the challenge of estimating grain size distribution, entrainment thresholds, and bed morphology among other factors, results in considerable uncertainties in the sediment transport predictions (Dey, 2014; Downs et al., 2016).

New measurement techniques are increasingly being employed to address these limitations and provide more precise insights into bedload transport dynamics. Several recent studies have explored the potential for seismic sensors (such as geophones) to monitor environmental and geomorphic processes (e.g. Burtin et al., 2008; Roth et al., 2016; Dietze and Gimbert, 2019; Lagarde et al., 2021). Geophones, which are typically used for seismic studies, have important applications in the field of bedload transport monitoring. Previously, impact plate geophones have been strategically deployed in riverbeds to measure impacts on the bed (e.g. Rickenmann et al., 2014; Downs et al., 2016; Rickenmann et al., 2022) and seismic geophones have been deployed on river banks to capture the ground vibrations caused by bedload particles interacting with the river bed (e.g. Burtin et al., 2008; Schmandt et al., 2013; Barrière et al., 2015). These vibrations can be analysed to estimate the timings, intensity and frequency of bedload transport in rivers. This innovative use of geophones provides a non-intrusive and continuous monitoring method that overcomes some limitations associated with traditional bedload measurement techniques, facilitating the monitoring of bedload transport under conditions that were previously not possible (Burtin et al., 2010). Geophones record a range of environmental signals that are filtered by their passage through the subsurface. The potential sources for these signals include precipitation, wind, tides, traffic, turbulent motion in rivers, and the impact of bedload on riverbeds (Wilcock et al., 1999; Burtin et al., 2008; Rindraharisaona et al., 2022). Previous studies have focused on the frequency characteristics of seismic energy to discriminate different sources of seismic noise (Burtin et al., 2008; Burtin et al., 2014; Gimbert et al., 2014). The key discrimination for river induced seismic signals is between coarse bedload transport and water turbulence. It has been suggested that bedload transport induces broadband higher frequency seismic waves than the continuous signal from river turbulence (Schmandt et al., 2013; Gimbert et al., 2014; Vore et al., 2019). Tsai et al. (2012) and Gimbert et al. (2014) developed a physical inversion model that inverts recorded river seismic signals, using field observations such as ground seismic properties and grain size distributions, to estimates of bedload transport and water depth. Many studies have successfully utilised and edited this model to provide these estimates in a range of fluvial settings (e.g. Dietze and Gimbert, 2019; Bakker et al., 2020). However, due to the overlap in bedload and turbulence frequency bands observed in these studies it makes it difficult to accurately differentiate between the signal sources.

By correlating the bedload induced seismic data with river discharge, crucial insights have been gained

into the dynamics of sediment transport and how it responds to variations in hydraulic characteristics. Many studies found a hysteretic relationship between these parameters which have been interpreted to be evidence of bedload transport, as significant hysteresis is not expected in the relationship between river stage and turbulence (Hsu et al., 2011; Turowski et al., 2013; Roth et al., 2016; Roth et al., 2017). As outlined above, factors like particle size, shape and bed structure can influence the initiation of bedload transport on rivers, such that sediment entrainment thresholds may vary relative to changes in flow conditions. Bedload transport may even continue after the water level has decreased below the initial entrainment threshold, or may initiate and cease at different levels, due to changes in the hydraulic characteristics of the channel as a result of deposition upstream or the formation of new bars which can also affect the availability of sediment for mobilisation. This interpretation of hysteresis has become a foundational assumption for many fluvial seismic studies, with some studies reporting a clockwise pattern of hysteresis where bedload transport peaks before the peak in water level, and some recording an anticlockwise pattern where the peak in water level occurs prior to the peak in bedload transport. Clockwise patterns are associated with readily available sediments (Reid et al., 1985; Kuhnle, 1992; Hassan et al., 2006; Gaeuman, 2010; Mao, 2012; Mao et al., 2014), while anticlockwise patterns are thought to be caused by processes that increase sediment supply after a flood peak (Reid et al., 1985; Kuhnle, 1992; Lee et al., 2004; Mao et al., 2014). These previous seismic studies (e.g. Hsu et al., 2011; Chao et al., 2015) have shed light on the invaluable use of geophones for bedload monitoring purposes, however they generally had little independent data to constrain when bedload was being transported.

These uncertainties in the overlapping frequency bands of river-induced seismic signals and the assumptions in interpreting bedload transport processes using the relationship between seismic power and water level make the interpretation of bedload transport occurrence based on seismic data alone somewhat subjective. Therefore, it is beneficial to have an independent measure of bedload transport to cross-check with the seismic signals. To test some of the assumptions used in interpreting geophone data, we combine geophones deployed on riverbanks with acoustic hydrophones deployed in the water column to independently classify when coarse bedload is transported. Hydrophones have been used to detect and record underwater sound, making them particularly useful for applications in the fields of marine biology, underwater communication, and sonar systems (Ballance et al., 2023; Bountourakis et al., 2023). Some previous bedload studies (e.g. Rickenmann et al., 2022; Stark et al., 2024) have used hydrophones that are deployed in pipes to record the sound of particle impacts with the instrument. However, in contrast to geophones, they can also be suspended in the water column to record the full acoustic signal of impacts between the particles and the bed as well as inter-particle collisions. These suspended acoustic hydrophones, herein referred to as acoustic hydrophones, are sensitive to even the interaction of sand particles in low flow and can therefore record col-

lisions of the full range of particle sizes within the local river channel making them a potentially very useful method for grain size analysis. However, it is logistically difficult to deploy acoustic hydrophones routinely as they have to be placed within a river water column for the duration of the measurements, thus requiring careful methodological approach and appropriate housing to protect the instrument during high flow events (Osborne et al., 2021). On an event-by-event basis they can provide independent data to critique the seismic bedload transport information obtained from geophones and to test whether hysteresis in the relationship between the fluvial seismic signal and water level is in fact a fingerprint of bedload transport.

Here, we use co-located acoustic hydrophones (`https://jezrileyfrench.co.uk/hydrophones.php`) to evaluate the application of geophone data in characterising the onset of coarse bedload transport, and critique assumptions that use hysteresis as a characteristic of bedload transport from geophone data. Our study determines bedload mobilisation thresholds and evaluates the influence of antecedent events through independent seismic and hydroacoustic characterisations through multiple flood cycles. By integrating seismic, water level, and hydroacoustic data we aim to gain insights into bedload transport thresholds, examine hysteresis patterns, and shed light on the intricate relationship between sediment transport and discharge. Our analysis focuses on a relatively stable section of the gravel-bed River Feshie, in the Scottish Cairngorms (Figure 1) and analyses seismic signals from the three largest flow events in 2022. We explore how hydrographic sequencing (Ockelford and Haynes, 2013; Ockelford et al., 2019) at the River Feshie affects bedload transport entrainment thresholds through the independent analysis of seismic and hydroacoustic data.

2 Methods

2.1 Field site: River Feshie

The River Feshie in Scotland is an alluvial tributary of the River Spey and drains a catchment of $\sim$ 240 km^2 with a maximum elevation of just over 1200 m (Figure 1) (Ferguson and Werritty, 1983). The bedrock has low permeability which results in a hydrograph that is very responsive to rain and snowmelt events (Chełmicki and Krzemień, 1999). The headwaters sit on the peat-rich plateau of the Cairngorms (upstream of SG1 in Figure 1) and then flow downstream through glacial outwash gravels (downstream of SG1 in Figure 1). The Feshie is supplied largely by the erosion of glacial moraine and outwash channels resulting in a broad, braided gravel-dominated river (Ferguson and Werritty, 1983; Brasington et al., 2000). We focus on a $\sim$500 m long (Figure 1 b), single-thread reach just downstream of a wide multi-thread braided section (Figure 1 and 2). Within the study site, the channel width varies between 25 m to 70 m and has a local slope of $\sim$0.006. The bedrock is predominantly Moinian schist and granite which dominate the bedload (Ferguson and Werritty, 1983). The average grain sizes in the bar adjacent to the geophone station measured using

the Wolman pebble count method (Wolman, 1954) routinely before and after the 2022 events ranged from 5 mm to 194 mm with specific grain size fractions: D_{16} = 14 mm, D_{50} = 35 mm and D_{84} = 72 mm.

A stream gauge that is currently located approximately 12 km downstream from our site at Feshiebridge (SG3 in Figure 1), maintained by SEPA (Scottish Environment Protection Agency), records a variable flow regime with peak flows exceeding 100 m^3s^{-1} and a maximum peak flow of 260 m^3s^{-1} since recording began in December 1992. From flow data over the last 7 years at Feshiebridge (SG3) (Figure 3a) it can be seen that there are generally larger flows occurring during winter and spring. Flow patterns of 2022 were generally similar to previous years with low flows during summer and larger peaked flows in spring, autumn and winter. Summer flows in 2022 were particularly low, and were bounded by large events in early spring and autumn. The largest event of 2022, which we use for this analysis, peaked at around 138 m^3s^{-1} at SG3 in September. Prior to this there had only been six other peaks that exceeded this level over 7 years (Figure 3a); the largest of these occurring in December 2015 as a result of Storm Frank that caused widespread flooding across much of Scotland, Northern England and Wales (Barker et al., 2016). Historically, in the late 1970s, a stream gauge was maintained in the same stretch as our study site by Ferguson and Werritty (1983) and recorded a mean flow of 3-4 m^3s^{-1} with regular floods reaching 20-30 m^3s^{-1} and the largest recorded floods exceeded 100 m^3s^{-1}.

2.2 Data collection

2.2.1 Stream Gauge Data

This study uses water level (stage) measurements recorded at three stream gauge sites on the River Feshie. To measure water level at our study site, we deployed a LiDAR (Light Detection and Ranging) water level sensor on the remains of a footbridge at site SG2 which measures the distance to the water surface every 5 minutes. The water level data was corrected for the height of the sensor above the riverbed to provide approximate water depth measurements, assuming the river bed was fixed. Repeat measurements of the distance from the sensor to the river bed confirmed that the bed was stable at this location and the elevation of the bed remained constant during our study period. Although we can convert to water discharge using these data combined with channel geometry measurements, we don't have good constraints to accurately undertake this conversion which would induce uncertainty and therefore have chosen to work with the primary water level observations. We also have access to water level and discharge data collected every 15 minutes at stream gauges SG1 and SG3, located approximately 10 km upstream and downstream of our site (Figure 1). These data are managed by Dr Andrew Black (University of Dundee) and SEPA, respectively. We use the SEPA data as the historic record, since our local sensor has only been operational since the end of 2020.

The three events analysed in this study occurred on the 11^{th} - 14^{th} March 2022 (three successive peaks

with a maximum water level of 1.27 m at SG2), 30th September - 1st October 2022 (one peak with a maximum water level of 1.69 m at SG2, a roughly once-in-a-year event), and 2nd - 3rd November 2022 (one peak with a maximum water level of 1.30 m at SG2). These events are herein referred to as the 'March event', the 'September-October event', and the 'November event', respectively. The March event followed a series of snowmelt cycles that caused three repeated peaks in water level, resulting from rainfall on snow combined with snowmelt and peaked at 84 m^3s^{-1} at the SEPA station SG3. The larger September-October event was of a shorter duration and occurred following intense precipitation in the catchment that coincided with the tailend of Hurricane Fiona that hit Canada in mid-late September 2022, resulting in peak discharge of 138 m^3s^{-1} at SG3. The November event was an early winter storm with similar magnitude to the March event, however it occurred as a result of high rainfall alone, reaching peak discharge at 90 m^3s^{-1}. The three peaks in the first event allow us to test the consistency of the onset of bedload, the second event allows us to explore the impact of a large event on these thresholds of motion, and the third event allows us to explore the new behaviour of the river after a large event. Thus combining data from successive high flow events, with only a few small scale peaks occurring in between (Figure 3b), demonstrates how the technique can be used to make inferences about the effects of antecedent events on the mobilisation of bedload.

2.2.2 Seismic and Hydroacoustic Data

This study integrates seismic and hydroacoustic data to study the mobilisation and transport of bedload along a short (∼100 m) stretch of the River Feshie (Figure 1). We use the co-located stream gauge sensor (SG2) to analyse the dependence of the seismic and hydroacoustic data on water level.

We compare data from two 3-component PE6B (4.5Hz) geophones connected to Digos DataCube loggers recording at a sampling rate of 200 Hz. The geophone data was continuously recorded. The geophones were buried in soil at approximately 10 cm depth (base of instrument to surface), levelled and oriented with the North-South (horizontal) component aligned along the downstream river direction. The geophone at site W_07 was located within approximately 5 m of the river and 1 m above the base flow water surface. It was well sited to record a strong river signal as the small source-to-sensor distance minimises the attenuation of high frequencies, which is important for this study as we are wanting to resolve frequencies of bedload transport (Figure 1). The geophone at site E_06 was located approximately 300m from the river as a control site to characterise other sources of environmental noise, such as precipitation and wind as the impact of rain on the ground and the movement of vegetation by wind can be recorded by geophones (Dean, 2018; Rindraharisaona et al., 2022). Both sites have similar geology with high-velocity Moinian schist bedrock overlain by low-velocity glacial till (Ferguson and Werritty, 1983). Signals which are common to both W_07 and E_06 we identified as non-river environmental noise, and this approach allowed us to confirm that the

relatively high broadband noise level prior to the water rising is due to hydrometeorological noise. Generally, seismic bedload studies have used the vertical component of seismic waves as, due to the impact direction of bedload on the river bed, it was assumed that the emitted seismic waves would be best represented by Rayleigh waves with strong vertical displacements (Tsai et al., 2012; Dietze et al., 2019). Here, we present the analysis of the stream-parallel component. This was chosen because, although using the vertical and the stream-perpendicular components for the analysis gave similar results, the vertical component tended to be noisier due to its susceptibility to rain interference (see Supplemental Material S2) and theoretically the stream-parallel component should give the strongest river-related signal (Roth et al., 2016). The area is anthropogenically very quiet with little traffic on the estate roads, so there is minimal interference from these sources. The geophones are expected to record both the interaction of turbulence in the water with the bed and direct collisions of particles with the bed. It has previously been found that seismic waves emitted from bedload collisions resulted in higher frequencies than those from turbulence, with bedload generally found to occur in the range of 30-60 Hz and turbulence around 1-20 Hz (Tsai et al., 2012; Gimbert et al., 2014; Dietze and Gimbert, 2019). However, studies by Schmandt et al. (2013) and Schmandt et al. (2017) found that the bedload signals could be recorded in a range of frequencies from 15 Hz to 100 Hz.

To independently characterise bedload motion recorded within the study site, we deployed a hydrophone (Jez Riley French D-series, `https://jezrileyfrench.co.uk/hydrophones.php`) within the river at site H1 connected to our own Raspberry Pi logger, to record the hydro-acoustic signal of turbulence and bedload motion. In previous hydro-acoustic studies hydrophones have been deployed in metal pipes or attached to metal plates embedded in the river bed (Barrière et al., 2015), attached to the bottom of boats or river surveying equipment such as river boards (Geay et al., 2020), or attached to man-made infrastructure, such as bridges or metal frames (Belleudy et al., 2010), however this was logistically not an option in our study site. Instead, the hydrophone was mounted within a roughly 40 kg (0.4 m x 0.3 m x 0.3 m) granite block with a hollow cylindrical core of diameter 0.2 m in order to protect it from damage by direct impacts from mobile material (see Supplemental Material S1). The hydrophone block was located approximately 5 m downstream of the geophone at site W_07 and 40cm from the river bank (Figure 1). The recording system was built using a PiZero, a Witty Pi for scheduling and a HiFiBerry DAC+ADC Pro sound card (sampling at 44.1 kHz); due to the size of the datafiles, we recorded a 30 second sample every 15 minutes. Data were recorded at two different gains of 30 dB and 40 dB to manage potential issues of data quality. In addition to measuring collisions between particles and the bed, like geophones, acoustic hydrophones have the potential to record collisions of particles in suspension. The hydroacoustic data provides independent evidence of bedload motion within the channel. It was used as a complementary data set to the seismic data to confirm the occurrence and timing of bedload motion, which is challenging using seismic data alone due

to the overlapping frequencies of bedload and turbulence signals, as well as other environmental noise.

2.3 Data processing and analysis

We pre-process the seismic data by removing the instrument response through ObsPy using information provided by Digos on the specific instrument used. We then apply a bandpass filter in the frequency domain (between 4.5 Hz and 99 Hz) to the data prior to deconvolution to remove the frequencies most affected by the instrument. The data is then detrended to remove the mean trend of the signal using ObsPy. We computed the power spectral density (PSD) using Welch's method (Welch, 1967) with a 1-minute window and no overlap, to quantify the variation in seismic power as a function of time and frequency, which we compare to water level. In order to isolate the bedload signal, the standard methodology is to then average the PSD over the relevant frequency bands (Tsai et al., 2012; Bakker et al., 2020; Lagarde et al., 2021). This frequency range is typically around 30-60 Hz with turbulence found to be approximately 1-20 Hz (Tsai et al., 2012; Gimbert et al., 2014; Dietze and Gimbert, 2019). This approach allows us to compute the PSD for the seismic energy recorded within the frequency range commonly associated with the occurrence of bedload transport. The data are plotted as a visual representation of the frequencies of the signal over time as a spectrogram and then as a time varying PSD plot to show the temporal change in seismic power over the chosen frequency bands.

Here, we do not use the models developed by Tsai et al. (2012) and Gimbert et al. (2014) for our analysis as we wanted to take a data driven approach. Although these models have been successfully used in other studies and calibrated with field and flume measurements (Bakker et al., 2020; Lagarde et al., 2021), we wanted to focus on the real data rather than applying a model to interpret our data and integrating assumptions into the analysis based on the model outputs. The structure of our data is more complicated than the models can handle and thus we believe it is important to interpret the real data.

The raw hydro-acoustic data contains considerable information about the processes occurring in the river. There is a distinct audible signal from turbulence (gurgling), smaller grain sizes being transported (tinkling and tapping), and larger grain sizes being transported (thudding and knocking), which can be used to manually classify the dominant process (see Audio 1-3). For the duration of each of the three high flow events considered here, the 30 second hydro-acoustic recordings taken every 15 minutes were manually categorised by whether bedload was being transported. The recordings were categorised as 'Bedload Transport' if they were dominated by moving pebbles with more than 10 pebble hits over a 5 second window, however if there was only the occasional pebble movement (<10 per 5 seconds) and it was dominated by turbulence noises the files were classified as 'No Bedload Transport'. The categorisation into the larger and smaller grains being transported is more ambiguous as it relied on an audible identification of a change in frequency; more

could be done to look at the frequency characteristics of the hydro-acoustic data but this was not carried out for this work. For this work we have categorised the smaller grains as 'Bedload Transport (phase 1)' and the larger grains as 'Bedload Transport (phase 2)'. It was assumed that the condition remained constant between each recording within a single transport phase and therefore the phases were assumed constant. The same researcher processed all the hydro-acoustic data to minimise errors in the categorisation. At low water levels ($\sim$ 0.6 m) the hydrophones are exposed and therefore don't record any river related signals so are excluded from our analysis. Categorising the hydroacoustic data provides independent evidence when bedload transport took place that can be overlain on the seismic analysis to test the thresholds of entrainment for coarse bedload. It also provides a reliable independent measurement of bedload transport occurrence which is required to interpret hysteretic patterns observed in PSD versus water level data.

All stream gauge data, including those accessed from gauges SG1 and SG3, were linearly interpolated and resampled to one-minute intervals so that they could be combined with the geophone data analysed in minute long windows. Although the water level hydrographs during a high flow event are fairly smooth and it is easy to interpolate between the 15 minute samples, there may be some very small variability that is missed, particularly at base flows. However, 1 minute interpolated data does not mask any of the 15 minute recorded data. This also provided a richer database, as resampling the geophone data to 15 minute intervals to match the original stream gauge data sample rate would potentially miss important information from the propagating flood waves.

3 Results

The results compare the co-located geophone and hydrophone data at site W_07 and H1, respectively, and geophone data collected at a control site approximately 300 m from the river (E_06). This comparative analysis is supported by locally measured stream gauge data at SG2 (Figure 1c). The results describe the river-induced seismic signals at the two geophone sites, the observed transport thresholds over three successive high flow events, and the robustness of using hysteresis as a fingerprint of bedload transport.

3.1 Comparison of the river site with the non-fluvial control site

First we compare and contrast the geophone data recorded beside the river (W_07) and at the control site (E_06) in order to discriminate background environmental signals from those sourced from the river channel.

The water-level time series and spectrograms derived from the geophone data at each site are plotted in Figure 4 for two different events. The November event is not shown because the control site geophone E_06 was not recording at this time. Prior to the water rising, all the spectrograms show vertical broadband streaks of high amplitude (approximately -140 to -145 dB), which correspond to the periods of rain that

preceded the water level rises as we observed no snowmelt-only hydrological events (Figure 4 (c-f)). Similarly, when the water level drops, it is likely that there will be less rain at the site, and fewer vertical streaks on the spectrogram, as the water level would not be dropping if there was still significant rain across the catchment. This assumption does not necessarily hold true for large catchments as local conditions may vary from catchment wide conditions, such as rainfall patterns, however our interpretation makes this assumption due to the relatively small catchment size. Some of these streaky broadband signals could also be a result of wind but it is difficult to differentiate the two without further meteorological data as they tend to have similar characteristics and occupy similar frequency bands (Rindraharisaona et al., 2022).

In contrast to the control site we see that the PSD time-series measured at the river bank station, W_07, evolves as the water level changes. During periods of base level flow, when the water is low, the greatest power is recorded within a frequency range of approximately 5-35 Hz and is continuous, even during low flows prior to and following the large events. There is a sudden onset of higher frequency (30-80 Hz) high power seismic signals at W_07 recorded during the peak of the flood waves. During the highest water levels, these high power bands extend to higher frequencies, up to around 85 Hz, but once the river level drops towards base levels these higher frequency signals become less dominant. These high power, high frequency signals are absent from the control site.

In order to develop further understanding of the subsequent, more detailed results (see below), we make some initial, first-order interpretations of the signals listed above. We interpret the constant seismic signal during low flows to be the background river signal (turbulence); this feature is absent at the control site. The frequency values we observe for this signal is slightly higher than those found in previous studies but is most likely a result of site characteristics. The band of higher frequency seismic noise during the event peaks suggests that there is a separate signal in addition to that derived from turbulence, which is not present when the water levels return back to base levels. The absence of these signals at the control site enforces the interpretation that these are river related signals, to be determined by the hydroacoustic data. These comparisons allow us to identify the seismic signals that are induced by river-related processes, and specifically those induced by bedload transport, which are then used throughout the rest of this study to analyse transport thresholds and patterns.

Having documented the fingerprints of different physical processes within the time-frequency domain (Figure 4), we simplify the analysis by focusing on the 30-80 Hz band, as previous studies (e.g. Burtin et al., 2008; Roth et al., 2016; Turowski et al., 2015) have found that bedload transport produces signals at higher frequencies than turbulence, which going by our interpretation from Figure 4 would be >30 Hz. Specifically, in minute long windows shown in the spectrogram, we average the values of the power over the 50 to 60 Hz range for three distinct high flow events to calculate a single scalar value at each time, which we refer to as

the average power spectral density (aPSD) in the plots (See Section 2: Data processing and analysis). This narrower frequency range was chosen as there was less influence from meteorological and turbulence seismic signals, making the bedload transport the strongest signal observed for those frequencies.

The aPSDs calculated using the selected 50-60 Hz frequency band highlight the use of site E_06 as a control site and the strength of the river-induced seismic signals recorded at W_07. At the control site the PSD is dominated by the contributions from the broadband intermittent meteorological (wind and rain) signals. Consequently the aPSD shows large scatter that is independent of the water level (Figure 5 a,b). In contrast, the aPSD at the site beside the river, W_07, mirrors the variations in water level for all three events, showing a close parallel between the two (Figure 5 c-e). The meteorological noise is still visible at site W_07 prior to the hydrological peaks, but the river-induced seismic noise is dominant above base water levels ($\sim$ 0.90 - 1.10 m) as turbulence increases and bedload begins to be mobilised.

3.2 Analysis across three successive high flow events

3.2.1 Entrainment thresholds of coarse bedload

Using the hydrophone data, we classify whether bedload is being transported at site W_07, independent of the geophone data, and include this information on the water-level and the concomitant aPSD plot (Figure 5 c-e). The salmon and red shaded regions in Figure 5 c-e indicate when bedload is being transported, with the blue shading highlighting when only turbulence was observed, and white regions when the hydrophone was exposed out of the water and therefore not recording any sound. All three of the high flow events recorded the mobilisation of bedload during the peaks in water level, with the salmon colour, labelled 'Bedload transport (phase 1)' indicating the movement of bedload material. During the largest of the three events (the September-October event) there was also an audible shift in frequency of the recordings at the highest water level ($>\sim$ 1.50 - 1.60 m), which is shown in the reddish colour and labelled 'Bedload transport (phase 2)' in Figure 5d at the peak of the event, which lasted approximately 135 minutes. Recordings during the two transport phases and the only turbulence phase of the September-October event (Audio 1-3) highlight the audible changes during these processes. This audible frequency drop in the hydroacoustic data from 'Bedload transport (phase 1)' to 'Bedload transport (phase 2)' from 13:15 to 15:30 on the 30th September 2022 coincides with a shift to lower frequencies in the geophone data (Figure 4f and Supplemental Material S2), where the lower frequency end of the high amplitude seismic power dips from about 40 Hz to around 30 Hz at the same time as the peak of the hydrograph (30th September 14:00) and then rises back up following the peak. The gaps between the hydroacoustic categorisations in Figure 5 c-h are due to the 15 minute hydroacoustic sampling interval resulting in a range of water levels at which mobilisation of coarse bedload starts. Here, this water level range is greater during the rising limb than the falling limb (Figure 5f-h) due

to the rapid rate of increase in water level relative to the quarter-hourly hydrophone recordings compared to the gradually waning falling limb. Similar features would be observed in a rapidly decreasing flow, however this was not the case in the events analysed here.

We compare the timing of onset of bedload transport with the time-equivalent water level to explore systematic changes in the threshold for initiation and arrest of motion across the three events. Figures 5 and 6 reveal that bedload mobilisation during the moderate March event consistently starts and stops at a water level of ∼1.00 m. This is the case across all three daily peaks, labelled 1-3 in Figures 5c and 6b and c. However, during the largest September-October event coarse bedload transport initiates at between 0.95 m and 1.08 m, accounting for the uncertainty in the sampling period of the hydroacoustic data. The previously mentioned audible drop in frequency of the hydroacoustic data occurs between 1.50 m and 1.59 m and continues throughout the peak (at 1.69 m) and falling limb and stops at around 1.39 - 1.44 m, labelled 'Bedload transport (phase 2)' in Figure 5 and 6. At this point on the falling limb the audible frequency of the hydroacoustic recordings increases to a level similar to that of the initial mobilisation; bedload transport is sustained until the water level drops to ∼0.87 m. The September-October event therefore had coarse bedload mobilisation initiating at ∼1.00 m on the rising limb and ceasing at ∼0.87 m on the falling limb. The third event in November is much like the early March event in that the mobilisation of bedload starts and stops at the same level on the rising and falling limb of the hydrograph. However, for this event the entrainment threshold is now similar to that at the end of sediment transport in the September event at ∼ 0.79 - 0.87 m.

3.2.2 Hysteresis patterns

Consider the water-level versus aPSD plots in Figure 5 f-h and Figure 6a. These allow us to test the validity of the assumption that hysteresis in the water level versus PSD is a reliable indicator of bedload transport processes.

As noted above, bedload transport occurred during all three events which was independently evidenced through the hydroacoustic data. Looking at the water level versus aPSD plots it is clear that both the March and November events have similar seismic signals on the rising and falling limbs of the hydrograph and show minimal signs of hysteresis despite independent evidence from the hydroacoustic data that bedload was actively being transported. There is slight clockwise hysteresis seen for the largest peak of the March event and for only the largest water levels (above approximately 1.10 m) in the November event, however there is no hysteresis for water levels below this despite there being evidence from the hydroacoustic data of bedload transport occurring from approximately 1.00 m in the March event and 0.79 - 0.87 m for the November event. The two events also show very similar aPSD values to each other on the rising and falling

limbs, suggesting that the nature of coarse bedload transport may be comparable in both events.

In contrast, the aPSD analysed over the 50-60 Hz range in the larger September-October event does exhibit some anticlockwise hysteresis, but only between $\sim$ 1.00 m and 1.40 m (Figure 5 g). Until around 12:00 on the 30th September (at water levels $<$ 1.00 m), the aPSD is relatively constant at around -160 dB for this event whilst the rainfall dominates the seismic signal, as evidenced in Figure 5 d and discussed above in section 3.1. Once the water level reaches $\sim$1.00-1.10 m, the aPSD during the rising limb in Figure 5g appears to increase linearly until around 1.4 m at -148 dB where it levels off slightly until the peak of the event. During the falling limb the decrease in aPSD is less steep until $\sim$1.15 m, resulting in a sustained high aPSD which can also be seen on Figure 5 d where the aPSD remains close to peak levels for a short time after the peak even once the water level has begun to decrease. The largest variation in aPSD value between the rising and falling limb occurs at a water level of 1.2 m with the aPSD on the falling limb measuring approximately 7 dB higher than that on the rising limb. Below $\sim$1.15 m the value of aPSD falls much more rapidly. The overlap of the aPSD at water levels greater than 1.4 m on the rising and falling limb coincides with the transport of 'Bedload transport (phase 2)' from the hydroacoustic data. These water levels exceed the levels of the March and November events and so this behaviour is not visible on Figures 5f and 5h.

In summary, the initial entrainment threshold water depth that was observed in March 2022 dropped by about 15-20% ($\sim$1.00 m to $\sim$ 0.80-0.85 m) following the September-October event peak and this new lower threshold was maintained for the subsequent November high flow event. The March and November events show very little hysteresis, especially at lower water levels, whereas the larger September-October event shows a larger degree of anticlockwise hysteresis for water levels between $\sim$ 1.00 m and 1.40 m (when bedload transport is observed to initiate), and then behaves linearly at water levels above 1.40 m. Due to the noise from meteorological signals at the initial stages of the high flow events, it is difficult to identify any features in the seismic data that would indicate the initial transport of the coarse bedload, which is why the hydroacoustic data has proven very useful in this analysis.

4 Discussion

Due to the hazards and risks derived from the transport of coarse bedload, it is important to be able to monitor when and where the transport occurs within rivers. The seismic and hydroacoustic measurements at our field site in the alluvial River Feshie, recorded information on the mobilisation of coarse bedload. One of the strengths of our study is using three successive bedload transport events to assess the variations in thresholds of bedload entrainment, and the water-level versus seismic power hysteresis pattern variations through successive events.

We see the coarse bedload transport threshold changes following the largest of the three events suggesting that there is a dependence on the recent history of larger discharge events. Without evidence of dramatic changes in channel profile and bed structure, we speculate that there may have been a change to grain organisation and sorting on the bed following the largest event observed in 2022 which reduces the shear stress needed to entrain coarse bedload therefore allowing it to be more easily re-mobilised in a subsequent event (Jain et al., 2021). This could be a result of the very rapid fall in water level during the largest event compared to the March and November events inhibiting the bed to find a stable form (Turowski et al., 2011; Masteller et al., 2019; Luo et al., 2023). Since there were three other smaller water level peaks that only just exceeded the threshold of entrainment for the March event it is possible these caused local reorganisation and strengthening of the bed up until the September-October event. At which point the significantly increased discharge could have cause a break in the local armour layer leading to a deposition of unsorted material during the falling limb. The new 0.8 m threshold is exceeded a number of times between the September-October and November events, and most likely resulted in movement of only the smallest grain sizes. This was therefore unlikely to contribute to the development of an armour layer which would have caused an increase to the threshold for the November event which is not observed in the data.

We hypothesise that, in the absence of a further large flow event like the September-October 2022 event, over cycles of moderate scale events, such as snow melt cycles or moderate rainfall events like the March and November events, the bed will progressively regain its strength as the clasts locally reorganise, bedforms stabilise, and the water level threshold for mobility will again rise to a higher value (Ockelford et al., 2019; Luo et al., 2023). This hypothesis is supported by the observation that in the initial March event, the daily rainfall plus snowmelt cycles were just sufficient to initiate the motion of bedload at their peak suggesting that these moderate events have helped the system find a more stable configuration over time. Since events of a similar size to the March and November events are expected to happen approximately once every 5-6 months (Figure 3), there is potential for the river to undergo somewhat frequent local sorting of material before a large (approximately one in one year) event like the September-October event breaks through the sorted material and causes large amounts of resorting.

Prior to this study, hysteresis in the water-level versus seismic PSD plot was viewed as an indicator of bedload transport processes, with a purely turbulence signal expected to have a distinct lack of hysteresis (Burtin et al., 2008; Hsu et al., 2011; Turowski et al., 2015). In our study bedload was transported in all three events, as evidenced with the hydroacoustic data, but distinct hysteresis in the high frequency seismic signal only occurred in the largest event when using co-located geophone and stream gauge data from SG2; thus using hysteresis in the water-level versus seismic data alone as an indicator of bedload transport processes is insufficient to analyse bedload transport events. Although a small degree of hysteresis was observed for

the March and November events, it only occurred for the largest peak of the March event and only at water levels above approximately 1.10-1.20 m in the November event. During the smaller two peaks of the March event and the lower water levels of the November event, there were no hysteresis patterns observed despite the independent evidence from the hydroacoustic data that bedload transport did occur. This shows that hysteresis does not systematically correlate with the transport of bedload as evidenced from the independent hydroacoustic data.

Our findings are in agreement with Roth et al. (2017) who found that hysteresis may not be an effective measure of bedload transport as they identified that the seismic power tracks more closely to the changing water levels than the sediment transport rates measured using impact plate geophones. In addition to the general variation in PSD during the rising and falling limb of the September-October event, we also see a levelling off of the PSD for water levels above 1.40 m. One possible cause for a levelling off like this could be due clipping of the waveforms when the amplitude of the recorded signal exceeds the upper limit of the geophones recording range, resulting in a loss of data. However, this is not the case here and the observed behaviour is real (See Supplemental Material S3). We speculate this levelling off in PSD to be most likely caused by the presence of a sheet flow of granular material, which would make it difficult to increase the frequency and magnitude of collisions with the bed (Palucis et al., 2018), thus reducing the seismic power measured in the high frequencies with increasing water level. Although there may be a limit on the grain-to-bed interactions during granular sheet flow, there will likely be increased grain-to-grain interaction which is possible to record with the hydroacoustics. Further analysis into the frequency characteristics of hydroacoustic data would potentially shed some light on this.

In conjunction with the expected hysteresis at high frequencies, previous studies have suggested that analysing the low frequency band ($<\sim$1-30 Hz, e.g. Dietze and Gimbert, 2019; Chao et al., 2015; Burtin et al., 2008) can effectively isolate the turbulence signal. By focusing on this frequency range, it was suggested that a lack of hysteresis would be observed in the water-level versus PSD plot (Tsai et al., 2012). However, findings from this study challenge these assumptions, especially in relation to the largest event analysed. Contrary to expectations, hysteresis is also observed in the lower frequency range that was interpreted to be the turbulence signal from the data in Figure 4, as shown in Supplemental Material S4. This analysis may be complicated by the fact that bedload and turbulence can occupy overlapping frequency ranges, and therefore discrimination of the frequency bands of interest is very important.

Looking forwards, long-term monitoring on this reach will allow observing a series of successive events with varying durations. This will provide a more comprehensive understanding of the factors influencing the threshold for bedload mobilisation. In particular, we can assess whether the bedload mobilisation threshold is primarily influenced by the magnitude of high flow events, the duration of individual events or the periods

between events. Furthermore, we can explore the relationship between these dynamics, the arrangement of the riverbed structure, and the calculation of the entrainment threshold parameter, i.e. the Shields stress.

5 Conclusions

Developing a clear, robust methodology for understanding and digitally monitoring bedload transport and fluxes is fundamental for informing engineering and flood risk models, particularly with the concerns regarding the increased magnitude and frequency of flood events as a result of climate change. The use of seismic sensors is a key step forward and provides the opportunity to monitor bedload transport in previously inaccessible conditions. Combining seismic data with other measurement techniques, such as hydroacoustic data as done in this study, allows for the independent interpretation of bedload mobilisation. This cross-checking of complementary methods increases confidence in identifying bedload transport. By studying three successive bedload transport events, we test for variations in the flow conditions in an alluvial river that characterise the onset and termination of particle entrainment, thereby exploring the presence of hysteresis in seismic data as a fingerprint of coarse bedload transport. Through the use of hydroacoustic data to independently characterise bedload transport, our study found that bedload transport occurred during all three events but that mobilisation initiated and terminated at different water levels. Notably, these entrainment thresholds were influenced by preceding events, with a discernible drop in the threshold flow depth of approximately 15 - 20 % following the largest of the three events. Our study also reveals that while hysteresis in seismic data, in relation to water level, can sometimes be indicative of bedload transport processes, the degree of hysteresis is dependent on the magnitude of the event and is not a definitive requirement. Being able to accurately distinguish between distinct seismic signals associated with bedload transport and water turbulence is crucial, and will enable us to improve our ability to estimate bedload transport fluxes and gain deeper insights into the complex dynamics of alluvial rivers impacted by climate change. Our study shows the value in combining seismic and hydroacoustic data for long-term digital monitoring of bedload transport and suggests the possibility that this combination of data will allow us to identify different granular flow regimes in the field. Routine monitoring with such digital systems enables us to understand the systematic evolution in the onset of bedload transport and will be of direct use in calibrating widely used flood and bedload transport engineering models.

References

An, C., Parker, G., Hassan, M., and Fu, X. "Can magic sand cause massive degradation of a gravel-bed river at the decadal scale? Shi-ting River, China". In: *Geomorphology* 327 (Oct. 2018). DOI: 10.1016/j.geomorph.2018.10.026.

Bakker, M., Gimbert, F., Geay, T., Misset, C., Zanker, S., and Recking, A. "Field Application and Validation of a Seismic Bedload Transport Model". en. In: *Journal of Geophysical Research* (2020), p. 22.

Ballance, L. T., Pitman, R. L., Barlow, J., Pusser, T., D.A., Annamaria I., Hayslip, C., Irvine, L., Steel, D., Baker, C. S., Gillies, D., Baumann-Pickering, S., Trickey, J. S., and Gisborne, B. "Acoustic recordings, biological observations, and genetic identification of a rare(?) beaked whale in the North Pacific: Mesoplodon carlhubbsi". en. In: *Marine Mammal Science* (2023). _eprint: https://onlinelibrary.wiley.com/doi/pdf/10.1111/mms.13059. ISSN: 1748-7692. DOI: 10.1111/mms.13059. URL: https://onlinelibrary.wiley.com/doi/abs/10.1111/mms.13059 (visited on 10/30/2023).

Barker, L., Hannaford, J., Muchan, K., Turner, S., and Parry, S. "The winter 2015/2016 floods in the UK: a hydrological appraisal". en. In: *Weather* 71.12 (2016), pp. 324–333. ISSN: 1477-8696. DOI: 10.1002/wea.2822. URL: https://onlinelibrary.wiley.com/doi/abs/10.1002/wea.2822 (visited on 10/20/2023).

Barrière, J., Oth, A., Hostache, R., and Krein, A. "Bed load transport monitoring using seismic observations in a low-gradient rural gravel bed stream: Seismic monitoring of bedload transport". en. In: *Geophysical Research Letters* 42.7 (Apr. 2015), pp. 2294–2301. ISSN: 00948276. DOI: 10.1002/2015GL063630. URL: http://doi.wiley.com/10.1002/2015GL063630 (visited on 10/28/2020).

Belleudy, P., Valette, A., and Graff, B. "Monitoring of bedload in river beds with an hydrophone: first trials of signal analyses". en. In: *Dittrich, A.; Koll, K.; Aberle, J.; Geisenhainer, P. (Hg.): River Flow 2010* (2010). URL: https://hdl.handle.net/20.500.11970/99836.

Bogen, J. "The hysteresis effect of sediment transport systems". en. In: *Norsk Geografisk Tidsskrift - Norwegian Journal of Geography* 34.1 (Jan. 1980), pp. 45–54. ISSN: 0029-1951, 1502-5292. DOI:

10.1080/00291958008545338. URL: http://www.tandfonline.com/doi/abs/10.1080/00291958008545338 (visited on 11/16/2020).

Bountourakis, V., Elvander, F., and Pulkki, V. *Using optimal mass transport in bearing-time records for underwater target localization and tracking*. June 2023.

Brasington, J., Rumsby, B. T., and Mcvey, R. A. "Monitoring and modelling morphological change in a braided gravel-bed river using high resolution GPS-based survey". en. In: (2000), p. 18.

Buffington, John M. and Montgomery, David R. "A systematic analysis of eight decades of incipient motion studies, with special reference to gravel-bedded rivers". en. In: *Water Resources Research* 33.8 (1997). _eprint: https://onlinelibrary.wiley.com/doi/pdf/10.1029/96WR03190, pp. 1993–2029. ISSN: 1944-7973. DOI: 10.1029/96WR03190. URL: https://onlinelibrary.wiley.com/doi/abs/10.1029/96WR03190 (visited on 03/27/2024).

Bunte, K. and Abt, S. R. "Effect of sampling time on measured gravel bed load transport rates in a coarse-bedded stream". In: *Water Resources Research* 41.11 (2005). DOI: https://doi.org/10.1029/2004WR003880. URL: https://agupubs.onlinelibrary.wiley.com/doi/10.1029/2004wr003880 (visited on 10/30/2023).

Bunte, K., Abt, S.R., Potyondy, J. P., and Ryan, S. E. "Measurement of Coarse Gravel and Cobble Transport Using Portable Bedload Traps". EN. In: *Journal of Hydraulic Engineering* 130.9 (Sept. 2004). Publisher: American Society of Civil Engineers, pp. 879–893. ISSN: 0733-9429. DOI: 10.1061/(ASCE)0733-9429(2004)130:9(879). URL: https://ascelibrary.org/doi/10.1061/%28ASCE%290733-9429%282004%29130%3A9%28879%29 (visited on 10/30/2023).

Burtin, A., Bollinger, L., Vergne, J., Cattin, R., and Nábělek, J. L. "Spectral analysis of seismic noise induced by rivers: A new tool to monitor spatiotemporal changes in stream hydrodynamics". en. In: *Journal of Geophysical Research* 113.B5 (May 2008). ISSN: 0148-0227. DOI: 10.1029/2007JB005034. URL: http://doi.wiley.com/10.1029/2007JB005034 (visited on 10/28/2020).

Burtin, A., Hovius, N., McArdell, B. W., Turowski, J. M., and Vergne, J. "Seismic constraints on dynamic links between geomorphic processes and routing of sediment in a steep mountain catchment". en. In: *Earth Surface Dynamics* 2.1 (Jan. 2014), pp. 21–33. ISSN: 2196-632X. DOI:

10.5194/esurf-2-21-2014. URL: https://esurf.copernicus.org/articles/2/21/2014/ (visited on 10/28/2020).

Burtin, A., Vergne, J., Rivera, L., and Dubernet, P. "Location of river-induced seismic signal from noise correlation functions: Location of river seismic signal". en. In: *Geophysical Journal International* 182.3 (Sept. 2010), pp. 1161–1173. ISSN: 0956540X. DOI: 10.1111/j.1365-246X.2010.04701.x. URL: https://academic.oup.com/gji/article-lookup/doi/10.1111/j.1365-246X.2010.04701.x (visited on 10/28/2020).

Chao, W.-A., Wu, Y.-M., Zhao, L., Tsai, V. C., and Chen, C.-H. "Seismologically determined bedload flux during the typhoon season". en. In: *Scientific Reports* 5.1 (July 2015), p. 8261. ISSN: 2045-2322. DOI: 10.1038/srep08261. URL: http://www.nature.com/articles/srep08261 (visited on 10/28/2020).

Chełmicki, W. and Krzemień, K. "Channel Typology for the River Feshie in the Cairngorm Mts, Scotland". en. In: *Prace Geograficzne* (1999), p. 12.

Church, M. "Bed Material Transport and the Morphology of Alluvial River Channels". In: *Annual Review of Earth and Planetary Sciences* 34.1 (2006), pp. 325–354. DOI: 10.1146/annurev.earth.33.092203.122721. URL: https://doi.org/10.1146/annurev.earth.33.092203.122721 (visited on 04/12/2021).

Church, M., Hassan, M. A., and Wolcott, J. F. "Stabilizing self-organized structures in gravel-bed stream channels: Field and experimental observations". en. In: *Water Resources Research* 34.11 (1998). _eprint: https://onlinelibrary.wiley.com/doi/pdf/10.1029/98WR00484, pp. 3169–3179. ISSN: 1944-7973. DOI: 10.1029/98WR00484. URL: https://onlinelibrary.wiley.com/doi/abs/10.1029/98WR00484 (visited on 03/10/2023).

Cox, J. R., Huismans, Y., Knaake, S. M., Leuven, J. R. F. W., Vellinga, N. E., Vegt, M. van der, Hoitink, A. J. F., and Kleinhans, M. G. "Anthropogenic Effects on the Contemporary Sediment Budget of the Lower Rhine-Meuse Delta Channel Network". en. In: *Earth's Future* 9.7 (2021). _eprint: https://onlinelibrary.wiley.com/doi/pdf/10.1029/2020EF001869, e2020EF001869. ISSN: 2328-4277. DOI: 10.1029/2020EF001869. URL: https://onlinelibrary.wiley.com/doi/abs/10.1029/2020EF001869 (visited on 10/30/2023).

Dean, T. “The seismic signature of rain”. en. In: *ASEG Extended Abstracts* 2018.1 (Dec. 2018), pp. 1–8. ISSN: 2202-0586. DOI: 10.1071/ASEG2018abP068. URL: https://www.tandfonline.com/doi/full/10.1071/ASEG2018abP068 (visited on 12/06/2022).

Dey, S. *Fluvial Hydrodynamics*. en. GeoPlanet: Earth and Planetary Sciences. Berlin, Heidelberg: Springer Berlin Heidelberg, 2014. ISBN: 978-3-642-19061-2 978-3-642-19062-9. DOI: 10.1007/978-3-642-19062-9. URL: http://link.springer.com/10.1007/978-3-642-19062-9 (visited on 11/20/2020).

Dietze, M. and Gimbert, F. “The seismic view on sediment laden ephemeral flows – modelling of ground motion data for fluid and bedload dynamics in the Arroyo de los Piños”. en. In: (2019), p. 10.

Dietze, M., Lagarde, S., Halfi, E., Laronne, J. B., and Turowski, J. M. “Joint Sensing of Bedload Flux and Water Depth by Seismic Data Inversion”. en. In: *Water Resources Research* 55.11 (2019), pp. 9892–9904. ISSN: 1944-7973. DOI: https://doi.org/10.1029/2019WR026072. URL: https://agupubs.onlinelibrary.wiley.com/doi/abs/10.1029/2019WR026072 (visited on 02/26/2021).

Downs, P. W., Soar, P. J., and Taylor, A. “The anatomy of effective discharge: the dynamics of coarse sediment transport revealed using continuous bedload monitoring in a gravel-bed river during a very wet year: Dynamics of coarse sediment transport using continuous monitoring”. en. In: *Earth Surface Processes and Landforms* 41.2 (Feb. 2016), pp. 147–161. ISSN: 01979337. DOI: 10.1002/esp.3785. URL: http://doi.wiley.com/10.1002/esp.3785 (visited on 10/28/2020).

Ferguson, R. I. and Werritty, A. “Bar Development and Channel Changes in the Gravelly River Feshie, Scotland”. en. In: *Modern and Ancient Fluvial Systems*. Ed. by J. D. Collinson and J. Lewin. Oxford, UK: Blackwell Publishing Ltd., Feb. 1983, pp. 181–193. ISBN: 978-1-4443-0377-3 978-0-632-00997-8. DOI: 10.1002/9781444303773.ch14. URL: http://doi.wiley.com/10.1002/9781444303773.ch14 (visited on 10/28/2020).

Gaeuman, D. “Mechanics of Bedload Rating Curve Shifts and Bedload Hysteresis in the Trinity River, California”. en. In: (2010).

683 Geay, T., Zanker, S., Misset, C., and Recking, A. “Passive Acoustic Measurement of Bedload
684 Transport: Toward a Global Calibration Curve?” en. In: *Journal of Geophysical Research: Earth*
685 *Surface* 125.8 (2020). _eprint: https://onlinelibrary.wiley.com/doi/pdf/10.1029/2019JF005242,
686 e2019JF005242. ISSN: 2169-9011. DOI: 10.1029/2019JF005242. URL: https://onlinelibrary.
687 wiley.com/doi/abs/10.1029/2019JF005242 (visited on 01/13/2022).

688 Gimbert, F., Tsai, V. C., and Lamb, M. P. “A physical model for seismic noise generation by
689 turbulent flow in rivers”. en. In: *Journal of Geophysical Research: Earth Surface* 119.10 (Oct.
690 2014), pp. 2209–2238. ISSN: 21699003. DOI: 10.1002/2014JF003201. URL: http://doi.wiley.
691 com/10.1002/2014JF003201 (visited on 10/28/2020).

692 Gomez, B. and Soar, P. J. “Bedload transport: beyond intractability”. In: *Royal Society Open*
693 *Science* 9.3 (Mar. 2022). Publisher: Royal Society, p. 211932. DOI: 10.1098/rsos.211932. URL:
694 https://royalsocietypublishing.org/doi/10.1098/rsos.211932 (visited on 10/30/2023).

695 Habersack, H.M., Nachtneb El, H.P., and Laronne, J.B. “The continuous measurement of bed-
696 load discharge in a large alpine gravel bed river”. In: *Journal of Hydraulic Research* 39.2 (Apr.
697 2001). Publisher: Taylor & Francis _eprint: https://doi.org/10.1080/00221680109499813, pp. 125–
698 133. ISSN: 0022-1686. DOI: 10.1080/00221680109499813. URL: https://doi.org/10.1080/
699 00221680109499813 (visited on 03/27/2024).

700 Hassan, M. A., Egozi, R., and Parker, G. “Experiments on the effect of hydrograph characteristics
701 on vertical grain sorting in gravel bed rivers”. en. In: *Water Resources Research* 42.9 (2006).
702 ISSN: 1944-7973. DOI: https://doi.org/10.1029/2005WR004707. URL: https://agupubs.
703 onlinelibrary.wiley.com/doi/abs/10.1029/2005WR004707 (visited on 12/03/2020).

704 Hauer, C., Leitner, P., Unfer, G., Pulg, U., Habersack, H., and Graf, W. “The Role of Sediment
705 and Sediment Dynamics in the Aquatic Environment”. en. In: *Riverine Ecosystem Management:*
706 *Science for Governing Towards a Sustainable Future*. Ed. by Stefan Schmutz and Jan Sendzimir.
707 Cham: Springer International Publishing, 2018, pp. 151–169. ISBN: 978-3-319-73250-3. DOI: 10.
708 1007/978-3-319-73250-3_8. URL: https://doi.org/10.1007/978-3-319-73250-3_8 (visited
709 on 04/15/2024).

710 Holmes, R. “Measurement of Bedload Transport in Sand-Bed Rivers: A Look at Two Indirect
711 Sampling Methods”. en. In: (2010), p. 17.

Hsu, L., Finnegan, N. J., and Brodsky, E. E. "A seismic signature of river bedload transport during storm events". en. In: *Geophysical Research Letters* 38.13 (July 2011). ISSN: 00948276. DOI: 10.1029/2011GL047759. URL: http://doi.wiley.com/10.1029/2011GL047759 (visited on 10/28/2020).

Jain, R., Tschisgale, S., and Fröhlich, J. "Impact of shape: DNS of sediment transport with non-spherical particles". en. In: *Journal of Fluid Mechanics* 916 (June 2021). Publisher: Cambridge University Press, A38. ISSN: 0022-1120, 1469-7645. DOI: 10.1017/jfm.2021.214. URL: https://www.cambridge.org/core/journals/journal-of-fluid-mechanics/article/impact-of-shape-dns-of-sediment-transport-with-nonspherical-particles/0B3ED0C2B19C84AB97EB83F7362389A8 (visited on 05/31/2023).

Kothyari, U. C. and Jain, R. K. "Influence of cohesion on the incipient motion condition of sediment mixtures". en. In: *Water Resources Research* 44.4 (2008). ISSN: 1944-7973. DOI: 10.1029/2007WR006326. URL: https://onlinelibrary.wiley.com/doi/abs/10.1029/2007WR006326 (visited on 03/10/2023).

Kuhnle, R. A. "Bed load transport during rising and falling stages on two small streams". en. In: *Earth Surface Processes and Landforms* 17.2 (1992), pp. 191–197. ISSN: 1096-9837. DOI: https://doi.org/10.1002/esp.3290170206. URL: https://onlinelibrary.wiley.com/doi/abs/10.1002/esp.3290170206 (visited on 12/03/2020).

Lagarde, S., Dietze, M., Gimbert, F., Laronne, J. B., Turowski, J. M., and Halfi, E. "Grain-Size Distribution and Propagation Effects on Seismic Signals Generated by Bedload Transport". en. In: *Water Resources Research* 57.4 (2021). ISSN: 1944-7973. DOI: https://doi.org/10.1029/2020WR028700. URL: https://agupubs.onlinelibrary.wiley.com/doi/abs/10.1029/2020WR028700 (visited on 05/31/2021).

Lee, K. T., Liu, Yi-Liang, and Cheng, Kai-Hung. "Experimental investigation of bedload transport processes under unsteady flow conditions". en. In: *Hydrological Processes* 18.13 (2004), pp. 2439–2454. ISSN: 1099-1085. DOI: https://doi.org/10.1002/hyp.1473. URL: https://onlinelibrary.wiley.com/doi/abs/10.1002/hyp.1473 (visited on 12/03/2020).

Lisle, T. E. and Madej, M. A. "Spatial variation in armouring in a channel with high sediment supply". en. In: *Dynamics of gravel-bed rivers* (1992), pp. 277–293.

Luo, M., Jiang, Y., Wang, S., Liu, X., and Huang, E. "The effect of stress history on fluctuation of bedload transport rate and bed topography in gravel-bed streams". en. In: *Journal of Hydrology* 616 (Jan. 2023), p. 128732. ISSN: 00221694. DOI: 10.1016/j.jhydrol.2022.128732. URL: https://linkinghub.elsevier.com/retrieve/pii/S0022169422013026 (visited on 06/01/2023).

Mao, L. "The effect of hydrographs on bed load transport and bed sediment spatial arrangement". en. In: *Journal of Geophysical Research: Earth Surface* 117.F3 (2012). ISSN: 2156-2202. DOI: https://doi.org/10.1029/2012JF002428. URL: https://agupubs.onlinelibrary.wiley.com/doi/abs/10.1029/2012JF002428 (visited on 11/30/2020).

Mao, L., Dell'Agnese, A., Huincache, C., Penna, D., Engel, M., Niedrist, G., and Comiti, F. "Bedload hysteresis in a glacier-fed mountain river". en. In: *Earth Surface Processes and Landforms* 39.7 (2014). _eprint: https://onlinelibrary.wiley.com/doi/pdf/10.1002/esp.3563, pp. 964–976. ISSN: 1096-9837. DOI: https://doi.org/10.1002/esp.3563. URL: https://onlinelibrary.wiley.com/doi/abs/10.1002/esp.3563 (visited on 11/30/2020).

Masteller, C., Finnegan, N., Turowski, J., Yager, E., and Rickenmann, D. "History-Dependent Threshold for Motion Revealed by Continuous Bedload Transport Measurements in a Steep Mountain Stream". en. In: *Geophysical Research Letters* 46.5 (2019), pp. 2583–2591. ISSN: 1944-8007. DOI: 10.1029/2018GL081325. URL: https://onlinelibrary.wiley.com/doi/abs/10.1029/2018GL081325 (visited on 03/27/2023).

Ockelford, A. and Haynes, H. "The impact of stress history on bed structure". en. In: *Earth Surface Processes and Landforms* 38.7 (2013), pp. 717–727. ISSN: 1096-9837. DOI: 10.1002/esp.3348. URL: https://onlinelibrary.wiley.com/doi/abs/10.1002/esp.3348 (visited on 03/06/2023).

Ockelford, A., Woodcock, S., and Haynes, H. "The impact of inter-flood duration on non-cohesive sediment bed stability". en. In: *Earth Surface Processes and Landforms* 44.14 (2019), pp. 2861–2871. ISSN: 1096-9837. DOI: 10.1002/esp.4713. URL: https://onlinelibrary.wiley.com/doi/abs/10.1002/esp.4713 (visited on 03/06/2023).

Osborne, Wm A., Hodge, R., Love, G., Hawkin, P., and Hawkin, R. "Babbling brook to thunderous torrent: Using sound to monitor river stage". en. In: *Earth Surface Processes and Landforms*

n/a.n/a (2021). ISSN: 1096-9837. DOI: 10.1002/esp.5199. URL: https://onlinelibrary.wiley.com/doi/abs/10.1002/esp.5199 (visited on 09/16/2021).

Palucis, M. C., Ulizio, T., Fuller, B., and Lamb, M. P. "Intense Granular Sheetflow in Steep Streams". en. In: *Geophysical Research Letters* 45.11 (2018), pp. 5509–5517. ISSN: 1944-8007. DOI: 10.1029/2018GL077526. URL: https://onlinelibrary.wiley.com/doi/abs/10.1029/2018GL077526 (visited on 10/30/2023).

Pitlick, J., Cui, Y., and Wilcock, P. "Manual for Computing Bed Load Transport Using BAGS (Bedload Assessment for Gravel-bed Streams) Software". In: (Jan. 2009).

Pretzlav, K., Johnson, J., and Bradley, D. N. "Smartrock Transport in a Mountain Stream: Bedload Hysteresis and Changing Thresholds of Motion". en. In: *Water Resources Research* 56.11 (2020), e2020WR028150. ISSN: 1944-7973. DOI: https://doi.org/10.1029/2020WR028150. URL: https://agupubs.onlinelibrary.wiley.com/doi/abs/10.1029/2020WR028150 (visited on 02/03/2021).

Reid, I., Frostick, L. E., and Layman, J. T. "The incidence and nature of bedload transport during flood flows in coarse-grained alluvial channels". en. In: *Earth Surface Processes and Landforms* 10.1 (1985), pp. 33–44. ISSN: 1096-9837. DOI: 10.1002/esp.3290100107. URL: https://onlinelibrary.wiley.com/doi/abs/10.1002/esp.3290100107 (visited on 09/14/2021).

Rickenmann, D. "Hyperconcentrated Flow and Sediment Transport at Steep Slopes". EN. In: *Journal of Hydraulic Engineering* 117.11 (Nov. 1991). Publisher: American Society of Civil Engineers, pp. 1419–1439. ISSN: 0733-9429. DOI: 10.1061/(ASCE)0733-9429(1991)117:11(1419). URL: https://ascelibrary.org/doi/10.1061/%28ASCE%290733-9429%281991%29117%3A11%281419%29 (visited on 10/30/2023).

Rickenmann, D., Ammann, L., Nicollier, T., Boss, S., Fritschi, B., Antoniazza, G., Steeb, N., Chen, Z., Wyss, C., and Badoux, A. "Comparison of calibration characteristics of different acoustic impact systems for measuring bedload transport in mountain streams". English. In: *Earth Surface Dynamics* 10.6 (Nov. 2022). Publisher: Copernicus GmbH, pp. 1165–1183. ISSN: 2196-6311. DOI: 10.5194/esurf-10-1165-2022. URL: https://esurf.copernicus.org/articles/10/1165/2022/ (visited on 01/23/2023).

Rickenmann, D., Turowski, J. M., Fritschi, B., Wyss, C., Laronne, J., Barzilai, Ronel, Reid, Ian, Kreisler, Andrea, Aigner, Johann, Seitz, Hugo, and Habersack, Helmut. "Bedload transport measurements with impact plate geophones: comparison of sensor calibration in different gravel-bed streams". en. In: *Earth Surface Processes and Landforms* 39.7 (June 2014), pp. 928–942. ISSN: 01979337. DOI: 10.1002/esp.3499. URL: http://doi.wiley.com/10.1002/esp.3499 (visited on 10/28/2020).

Rindraharisaona, E. J., Réchou, A., Fontaine, F. R., Barruol, G., Stamenoff, P., Boudevillain, B., Rigaud-Louise, F., and Delcher, E. "Seismic Signature of Rain and Wind Inferred From Seismic Data". en. In: *Earth and Space Science* 9.10 (2022). ISSN: 2333-5084. DOI: 10.1029/2022EA002328. URL: https://onlinelibrary.wiley.com/doi/abs/10.1029/2022EA002328 (visited on 12/06/2022).

Roth, D. L., Brodsky, E.E., Finnegan, N.J., Rickenmann, D., Turowski, J.M., and Badoux, A. "Bed load sediment transport inferred from seismic signals near a river". en. In: *Journal of Geophysical Research: Earth Surface* 121.4 (Apr. 2016), pp. 725–747. ISSN: 2169-9003, 2169-9011. DOI: 10.1002/2015JF003782. URL: https://onlinelibrary.wiley.com/doi/abs/10.1002/2015JF003782 (visited on 10/28/2020).

Roth, D. L., Finnegan, N. J., Brodsky, E. E., Rickenmann, D., Turowski, J. M., Badoux, A., and Gimbert, F. "Bed load transport and boundary roughness changes as competing causes of hysteresis in the relationship between river discharge and seismic amplitude recorded near a steep mountain stream". en. In: *Journal of Geophysical Research: Earth Surface* 122.5 (May 2017), pp. 1182–1200. ISSN: 21699003. DOI: 10.1002/2016JF004062. URL: http://doi.wiley.com/10.1002/2016JF004062 (visited on 11/16/2020).

Schmandt, B., Aster, R. C., Scherler, D., Tsai, V. C., and Karlstrom, K. "Multiple fluvial processes detected by riverside seismic and infrasound monitoring of a controlled flood in the Grand Canyon". en. In: *Geophysical Research Letters* 40.18 (Sept. 2013), pp. 4858–4863. ISSN: 0094-8276, 1944-8007. DOI: 10.1002/grl.50953. URL: https://onlinelibrary.wiley.com/doi/abs/10.1002/grl.50953 (visited on 10/28/2020).

Schmandt, B., Gaeuman, D., Stewart, R., Hansen, S.M., Tsai, V.C., and Smith, J. "Seismic array constraints on reach-scale bedload transport". en. In: *Geology* 45.4 (Apr. 2017), pp. 299–302. ISSN:

826 0091-7613, 1943-2682. DOI: 10.1130/G38639.1. URL: https://pubs.geoscienceworld.org/
827 geology/article/45/4/299-302/195340 (visited on 04/10/2024).

828 Stark, K., Cadol, D., Varyu, D., Halfi, E., and Laronne, J.B. "Strengths and weaknesses of
829 acoustic pipe microphone systems in ephemeral, sandy, gravel-bed rivers". en. In: *Earth Surface*
830 *Processes and Landforms* 49.4 (2024), pp. 1383–1396. ISSN: 1096-9837. DOI: 10.1002/esp.
831 5774. URL: https://onlinelibrary.wiley.com/doi/abs/10.1002/esp.5774 (visited on
832 03/27/2024).

833 Thorne, P. D. "An overview of underwater sound generated by interparticle collisions and its
834 application to the measurements of coarse sediment bedload transport". en. In: *Earth Surface*
835 *Dynamics* 2.2 (Dec. 2014), pp. 531–543. ISSN: 2196-632X. DOI: 10.5194/esurf-2-531-2014.
836 URL: https://esurf.copernicus.org/articles/2/531/2014/ (visited on 10/28/2020).

837 Tsai, V. C., Minchew, B., Lamb, M. P., and Ampuero, J.-P. "A physical model for seismic noise
838 generation from sediment transport in rivers". en. In: *Geophysical Research Letters* 39.2 (Jan.
839 2012). ISSN: 00948276. DOI: 10.1029/2011GL050255. URL: http://doi.wiley.com/10.1029/
840 2011GL050255 (visited on 10/28/2020).

841 Turowski, J. M., Badoux, A., and Rickenmann, D. "Start and end of bedload transport in
842 gravel-bed streams". en. In: *Geophysical Research Letters* 38.4 (Feb. 2011). ISSN: 00948276. DOI:
843 10.1029/2010GL046558. URL: http://doi.wiley.com/10.1029/2010GL046558 (visited on
844 10/28/2020).

845 Turowski, J. M., Böckli, M., Rickenmann, D., and Beer, A. R. "Field measurements of the energy
846 delivered to the channel bed by moving bed load and links to bedrock erosion". en. In: *Journal*
847 *of Geophysical Research: Earth Surface* 118.4 (Dec. 2013), pp. 2438–2450. ISSN: 21699003. DOI:
848 10.1002/2013JF002765. URL: http://doi.wiley.com/10.1002/2013JF002765 (visited on
849 10/28/2020).

850 Turowski, J. M., Wyss, C. R., and Beer, A. R. "Grain size effects on energy delivery to the
851 streambed and links to bedrock erosion". en. In: *Geophysical Research Letters* 42.6 (Mar. 2015),
852 pp. 1775–1780. ISSN: 0094-8276, 1944-8007. DOI: 10.1002/2015GL063159. URL: https://onlin
853 elibrary.wiley.com/doi/abs/10.1002/2015GL063159 (visited on 10/28/2020).

Vore, M. E., Bartholomaus, T. C., Winberry, J. P., Walter, J. I., and Amundson, J. M. "Seismic Tremor Reveals Spatial Organization and Temporal Changes of Subglacial Water System". en. In: *Journal of Geophysical Research: Earth Surface* 124.2 (2019), pp. 427–446. ISSN: 2169-9011. DOI: 10.1029/2018JF004819. URL: https://onlinelibrary.wiley.com/doi/abs/10.1029/2018JF004819 (visited on 01/23/2023).

Welch, P. "The use of fast Fourier transform for the estimation of power spectra: A method based on time averaging over short, modified periodograms". In: *IEEE Transactions on Audio and Electroacoustics* 15.2 (June 1967). Conference Name: IEEE Transactions on Audio and Electroacoustics, pp. 70–73. ISSN: 1558-2582. DOI: 10.1109/TAU.1967.1161901. URL: https://ieeexplore.ieee.org/document/1161901 (visited on 11/10/2023).

Wilcock, P. and Crowe, J. C. "Surface-based Transport Model for Mixed-Size Sediment". en. In: *Journal of Hydraulic Engineering* 129.2 (Feb. 2003), pp. 120–128. ISSN: 0733-9429, 1943-7900. DOI: 10.1061/(ASCE)0733-9429(2003)129:2(120). URL: http://ascelibrary.org/doi/10.1061/%28ASCE%290733-9429%282003%29129%3A2%28120%29 (visited on 10/08/2021).

Wilcock, W., Webb, S., and Bjarnason, I. "The effect of local wind on seismic noise near 1 Hz at the MELT site and in iceland". In: *Bulletin of the Seismological Society of America* 89.6 (Dec. 1999), pp. 1543–1557. ISSN: 0037-1106. DOI: 10.1785/BSSA0890061543. URL: https://doi.org/10.1785/BSSA0890061543 (visited on 03/20/2023).

Wolman, M. G. "A method of sampling coarse river-bed material". en. In: *Eos, Transactions American Geophysical Union* 35.6 (1954), pp. 951–956. ISSN: 2324-9250. DOI: 10.1029/TR035i006p00951. URL: https://onlinelibrary.wiley.com/doi/abs/10.1029/TR035i006p00951 (visited on 10/20/2023).

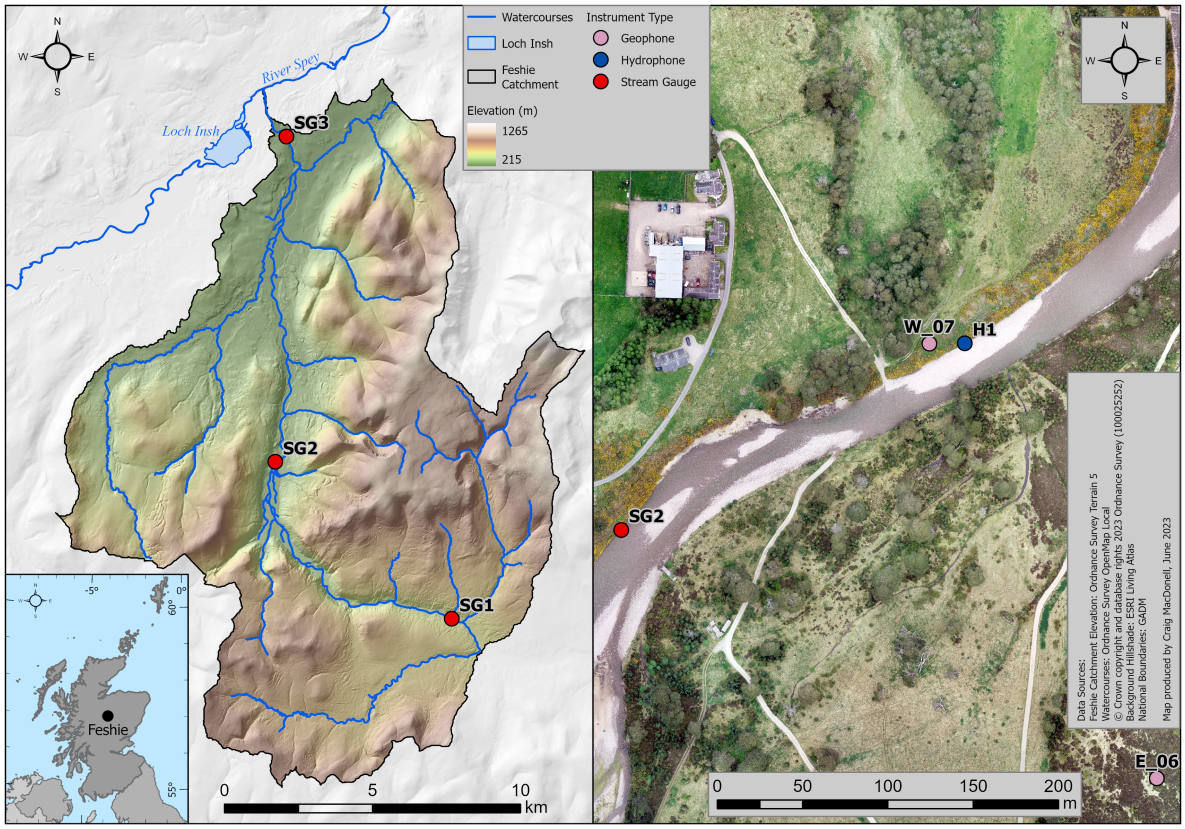


Figure 1: Maps of the River Feshie fieldsite at the (a) catchment scale showing the three stream gauge sites, (b) reach scale showing the sites of instruments used in this study, and (c) national scale. Photos of the field deployments can be found in Supplemental Material S1.

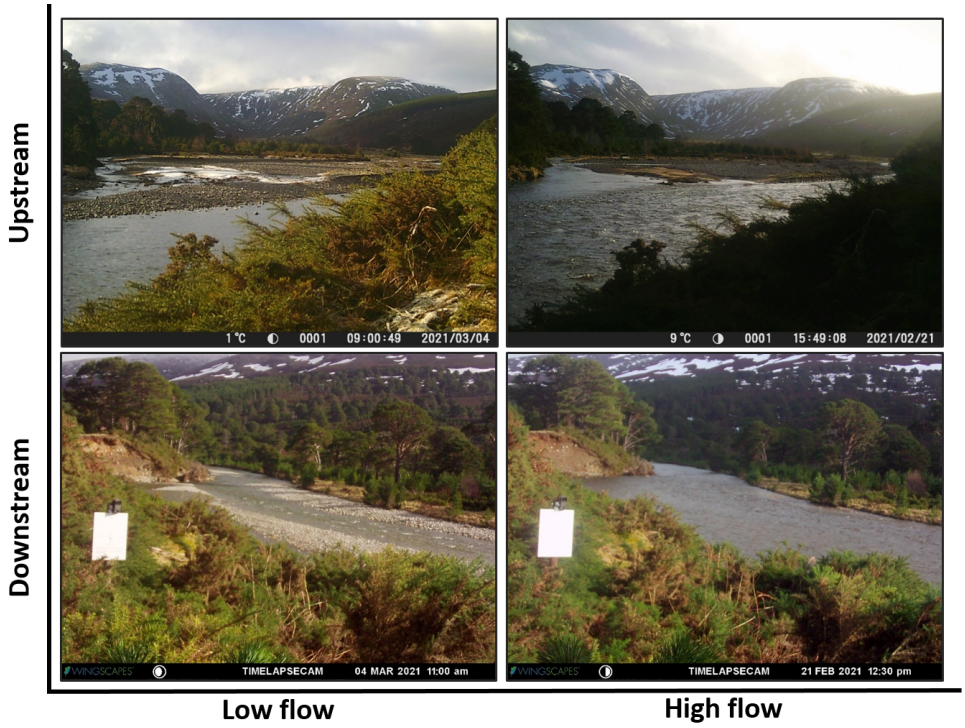


Figure 2: Photos from the River Feshie fieldsite looking upstream and downstream from SG2 during high flow and low flows. Images are taken from February and March 2021 as these had the clearest conditions and are representative of general high and low flows at the site. During the low flow event the SEPA stream gauge at SG3 measured a water level of 0.76 m and the high flow event photographed here peaked at 2.15 m at SG3.

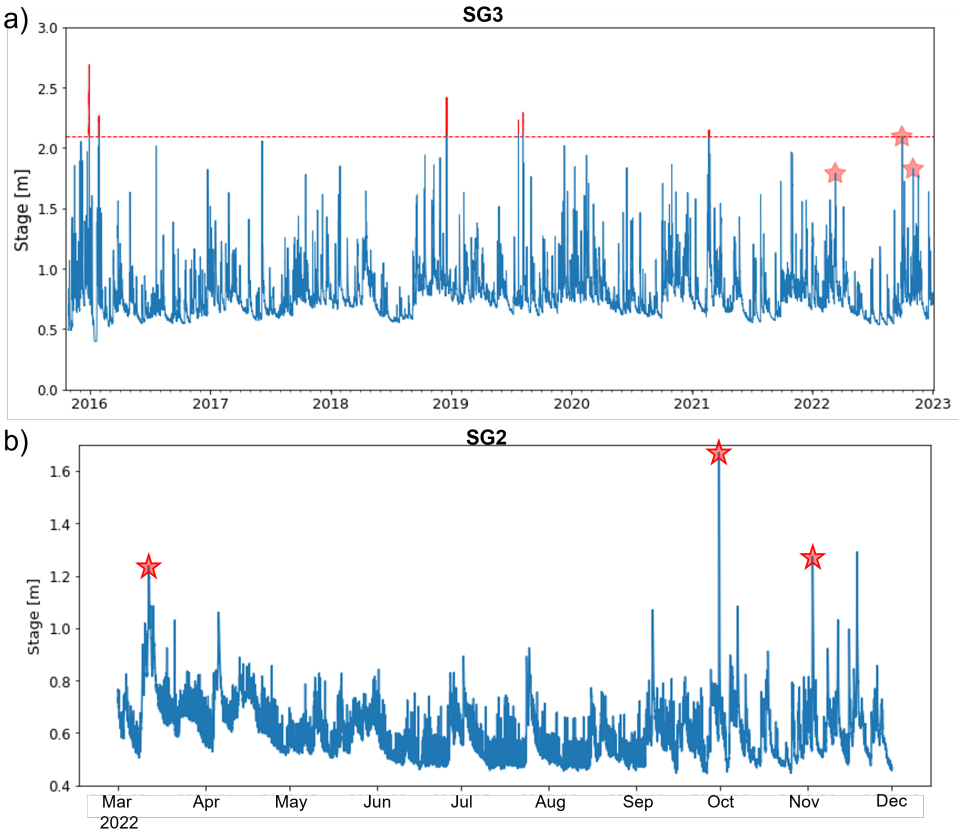


Figure 3: (a) Stage measurements from SEPA stream gauge at SG3 from 27th October 2015 to 31st December 2022. Red stars mark the three largest events in 2022 that are analysed in this study. Red line marks the water level of the largest event in 2022, with peaks that have previously exceeded this value also marked in red. (b) Stage measurements from local stream gauge sensor at SG2 from March through November 2022, showing the three largest events with the red stars.

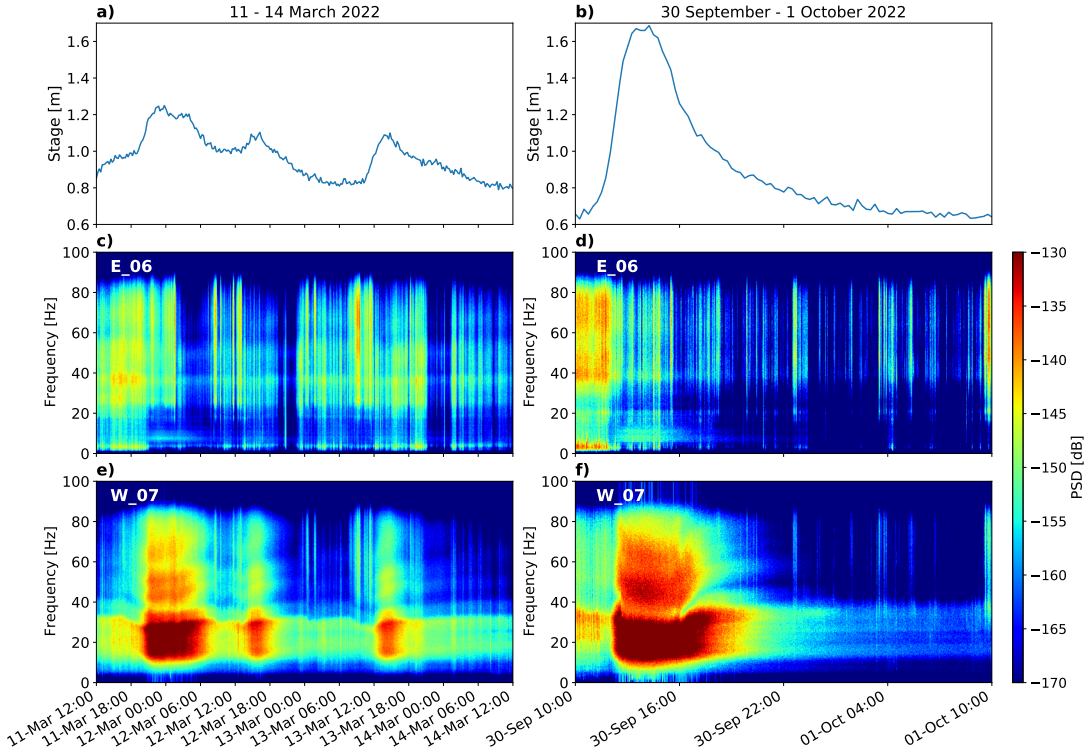


Figure 4: Data for two distinct high flow events in March and September-October 2022, one in each column. Included in this plot are; (a, b) the time-series of the water level at SG2, (c, d) the spectrograms of the geophone data (in 1 minute windows) at the control site to highlight environmental noise such as wind and rain, and (e, f) the spectrograms of the geophones at the river site which is dominated by signals of turbulence and sediment transport.

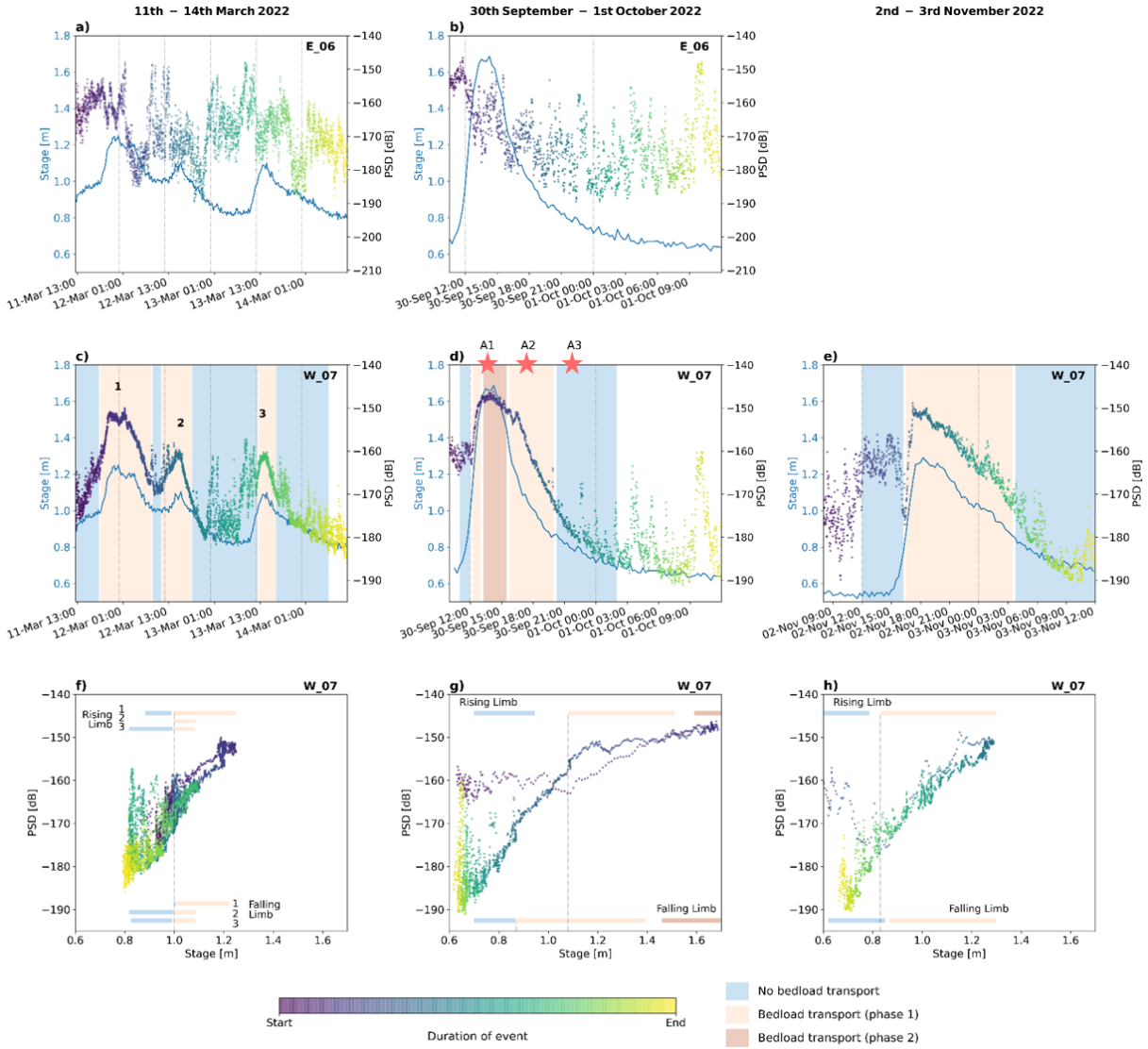


Figure 5: Plots summarising the time series of the water level (blue line) and seismic power averaged over the frequency range 50-60 Hz (points coloured by time) for the three largest flow events in 2022. Each column displays a different event showing; (a, b) the aPSD and water level timeseries' for the control site highlighting the environmental noise around the water level peaks, (c, d, e) the aPSD timeseries for the river site layered on top of the independent classification of bedload transport activity using the hydroacoustic data (white shading shows gaps in the data or when the hydrophone was exposed, blue shows periods where the hydrophone records only turbulence, salmon shows when bedload transport starts (phase 1) and red shows when there is an audible shift to lower frequencies on the hydrophone interpreted to be mobilisation of larger grains during bedload transport (phase 2)), (f, g, h) the PSD versus stage relationship with the hydrophone bedload transport classifications shown as bars for the rising and falling limbs of the hydrological peaks. Numbers 1, 2, 3 in c and f are separate labels for each of the peaks in the March event. Red stars in d) show the timings of the hydrophone recordings included in supplemental Audio 1-3, labelled A1, A2 and A3.

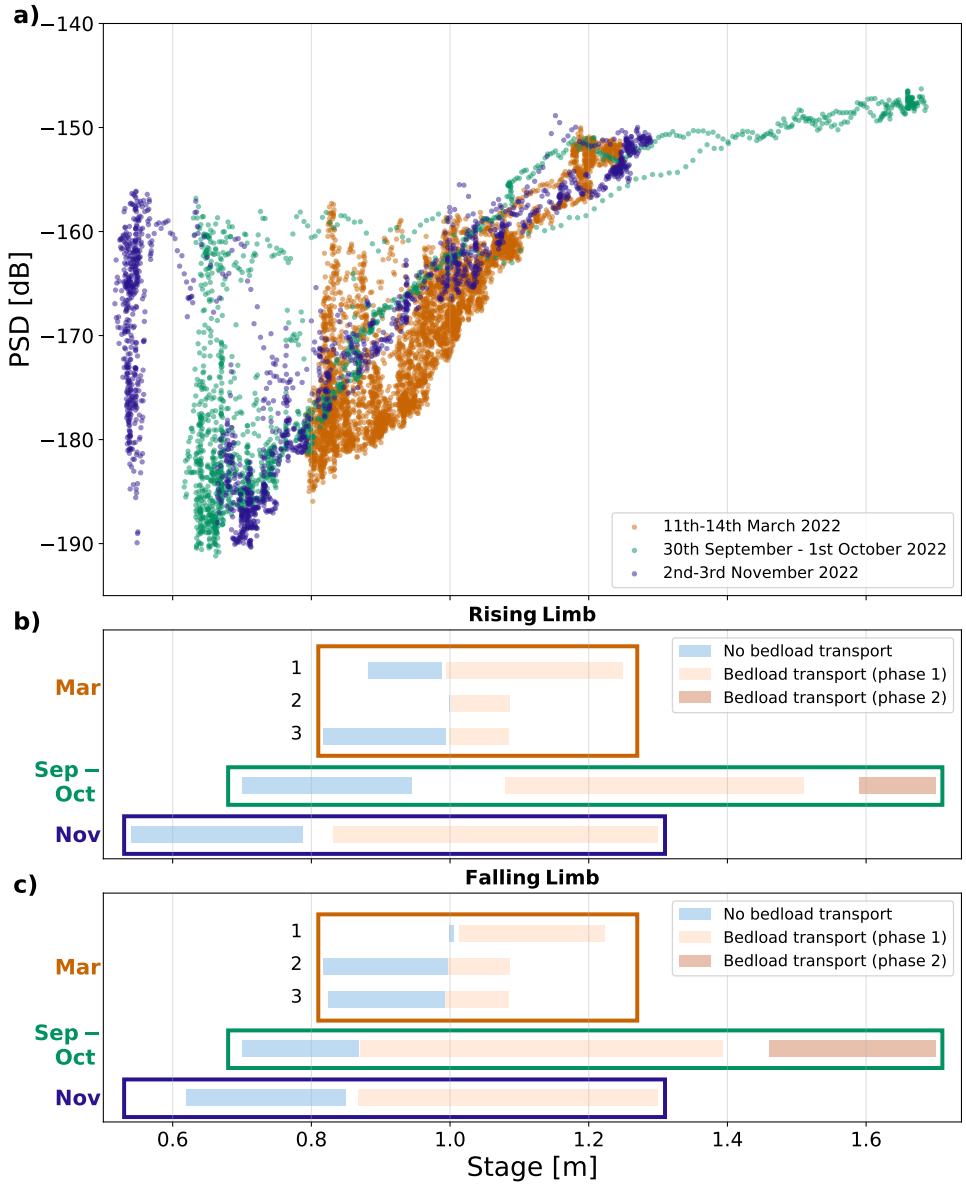


Figure 6: (a) Superposition of the PSD versus water level relationships for three distinct high flow events to enable a clearer comparison of the similarities and differences between each event. (b) Bedload activity transitions from independent interpretation of hydroacoustic data that occurred on the rising limbs of flood peaks for all three events; note that for the March and September events bedload started being transported at a water level of ∼1.00-1.10 m whilst transport during the November event initiated at a water level of ∼0.80 m. (c) Bedload activity transitions from independent interpretation of hydroacoustic data that occurred on the falling limbs flood peaks for all three events; note that for the March event bedload stopped being transported at a water level of ∼1.00 m whilst the arrest of bedload transport occurred at ∼0.85 m for the September and November events.

Audio file captions

Audio 1: Hydrophone audio recording from 13:30 on the 30th September 2023 during the water level peak of the September-October event showing the lower frequency signals observed in the hydroacoustic data, attributed to larger grains being transported.

Audio 2: Hydrophone audio recording from 17:15 on the 30th September 2023 showing the higher frequency signals recorded at water levels below approximately 1.6 m during the September-October event which were categorised as the movement of smaller particles.

Audio 3: Hydrophone audio recording from 21:45 on the 30th September 2023 during of the background turbulence signal following the cessation of bedload transport during the September-October event.